Karlsruhe Institute of Technology

ENERGY-SCALE SYSTEMATICS AT THE KATRIN MAIN SPECTROMETER

Zur Erlangung des akademischen Grades eines
Doktors der Naturwissenschaften
von der Fakultät für Physik
des Karlsruher Instituts für Technologie
genehmigte
Dissertation

von

Dipl.-Phys. Marcel Kraus

aus Speyer

Referent: Prof. Dr. Guido Drexlin
Insitut für Experimentelle Kernphysik, KIT
Korreferent: Prof. Dr. Ulrich Husemann
Insitut für Experimentelle Kernphysik, KIT

Tag der mündlichen Prüfung: 12.02.2016

Declaration of authorship
I declare that I have developed and written the enclosed thesis in hand completely by myself, and have not used sources or means without any declaration in the text.

Erklärung der Selbstständigkeit
Hiermit versichere ich, die vorliegende Arbeit selbstständig angefertigt, alle dem Wortlaut oder Sinn nach entnommenen Inhalte anderer Werke an den entsprechenden Stellen unter Angabe der Quellen kenntlich gemacht und keine weiteren Hilfsmittel verwendet zu haben.

....

Marcel Kraus
Karlsruhe, den 22. Januar 2016

Introduction

This thesis deals with the systematic uncertainties related to the high-precision energy filtering of electrons at the Karlsruhe Tritium Neutrino (KATRIN) experiment. A high degree of understanding of corresponding effects is essential to reach the targeted ν-mass sensitivity of 200 meV (90% C.L.). From the hardware side of the complex HV system at KATRIN, major contributions have been made to develop the necessary equipment to generate ultra-stable electric potentials and to measure their long-term stability with at highest precision. In particular, a detailed model of the influence caused by ripples of the applied voltages on the transmission properties of the large-scale main spectrometer has been implemented and verified trough dedicated measurements.

The experimental observation of neutrino oscillations has established non-vanishing neutrino masses, resulting in the 2015 Nobel prize for physics. Since more than a decade, the research field of neutrino physics is characterized by a rapid development. Even though neutrinos are highly elusive particles with weak interaction only, they affect the universe at the microscopic as well as the macroscopic scale. Neutrino masses in particular hint to physics beyond the Standard model of elementary particles (SM). As oscillation experiments only carry information on the differences between (squared) mass eigenstates, a variety of experimental approaches to estimate the absolute mass scale have been developed. Cosmological methods suffer from a large degree of model dependency, while experiments following the Magnetic-adiabetic collimation combined with an electrostatic filter (MAC-E) filter principle allow to model-independently measure the neutrino mass, relying only on decay kinematics.

Based on the MAC-E filter principle, the KATRIN experiment combines a windowless gaseous tritium source (WGTS) of ultra-high luminosity with a low background and a high-resolution spectrometer. By utilizing the well established MAC-E filter principle, this experiment pushes the frontier of technical feasibility to the ultimate limit for each sub-component to obtain a ν-mass sensitivity of 200 meV (90 % C.L.). This value surpasses the limit given by predecessor experiments by one order of magnitude.

A crucial role to accomplish this challenging experimental goal is played by the electrical potentials applied to the large main spectrometer, as they define the analyzing potential. The central objectives of the thesis in hand are the implementation of a high voltage system which meets the high-stability requirements of the KATRIN experiment, the validation of its design parameters and the determination of the influence of HV distortions on the neutrino mass result.

Outline

The first chapter of this thesis gives a brief overview on neutrino physics and key experimental results of the past. Starting with a short introduction to the phenomenon of neutrino oscillations, a summary of key results is presented, which have established neutrinos as particles with non-vanishing mass. This is followed by a survey to incorporate neutrino masses into the framework of particle physics. In a last step, the most recent neutrino mass limits are given and the precise measurement of the tritium beta-spectrum is discussed as a high-precision, model-independent method to determine the electron anti-neutrino mass purely based on kinematics.

The second chapter gives an overview of the experimental setup of KATRIN and its MAC-E filter principle. At first, the energy scale systematics caused by imperfections of the high voltage are discussed thoroughly. Then a brief summary of all main components is given with the focus clearly put onto the spectrometer and detector section (SDS).

In the scope of this thesis specific measurements with the SDS part of the experiment were performed. Therefore a more detailed description of the setup and its working conditions is given in chapter three. A key component here was played by the electron gun (e-gun) as source of electrons with well-defined energy and high angular resolution. This is of great importance, as it is essential to investigate the transmission properties of the main spectrometer.

A detailed description of the high voltage system and of the contributions to it made in the scope of this thesis is given in chapter four. Apart from the non-trivial task of generating and measuring potentials with the required stability, the high voltage system has been upgraded to allow a fully automated operation.

Focusing on measurements that were performed with the monitor spectrometer, chapter five gives an overview of its unique capabilities in determining the analyzing potential. These investigations have revealed the excellent DC stability of the KATRIN voltage dividers and of the utilized implanted Kr/Rb sources. In addition, the possibility to discover AC fluctuations of the retardation potential through measurements of the krypton line shape is explored.

Chapter five deals in particular with the central theme of energy scale systematics and the high voltage stability of the main spectrometer. An in-depth is given of the relationship between HV ripples and the fields inside the vessel. Moreover, a proper statistical description of the spectrometer acting as a binomial experiment with Poisson distributed population is derived.

In a final step of analysis, the response function is extended to implement the knowledge gained from the previous results in chapter seven. This step embeds this thesis in the global scope of the KATRIN analysis framework. Chapter eight summarizes and all presented affords and concludes with an outlook.

Contents

CHAPTER 1

Neutrino Physics

The Nobel Prize 2015 in physics was awarded to T. Kajita and A. B. McDonald for the experimental observation of neutrino oscillations. This shows the major importance and the growing interest in neutrinos that, due to their evasive behavior, were initially regarded as theoretical constructs only. Due to their weak interacting, neutrinos still have many unknown properties and hint to new physics beyond the SM, resulting in a rapidly growing field of research. The main objective of the KATRIN experiment is the determination of the electron anti neutrino mass $\mathrm{m}_{\bar{\nu}_e}$. Rather than giving a complete historical overview or a detailed description of neutrino physics in general this chapter focuses on the introduction of the necessary theoretical foundation to motivate the need for research at the frontier in the field of neutrino physics.

1.1 Neutrinos in the Standard Model

The SM describes quarks and leptons to interact via intermediating gauge bosons as representatives of the weak, strong and electromagnetic force. Gravitational forces are not further discussed here, as quantum field theories of this interaction yield non-renormalizable terms and a fully closed quantum description of gravity still remains to be found. Furthermore, the mechanism of spontaneous symmetry breaking used to generate particle masses manifests as an additional particle, the Higgs boson that only recently was discovered at the Large Hadron Collider (LHC) ([ATL12], [CMS12]), thereby providing the SM with its last and previously unobserved particle. All quarks and leptons are fermions.

In the following the focus lies on neutrinos and the weak force. Within this framework, three generations of neutrinos are known as eigenstates of the weak force, which are grouped with their leptonic counterparts into doublets. Furthermore the weak interaction is described as a theory of pure V-A couplings that violates parity maximally. Therefore the leptonic doublets consist of left-handed particles, whereas right-handed antiparticles remain singlets of the underlying SU(2) gauge-symmetry. Neutrinos thus are massless particles within the original SM.

1.2 Beyond the Standard Model

As is mentioned, neutrinos are massless fermions in the framework of the SM. However, the experimental observation of neutrino oscillations requires at least two neutrinos to have non-vanishing masses. Consequently, massive neutrinos directly hint at physics beyond the SM. The empirical description of neutrino oscillations can be carried out by treating the mass-eigenstates of these particles to be different from their flavor-eigenstates. Neutrinos thus may have properties beyond the framework of the SM, implying the existence of so called sterile neutrinos, that interact gravitationally but not weakly. The KATRIN experiment is able to measure such mass-eigenstates as an additional scientific goal. In the following paragraphs, the experimental evidence for oscillations is shortly cited and the theory of neutrino masses amongst together with aspects of sterile neutrinos are outlined and the current state of neutrino mass determination is surveyed.

Neutrino oscillations

The Nobel prize in physics 2015 has been awarded to T. Kajita and A. B. McDonald, for their leader ships in the Super-Kamiokande ([Kaj98]) and Sudbury Neutrino Observatory (SNO) ([Hel02]) collaborations. These experiments found significant evidence for neutrino oscillations. The neutrino rest mass has to be non-zero for at least two of the three known neutrinos. To fully describe this phenomenon requires a quantum field theory approach, for illustrative purposes it is however sufficient to use a simpler model, following [Zub11].

Inside the quark-sector, the Cabibbo-Kobayashi-Maskawa (CKM) matrix is an established method of connecting the flavor-eigenstates with the mass-eigenstates of quarks. For neutrino oscillations, an equivalent model can be used where the n flavor-eigenstates $|\nu_\alpha\rangle$ and the n mass-eigenstates $|\nu_k\rangle$ can be connected by a unitary $n \times n$ matrix U.For antineutrinos $|\bar{\nu}\rangle$ and neutrinos $|\nu\rangle$ this becomes

$$|\nu_\alpha\rangle = \sum_k \mathrm{U}_{\alpha k}\,|\nu_k\rangle \qquad \text{and} \qquad |\bar{\nu}_\alpha\rangle = \sum_k \mathrm{U}^*_{\alpha k}\,|\bar{\nu}_k\rangle\,. \tag{1.1}$$

In general, the matrix U can be parameterized by $n\,(n-1)/2$ mixing angles, $(n-2)(n-1)/2$ Dirac phases and $(n-1)$ Majorana phases ([Oli14]). Together with the time-evolution of a neutrino with a given momentum $\mathbf{p}_k$ and spatial coordinate vector $\mathbf{x}$

$$|\nu(\mathbf{x},t)\rangle = \mathrm{e}^{-i(E_k t - \mathbf{p}_k \mathbf{x})}\,|\nu_k\rangle\,, \tag{1.2}$$

a short calculation yields

$$\mathrm{P}(\nu_\alpha \to \nu_\beta)(L,E) = \sum_k |\mathrm{U}_{\alpha k}\mathrm{U}^*_{\beta k}|^2 + 2\,Re \sum_{k<l} \mathrm{U}_{\alpha k}\mathrm{U}^*_{\alpha l}\mathrm{U}^*_{\beta k}\mathrm{U}_{\beta l}\mathrm{e}^{-i\frac{L}{E}\frac{\Delta m^2_{kl}}{2}}\,. \tag{1.3}$$

Here, the so called baseline-length $L = |\mathbf{x}|$ and the difference of the squared masses $\Delta m^2_{kl} = m^2_k - m^2_l$ are introduced. The first term reflects an average transition probability, while the second one depends on the formerly introduced parameters and the energy E. Evidently, oscillations are only observable in the case of a non-diagonal matrix U and at least one non-vanishing neutrino mass. For a better understanding, we consider the case of only two generations of neutrinos, so that a unitary 2×2 matrix can be used, which is parameterized by one angle θ,

$$U = \begin{pmatrix} \cos(\theta) & \sin(\theta) \\ -\sin(\theta) & \cos(\theta) \end{pmatrix} . \tag{1.4}$$

For two generations of neutrinos the transition probability directly follows to be

$$\mathrm{P}(\nu_\alpha \to \nu_\beta)(L{,}E) = \sin^2(2\theta)\sin^2\left(\frac{L}{E}\frac{\Delta m^2_{12}}{4}\right) . \tag{1.5}$$

The model can be expanded to include three neutrinos, which will not be shown here. As seen in eq. (1.3), the observation of neutrino oscillations allows to determine the squared mass differences and mixing angles, but not the absolute mass scale. For this reason, experiments based on different techniques have to be utilized, see section 1.3.

Experiments searching for neutrino oscillations either investigate the appearance or disappearance channel of a specified neutrino flavor. For such measurements to be successful, a detailed knowledge of the neutrino flux, id est the number and energy of neutrinos emitted by a specific source has to be known with high accuracy. Typically solar, atmospheric, accelerator or reactor neutrinos act as source. Each source yields results sensitive in different regions, because of the natural processes that cause neutrinos to be emitted at certain energies and the non-fixed baseline lengths such as the distance of the earth to the sun. A summary of the current status of the measured oscillation parameters is given in table 1.1.

Neutrino mass generation

The observation of neutrino oscillations described in the previous paragraph requires non-vanishing neutrino masses. One possible way of implementing massive neutrinos into the framework of an extended SM is outlined in the following, based on [Kle14]. Here the

Table 1.1: Summary of neutrino oscillation parameters based on a global fit of current neutrino-oscillation data. Values in brackets indicate the invertered mass hierarchy scenario, the others the normal hierarchie scenario. The sqared mass difference is defined as $\Delta m^2 = m_3^2 - (m_2^2 + m_1^2)/2$. All results taken from [Oli14].

Paramater	best-fit (1-σ)
$\Delta m^2_{21}(10^{-5}\,\mathrm{eV}^2)$	$7.54^{+0.26}_{-0.22}$
$\lvert\Delta m\rvert^2(10^{-3}\,\mathrm{eV}^2)$	$2.43^{+0.06}_{-0.06}$ $(2.38^{+0.06}_{-0.06})$
$\sin^2\theta_{12}$	$0.303^{+0.017}_{-0.017}$
$\sin^2\theta_{23}$, $\Delta m^2 > 0$	$0.0437^{+0.033}_{-0.023}$
$\sin^2\theta_{23}$, $\Delta m^2 < 0$	$0.0455^{+0.039}_{-0.031}$
$\sin^2\theta_{13}$, $\Delta m^2 > 0$	$0.0234^{+0.0020}_{-0.0019}$
$\sin^2\theta_{13}$, $\Delta m^2 < 0$	$0.0240^{+0.0019}_{-0.0022}$
$\delta/2\pi$	$1.39^{+0.038}_{-0.027}$, $(1.31^{+0.029}_{-0.033})$

basic information is again taken from [Zub11].

Charged fermions can only acquire mass through Dirac-mass terms in the Lagrangian,

$$\mathcal{L} = m_D(\bar{\psi_L}\psi_R + \bar{\psi_R}\psi_L), \tag{1.6}$$

where ψ_L and ψ_R are the chiral representations of the fermionic field. Neutral particles such as the neutrino can however obtain their mass through another mechanism, as they can be represented as Majorana particles. With $\psi_L = \nu_L$, $\psi_R^c = \nu_R^c$, $\psi_R = N_R$ and $\psi_L^c = N_L^c$ the corresponding Lagrangian can be expressed as

$$\mathcal{L} = \frac{1}{2}(\bar{\nu}_L, \bar{N}_L^c)\begin{pmatrix} m_L & m_D \\ m_D & m_R \end{pmatrix}\begin{pmatrix} \nu_R^c \\ N_R \end{pmatrix} + h.c. \tag{1.7}$$

As usual an upper index c denotes the charge conjugate of a field and *h.c.* the hermitian conjugate. Note the N_L and N_R fields to be sterile neutrinos which do not participate in the weak interaction. In case of $m_D = 0$, this case yields purely Majorana-type masses, retrospectively Dirac-type masses for $m_L = m_R = 0$. For $m_L = 0$ and $m_R \gg m_D$ the eigenvalues of the mass matrix become

$$m_\nu = \frac{m_D^2}{m_R} \qquad \text{and} \qquad m_N \approx m_R. \tag{1.8}$$

Then small neutrino masses can be introduced by assuming their Dirac-masses to be in the order of MeV to GeV, i.e. in the mass region of the charged fermions, and the mass of the sterile neutrino m_N at the Grand Unified Theory (GUT) scale, i.e. around 10^{16}GeV. This is well known as the type-I see-saw mechanism, that leads to a hierarchical mass scenario. The type-II mechanism leads to the degenerate mass scenario if the mass m_L is not vanishing. Especially the nature of neutrinos as Majorana particles would lead to a violation of lepton number conservation. Inside the SM this number is conserved, however without underlying symmetry. Therefore the observation of Majorana neutrinos is an additional field of interest.

1.3 Neutrino mass determination

A variety of theories to generate massive neutrinos has been established and the experimental validation of neutrino oscillations necessarily renders at least two neutrinos to be massive. As neutrino oscillation experiments are not sensitive to the absolute mass scale, different approaches have to be taken to estimate them. Many approaches, such as cosmological surveys, strongly depend on the input models. Contrary to these experiments, the KATRIN experiment is free of model-dependency, only relying on kinematics of the nuclear beta decay. The spectroscopy here is peformed by the glsMAC-E principle.

Cosmology

A rather successful model to describe the evolution of the universe and its content from the Big Bang until the present day is the ΛCDM standard model of cosmology. It predicts a large number of neutrinos forming the cosmic neutrino background (CνB) with a number density of 336 cm^{-3} ([Zub11]). Even as most abundant fermionic matter in the universe, these particles have not yet been detected, owing to their very small cross sections. In fact, in cosmology only the sum of masses is accessible which contributes to the neutrino energy density of the universe by

$$\sum_k m_k = 93\Omega_\nu h^2 \,\mathrm{eV}, \tag{1.9}$$

with the Hubble parameter h and the contribution Ω_ν of relic neutrinos to the total energy density Ω_{tot} of the universe. The newest results of the Planck collaboration in 2015 ([Ade15]) give an upper limit of

$$\sum_k m_k \leq 0.23\,\mathrm{eV}\,(95\%\mathrm{C.L.}). \tag{1.10}$$

This rather small value is only obtained by a series theoretical assumptions.Also, this limit has been retained by combining several data sets and an analysis of several strongly correlated parameters. In fact, the standard model of cosmology would benefit greatly from an independent measurement of the neutrino masses that eliminates one free parameters and eases the determination of the others.

Neutrino-less Double Beta Decay

Majorana neutrinos are identical to their own antiparticles, so the observation of the $0\nu\beta\beta$ decay

$$2n \rightarrow 2p + 2e^-, \tag{1.11}$$

would allow to estimate the absolute mass of neutrinos and establish the neutrino as Majorana particle. The right-handed anti-neutrino $\bar{\nu}_e$ emitted at one vertex has to be absorbed as left-handed neutrino ν_e at the other vertex, see fig. 1.1. By exchanging a

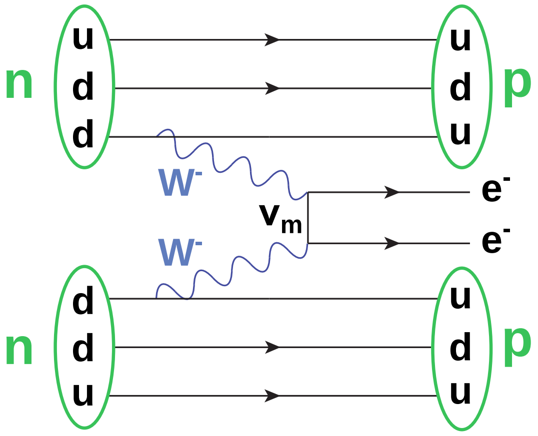

Figure 1.1: Feynman diagram of the $0\nu\beta\beta$ decay. The virtual neutrino emitted at one vertex gets absorbed at the second vertex. The process requires neutrinos to be identical to their antiparticles and is only allowed for massive neutrinos. Taken from [Har15].

virtual neutrino, this process is therefore only allowed for massive neutrinos, as it requires a 'helicity flip' between the two vertices. If the small recoil carried by the daughter nucleus is neglected, the two emitted electrons carry the entire decay energy. By measuring this energy, a peak is to be expected at the endpoint energy Q of the decay. Furthermore, the Majorana-phases δ_i can lead to cancellations, as the effective neutrino mass

$$\langle m_{\beta\beta}\rangle = \left|\sum_k |U_k|^2 m_k \mathrm{e}^{i\delta_k}\right|, \tag{1.12}$$

is an incoherent sum of the mass-eigenstates. The observation of the half-life $\mathrm{T}_{1/2}^{0\nu\beta\beta}$ of the $0\nu\beta\beta$ decay

$$T_{1/2}^{0\nu\beta\beta} = G(Q,Z)|M|\frac{\langle m_{\beta\beta}\rangle^2}{m_e^2}, \tag{1.13}$$

with $G(Q,Z)$ being a phase space factor, allows to estimate $\langle m_{\beta\beta}\rangle$. Additionally, the matrix element M of the nuclear transition has to be precisely known. Up to now, the GERDA collaboration has published ([Ago13]) one of the best limits for $\mathrm{T}_{1/2}^{0\nu\beta\beta}$ by measuring the half-life of the ^{76}Ge,

$$T_{1/2}^{0\nu\beta\beta} = 2.1 \cdot 10^{25}\,\mathrm{y}\,(90\%\,\mathrm{C.L.}). \tag{1.14}$$

This yields a neutrino mass limit of

$$\langle m_{\beta\beta}\rangle = 250 - 520\,\mathrm{meV}, \tag{1.15}$$

where the large uncertainty arises from the non-trivial computations of the matrix element.

Single Beta Decay

Precise measurements of the end-point of the single beta decay energy spectrum

$$n \to p + e^- + \bar{\nu}_e \tag{1.16}$$

yield a method to determine the electron anti-neutrino mass in an entirely model-independent way, only relying on kinematics. Energy conservation thus leads to a continuous β-spectrum with its end-point at the maximally available energy Q. Consequently it is the end-point that is of special interest to these experiments. From Fermi's golden rule the spectral shape can be calculated to be ([Dre13])

$$\begin{aligned}\frac{\mathrm{d}N^2}{\mathrm{d}E\mathrm{d}t} =& \frac{G_\mathrm{F}^2 \cos^2(\theta_\mathrm{C})}{2\pi^3}\,|M|^2\,F(Z+1,E)\,p\,(E+m_\mathrm{e}) \\ & (E_0-E)\sqrt{(E_0-E)^2 - m_{\bar{\nu}_\mathrm{e}}^2}\,\Theta(E_0-E-m_{\bar{\nu}_\mathrm{e}}).\end{aligned} \tag{1.17}$$

Here, the relativistic energy-momentum relation has been used for the special case of a super-allowed nuclear transition, G_F is the Fermi constant and $F(Z+1,E)$ the Fermi function. Also note that the observable mass m_{ν_e}

$$m^2_{\nu_e} = \sum_k |U_k|^2 m^2_k, \tag{1.18}$$

is an incoherent weighted sum over the mass-eigenstates, in contrast to the effective Majorana-mass.

In general, single beta-decay experiments have to optimize the luminosity of the source, the energy resolution of the detector and the signal-to-background ratio at the end-point in order to achieve high sensitivity. Over the last decades a series of experiments has used tritium as beta emitter, owing to its many advantages. First, the low end-point energy $Q \approx 18.6\,\mathrm{keV}$ allows to employ a MAC-E filter system for high-precision spectroscopy. The short half-life yields a high luminosity and therefore guarantees high statistics. As mentioned, the ^{3}He-decay of tritium is furthermore super-allowed and the very small nuclear charge results in a simple structure of the atomic shell of the daughter nuclei. Additionally, its gaseous phase at low temperatures provides the advantage of small systematics superior to solid sources.

The best model-independent measurements have been performed by making use of MAC-E filters by experiments in Troitzk ([Lob85]) and Mainz ([Ott94]). Their combined data yield an upper limit for the electron anti-neutrino mass of ([Oli14])

$$m_{\bar{\nu}_e} = 2.0\,\mathrm{eV}, \tag{1.19}$$

that is an order of magnitude larger than the sensitivity targeted in the next-generation experiment KATRIN.

CHAPTER 2

The KATRIN Experiment

As the next generation β-decay experiment KATRIN is targeted to determine the absolute mass scale of electron antineutrinos with unmatched sensitivity of $m_{\bar{\nu}_e} = 200\,\mathrm{meV}$ (90 % C.L.). To exceed the sensitivity of the predecessor experiments by one order of magnitude, KATRIN employs three distinct spectrometers of the MAC-E filter type in combination with a windowless gaseous tritium source of high luminosity. This is complemented by a two-stage tritium pump consisting of cryogenic and differential pumping elements along a multi pixel silicon detector for read out. Each element is specially developed and composed of state-of-the-art parts. The basic experimental setup is given by the MAC-E filter principle that has been used in several successful predecessor experiments. Having its advantage in well known and transmission properties, the MAC-E filter approach allows high-precision β-spectroscopy relying solely on decay kinematics. However, to reach the sensitivity goals the KATRIN experiment has to improve the knowledge of systematic effects by a factor of 100 and thereby push the frontier of technological innovation for most of its sub-components. The extended dimension of the KATRIN setup can lead to complex, previously unknown effects which can lead to deviations of previously established features from their assigned model values. Even with the knowledge obtained by the predecessor experiments, this makes studies, dedicated to the validation and adaption of established models indispensable. In the process of doing so, these studies have to simultaneously identify and describe new processes.

Keeping in mind the fundamental concepts of kinematic β-decay experiments, as introduced in section 1.3, the working principle of MAC-E filter type spectrometers will be outlined in more detail in the following section 2.1. This especially implies mechanisms known to cause background and the basic processes governing the transport of electrons through the MAC-E filter. After addressing these foundations, more advanced topics are discussed. A key issue are electric potential distortions which are reviewed in the most general way possible (section 2.2). These investigations will then be used to motivate the entire scope of this thesis. Finally, all sub-components of the KATRIN beam-line and their corresponding boundary conditions are described schematically in the last section of this chapter. (section 2.3).

2.1 The MAC-E filter

Single beta-decay experiments as KATRIN allow to conduct high-precision electron spectroscopy near the endpoint of the β-spectrum. Combining a high luminosity with a high resolution, the MAC-E filter provides a well established way to do so. Being based on the knowledge of electrical and magnetic fields, retarding spectrometers of this type have well known transport mechanisms for signal electrons. The following sections give a description of the experimental principle.

2.1.1 Functional principle

Originally proposed in [Bea80] and further advanced in [Kru83], spectrometers of the MAC-E filter type act as a high-pass filter for electrons which are collimated by magnetic fields. By measuring the total count-rate of transmitted electrons from tritium β-decay for different retarding potentials near the endpoint an integral spectrum is gained. Figure 2.1 shows an overview of the working principle described in detail throughout the next sections.

Magnetic guidance and collimation

Electrons emerging from beta-decay in the source are emitted isotropically, thus MAC-E filter type spectrometers utilize a magnetic field as a guiding system for these particles. As a result of the Lorentz force, charged particles such as electrons move around magnetic field lines on a cyclotron orbit (fig. 2.2(a)). Magnetic guiding, thus ensures a high angular acceptance of almost 2π and therefore a high luminosity of signal electrons reaching the detector. Momentum and hence energy of the particles can be parameterized by a component orthogonal to the magnetic field lines and one parallel to the field lines, visualized in fig. 2.2(b)

$$\mathbf{p} = \mathbf{p}_\perp + \mathbf{p}_{||} \qquad \text{and} \qquad E_{kin} = E_\perp + E_{||}. \tag{2.1}$$

As only the longitudinal part of the energy is being analyzed by a MAC-E filter, it is necessary to maximize this component which is equivalent to minimize the polar angle θ. With the Lorentz factor γ and the magnetic moment μ this is achieved by keeping their product

$$\gamma\mu = \frac{\gamma + 1}{2} \cdot \frac{E_\perp}{B} \tag{2.2}$$

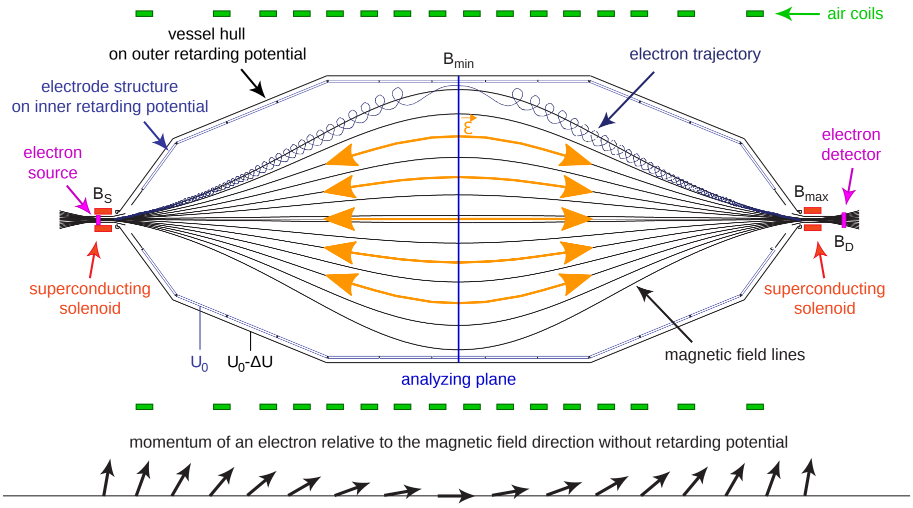

Figure 2.1: MAC-E filter principle. Electrons emitted from the source are guided by a magnetic field generated by superconducting solenoids at the ends of the spectrometer and so called air coils used for fine adjustment. During the propagation through the apparatus the transverse momentum gets adiabatically transformed into longitudinal momentum. The energy selection is accomplished with a electric field acting only on the longitudinal component of the momentum. Adapted from [Zac09]

constant along the electrons path. As the Q value of tritium is only $E_0 = 18.6\,\mathrm{keV}$, the emitted electrons can be treated non-relativistically to first order, so that the above equation, together with $\gamma\mu$ necessarily being a constant of motion, reduces to

$$\mu = \frac{E_\perp}{B} = \text{const.} \ , \tag{2.3}$$

for adiabatic transport. Reducing the magnetic field strength along the electron's trajectory and together with energy conservation lead to the transverse energy component being transformed into the longitudinal component adiabatically. To ensure the adiabaticity during the transport the field gradients have to be kept small over one cyclotron motion, or in more mathematical terms

$$\frac{\Delta U}{U} \ll 1 \qquad \text{and} \qquad \frac{\Delta B}{B} \ll 1. \tag{2.4}$$

While the magnetic field strength decreases, the electric potential increases from either side of the spectrometer up to the analyzing plane (see next paragraph). It is obvious that both effects have to be precisely attuned to each other, as otherwise an electron could be reflected ('early retardation').

Electrostatic retardation

After the initially isotropic electrons have been collimated and their momentum has been largely aligned to the magnetic field, with only a very small fraction of transversal momentum remaining, the energy selection takes place. Here it has to be recalled that only

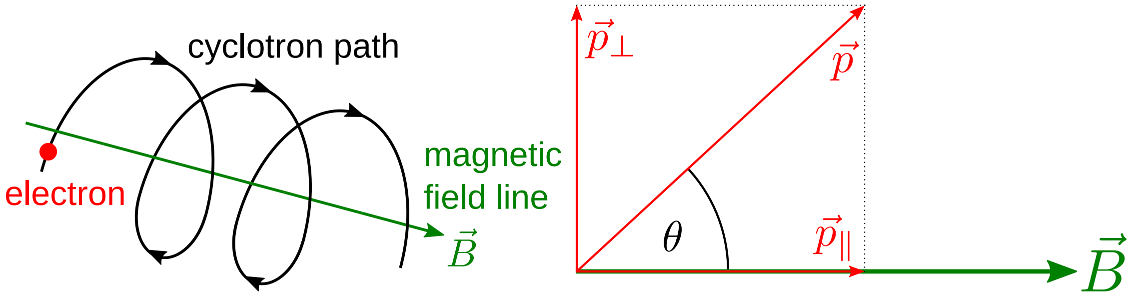

(a) Cyclotron motion **(b)** Definition of the polar angle

Figure 2.2: Schematic visualization of an electron's cyclotron orbit along a constant magnetic field line (a) and the illustration of the polar angle definition (b). Adapted from [Gro15b].

signal electrons with energies within a few eV below the endpoint region carry information about the neutrinos mass. For this reason an electrostatic retarding potential is applied to the whole spectrometer, leading to an electric field parallel to the magnetic field lines (for a detailed description see section section 4.2). The generated electric field is symmetrical with respect to the analyzing plane at the center of the spectrometer. According to

$$E_\parallel \geq qU_\mathrm{ret}, \tag{2.5}$$

only electrons with a longitudinal kinetic energy greater than the retarding potential are able to pass through the potential barrier and reach the detector.

Energy resolution

Equation 2.3 already implies that it is not possible to transform the transversal energy completely into longitudinal energy. To clarify the process qualitatively, one can imagine an electron propagating with a given kinetic energy $E_\mathrm{kin} = qU_\mathrm{ret}$ being perfectly aligned along a magnetic field line, where U_ret denotes the electric potential in the analyzing plane. Following eq. (2.5) such an electron will be transmitted because $E_\mathrm{kin} = E_\parallel = qU_\mathrm{ret}$. On the other hand an electron with the exactly the same energy but whose trajectory is not parallel to the magnetic field, will not be transmitted, as for non-zero magnetic field transverse energy remains $E_\perp \neq 0$, so that the transmission condition is broken, $E_\mathrm{kin} = E_\perp + E_\parallel < qU_\mathrm{ret}$. If one defines the missing energy for a non-aligned electron to be transmitted as $\mathit{\Delta} E$, it is straightforward to calculate the relation

$$\mathit{\Delta} E = \frac{E_\mathrm{kin,\ max}}{B_\mathrm{max}} B_\mathrm{min}, \tag{2.6}$$

with B_max denoting the highest magnetic field, $E_\mathrm{kin,\ max}$ the maximal kinetic affiliated to this field, and B_min being the smallest magnetic field of the filter. In this context it is common to speak of $\mathit{\Delta} E$ as 'energy resolution', although the term 'energy width' would be more appropriate. In the case of KATRIN it is given by

$$\mathit{\Delta} E = \frac{3 \cdot 10^{-4}\,\mathrm{T}}{6\,\mathrm{T}} \cdot 18.6\,\mathrm{keV} = 0.93\,\mathrm{eV}. \tag{2.7}$$

In section 2.2 discussing the transmission function it will be shown that this result is not in conflict with the design ν-mass sensitivity of 200 meV, as long as one is aware of the exact transmission properties.

Magnetic mirror effect

For electrons traveling from regions of low magnetic fields to the high field region, the reverse process of the previously described collimation will take place. This can cause an electron to be reflected magnetically. The condition for an electron to be mirrored is given by the maximal polar angle

$$\mathit{\Theta}_{\mathrm{max}} = \arcsin\sqrt{\frac{B_{\mathrm{source}}}{B_{\mathrm{max}}}}. \tag{2.8}$$

All electrons with starting angles $\mathit{\Theta} > \mathit{\Theta}_{\mathrm{max}}$ will be reflected. Note that this condition is entirely independent of the kinetic energy. At first glance this relation looks like a disadvantage of MAC-E filters, as it decreases the angular acceptance and therefore the source luminosity. However, electrons emitted with large polar angles suffer from potential systematic effects like increased scattering probabilities off tritium molecules in the source and enhanced energy losses due to synchrotron radiation. In fact the process of magnetic reflection is beneficial by minimizing systematic uncertainties that otherwise would influence the experimental sensitivity.

The magnetic field strength values adapted for the KATRIN experiment of $B_{\mathrm{source}} = 3.6\,\mathrm{T}$ for the source and B_{max} for the pinch (PCH) magnet, yield a maximal acceptance angle of $\mathit{\Theta}_{\mathrm{max}} = 50.77°$.

2.1.2 Background sources

Although a detailed understanding of the mechanisms leading to background in a MAC-E filter is not the main focus of this thesis (this lies in the investigation of transmission properties), a profound knowledge of background-generating mechanisms is crucial to perform a successful ν-mass analysis in a MAC-E filter type experiment. The challenge of clarifying background sources has been central part of many investigations. Accordingly only a schematic enumeration of the known background sources can be given here.

> **Secondary emission** caused by cosmic muons or other particles. If an external particle interacts with the stainless steel of the spectrometer near its inner surface, the emerging electrons can enter the flux tube via an $\mathbf{E} \times \mathbf{B}$ drift. Several countermeasures to reduce background caused by such particles have been taken. The first is also an intrinsic feature of MAC-E filters. Low-energy electrons emitted from the surface are reflected back to the surface via the Lorentz force, an effect known as

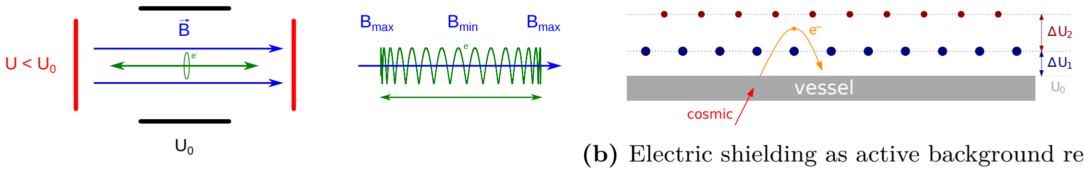

(a) The left side illustrates the principle of Penning traps. Electrons get confined axially by the magnetic field and radially by electric potential barriers. On the right side a magnetic bottle is shown, consisting of two connected magnetic mirrors it stores charged particles. Taken from [Gro15b].

(b) Electric shielding as active background reduction method. A cosmic particle (more generally just a particle independent of its origin), produces an electron via interaction with the stainless steel of the spectrometer. This effect gets counteracted by a double layered wire electrode on iteratively more negative potential. Taken from [Lei14]

Figure 2.3: Several mechanisms contributing to the background observable in MAC-E Filters.

magnetic shielding. As an additional active counter measure the KATRIN main-spectrometer features a double-layered inner wire electrode system (see fig. 2.3(b)). By setting the wire layers on a more negative potential than the vessel, negatively charged particles from the vessel are electrostatically reflected.

Another characteristic source of background is given by the decay of radioactive isotopes in the spectrometer itself. One source of this could be tritium molecules that made their way from the source section into the spectrometer volume.This however is suppressed to negligible levels by the pumping section (section 2.3.3). A more serious effect is the α-decay of the radon isotopes ^{119,220}Rn, emanated from all large surfaces like the spectrometer vessel itself and the non-evaporable getter (NEG) pumps. If an α-decay takes place, electrons with energies up to the keV-regime can be emitted. Those primary electrons will be stored in the volume and thus produce secondary electrons by ionization of residual gas molecules. During the first two KATRIN SDS measurement phases it was shown that this background-contribution can be reduced significantly by a liquid nitrogen (LN2)-cooled Cu-baffle system ([Sch14], [Har15]). Located between the NEG pumps and the sensitive spectrometer volume, the baffles prohibit radon atoms from entering the spectrometer via cryogenic adsorption ([Goe14]).

Magnetically stored particles are trapped by two magnetic mirrors of the two superconducting magnets at both ends which form a so called magnetic bottle ([Hig07], [Hig08]). As stated above an electron, independently of its kinetic energy, can be reflected when traveling from a low to a high field region (right side of fig. 2.3(a)). Interacting with residual gas, the stored electrons produce secondary electrons, while being slowly cooled down until being eventually released and leaving the trap via either source or detector-side of the spectrometer. Secondary electrons from stored high-energy particles are indistinguishable from signal electrons and contribute to the background.

Penning traps (see [Pen36], [Hae53a], [Hae53b], [Har89]) are created by the combination of magnetic and electric fields as shown in the left side of fig. 2.3(a). Given the geometry of MAC-E filters such traps easily can be created and have been observed in KATRIN's predecessor experiments ([Pic92], [Bel95]). Even small regions of space forming a Penning trap are sufficient to produce background rates of the order of 10^3 cps. Axially confined by the electric potential and radially confined by the magnetic field, electrons in such traps interact with residual gas to produce ions and photons as messenger particles. Not being bound by the Penning trap conditions, these particles can propagate over long distances to interact themselves with residual molecules - leading to tertiary electrons, which then contribute to the background. If a Penning trap is accumulates enough charged particles, an unstable plasma can be generated with macroscopic space charge distributions. In such cases, discharges and vacuum breakdowns can occur, which are able to harm the system. For this reasons Penning traps are not only to be prevented for background reasons but also to protect sensitive equipment. A thorough electromagnetic design of the system has allowed to fine adjust its individual parts so that small penning traps have been.

A large Penning trap is expected to form between the Pre-, and Main-Spectrometer if their applied potentials are both of the same order of magnitude. Attempts to remove this trap have been investigated ([Bec10]). It has been shown however that signal electrons are not affected if the Pre-Spectrometer is simply grounded ([Pra11]) and the increase in background for this case is negligible compared to the one expected to be induced by the trap.

More detailed descriptions and measurements on Penning traps at MAC-E filters and their discharge mechanisms can be found in works like [Mer12], [Hil11], [Byr05] and [Fra14].

2.2 Transmission Properties

As already mentioned the 'energy resolution' of the KATRIN MAC-E filter for 18.6 keV electrons is larger than the ν-mass sensitivity. At first sight this would seem to make it impossible to reach the designed sensitivity. However, this only holds as long as the transmission properties are not known precisely. Simply put, the transmission function reflects the probability of an electron of a certain energy emitted in the source with specified angular emission to be transmitted through the filter. The following paragraph gives a short overview of this important function. After a basic description is given, more advanced features of the transmission are investigated. The quintessence of these investigations will be that unknown distortions of any kind will yield a negative influence on the neutrino mass measurement and therefore has to be understood in great detail. With a working model of such effects at hand, the resulting systematic uncertainties can be controlled to an adequate level.

2.2.1 The Transmission Function

When discussing of the transmission function it is instructive to neglect in a first step the angular distribution of source-electrons and to define their momenta to be aligned parallel to the magnetic field lines of the MAC-E filter. Then the transmission function simply is the one of an ideal high-pass filter, i.e. a Heavyside step function. If one now allows electrons to have a non-vanishing polar angle, then it will take an ever larger amount of

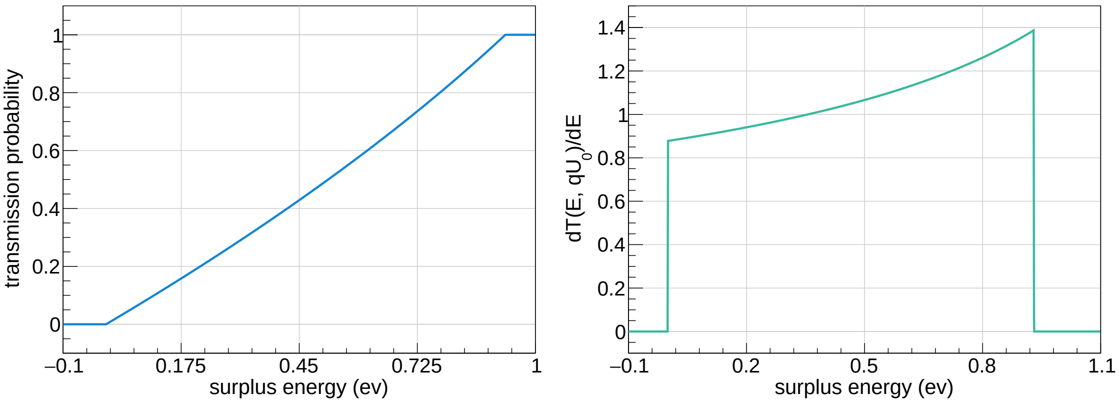

(a) Transmission function **(b)** Derivative of the transmission function

Figure 2.4: (a) Transmission function of a MAC-E filter type spectrometer with the KATRIN design parameters $B_{\mathrm{min}} = 3 \cdot 10^{-4}\,\mathrm{T}$, $B_{\mathrm{source}} = 3.6\,\mathrm{T}$, $B_{\mathrm{max}} = 6\mathrm{T}$ and $U_0 = 18.6\mathrm{kV}$, given an isotropic source. Starting at 0 surplus energies for electrons with zero pitch angle, the part of electrons transmitted to the detector rises until full transmission is reached for surplus energies identical to the 'energy resolution'. (b) Differentiated transmission function, to clarify the complex structure of the transmission function.

surplus energy to be transmitted if the polar angle Θ increases up to the maximal polar angle Θ_{max}. Electrons with a longitudinal energy smaller than the retarding potential will then be reflected, implying their transmission probability to be zero. Furthermore electrons with a surplus energy larger than the MAC-E filter energy resolution will always pass the filter, rendering their transmission probability to be equal to one. This leaves an interval of the size of the energy resolution to be modeled. As the shape of the transmission function strongly depends on the angular characteristics of the source, it is not possible to give a general answer to this problem. For an isotropic source, the transmission function can be calculated to be

$$\mathrm{T}(E - qU_{\mathrm{ret}}) = \begin{cases} 0 & , E - qU_{\mathrm{ret}} < 0 \\ \frac{1 - \sqrt{1 - \frac{E - qU_{\mathrm{ret}}}{E} \cdot \frac{B_{\mathrm{source}}}{B_{\mathrm{min}}}}}{1 - \sqrt{1 - \frac{B_{\mathrm{source}}}{B_{\mathrm{min}}}}} & , 0 \leq E - qU_{\mathrm{ret}} < \Delta E \\ 1 & , \Delta E \leq E - qU_{\mathrm{ret}}, \end{cases} \tag{2.9}$$

as shown in fig. 2.4 for the KATRIN design parameters. Even though the shape of the transmission function approximates a linear function, a neglection of the non-linear shape would induce systematic uncertainties of the order of of ten percent and more. While the differentiated transmission function (fig. 2.4(b)) does not provide meaningful physics, it facilitates understanding the non-trivial structure of the transmission function.

In this generic form the transmission function provides a basic picture of the transmission mechanisms in MAC-E filters but this simple representation certainly has its limits. Indeed each field parameter entering eq. (2.9) is prone to undergo perturbations and as a result will change not only the width but the transmission characteristics as a whole. Several effects are known to influence the field parameters; the most prominent ones will be mentioned in the following. A more detailed description can be found in [Gro15b]. First of all, calculations and measurements of the electrostatic field inside the spectrometer show a small but non-negligible radial dependency. In principle this requires to assign distinct transmission functions to all of the 148 pixels of the KATRIN detector. As the polar angle of electrons is not fixed, the exact analyzing point differs even for electrons traveling along the same magnetic field line. This effect that can be countered by optimizing the magnetic fields. Due to synchrotron losses of electrons propagating in strong magnetic fields the shape of the transmission function also has to be adapted. Finally, time-dependent fluctuations of magnetic and electrostatic fields will occur due to thermal and electrical couplings with stray fields and due to instabilities of the mains voltage. While the influence of the magnetic component is treated in [Erh16b], a basic introduction to the influence of non-constant values of the electric potential is given in the following section 2.2, more advanced modeling for in-depth transmission studies of the KATRIN spectrometer are being described in chapters 5 and 6.

Note that, with the approximations above, it is necessary to describe the transmission properties of the entire KATRIN system with a more complex function, the so called 'response function'. After implementing effects such as radiation losses, source inhomogeneities as well as a variety of other effects, this function obtains a much richer structure. A full model of the response function is given in chapter 7.

2.2.2 Electric field disturbances

In the following we start with a rather technical deduction to provide the tools to quantitatively describe distortions of the electric potential and to access their influence on the transmission properties of the MAC-E filter. Two specific examples are introduced first, namely Gaussian distributed and sinusoidal distortions, which is followed by the general result for arbitrary distortions with a given probability density function. After deriving a formula that establishes to first order an analytical connection between the characteristic properties of fluctuations and the estimated neutrino mass, the section concludes with an important result, so that each distortion can, in principle, can thus be corrected. Thereby the KATRIN sensitivity can be improved significantly. The experimental implications are non-trivial and are treated in chapter 6.

Distortions of the transmission function

In order to obtain non-approximate analytical results, it is necessary first to simplify the transmission function introduced in eq. (2.9)

$$\Theta(E - qU_{\text{ret}}) = \begin{cases} 0 & , E - qU_{\text{ret}} < 0 \\ 1 & , E - qU_{\text{ret}} \geq 0, \end{cases} \tag{2.10}$$

which is the well-known Heaviside function, reflecting the properties of a perfect high-pass filter. In this context it is important to note that a MAC-E filter exhibits a zero or perfect energy resolution only if the source emits only electrons with polar angle $\Theta_{\text{start}} = 0$ and the spectrometer's electric field is known a priori with absolute accuracy and precision. Indeed, a retarding potential in the keV-scale shows fluctuations around a central value $\tilde{U}_{\text{ret}}$,

$$U_{\text{ret}} \to \tilde{U}_{\text{ret}} = U_{\text{ret}} - \xi, \tag{2.11}$$

with the variable part given by ξ. The probability density function is usually given by the normal distribution around 0 and standard deviation σ,

$$f(\xi) = \frac{1}{\sqrt{2\sigma^2}} e^{-\frac{1}{2}(\frac{\xi}{\sigma})^2}. \tag{2.12}$$

From this it is straightforward to calculate the 'distorted' transmission function $\tilde{\mathrm{T}}$ to be

$$\begin{aligned} \tilde{\mathrm{T}}(E - qU_{ret}) &= \int\limits_{-\infty}^{\infty} T(E - q\tilde{U}_{\text{ret}}(\xi)) f(\xi) d\xi \\ &= \frac{1}{2}\left(1 + \operatorname{erfc}\left(\frac{E - qU_{\text{ret}}}{\sqrt{2\sigma^2}}\right)\right). \end{aligned} \tag{2.13}$$

Therefore a Gaussian distortion results in the cumulative distribution of the normal distribution if applied on a step-shaped transmission function. Speaking of voltage fluctuations one is usually interested in sinusoidal waveforms. This specific type of distortion occurs on a large variety of applications, starting with the frequency of the mains voltage coupling into the output of voltage supplies, and ending with the spectrometer acting as antenna, which picks up propagating electromagnetic waves emitted by mobile phones and other devices. The usual approach for this generic time-dependent distortion, can be expressed

$$U_{\text{ret}} \to \tilde{U}_{\text{ret}} = U_{\text{ret}} + A \cdot \sin(\xi), \tag{2.14}$$

so that $\tilde{\mathrm{T}}$ is given by the integral

$$\begin{aligned} \tilde{\mathrm{T}}(E - qU_{ret}) &= \frac{1}{2\pi} \int\limits_{-\pi}^{\pi} T(E - q\tilde{U}_{\text{ret}}(\xi)) d\xi \\ &= \begin{cases} 0 & ,E - qU_{\text{ret}} < -A \\ \arcsin\left(\frac{E - qU_{\text{ret}}}{A}\right) + \frac{1}{2} & , -A \leq E - qU_{\text{ret}} < A \\ 1 & ,E - qU_{\text{ret}} \geq A, \end{cases} \end{aligned} \tag{2.15}$$

as described in [Grö10], [Wie12] and [Kra12]. The perfect high-pass filter together with Gaussian and sinusoidal distortions is illustrated in fig. 2.5. The axis labels have to be treated with caution. For electrons of a given energy, the transmission probability is well-defined. The effect of distortions is only manifest, because the fluctuations are treated as unknown parameters. Both types of perturbation cause the function to broaden, however the exact shape differs. Note that electrons not only need a higher surplus energy for their transmission probability to be unity, but also electrons with negative surplus energies

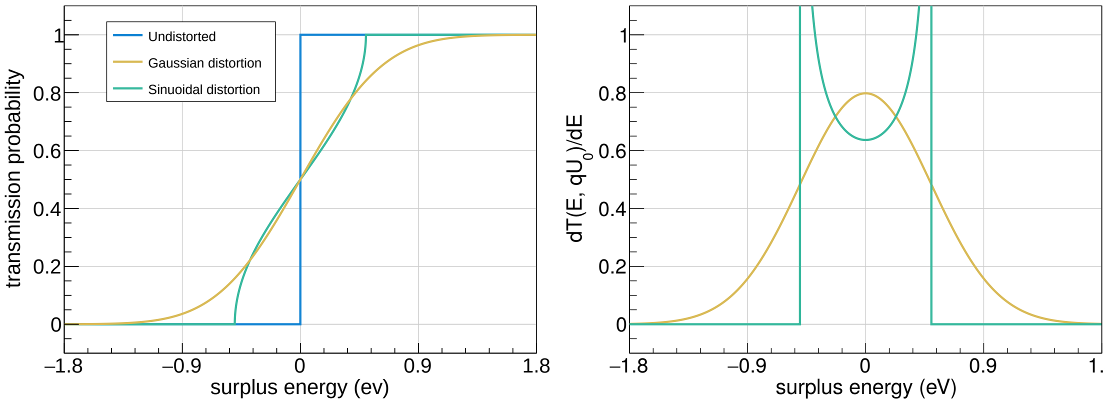

(a) Transmission probabilities **(b)** Derivative of the transmission probabilities

Figure 2.5: (a) The perfect high-pass filter is described by a Heaviside function. This shape can be distorted by fluctuations of the electric potential. Shown here are a Gaussian fluctuation with $\sigma = 0.5\,\mathrm{V}$ (yellow) and a sinusoidal wave with the amplitude $A = 0.5\,\mathrm{V}$ (green). Most importantly the sinusoidal distortion causes the transmission function to broaden by the size of the amplitude, with distinct edges at the transmission borders. On the other hand a Gaussian fluctuation leads to a smearing of the function. Both distortion types lead to significantly different line shapes. (b) Differentiated functions in the same color scheme. The ideal high pass filter with its potential being distorted gives the normal distribution as one would expect. The sinusoidal distortion leads to thea U-shaped distribution indicating the distinct edges seen in the integral case.

now can pass the filter. Most importantly, the Gaussian causes a broad tail at both ends, in distinct contrast to the sine-ripple that leads to very sharp ends. As expected, the differentiated form of the Gaussian perturbed transmission function, is normal distributed. In analogy to the spatial probability density function of a mathematical pendulum the density function of a sinusoidal-rippled electric potential is given by a U-shaped distribution (fig. 2.5(b)) . As mentioned above, this function has the distinct feature diverging at its boundaries.

Before a more realistic approach to determine the transmission properties under perturbations is taken in the next paragraph, the investigation will now be expanded to implement disturbances with arbitrary probability density functions. For this, the transmission probability is no longer treated as a fixed number but instead as a function of a statistical variable. In this case, the transmission probability T as function of surplus energy now becomes

$$\mathrm{T}(E - qU_{\mathrm{ret}}) = \int\limits_{-\infty}^{\infty} T(E - q\tilde{U}_{\mathrm{ret}}(\xi)) f(\xi)\, d\xi, \tag{2.16}$$

with a characteristic variate ξ and its PDF $f(\xi)$. Comparing this definition with eq. (2.15) the two results seem to be in conflict. This is actually not the case, as

$$\begin{aligned}\mathrm{T}(E - qU_{\mathrm{ret}}) &= \int\limits_{-\infty}^{\infty} T(E - q\tilde{U}_{\mathrm{ret}}(\Xi) f(\Xi)\, d\Xi \\ &= \int\limits_{-\infty}^{\infty} T(E - qU_{\mathrm{ret}} + \Xi) \frac{1}{\pi\sqrt{A^2 - \Xi^2}}\, d\Xi \\ &= \int\limits_{-\pi/2}^{\pi/2} T\left(E - qU_{\mathrm{ret}} + \sin(\xi)\right) \cdot \frac{1}{2\pi}\, d\xi,\end{aligned} \tag{2.17}$$

where

$$f(\Xi) = \frac{1}{\pi\sqrt{A^2 - \Xi^2}}, \tag{2.18}$$

and using the transformation

$$\Xi \rightarrow A\sin(\xi) \tag{2.19}$$

with the Jacobian determinant

$$\frac{\mathrm{d}\Xi}{\mathrm{d}\xi} = A\cos(\xi). \tag{2.20}$$

The new variable ξ is uniformly distributed on the closed interval $[-\pi/2,\, pi/2]$,

$$f(\xi) = \begin{cases} \frac{1}{\pi} & , \xi \in [-\pi/2,\, \pi/2] \\ 0 & , \text{otherwise.} \end{cases} \tag{2.21}$$

The power of this identity lies in its numerical behavior. Because of the divergent nature at its boundaries, the U-shaped distribution can be numerically implemented but consumes more computing time than the method using the above integral. It has to be mentioned that the obtained result shows no frequency dependency at all.

This simple model can now be expanded by a more appropriate transmission function. With the transmission function defined as in eq. (2.9), it is no longer possible to obtain analytically closed identities. One thus has to rely on numerical methods, as mentioned above. The results are shown in fig. 2.6. Here the effects of Gaussian and sinusoidal perturbations are less pronounced as in the previous case, but their essential features are still manifest. Again, it is highly instructive to consider the derivatives of the distorted functions, see fig. 2.6(b). While remaining mostly symmetrical, the derivative of the transmission function distorted by a Gaussian-distributed perturbation, differs evidently from a normal distribution. For better comparability, a Gaussian-distribution with $\sigma = 0.5\,(\mathrm{V})$, shown in deep blue, has been implemented. The green colored function represents the derivative of a

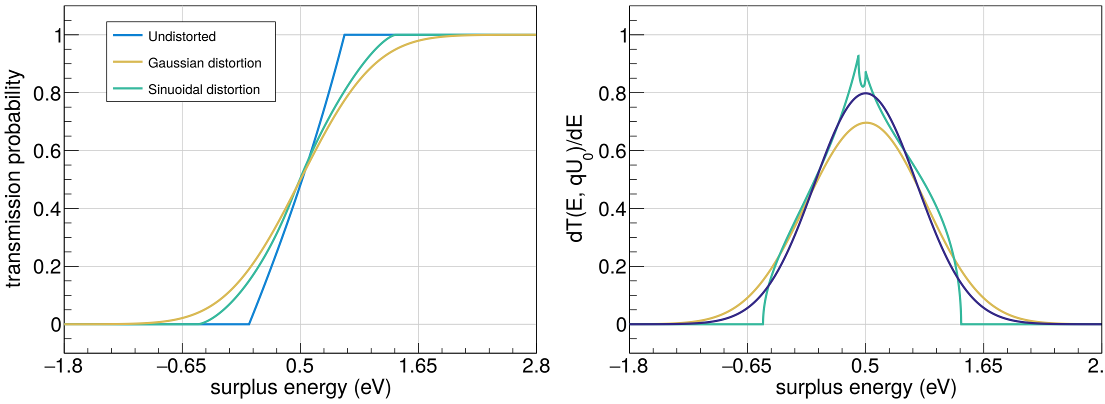

(a) Distortions of the realistic transmission function

(b) Differential distortions of the transmission function

Figure 2.6: (a) Representation of a more realistic transmission function, again with $A = \sigma = 0.5\,\mathrm{V}$. The clear distinction of Gaussian and sinusoidal distortion is not as present as in the case of the ideal high-pass filter but still visible. Most importantly the discrete edges of the function distorted by the sine-wave remain manifest. (b) Differentiated transmission functions. Note that the Gaussian fluctuation does not lead to a normal distribution anymore, for better comparison the Gaussian has been implemented (deep blue). The function rippled by the sine-wave is evidently asymmetrical and displays two local maxima.

transmission function rippled with a sine-wave. The perturbation causes the function to be highly asymmetric with two local maxima. The extremal points arise from the distortion with its sharp boundaries reaching the end of the spectrum on both sides. As the position of these two peaks depends directly on the energy resolution of the spectrometer and the ripple-amplitude, it provides the opportunity to simplify the precise characterization of the perturbation. Chapter 6, will investigate this effect in more detail.

It is evident that the broadening and reshaping of the transmission function will harm the determination of the neutrino mass. This motivates the in-depth investigations outlined in chapters 5-7, where methods to determine distortions and strategies to counteract their determined effects are given verified for KATRIN spectrometers.

Influence on the estimated neutrino mass

One task left is to simultaneously is a central result, quantify the influence of an arbitrary distortion of T on the neutrino mass-estimate. Given the differential β-decay spectrum $\frac{\mathrm{d}N}{\mathrm{d}E}(E_0, m_{\bar{\nu}_e}{}^2)$ and the transmission function $T(E - qU_{\mathrm{ret}})$, with E_0 denoting the kinematic endpoint of the tritium decay, $m^2_{\bar{\nu}_e}$, the elementary charge of the electron q and the retardation potential U_{ret}, the rate of electrons reaching the detector is given by

$$\frac{\mathrm{d}N}{\mathrm{d}t} = \int\limits_{qU_{\mathrm{ret}}}^{\infty} \frac{\mathrm{d}^2 N}{\mathrm{d}t\,\mathrm{d}E}\,\mathrm{d}E. \tag{2.22}$$

To take the transmission properties of the spectrometer into account, one has to consider the convolution

$$\left(\frac{\mathrm{d}^2 N}{\mathrm{d}t\,\mathrm{d}E}\right)_{\text{conv}} = \frac{\mathrm{d}^2 N}{\mathrm{d}t\,\mathrm{d}E} \otimes \mathrm{T}(E - qU_{\text{ret}}) = \int\limits_{-\infty}^{\infty} \frac{\mathrm{d}^2 N}{\mathrm{d}t\,\mathrm{d}E}(\tau)\;\; \mathrm{T}(E - (qU_{\text{ret}} + \tau))\,\mathrm{d}\tau. \tag{2.23}$$

This equation demonstrates the need to precisely determine the transmission function, as T directly enters the measured electron rate and skews the spectrum. In case of a perturbed form of the transmission function, one obtains

$$\begin{aligned}\left(\frac{\mathrm{d}^2 N}{\mathrm{d}t\,\mathrm{d}E}\right)_{\text{conv}} &= \frac{\mathrm{d}^2 N}{\mathrm{d}t\,\mathrm{d}E} \otimes \tilde{\mathrm{T}}(E - q\tilde{U}_{\text{ret}}) \\ &= \int\limits_{-\infty}^{\infty}\int\limits_{-\infty}^{\infty} \frac{\mathrm{d}^2 N}{\mathrm{d}t\,\mathrm{d}E}(\tau)\;\; \mathrm{T}(E - (qU_{\text{ret}} + \tau + \xi))\;\; f(\xi)\,\mathrm{d}\xi\,\mathrm{d}\tau.\end{aligned} \tag{2.24}$$

Making use of the substitution

$$E \to \tilde{E} := E - \xi, \tag{2.25}$$

the distortion of the retarding potential and the transmission function gives

$$\begin{aligned}&\left(\frac{\mathrm{d}^2 N}{\mathrm{d}t\,\mathrm{d}E}\right)_{\text{conv}} = \frac{\mathrm{d}^2 N}{\mathrm{d}t\,\mathrm{d}E} \otimes \tilde{\mathrm{T}}(E - q\tilde{U}_{\text{ret}}) \\ &= \frac{\mathrm{d}^2 N}{\mathrm{d}t\,\mathrm{d}E} \otimes \int\limits_{-\infty}^{\infty} \mathrm{T}(E - qU_{\text{ret}} + \xi)\;\; f(\xi)\,\mathrm{d}\xi = \int\limits_{-\infty}^{\infty} \frac{\mathrm{d}^2 N}{\mathrm{d}t(E)\,\mathrm{d}E} \otimes \mathrm{T}(E - qU_{\text{ret}} + \xi)\;\; f(\xi)\,\mathrm{d}\xi \\ &= \int\limits_{-\infty}^{\infty} \frac{\mathrm{d}^2 N}{\mathrm{d}t\,\mathrm{d}\tilde{E}}(\tilde{E} + \xi) \otimes \mathrm{T}(\tilde{E} - qU_{\text{ret}})\;\; f(\xi)\,\mathrm{d}\xi = \mathrm{T}(\tilde{E} - qU_{\text{ret}} + \xi) \otimes \int\limits_{-\infty}^{\infty} \frac{\mathrm{d}^2 N}{\mathrm{d}t\,\mathrm{d}\tilde{E}}\;\; f(\xi)\,\mathrm{d}\xi \\ &\qquad\qquad = \mathrm{T}(E - qU_{\text{ret}}) \otimes \frac{\mathrm{d}^2 N}{\mathrm{d}t\,\mathrm{d}\tilde{E}},\end{aligned} \tag{2.26}$$

where the commutativity of integral and convolution, as well as the commutativity of the convolution have been used. Two important physics statements can be drawn identity. On the one hand, it is equivalent for a distortion to either enter the energy of the electrons or the retarding potential. Therefore the systematic uncertainties in both cases are treatable in the same way. On the other hand, the effect of voltage fluctuations can be counteracted if their variance is known. The retarding potential is the superposition of vessel and all inner electrode potentials. Due to the strong capacitive coupling between the components and field inhomogeneities vessel voltage and retarding potential can a priori not be expected to undergo the same fluctuations. The connection between voltage ripples and analyzing potential will be discussed in chapter 6.

In the following the effect of distortions, either in the transmission function or on the source side, is calculated. Due to the fact that the exact spectral shape of β-decay electrons is not trivial, analytical results are not accessible in exact form. A common solution for this problem is to use the Taylor-Expansion up to the second-order

$$\left(\frac{\mathrm{d}^2N}{\mathrm{d}t\,\mathrm{d}E}\right)_{\text{T.-E.}}(m_{\overline{\nu}_e};0) = \gamma\,\Theta(E_0-E-m_{\overline{\nu}_e})\,(E_0-E) - \frac{\gamma}{2}m^2_{\overline{\nu}_e} + \mathcal{O}(m^4_{\overline{\nu}_e}), \tag{2.27}$$

where γ is a constant, instead. With respect to eq. (2.26) it is well motivated to consider the transmission function as normalized step-function for all following calculations. It is possible to derive formulas for Gaussian and sinusoidal-ripples. However, there is way to obtain a most general formula in case of a distortion with any given PDF [Kra12]. Let ξ be a variate distributed according to $f(\xi)$ with

$$\int\limits_{-\infty}^{\infty} f(\xi)\,\mathrm{d}\xi = 1, \tag{2.28}$$

then

$$\begin{aligned}
\left(\frac{\mathrm{d}^2N}{\mathrm{d}t\,\mathrm{d}E}\right)_{\text{conv}} &= \gamma\,\Theta(E_0-E-m_{\overline{\nu}_e}) \int\limits_{-\infty}^{\infty} f(\xi)\,\left[(E_0-E+\xi)^2 - \frac{1}{2}m^2_{\overline{\nu}_e}\right]\mathrm{d}\xi \\
&= \gamma\,\Theta(E_0-E-m_{\overline{\nu}_e}) \left\{\int\limits_{-\infty}^{\infty} f(\xi)\,\left[(E_0-E)^2 - \frac{1}{2}m^2_{\overline{\nu}_e}\right]\mathrm{d}\xi + \int\limits_{-\infty}^{\infty} f(\xi)\,\left[\xi^2 + 2\xi(E_0-E)\right]\mathrm{d}\xi\right\} \\
&= \gamma\,\Theta(E_0-E-m_{\overline{\nu}_e}) \left\{\left[(E_0-E)^2 - m^2_{\overline{\nu}_e}\right] + \underbrace{\int\limits_{-\infty}^{\infty} f(\xi)\xi^2\,\mathrm{d}\xi}_{=\mathrm{E}[\xi^2]} + 2(E_0-E)\underbrace{\int\limits_{-\infty}^{\infty} f(\xi)\,\mathrm{d}\xi}_{=\mathrm{E}[\xi]}\right\} \\
&= \gamma\,\Theta(E_0-E-m_{\overline{\nu}_e}) \left\{(E_0-E)^2 - \frac{1}{2}\left[m^2_{\overline{\nu}_e} - 2\mathrm{E}[\xi^2] - 4\mathrm{E}[\xi](E_0-E)\right]\right\},
\end{aligned} \tag{2.29}$$

which reduces for $\mathrm{E}[\xi] = 0$ to

$$\begin{aligned}
\left(\frac{\mathrm{d}^2N}{\mathrm{d}t\,\mathrm{d}E}\right)_{\text{conv}} &= \gamma\,\Theta(E_0-E-m_{\overline{\nu}_e}) \left[(E_0-E)^2 - \frac{1}{2}\left(m^2_{\overline{\nu}_e} - 2\underbrace{\mathrm{E}\left[\xi^2\right]}_{=\sigma^2}\right)\right] \\
&= \gamma\,\Theta(E_0-E-m_{\overline{\nu}_e}) \left[(E_0-E)^2 - \frac{1}{2}\left(m^2_{\overline{\nu}_e} - 2\sigma^2\right)\right].
\end{aligned} \tag{2.30}$$

Finally the calculation of the integral spectrum can be carried out, yielding

$$\frac{\mathrm{d}N}{\mathrm{d}t} = \frac{\gamma}{3}\left[(E_0 - qU_{\mathrm{ret}})^2 - m_{\overline{\nu}_e}^2\right]^{\frac{3}{2}}. \tag{2.31}$$

By comparing eq. (2.31) with the undistorted spectrum eq. (2.27), the shift in the neutrino mass squared follows to be

$$\mathit{\Delta} m_{\overline{\nu}_e}^2 = -2\sigma^2. \tag{2.32}$$

A similar result has been obtained in [Rob88], by another approach. With eq. (2.32) imperfections of the electric potential are fully taken into account.For the key area of high voltage fluctuations, the most prominent distortionsare expected to be of periodic nature. Depending on the actual wave-form it is not an easy task to construct the probability density function of an arbitrary perturbation. It is often useful to perform a Fourier transformation and to take into account only those frequencies that are dominant. Taking a closer look at the derivation in eq. (2.30), the assumption for the expectation value of the distortion to vanish needs further explanation. To measure the neutrino mass, the Q value has to be determined by a combined fit to the four relevant parameters ([Kle14]). To first order E_0-related systematic shifts could cancel out naturally. This is a strong feature of MAC-E filters, as absolute values only play a sub-dominant role, whereas the systems stability is highly important. Nevertheless, when calculating the transmission function it is of utmost importance to create a complete field-map. Inhomogeneities of the electric field, i.e. distortions with zero variance but non-vanishing expectation value, will cause a shift of $\mathit{\Delta} m_{\overline{\nu}_e}^2 = -2\mathrm{E}[\xi](E_0 - E)$, even in the differential spectrum. This effect gets more prominent in the integral spectrum, as it is not only proportional to the offset in energy itself, but also to the electron energy. For this reason dedicated studies in order to gain full understanding of the fields inside the KATRIN spectrometer have been performed ([Beh16], [Erh16b], [Gro15b]). Furthermore both source and spectrometer potentials can be distorted at the same time causing the systematic uncertainties to add quadratically. Therefore it has to be emphasized, that the actual measured voltage has to correspond to the potential difference between source and spectrometer. Finally, at this point it is not yet been clarified how the measured fluctuations of the high voltage are related to the actual potential inside the vessel. These relations are the central theme of chapter 6.

2.3 KATRIN Apparatus

With the need for a thorough understanding of systematic effects highlighted in the previous section, the technical challenges to each component of a MAC-filter type experiment lies at hand. The small number of electrons carrying information about the neutrino mass calls for a source of high luminosity. The utilized detector has to act with an efficiency near to unity. All fields have to be precisely adapted and fluctuations of them have to be measurable within ppm-range or even suppressed entirely. A schematic overview of the beam-line, having an approximate length of 70 m is shown in fig. 2.7. The basic setup of all segments gets outlined in the following.

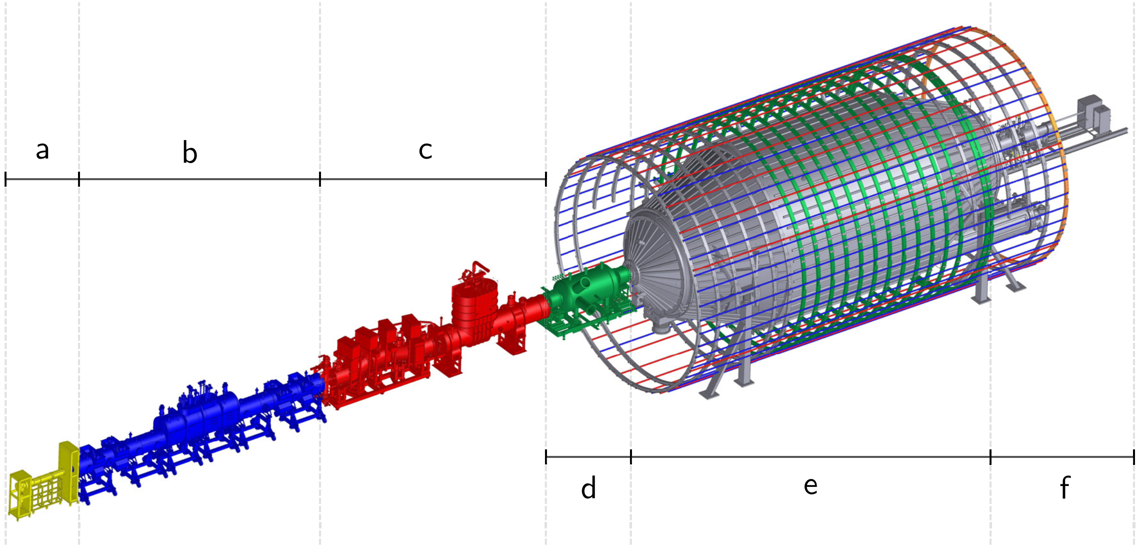

Figure 2.7: Schematic overview of the 70 m long beam-line of the KATRIN experiment and its sub-components. (a) Rear section, responsible for calibrations and monitoring of the windowless gaseous tritium source (b). Indicated in blue, the pumping section (c) consists of differential and cryogenic pumps to reduce the tritium flow and magnetically guide electrons into the pre-spectrometer (d), where a the majority of electrons gets reflected. Only electrons close to the kinematic endpoint are guided into the main-spectrometer (e) for the final energy selection. Electrons passing the filter are detected in the FPD (f) at the end of the beam-line. Figure adapted from [Kle14]

2.3.1 The tritium source

In order minimize energy losses of electrons due to scattering processes in the source, the KATRIN experiments utilizes a WGTS , where these effects are limited to scattering processes off gas molecules only. Apart from offering a high luminosity the source has to produce electrons at the highest stability. Determining and controlling these conditions has led to non-trivial technological challenges. A short summary of the basic functional parts that are employed in the WGTS is given in fig. 2.8.

Gaseous tritium pre-cooled to about 30 K is injected through a series of capillaries (providing a pressure of approximately 10^{-3} mbar), into a cylindrical tube of stainless steel measuring 10 m in length and 90 mm in diameter. A magnetic field of $B_{\text{source}} = 3.6\,\text{T}$ to guide signal-electrons out of the source is generated by three superconducting solenoids. The total extent of the cryostat is increased to 16 m by two differential pumping sections, the DPS1-R and DPS1-F. Each of these contains six turbo molecular pump (TMP) units to reduce the flow of gas molecules into the affiliated systems by two orders of magnitude. Tritium is pumped out and is processes in the closed inner loop system ([Stu10]). The purity of the tritium is expected to be greater than 95%, which is why a small fraction of the pumped-out gas is reprocessed at this stage before being re-injected into the central tube. A dedicated monitoring system allows to sample the precise isotopic gas-composition. To do so, Laser-Raman spectroscopy is used ([Sch13a], [Sch13b] and [Fis15]). The molecular

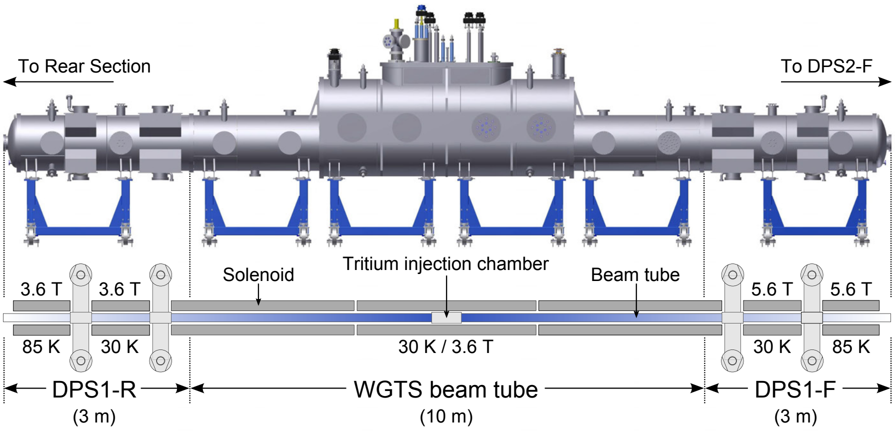

Figure 2.8: Side-view of a CAD model of the WGTS. The 10 m long beam tube of the tritium source is surrounded by three superconducting magnets generating a magnetic field of 3.6 T. Gaseous tritium is injected at a temperature of only 30 K. While electrons are guided out of the source, the flow of gas molecules out of the source gets reduced by a factor of 100 in two differential pumping sections that are attached at both ends of the source. Figure taken from [Har15].

flow at 30 K causes a Doppler broadening of the spectral shape. This necessitates low gas temperatures at 30 K with fluctuations smaller than 30 mK. For this reason the WGTS is embedded in a dedicated beam tube cooling system that is based on two-phase liquid-gaseous neon to provide the required stability at low temperatures ([Bod11], [Gro11], [Gro13]). Under the given preconditions an ultra-stable column density of $\rho d = 5 \cdot 10^{17}\,\mathrm{cm}^2$ is achieved.

2.3.2 Rear section

Located at the downstream end, the rear section provides a series of calibration and monitoring devices for the experiment.

Correspondingly, half of the emitted electrons traveling out of the source to reach the rear section, in addition to the large number of electrons that are reflected by the electromagnetic fields present in the spectrometers. This facilitates the long-term monitoring of the source activity by spectroscopy of X-ray radiation induced by electrons hitting the rear wall ([Röl13], [Röl11], [Röl15]). As mentioned in section 2.2.2 the potential of the source is of the same significance as the spectrometer potential itself. Therefore, a specific rear wall with optimized surface potential will allow to control the WGTS potential ([Bab11], [Bab14]).Finally an angular-resolved electron gun allows to measure the source column density via inelastic scattering ([Hug10], [Val11], [Bab14]). Additionally the cross section for inelastic scattering in the WGTS will be measured to determine the energy loss function ([Gro15b]).

2.3.3 The transport section

The transport section connects WGTS with the spectrometers. Superconducting magnets guide the electrons, whereas two pumping schemes are used to reduce the flow of gas at the same time. For the background to be sufficiently low, ultra high vacuum (UHV) conditions are needed in the spectrometer section. In particular the partial pressure of tritium has to be lower than 10^{-20} mbar, see [Mer12]. In view of the huge source luminosity with its large number of tritium molecules, Thereby the transport section has to reduce the tritium flow by at least fourteen orders of magnitude. Two distinct units are employed, based on different functional principles (CAD models of both are shown in fig. 2.9).

Differential pumping section (DPS)

The beam tube of the DPS2-F consists of five inter-connected beam tubes, which are tilted by 20° against each other and surrounded by five coaxial superconductors. The corresponding magnetic fields of about 5.5 T guides signal electrons adiabatically. Neutral molecules are not guided and therefore collide with the beam tube walls. By this the probability of being pumped out increases, so that four TMPs intersecting the beam tubes, and operating with a pumping speed of 2400 l/s each ([Luo06], [Luk12], [Jan15]) drastically reduce the gas flow. After the differential pumping of the DPS-1F, the gas flow is already reduced by a factor of 100, the large pumps in the DPS-2F further reduce it by roughly five orders of magnitude. Ions emerging from the WGTS are not being pumped out and can be trapped in the transport section. Therefore a Fourier transform-ion cyclotron resonance (FT-ICR) device estimates the amount of ions from the source inside the DPS2-F ([Ubi09], [Ubi11]). To prevent a build-up of ions, counter-methods are applied to reduce their number-density. This is realized by a combination of dipole and ring-shaped blocking electrodes inside the apparatus ([Rei09], [Win11], [Hac15]). For further reference see [Kos12].

Cryogenic pumping section

The adjacent CPS cryostat has a beam-line composed of seven individual segments, again tilted against each other by 15°, and seven superconducting magnets that are aligned accordingly. As already suggested by its name, the cryogenic pumping section uses the concept of cryo-sorption instead of classical pumps. A 3 K cold layer argon frost coats the inner surface of the beam tube and adsorbs molecules. Successful validation of the working principle of such a pump was given by the TRAP experiment, where a reduction factor of $3 \cdot 10^7$ was measured ([Eic08]). This technique reduces the gas flow into the spectrometer section by additional seven orders of magnitude. As the carrying capacity of the adsorption process of tritium molecules has to be limited for safety reasons, a regeneration cycle will be carried out after three months of continuous measurement operation. By then the accumulated activity of adsorbed tritium will be approximately 37 GBq. In addition, the CPS features several devices fulfilling monitoring and calibration purposes. A real-time estimation of the electron rate emitted by the source is accomplished with the forward beam monitor. Non-trivial technological challenges have to be considered here, as of the rates this detector has to handle are rather high. ([Bes10], [Bab11]). For energy calibration a condensed krypton source will be deployed, see [Bot12], [Bau13b], [Dyb16] and [Res17].

2.3.4 The spectrometer section

The spectrometer section of the KATRIN experiment consists of three spectrometers, all of them following to the MAC-E filter principle. Two of them are connected adjacent to

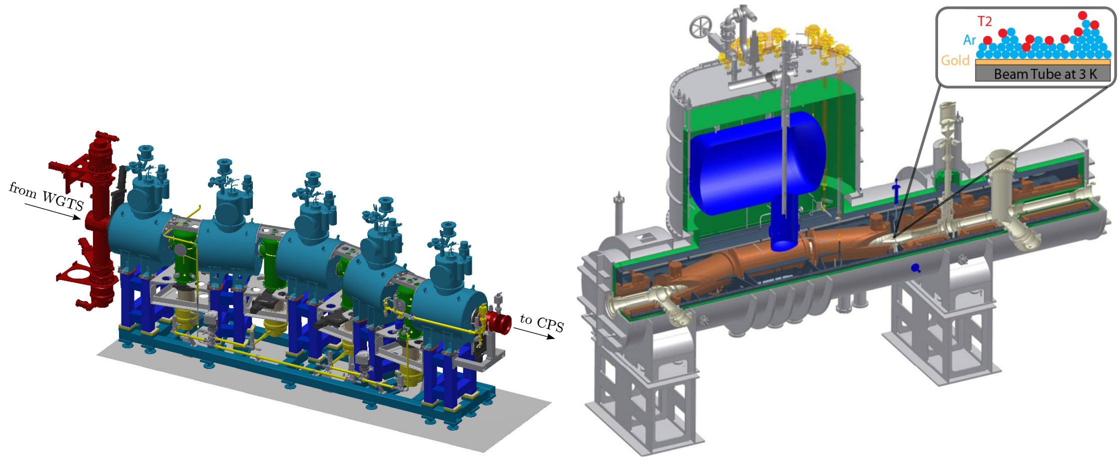

(a) Differential pumping section. Adapted from [Jan15].

(b) Cryogenic pumping section. Adapted from [Wan13].

Figure 2.9: (a) The DPS2-F, composed of five tilted beam tubes and magnets. Four turbo molecular pumps reduce the gas flow by five orders of magnitude. (b) The cryogenic pumping section (CPS) is composed of seven tilted segments. Tritium molecules are adsorbed by a layer of argon frost on the inner surface.

each other in the main beam line, while the third one stands alone, the former being the pre-, and main-spectrometer meter, the latter is the so called monitor-spectrometer.

The pre-spectrometer

The pre-spectrometer has a length of 3.4 m and measures 1.7 m in diameter. As only a small fraction of the electrons propagating from the source will carry information on the neutrino mass the option of a pre-filter was implemented into the setup. Without pre-filter, the large flux of electrons could induce background in the main-spectrometer due to scattering off residual gas molecules. For this reason, the pre-spectrometer is installed and can be operated at $-18.6.. - 8.6\,\mathrm{keV}$ to achieve a pre-filtering of the electrons. If kept at a potential 300 V below the endpoint, the flux of electrons can be reduced by seven orders of magnitude from the pre-spectrometer. However, this field configuration is known to cause a large Penning trap between the two spectrometers. If operated at zero potential, this trap can be avoided completely ([Pra12]). However, until the actual tandem measurements will take place, the exact electrostatic field configuration during tritium mode is not known, as active countermeasures against the Penning trap might be possible.

The pre-spectrometer has been main topic for many extensive investigations. In particular, it has been an ideal test facility in deepening the knowledge of transmission and background processes in MAC-E filters and therefore has significantly influenced the development of the main-spectrometer ([Fra06], [Hab09], [Fra10], [Mer12], [Wan13], [Goe14]).

The Main Spectrometer

The most prominent functional part of the KATRIN experiment, is formed by the main-spectrometer. There, the highly precise energy selection of incoming signal electrons is conducted. With a length of 23.3 m, a diameter of 10 m, and a mass of 200 metric tons of stainless steel, the main spectrometer is by far the largest spectrometer in the setup. Its huge dimensions are caused by the MAC-E principle, see section 2.1.1. With a volume of 1240 m^3 and a surface area of 690 m^2 it is the dominant source of background in the experiment. As the background design value only allows 10 mcps, the electromagnetic design of the spectrometer has been performed with great care.As a result, the first background rates obtained during the first SDS measurement phase were several orders of magnitude smaller than in previous MAC-E filter type experiments([Wan13], [Sch14], [Goe14]). Detailed studies of the remaining background sources have been conducted and sophisticated devices have been developed to decrease the remaining background further ([Har15],[Hil16], [Beh16]). A detailed model of the complete background present in the spectrometer is currently being developed ([Tro16]). Superconducting solenoids at both ends, the PS2 magnet with 4.5 T located at the pre-spectrometer side, and the pinch magnet at the detector side with 6.0 T, generate the flux-tube inside of the spectrometer. In order to compensate the earth magnetic field and to center and adjust the magnetic field, a set of large air coils surrounds the spectrometer. For a detailed description of this system and its performance during the second measurement phase, see section 3.2. The electric retarding field necessary for the energy selection process is generated by applying voltages up to 35 kV directly on the whole vessel. A double layered wire electrode consisting of eleven segments, each of them assignable with individual voltages, is mounted inside the spectrometer in a ring-like arrangement. This structure also allows the electric blocking of secondary electrons from the wall and a so called dipole mode to remove stored electrons with less than 1 keV of surplus energies. A more detailed description is given in section 3.3.

The Monitor Spectrometer

The purpose of the monitor spectrometer's lies in the verification and long-term monitoring of the voltage applied to the main spectrometer. This apparatus is of rather small size, with only 4 m in length and 1 m in diameter. Nevertheless, it features the same energy resolution as its bigger counter part and is essential to the experiment. While the main high voltage (HV) of the experiment is measured with the KATRIN HV dividers (see section 4.4), the monitor spectrometer allows a completely independent way to verify the stability of the voltage. By using radioactive isotopes of krypton implanted in a solid source of highly ordered pyrolytic graphic (HOPG), this spectrometer measures spectral lines from the radioactive decay of the Krypton and hence compares the voltage to a constant of nature ([Zbo11], [Sle11]). As the decoupling of different drifting-effects of the MoS setup along solid state effects together with proving the desired stability is a non-trivial task, considerable efforts were needed during development and characterization of this source type. However, the result is a highly reliable system, exceeding the requirements by one order of magnitude ([Erh12], [Erh14]). The spectrometer itself was installed and commissioned at the KIT from 2010 to 2012 ([Sch11], [Gou10]).

As it will be shown in chapter 5 of this thesis, this instrument can be used to search, evaluate and counteract high voltage systematics. It will be shown that the method is in fact sensitive not only to slow drifts of the voltage but also voltage fluctuations. Furthermore it can be utilized to calibrate the KATRIN voltage dividers against a constant of nature and

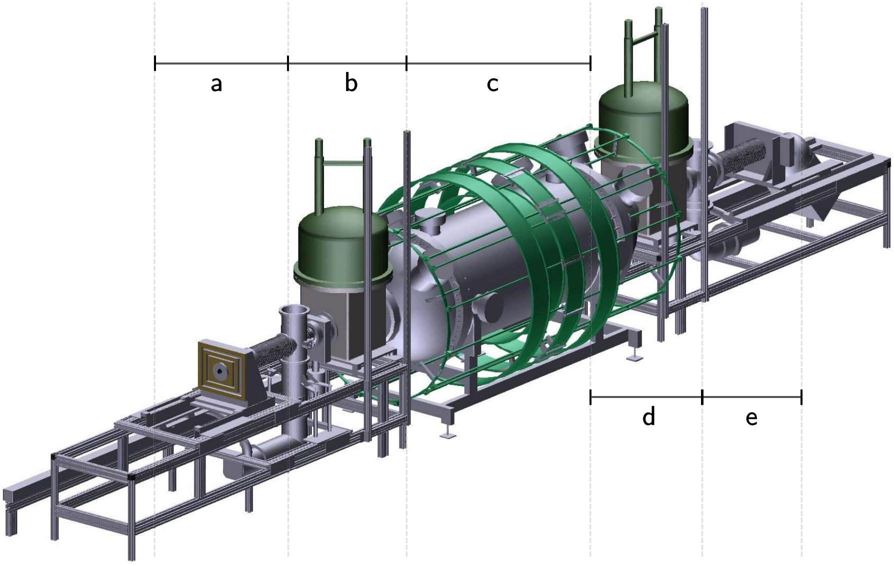

Figure 2.10: CAD model of the monitor spectrometer. As the MoS is standing outside the main beam-line, it has its own krypton source (a). Two superconducting solenoids (b, d) generate the magnetic field guiding signal electrons into the spectrometer (c). For fine adjustments of the magnetic field a system of magnet coils is mounted around the vessel. The utilized detector (e) consists of only five pixel, where only one of them is thought to take actual measurements of the krypton spectrum, while the other four are installed for alignment reasons. Adapted from [Kle14].

therefore verify their stability in a manner independent of classically employed electrically methods.

2.3.5 The detector section

Located at the most upstream side of the KATRIN beam-line, the focal plane detector (FPD) counts all electrons that have passed the filter. A model of the whole system is shown in fig. 2.11. Two superconducting solenoids, the pinch magnet in the front at 6.0 T and the detector magnet at 3.6 T guide electrons adiabatically onto the detector wafer. The electrons are counted by a silicon PIN-diode array consisting of 148 individual pixels with high efficiency. With a thickness of 500 μm, the 90 mm diameter sensitive area of the wafer is divided in equally sized pixels. Thereby both azimuthal- and radial-dependent mapping of the sensitive spectrometer-volume is achieved. This is important to normalize volume-dependent background effects and to obtain a proper weighting of field inhomogeneities entering the transmission function. To minimize background at the wafer, the detector is housed in lead and copper shielding and features an active veto against cosmic induced particles. Furthermore signal electrons can be post-accelerated to a region with ultra low background and small noise level by a copper electrode. The flapper valve allows the separation of the detector section from the rest of the system. The intrinsic detector background is rather small and regular energy calibrations with the two integrated sources are possible [Ams15]. Detailed descriptions can be found in [Har12], [Wal13] and [Sch14].

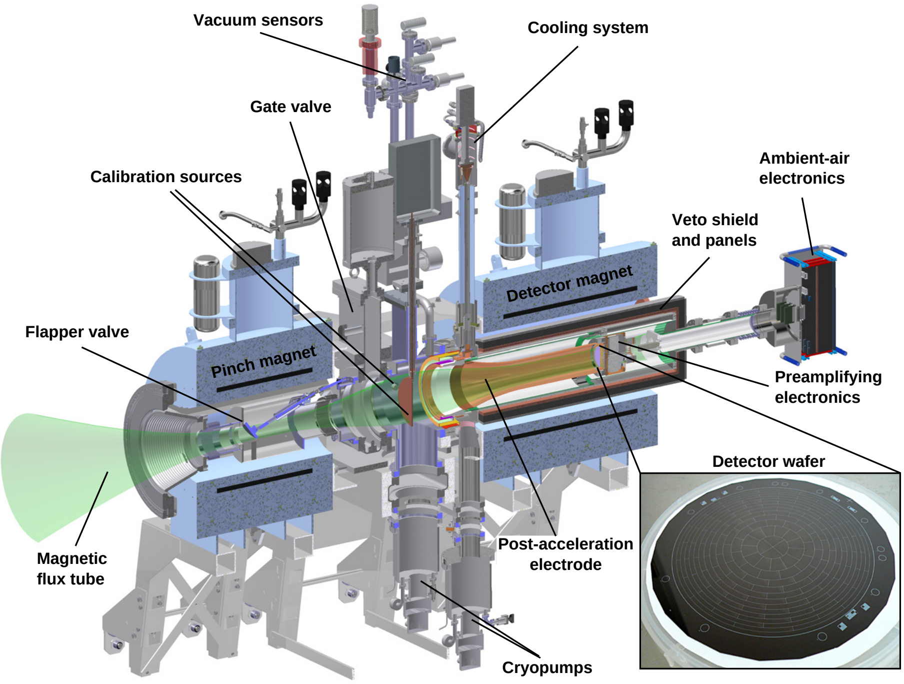

Figure 2.11: Schematic drawing of the detector section and the silicon detector wafer. Two superconducting solenoids guide signal electrons adiabatically to the wafer where they are counted. Background particles are passively shielded by lead and copper housing, while an active veto-system counters events induced by incoming cosmic particles. Adapted from [Ams15].

CHAPTER 3

Spectrometer and detector section

A detailed knowledge of the complicated mechanisms which produce background as well as the exact characterization of the transmission properties of the main spectrometer are substantial to understand and limit systematic effects and to reach the targeted sensitivity in determining the electron anti neutrino mass in KATRIN. In a first commissioning phase of the spectrometer and detector section (SDS-I), the spectrometer and detector section has proven its functionality in 2013. After these first investigations the SDS setup was upgraded to accomplish a more precise description of the fields and to optimize the electromagnetic and cryogenic configuration. Subsequently, a second commissioning phase (second commissioning phase of the spectrometer and detector section (SDS-II)) was conducted in two parts (SDS-II part A (SDS-IIA), SDS-II part B (SDS-IIB)). The first half of SDS-II was performed from October 2014 to March 2015, while SDS-IIB was conducted from June 2015 to September 2015. Following to a bake-out of the main-spectrometer, SDS-IIB mainly aimed to investigate the background. All measurements performed and analyzed in this thesis have resulted from SDS-IIA. The focus of this chapter is on giving a summary of the conditions under which the measurements were taken. An in-depth description of the spectrometer and detector section will thus be given here. Especially the e-gun is of importance here, as it was developed for the commissioning measurements and is not a part of the later KATRIN beam-line. Figure 3.1 gives a schematic overview of the whole system. On the most upstream side of the main-spectrometer, the e-gun is mounted (section 3.4), while the FPD is located at the downstream side of the spectrometer. The latter will not be discussed any further as it was already described in section 2.3.5. Electrons are guided between these two components by a magnetic field that is generated by superconducting solenoids and the so called air-coil system (section 3.2). As the whole spectrometer needs to provide ultra-high vacuum conditions, pumps that are based on different techniques are installed (section 3.1). The electric potential is fine-tuned with the inner electrode (IE) system, described in section 3.3. Note that the high voltage system used for generating the potentials is a main topic of this thesis and therefore described in great detail in the next chapter 4. The setup for monitoring and controlling the apparatus is described in the last section (section 3.5).

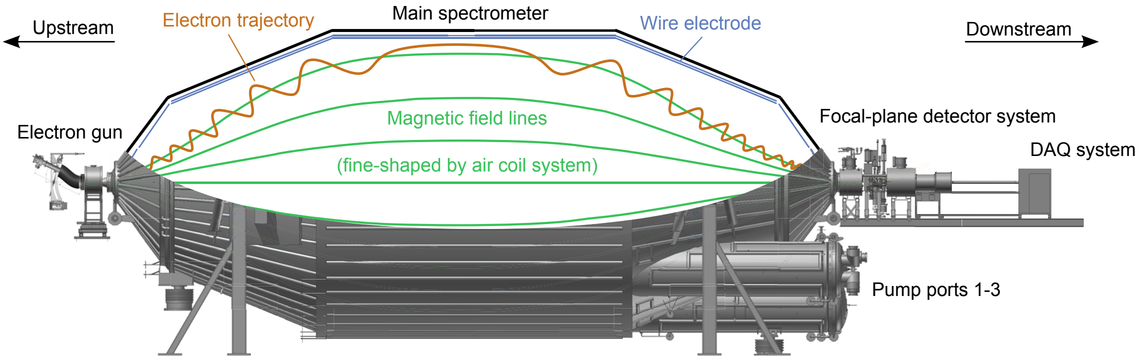

Figure 3.1: Overview of the SDS-II setup.The e-gun is located at the upstream side of the spectrometer and the FPD on the downstream side. During tritium mode measurements the e-gun is replaced by the beam line which is continued in this direction by the pre-spectrometer. The air-coil system and the pre-spectrometer magnet 1 (PS1) are not shown. Electrons are guided by the magnetic field from e-gun to the FPD. The IE is located inside the main-spectrometer vessel and allows to fine tune the electric fields by segmentation. Figure from [Har15].

3.1 Vacuum system

The large spectrometer volume has to fulfill rather stringent vacuum conditions of only $\approx 10^{-11}$ mbar ([Wol15]). With the additional large surfaces of the IE the setup has been shown to to feature an outgassing rate of approximately $(1.4 - 2.5)10^{-12}$ mbar l/s ([Wol16]) during SDS-I, which is close to nominal values. Note that this number requires an extended baking-out phase at 200 C. The UHV-pumping system is mounted at three large pump ports of the downstream side of the apparatus. There, a total of six TMP devices plus a NEG pump system and a LN2 cooled baffle system are installed. In addition, systems for controlled gas inlet and pressure measurements are mounted. For the initial pump-down of the vessel, a screw pump with a pumping speed of 630 m^3/h is used. The actual system is described in more detail in [Wol16] and [Har15].

Differential Pumps

Two of the pump ports are equipped with a total of six large TMPs. The net pumping speed for hydrogen inside the vessel of these devices together is 10^4 l/s [Wol16]. They are supported by additional smaller TMPs with a capacity of 300 l/s and a screw pump for prevacuum. The main purpose of the TMPs is the removal of noble gases, while the NEG pumps very effectively pump hydrogen.

Getter Pumps

All pump ports are foreseen to be equipped with 1000 NEG strips of 1 m. Activation of this material requires a bakeout procedure. During SDS-I these were partially activated at temperatures of 300 C, resulting in a total pumping speed of 10^6 l/s for remaining hydrogen inside the vessel. Owing to technical issues, the spectrometer has been limited to maximum bake-out values of 200 C since then. The reason for this lies in the allowed thermal range of the CuBe rods that are mounted inside the spectrometer for potential distribution of the inner electrode. These rods did deform at temperatures beyond 200 C, thereby causing short-circuits during SDS-I. An electrical heating system has thus been developed and installed inside pump port three. This local heating has allowed to activate the NEG pump at 400 C.

Baffle System

The NEG pumping system comes with the drawback of emanating unstable ^{219}Rn atoms into the volume. This isotope can decay by emitting an α particle inside the vessel and cause background by electron emission. To counter this effect, a baffle system is mounted between the NEG strips and the main volume, as shown in fig. 3.2. Radon atoms now are trapped via cryosorption on its cold surface, thus decaying outside the sensitive volume. The main component of the baffle system are 22 V-shaped copper blades that are cooled by liquid nitrogen. Cooling of the blades is achieved through pipes of stainless-steel attached to them, that are flooded with liquid nitrogen. From a technical point of view the baffle system is elevated on high voltage, while the liquid nitrogen supply vessel is grounded. The combination of high voltages, vacuum and cryogenic temperatures have posed a non-trivial challenge in constructing proper decouplings. To ensure that radon atoms hit the cold surface at least once, the baffle blocks the direct line of sight between the NEG strips and the fiducial volume. Accordingly, the effective pumping speed of the getter pump is reduced to $3.75 \cdot 10^5$ l/s, [Wol16]. For automated control of the nitrogen flow and the baffle temperatures, three temperature sensors are mounted on each baffle. Measurements have shown the temperature of the baffles to adjust to around 86 K, which is higher than the boiling temperature of nitrogen of 77 K. This offset is due to limited thermal coupling and the pressure of 1.5 bar of the nitrogen supply.

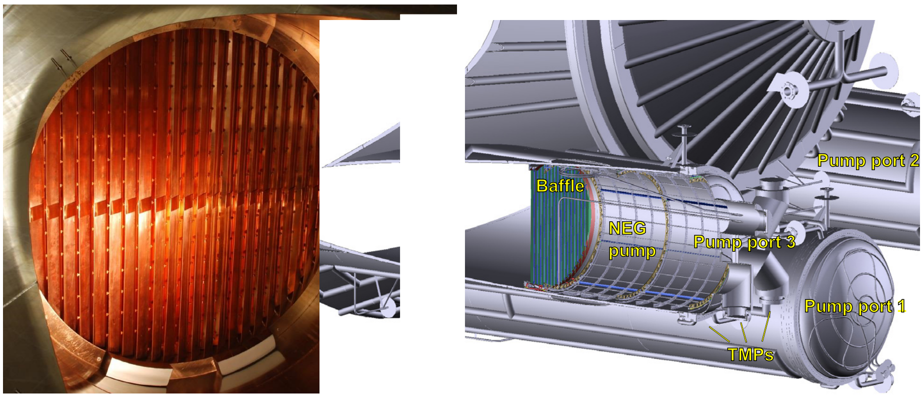

(a) Baffle **(b)** NEG pumps

Figure 3.2: (a) A photograph of the baffle mounted inside pump port three, taken from the inside of the spectrometer. The 22 V-shaped copper blades are clearly visible. Figure from [Goe14] (b). CAD drawing of the pump ports. A cross section of pump port three shows the location of baffle and NEG pump. Taken from [Har15].

3.2 Magnet System

Magnetic fields guide electrons from the source to the detector, and thus play an important role not only with respect to background processes but also the central topic of this thesis, the transmission properties and their systematic uncertainties. As discussed in section 2.1.1, the energy resolution of a MAC-E filter is directly connected to the ratio of minimum and maximum magnetic fields. In addition, when propagating along different magnetic field lines, transmitted electrons will pass the analyzing plane at different radial and azimuthal positions. Inhomogeneities of the electric potential thus require to create a complete map of the electric field at the analyzing plane and elsewhere. First, the magnetic fields are discussed, where four different magnetic field configurations were used during SDS-II, see fig. 3.3. Only one of these was used during the measurements conducted in the scope of this thesis. According to the design specifications, the standard configuration for tritium measurements is given by the 3.8 G setting [Ang05], shown in orange. This configuration exhibits two minima of the magnetic field. This setting fulfills the transmission conditions and therefore is best suited for measurements that involving the e-gun. Table 3.1 summarizes all magnet currents for generating this field.

Superconducting solenoids

A total of four superconducting solenoids is mounted in the SDS setup to generate the guiding magnetic fields at both ends of the spectrometers. At the upstream side, the so called pre spectrometer magnets 1 and 2 are located. Measuring 400-mm in diameter, these

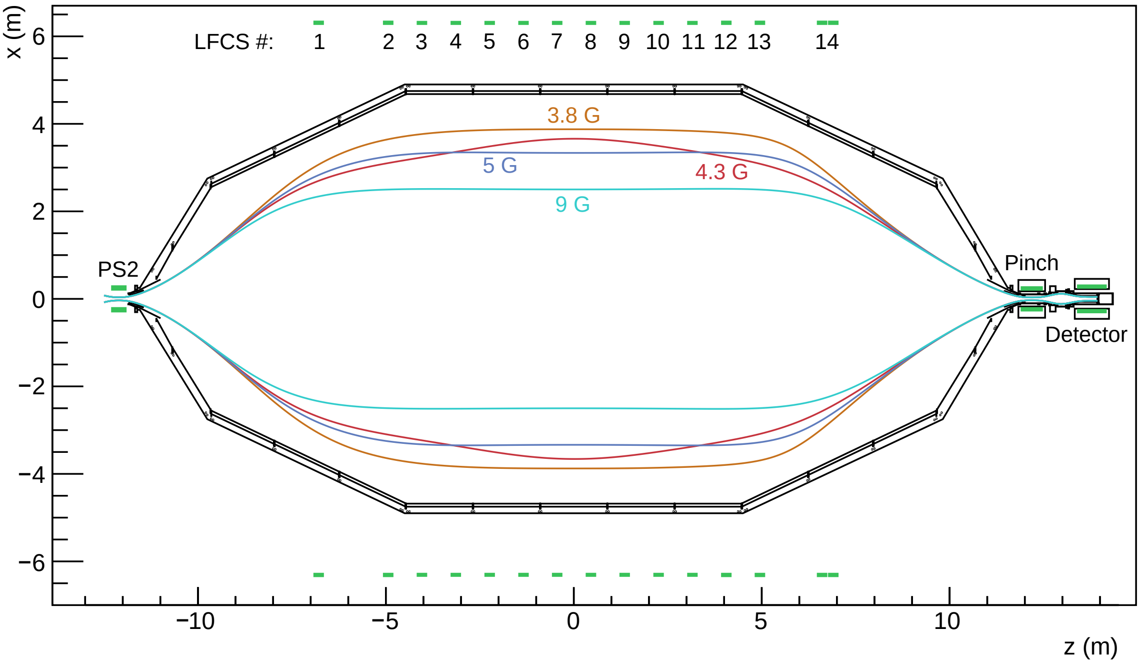

Figure 3.3: Visualization of the flux tube boundaries for different magnetic field configurations. The 3.8 G setting is the only one that has been used during measurements connected to this thesis, as it is the nominal field for tritium measurements.. Adapted from [Har15]

warm-bore magnets are able to produce maximal fields of 4.5 T each at a corresponding current of 157 A. The PS2 magnet is located at a distance of 12.1 m from the analyzing plane. The PS1 had to be moved between SDS-IIA and SDS-IIB. Initially it was located at the distance 3.4 m with respect to the position of PS1 and with a field of 3.0 T. During the second part of SDS-II the magnet was moved further downstream to its final position in the KATRIN beam-line and operated at its nominal field of 4.5 T. The reason top operate this magnet at non-nominal fields and a different position in SDS-IIA was the e-gun. This device, or more precisely an optimized transmission condition for its emitted electrons, made it necessary to adapt the experimental setup. The other two warm-bore superconducting solenoids are located on the downstream side of the spectrometer and

Table 3.1: Configuration of the magnet currents for transmission measurements during SDS-II. Explained in the next section, the PS1, PS2, Pinch and Detector magnet are superconducting solenoids, while the LFCS1-LFCS14, the vertical EMCS and the horizontal EMCS are parts of the air coil system. The currents are given in Ampere and correspond to the 3.8 G, two minima setting. The PS1 magnet is included here. For some some measurements during SDS-II, a different configuratin was used, optimized for a non-active PS1 configuration.

Magnet	Ampere
PS1	104.0
PS2	156.0
LFCS1	21.14
LFCS2	25.66
LFCS3	20.30
LFCS4	28.36
LFCS5	38.82
LFCS6	27.52
LFCS7	34.37
LFCS8	50.68
LFCS9	10.37
LFCS10	44.44
LFCS11	37.19
LFCS12	20.96
LFCS13	43.32
LFCS14	-50.35
vert. EMCS	50.0
horic. EMCS	9.0
Pinch	72.63
Detector	46.80

are part of the detector system. Closest to the main spectrometer is the PCH magnet. This magnet provides the highest magnetic field of the experiment and plays an important role in defining the energy resolution of the MAC-E filter. The field of this device was set to 5.0 T. The last superconducting magnet in the KATRIN beam-line is the detector (DET) magnet, where electrons that are transmitted through the filter are projected onto the detector wafer. During SDS-IIA this magnet was operated at 3.0 T.

Air Coil System

In order to fine-shape the magnetic field and to compensate the earths' magnetic field, the so called air-coil system is used ([Glu13]). Figure 3.4 illustrates the arrangement and dimension of this system. Large rings act as holding structure for the actual coils. The system consists of two sub-systems, the low-field correction system (LFCS) and the earth magnetic field compensation system (EMCS). The latter compensates the earth's magnetic field, which can be considered to be constant in direction and absolute value. A total of 16 current loops in horizontal planes and 10 loops in vertical planes compensate the vertical ($B_{\text{vert}} = 43.6\,\mu\text{T}$) and horizontal components ($B_{\text{hor}} = 5\,\mu\text{T}$) of the earth field [Glu13]. Without the compensation the flux tube inside the main spectrometer would not be axially symmetric and would not be oriented along the direction of the beam-line. In terms of transmission properties this would shift the analyzing plane from the region of the highest retarding potential and lead to non-negligible systematic uncertainties. With respect to the spectrometer axis, the LFCS consists of fourteen coaxial coils, measuring 12.6 m in diameter. Apart from allowing fine-adjustments of the whole flux tube, these magnetic systems also provide a means to change the minimal field in the analyzing plane B_{min}. By varying the currents of the power supplies that are connected to the individual coils, the magnetic field in the analyzing plane can be adjusted to values in the interval $[0.33\,\text{mT}, 1.00\,\text{mT}]$. The upper boundary is given by the maximal current of the power supplies, while the finite size of the vessel defines the lower value. In addition, the ring 14 is flipped in polarity compared to all other magnets. As the pre-spectrometer magnet 2 (PS2) and PCH magnets are driven at different field strengths, this coil is used to compensate

Figure 3.4: Photography from the upstream to the downstream side of the spectrometer without e-gun. The rings surrounding the vessel serve as holding structure for the air-coil system. Photo: Karlsruhe Institute of Technology (KIT), 2009.

for the asymmetric stray fields.

This thesis, dealing with the influence of high voltage fluctuations to the transmission function, only requires the transmission condition to be fulfilled. Thus, the magnetic guiding details are less relevant to measurements with and without active artificial ripple. It has to be emphasized however that the design sensitivity can only be reached by a very precise knowledge of the magnetic fields and the means to measure them with high accuracy. A detailed description of the magnetic fields, the corresponding measuring devices and their influence on the transmission properties can be found in [Erh16b] and [Erh16a].

3.3 Inner Electrode

The functional principle and the structure of the inner electrode were discussed in section 2.1.2. Figure 3.5 compares a picture of it from the inside of the main spectrometer to its implementation in the simulation code KASSIOPEIA. The electrode consists of 15 rings, each of them consisting of an inner and an outer wire layer with an additional separation between west and east side. Rings seven to eleven are electrically shorted, because no fine-shaping of the electric field in the central region of the vessel is necessary. A total of $11\,\text{rings} \otimes 2\,\text{wire layers} \otimes 2\,\text{half rings} = 44\,\text{potentials}$ have to be generated and distributed to the individual segments. From the side of the high voltage system, the technical realization is discussed in chapter 4. The distribution of voltages inside of the vessel from the high voltage feedthroughs to the associated wire electrode segment is realized by rods made of CuBe. During the bake-out before SDS-I, the system started to deform slightly under high temperatures, resulting in short-circuits between different rings and wire layers. An overview of the short-circuits is given in fig. 3.6. The rings of the inner electrode have been numbered from two to sixteen, while the anti Penning electrodes are labeled as ring one and seventeen, even though they are strictly speaking not part of the inner electrode. All existing short-circuits only affect outer and inner wire layers as well as rings that do not have to be on different potentials for measurements of the transmission function. One additional short-circuit was observed during SDS-IIB between the layers of ring twelve.

During the commissioning measurements, a generic potential configuration for the IE was

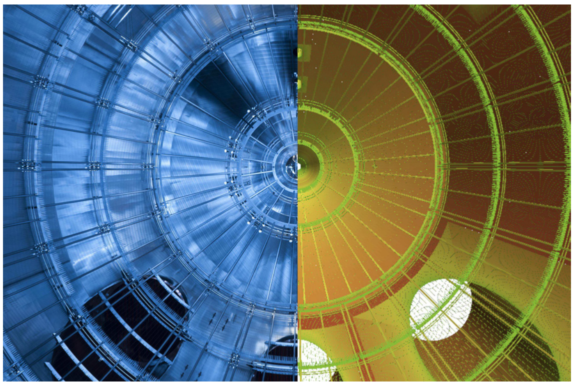

Figure 3.5: Photograph (left) and simulation of the implemented geometry (right) of the inner electrode system in the main-spectrometer. The perspective is from upstream to downstream side, as indicated by the three visible pump ports. Adapted from [Cor14]

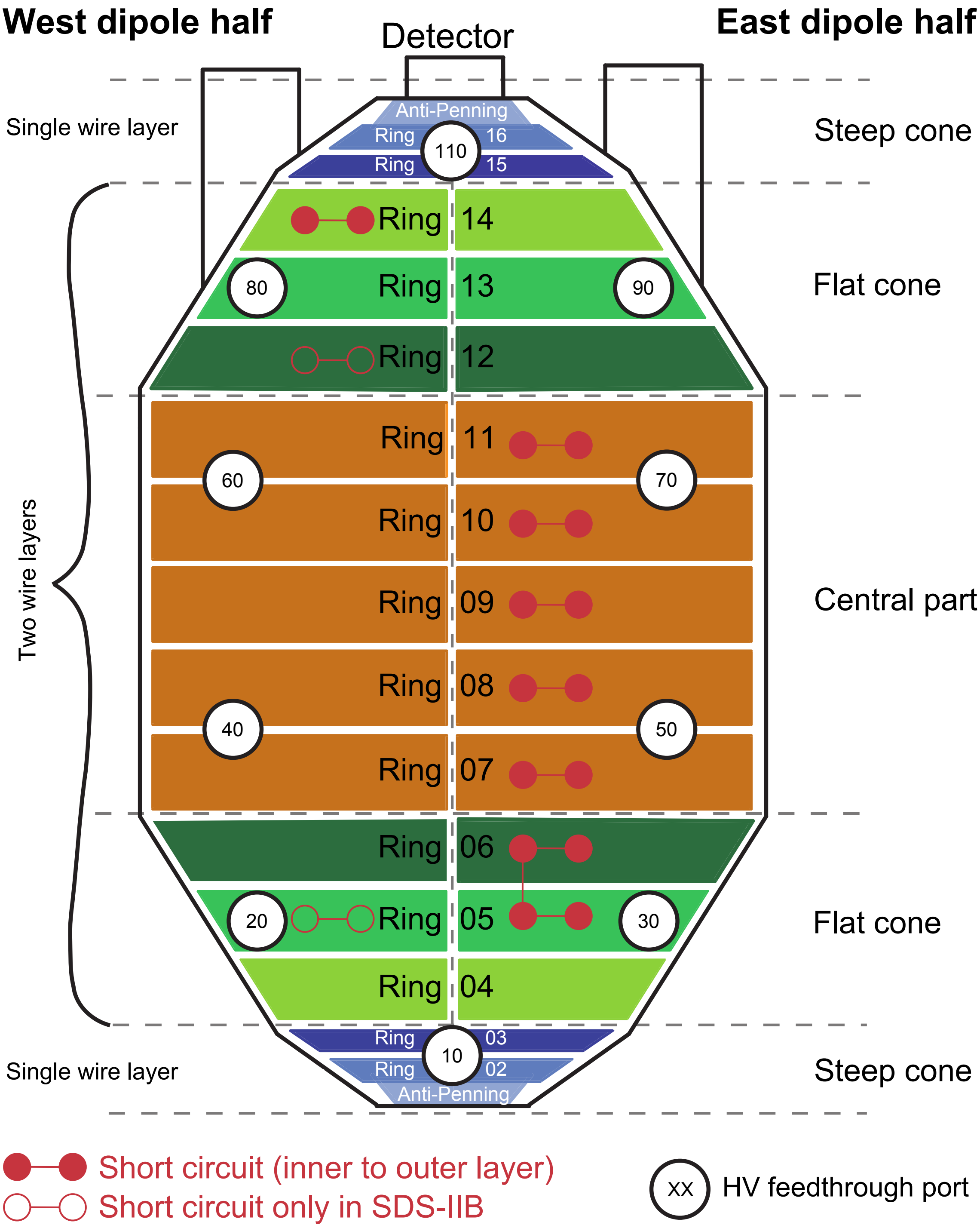

Figure 3.6: Overview of the inner electrode system and status of short-circuits. The nomenclature of the IE rings ranges from rings 2 to ring 16, the anti Penning electrodes are designated ring 1 and ring 17. The short-circuits occurring during the bake-out of the main spectrometer due to high temperatures only affect the outer and inner layers of the dual-layer rings as well as two rings in the upstream flat cone that play no role for transmission studies. An additional short-circuit between the layers of ring twelve was only observed during SDS-IIB. Adapted from [Har15]

chosen, see table 3.2. In doing so, the potential of the vessel is typically set to 18.4 kV and the inner electrode potential to 18.6 kV. This is one of the standard configurations common to many measurements during both commissioning phases and will likely be implemented during the tritium scanning mode. To fulfill the transmission conditions, only the steep cones have to be elevated onto a potential which is 100 V more positive than all other segments.

In conclusion, the short-circuits of the wire electrode system, only affect the background reduction due to the non-available double layer principle but do not affect the transmission properties and therefore play no role for the investigations of high voltage ripples. The configuration is simple but respects the transmission conditions and results in no further complications due to more complex electric field setups.

Table 3.2: Configuration of inner electrode potentials used for the measurements discussed in this thesis.The chosen setup fulfills the transmission conditions and introduces no other systematic effects. The inner electrode potential is set to 18.6 kV, close to the endpoint of tritium β-decay. Only the steep cones are elevated onto a potential which is 100 V more positive to fulfill transmission conditions.

Location	Ring	Voltage (kV)
Steep cone	02-03	18.500
Flat cone	04-06	18.600
Central part	07-11	18.600
Flat cone	12-14	18.600
Steep cone	15-16	18.500

3.4 Electron Source

The investigation of the transmission properties and implementation of a detailed field map of the static fields inside of the main spectrometer requires an electron source, which emits mono-energetic particles at ultra-stable rates with a fixed, but adjustable, starting position and angle. The e-gun shown in figure fig. 3.7, was of major importance for the measurements of SDS-II. The basic functional principle consists of two parallel plates elevated onto different potentials, and housed in a rotatable vacuum chamber. Electrons that are created by the photoelectric effect at the first plate, the back plate, are accelerated by high electric fields between this plate and the second one, the so called front plate. Between these two plates the acceleration is non-adiabatic, which allows to adjust the polar angle of an electron by rotating this sub-system inside the vacuum chamber, see fig. 3.8. In a second step, the electrons are accelerated adiabatically and conservation of the magnetic moment μ, in a region between the grounded housing and the front plate. In total, the energy of an electron is defined by the potential of the back plate and its pitch angle, i.e. by the relative position of the rotable box that houses the plates inside the vacuum chamber. The angular resolution has been determined in ([Beh16], [Erh16b]). A major advantage of the measurement and analysis strategy is the fact that only relative deviations between undistorted and rippled transmission function measurements are of

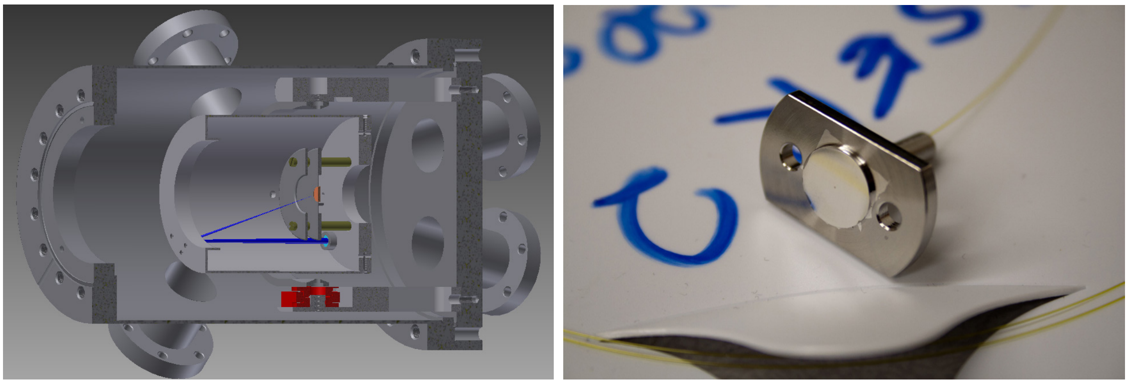

(a) CAD drawing of the e-gun chamber **(b)** Optical fiber

Figure 3.7: (a) CAD drawing of the e-gun with the vacuum chamber and the rotatable box containing the front and back plate. High electric field, non-adiabatically accelerate electrons, which are emitted by the photoelectric effect at the front plate. Thereby the starting angle is defined. Between the grounded housing and the front plate, electrons then get accelerated adiabatically to their final energies defined by the back-plate potential. (b) Photograph of the optical fiber for transporting UV light to the silver surface. The light that propagates through the 200 μm thick fiber shines onto the silver surface, which subsequently emits electrons via the photoelectric effect. During SDS-II, a gold layer rather than silver was used. Figures adapted from [Han13].

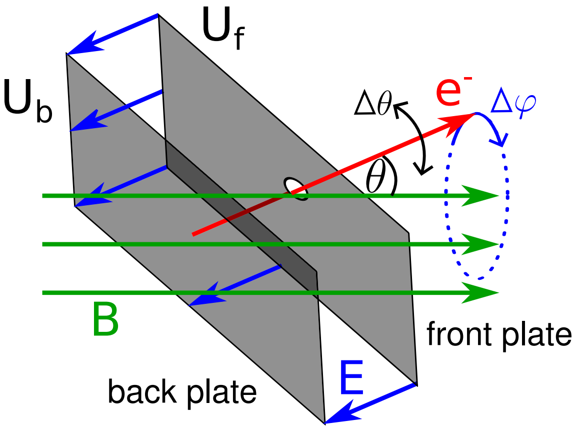

Figure 3.8: Schematic of the e-gun working principle. Electrons are produced on the backplate and accelerated by the high field caused by the front plate. The system effectively is a plate capacitor. Electrons pass through a hole in the front plate with an angle that is defined by the relative position between magnetic field lines and the rotatable system. The angular resolution of electrons can be neglected in the context of this thesis. Taken from [Wan13]

interest. Therefore, the angular resolution is of no importance to validate the developed theoretical model. The corresponding effect is implemented by an additional parameter that enters the fit functions. On the other hand, when investigating the radial and azimuthal dependency of the retarding potential, the starting position of electrons has to be known. This can be adjusted by changing the position of the unit the large manipulator is mounted on. The mapping between starting position, the direction of the magnetic field at the corresponding location and the associated position in the analyzing plane can be found in the cited works. To reduce systematic effects and to optimize the effective rate, the e-gun was aligned in parallel to the lines of the magnetic field during all measurements carried out for this work. From a practical point of view, two additional remarks have to be made. First, the used sources for UV light (LASER and LED), are monitored to verify the quality of the electron rate. After reasonable heating-up cycles of the order of minutes, the rate of emitted electrons is stable for both light sources. Due to aging effects of the electron emitting surface, the rates visibly decreased over time. Nevertheless, this effect is in the order of a few counts per hour and can be neglected in comparison with the typical rates used in measurements of 5 kcps. Secondly, the back-plate potential was generated by a two quadrant offset supply of negative polarity in series with a battery pack of positive polarity. Both components were elevated onto the spectrometer potential. Hence, no systematic effects of the high voltage enter the system. As it is a main objective of this work to investigate these effects, a different configuration was used during the transmission function measurements related to HV systematics. A second high voltage supply of high precision was used to generate the back plate potential, which thus decoupled the e-gun electrically from the main spectrometer. This allowed to ripple the analyzing potential independently.

In summary, the e-gun is an indispensable tool to investigate the spectrometer characteristics and its MAC-E filter characteristics. Ultra-stable rates and high energy resolution as well as adjustable angular selectivity are major features of this system. The analyzing techniques and the corresponding measurements carried out for this thesis, however, do not rely neither on energy nor angular resolution and thereby feature minimized systematical effects. The development of the e-gun is described in more detail in [Zac15] and [Han13]. Further, measurements taken during SDS-I are described in [Gro15a] as well as [Gro15b], while the newest results from SDS-II can be found in [Beh16] and [Erh16b].

3.5 Slow Control and data management

The data acquisition (DAQ) system of the detector samples experiment-specific information at small time scales. All sub-systems of KATRIN comprise a total of several thousand sensor and controlling channels that need to be handled ([Kle14]). Safety-relevant components are monitored and controlled by Simatic PCS-7 system ([Sie14]), while systems with no safety relevance are read out and set with a series of compact field point (cFP) units that are based on the LabView environment. Both systems together define the Slow Control system of KATRIN. Exemplary for the PCS-7 controlled systems, the vacuum system is mentioned here. Exemplary for the cFP controlled ones the air coil system is mentioned. Safety-relevant systems only allow an operation by a defined group of experts.

The high voltage system for obvious reasons is of major safety relevance. During routine measurements, it needs to be controlled by experimentalists. A basic feature of the HV system is the fact that it is connected to both, cFP units and PCS-7, while the former has only access to channels that are needed for measurements and are strictly limited to well-defined and safe configurations. An operator is thus able to control and monitor the DAQ and Slow Control channels through a C++ based software package, object-oriented real-time control and acquisition (ORCA) system. Sensor data that can be displayed in real-time by interfaces of both systems are additionally stored in a chain of SQL-databases. The advanced data-extraction infrastructure (ADEI) system provides world-wide access to all recorded data ([Chi10]). A PHP-based back-end system preprocesses data and organizes the database-access. A web-based front-end allows users easy access to sensor and detector data and to their visualization, as well as simple pre-analysis functions. For automation of measurements, ADEI also provides a module for the reverse direction of communication, which allows to control the experimental parameters via ORCA. A more high level analysis, which is beyond the simple ADEI packages, is enabled by the KDBServer package on the server side and the KATRIN library (KaLi) package on the client computer side. A major feature here lies in calibrations that are automatically applied by system in agreement with the corresponding timestamps or run numbers. A schematic overview of the complicated layered system is given in fig. 3.9.

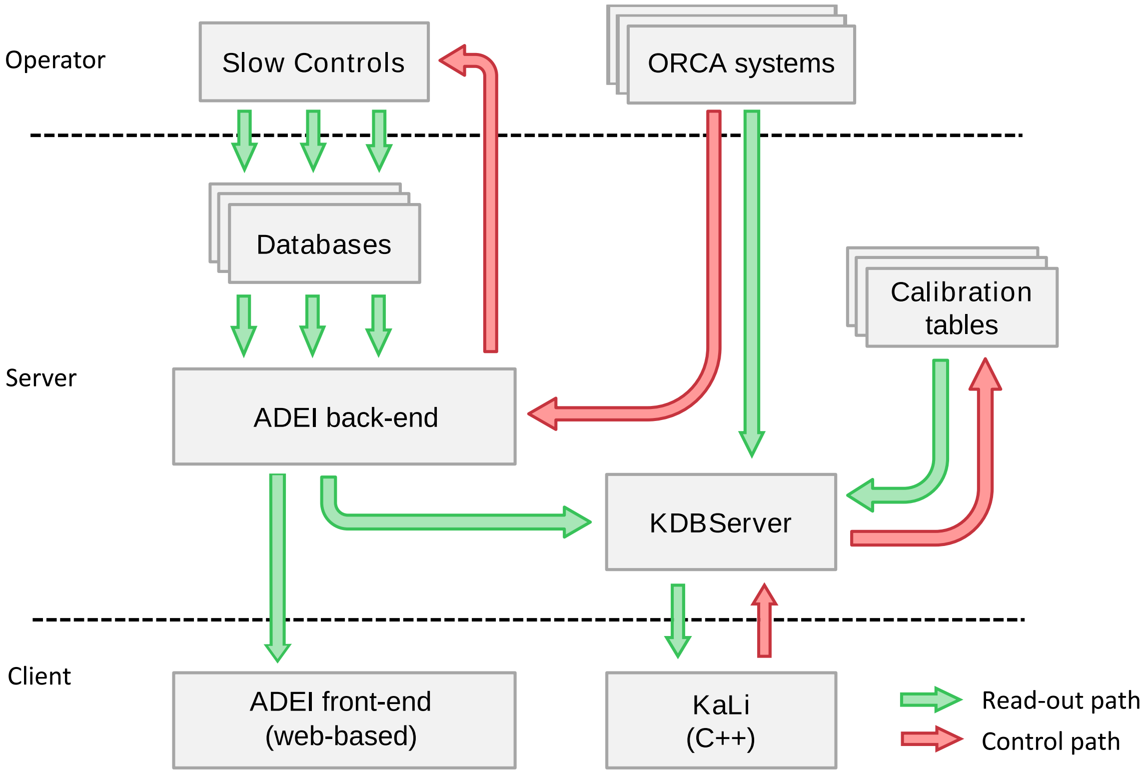

Figure 3.9: Schematic overview of the Slow Control and database systems. The PCS-7 system is implemented in an independent chain and not displayed here. An operator is able to read out and set Slow Control channels through ORCA scripts. The database servers store information and pass control values onto the associated cFP units and automatically apply calibrations. For worldwide near-time monitoring and basic analysis works, ADEI provides a web-based front-end. Detailed analysis and data-extraction is managed by KaLi. Adapted from [Har15]

CHAPTER 4

High voltage system

Figure 4.1: Part of the safety fence, as seen from the outside of the high voltage area. Kindly provided by Klaus Mehret.

Systematics associated with the retarding potential have a major impact on the neutrino mass sensitivity. For these reasons, an ultra-stable generated voltage that is monitored with highest precision is needed for the KATRIN experiment. These requirements have resulted in the development of a sophisticated, decentralized high voltage system with each of its sub-components pushing the limits of technical feasibilities and expanding the frontier of electrical measurement techniques. This involves not only the tasks of generating and measuring voltages but also of building a smart safety system that prevents man and machine from any harm in a fully automated way. As one of the installed safety features, the safety fence is shown in fig. 4.1.

This section gives a detailed overview of the components involved and their working principle. A key issue in the design and implementation was to meet the design goal of high voltage instabilities to fulfill $\sigma \leq 60\,\mathrm{mV}$ or even exceeding it. A schematic drawing of the overall system is given in fig. 4.2. The whole setup can be categorized in four distinct parts. The first one of these includes all components responsible for generating high voltage and distributing it, being indicated in blue. For the purpose of fine adjusting the electric fields and reducing background, the inner electrode system is built of many different segments, with each one having a unique potential (section 4.2.1). The resulting rather complicated

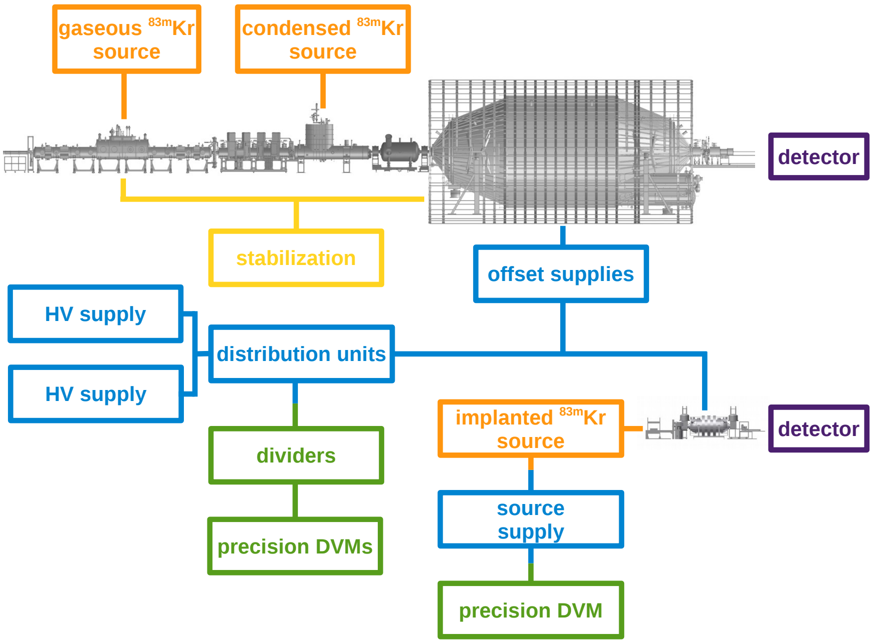

Figure 4.2: Schematic overview of the KATRIN high voltage system. All components can be distinguished by their functional principle into four different categories. The generation and distribution units are shown in blue. Here, two supplies provide the main-spectrometer vessel and the monitor-spectrometer with the necessary high voltages, while a series of offset supplies allow fine adjustment of the fields. These potentials are smoothed by active and passive ripple-suppression devices in yellow. The voltage-measurement is performed by two high-precision HV dividers and precision voltmeters (green). For purposes of energy calibration and monitoring, different krypton sources provide ultra-stable electron lines (orange) that are counted by the detectors (purple). Inspired by [Bau13b], spectrometer models taken from [Kle14].

voltage distribution topology has been reduced to only two parts. The first part is given by the power supply for generating the global voltage that is applied to vessel and monitor spectrometer. The second part is given by the offset power supplies that electrically are based on the main potential and allow to apply individual settings for a specific component. As two high-precision HV dividers are utilized, and as the spectrometers have to be able to run in connected and in single mode, dedicated distribution units allow a large variety of configurations. This is also the reason for the second high voltage supply connected to these units. When both spectrometers are performing separate measurements while being disconnected, individual potentials are needed.

Even the most stable means of generating high voltage offsets will result in rippled potentials because several distortions inevitable couple into them, see section 6.2. Therefore an active system for smoothening the main retarding potential is deployed (yellow), namely the post regulation setup described in section 4.2.2. Additional smoothening capacitors between all components suppress high-frequent distortions. Especially important is the fact that the source side is grounded but still has to be AC-connected to the main spectrometer.

Even with the filter being highly stable, the distortions would also apply to the source side significantly influence the retarding potential without active smoothening and therefore yield the same negative influences on the neutrino mass sensitivity. A precise measurement of the voltages is thus of the same importance as generating it. This comes from the fact that uncertainties of the measurement will lead to the same loss of neutrino mass sensitivity. For this reason two high voltage dividers have been developed, built and characterized for the KATRIN experiment (section 4.4). Together with two precision digital voltmeters these dividers form the complete measurement chain, as illustrated in green. For further details, see section 4.5. Finally, several electron sources allow for energy calibration via comparison to a constant of nature, as shown in orange. For the latter, the scope of this thesis only contains the monitor-spectrometer and its implanted Krypton source, where the condensed and gaseous calibration sources are subject to other works in progress ([Res17]).

4.1 Safety Systems

With a capacitance of several hundred nanofarads and voltages up to $-35\,\mathrm{kV}$, the main-spectrometer stores an amount of electrical power comparable to a defibrillator. Contrary to the monitor spectrometer the outer surface of the main spectrometer is not isolated and therefore poses danger to persons that get in contact with it. Additionally, the aimed neutrino-mass sensitivity requires delicate electronics throughout the whole system, that is not easily interchanged and has to be protected against any harm. With complicated preconditions like the large vessel volume being under ultra-high vacuum, cold surfaces and points where these meet with the applied voltage, it is of major importance to prevent the system from discharges. The central goal however, is the safety of the personal. An operator has to be sure to work in a safe environment, which protects against unintentional contact with the high voltage. For these reasons a layered safety system was employed in the spectrometer and detector section of the KATRIN experiment.

The first step in taking a safe working environment for operators is to define a high voltage envelope that encloses all electrically live components. Thereby unintentional contact with dangerous voltage levels is avoided. Consequently, the whole spectrometer is surrounded by a fence, which is grounded redundantly at two points per segment. A key feature here is the mesh size and the expansion of gaps as functions of voltage and distance. The closed protection surface of this fence is only broken by four doors allowing entrance to the high voltage area and the spectrometer. All of them are monitored for their opening status. These status signals are hard-wired to a programmable logic controller (PLC), see fig. 4.3(a). At this unit, all safety-relevant data from all devices of the high-voltage system is gathered. If any of this status-bits gives an alarm, the control unit immediately shuts down the high voltage by triggering the interlocks of all supplies and additionally causes a large grounding switch to close, see fig. 4.3(b). In order to prevent discharges due to fast transfers of electric currents, first only one of the red clamps close and discharge the system slowly through power resistors with $\Omega = 100\,\mathrm{MOhm}$. After a $10\,\mathrm{ms}$ interval, the second clamp closes and couples the spectrometer directly to ground potential. At this point practically all charge carriers will already be drained. The reason for the second clamp lies in redundancy, as in principle mechanical blocking has to be considered, and in terms of safety grounding contact always has to be established directly without intermediate

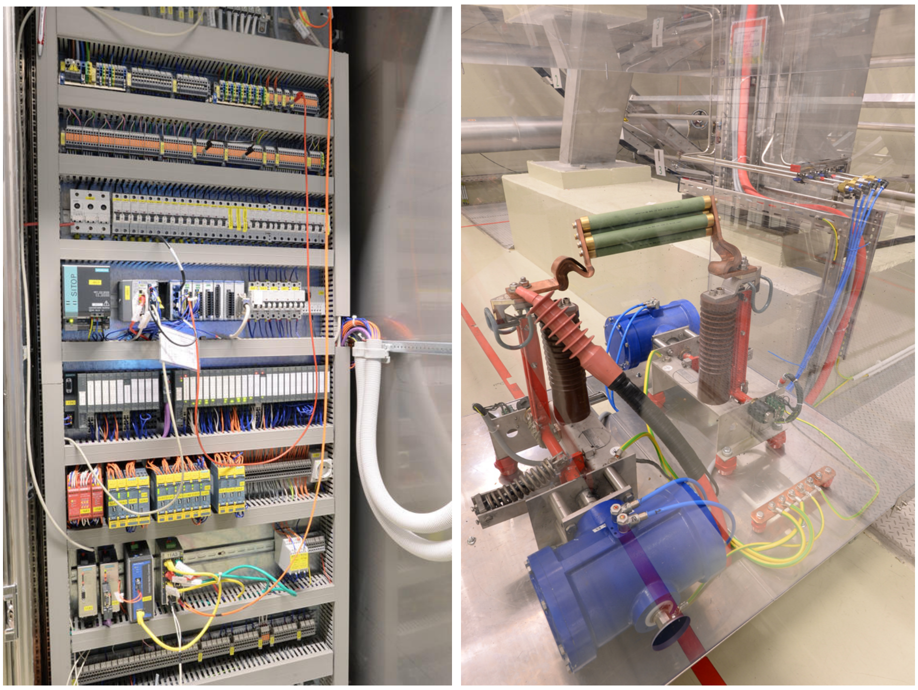

(a) Programmable logic controller **(b)** Grounding switch

Figure 4.3: Exemplary safety measures. (a) The PLC of the high voltage system. Every sub-component of the system provides status signals through hard-wired paths to a central intelligence unit. In case of failure the whole system is automatically discharged by a large grounding switch (b). Originally used in railroad applications this switch is capable of conducting large currents. To guarantee operability even in case of breakdown of the mains-voltage this device is driven pneumatically by pre-pressured containers, as seen in blue in the front and the back of the picture. If triggered, the grounding switch will firstly discharge the system over large resistors, to prevent the spectrometer and adjoint components from harm and will connect directly to ground potential only 10 ms after that. Figures kindly provided by Klaus Mehret.

resistors. Additionally the grounding switch acts entirely independently from the mains voltage by using pneumatics. Pressurized containers are used in closing the grounding connections, which are located in the front and the back of fig. 4.3(b) (blue). Apart from the HV systems' own status information the PLC also receives data on a global scale, from each of KATRIN's sub-components. For instance in the worst case scenario of a complete vacuum breakdown, discharges are expected and the system has to be shut-down. Accordingly, the PLC has a defined vacuum limit at which this takes place. Generally, many parameters have to be monitored constantly, resulting in sophisticated lock lists.

Standard operation requires the system to be shut down only in urgent cases. The corresponding clearance procedure can be restricted to a group of experts only. Nevertheless, the commissioning measurements have made it necessary to access the high-voltage area rather frequently to adjust components, where other parts remain unchanged. For this reason different clearance procedures have been developed, each of them dedicated to another level of clearance with an according group of people that are allowed to perform the procedure. The first category of these procedures consists of tasks that only members of the high voltage task can perform. Especially the initial-start up after maintenance phases with detailed isolation-test, checking of all interlocks functioning properly and clearance after upgrades fall in this category. The second category are clearance procedures which can be handled by standard operators. If the high voltage has been ramped down and turned off intentionally but no safety lock has been broken, it is not necessary to go through detailed investigations of the whole system again, which would only slow down measurements.

An essential part of both checklists is a check of the integrity of the high voltage envelope. Naturally, this implies the safety-fence and its proper grounding. However, in addition to the access doors, the envelope is broken at many locations by an array of cables, pipes and alike that necessarily pass through the barrier. Evidently, these also have to be considered. For this reason, signs to clearly mark such materials have been employed, see fig. 4.4. Each item that passes through the high voltage envelope is assigned such a sign at the breakthrough point. Conducting materials like copper clearly pose a possible threat if passing near charged surfaces. However, this is also true for insulators, as they can get capacitively charged if they are in regions where electric fields are present. As a consequence, also insulators are marked with a sign and the exact media type is specified. Note, also that all items that pass the envelope are electrically connected to ground potential at least at the breakthrough point. For archiving purposes the date of review, the name of the inspector and an unique identification number are also given on the sign. With this information a central list summarizes all mounted items. A registered item is checked for sufficient distance to the high voltage, conductivity and at least one point where it is electrically connected to the ground potential. These signs then ensure safety for every person that either gives high voltage clearance or is conducting hardware-work during measurements. Furthermore the application of this method accelerates the procedures after larger hardware-upgrades. Without keeping record of every single connection after maintenance or upgrades the whole system may have to be checked. By detailed book-keeping this can be restricted to newly built-in components only.

Additionally to the clearance procedure, some features of the HV control are also restricted to operation by experts. On the top-expert level each set value can be changed. On the other hand, for a normal operator the access is strictly limited. For one, the inner electrode only allows certain maximum potential differences between its individual segments. The voltage power supplies however, can provide larger voltages than allowed so that a two-layer safety is employed to prevent the components from damage. Firstly, the supplies are limited by their own hardware limits, that are adjustable by potentiometers. Furthermore, the protection circuits that are built-in into the HV cabinet, only allow only secure voltages. Secondly, the central controlling unit of the voltage system limits potentials only to specified and safe values. Likewise, the control of ramping speeds, maximal currents et cetera is only given for experts.

In conclusion one can state that an operator can be sure to work in a safe working environment with the safety-system being fully automated and highly reliable. In addition to the most important safety of the personal, the system also protects the apparatus from

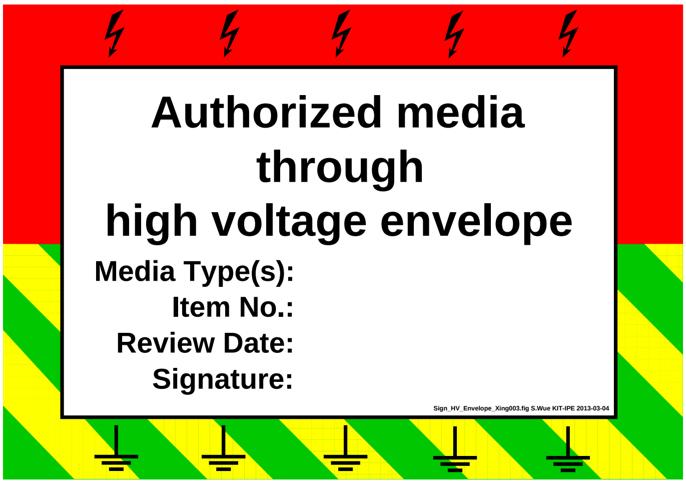

Figure 4.4: Sign for authorized media that passes through the high voltage envelope. Every cable, pipe or alike that passes through the otherwise sealed safety-surface is visibly marked at the breakthrough point with one of these signs. The exact media type, i.e. copper connection, compressed air hose, etc., is specified. For archiving purposes each item is designated a unique identifier, the review date and the signature of the inspector. Additionally all items are summarized in one central document. Clearly, any conducting material coming close to the high voltage of the main spectrometer poses the threat of carrying an electric charge. This also holds for insulators. Due to capacitive charging, these can slowly charge-up over long time periods. Therefore these signs give a fast overview after updates of the system.. Taken from [Wüs13].

harm. The adapted safety system has been proven to be fully functional and reliable during two commissioning phases of the spectrometer-detector section. At present, the source and transport sections are currently being integrated into the beam line (December 2015) and the corresponding extensions for the system are in preparation.

4.2 Main spectrometer HV system

The energy selection of signal electrons takes place at the analyzing plane which has to be to be well-defined in space. Also, the electromagnetic fields there have to be known with highest precision. Furthermore the sources of background such as Penning traps (as discussed in section 2.1.1), require the fields to be fine-adjusted. Therefore the high-voltage provision for the main spectrometer is a complex sub-system with several hundreds of channels that are simultaneously monitored. In this section, the principal generation and distribution of voltages is described in detail. In addition, an apparatus of the size as the main-spectrometer will act as a large receiver for electromagnetic waves. These can cause disturbances of the analyzing potential and thus have to be suppressed in order to fulfill the design requirement $\sigma \leq 60\,\mathrm{mV}$. Even the most stable high voltage power supplies provide their full stability only directly at their output and are not able to smoothen ripples. Therefore the implemented post-regulation setup actively reduces such distortions, see section 4.2.2.

4.2.1 Voltage generation and distribution

The general philosophy of the HV system is to generate a large variety of potentials through a layered topology. As the large number of inner electrode segments, each composed of an inner and an outer layer, has to be elevated onto an individual potential, an equally large number of different HV feeds has to be provided. In view of the stringent design requirements due to the allowed the total systematic uncertainty budget,the use of independent devices that can supply voltages up to the needed $-35\,\mathrm{kV}$ is financially impossible and unpractical in terms of control technology. It is much more advantageous to apply a global high voltage and use additional power supplies, that are electrically footed on this potential. In this way small individual offsets can be generated for the different segments of the inner electrode, see fig. 4.5. The figure gives a schematic overview and a picture of the actual system as built in the basement of the KATRIN experimental hall and of the high voltage topology.

A high voltage supply capable of generating voltages up to $-35\,\mathrm{kV}$ thus provides the whole system with a common potential. This supply does not necessarily have to be particularly stable, as the post-regulation described in the next section, will take over the stabilization regardless of the initial ripple. To enable the electric shielding feature of the inner electrode, it has to be elevated onto a more negative potential than the vessel. Therefore the so called inner electrode common potential is generated by an offset power supply, which is electrically footed on the global potential. This device is able of an output of up to $-2\,\mathrm{kV}$. Such small potentials by comparison, allow much larger relative instabilities and consequently, are purchasable at low prices.Moreover, high voltage power supplies with such small relative instabilities are beyond technical ordinariness, are not available on small time scales and subject of R&D works.

To allow fine-adjusting the electric field, the inner electrode is segmented into seventeen rings, each with an outer and an inner wire layer. In principle all of them have to be provided with individual potentials so that another layer is needed inside the topology. A total of 46 offset power supplies form this last layer. Their polarity is always positive, as the inner electrode common potential is already sufficiently large negative voltages. Furthermore, only small potential differences between parts of the inner electrode in the order of $100\,\mathrm{V}$ are needed. Therefore these power supplies are only able to generate voltages of up to $500\,\mathrm{V}$. Aside from the key task of generating the voltages, the cabinet also iq equipped with built-in digital voltmeters. One of them is located at each dipole-half. Two multiplexers allow the sequential monitoring of all inner electrode potentials.

In this configuration it is obvious that ripples present in the different layers will add quadratically. From this, the question arises of whether the design values of KATRIN can be met. However,the applied positive offset potentials only have extremely small ripples, that are smaller than five millivolts [Ren14]. In addition the global potential is smoothened by the post-regulation setup. The strong capacitive coupling between inner electrode and vessel (see section 6.3.3)the post-regulation setup will not only able to reduce ripples of the vessel potential but of the inner electrode potential as well.

The implementation of an ideal scanning strategy for the tritium spectrum requires prior knowledge of the time scale to reach a certain stability level after setting of a new

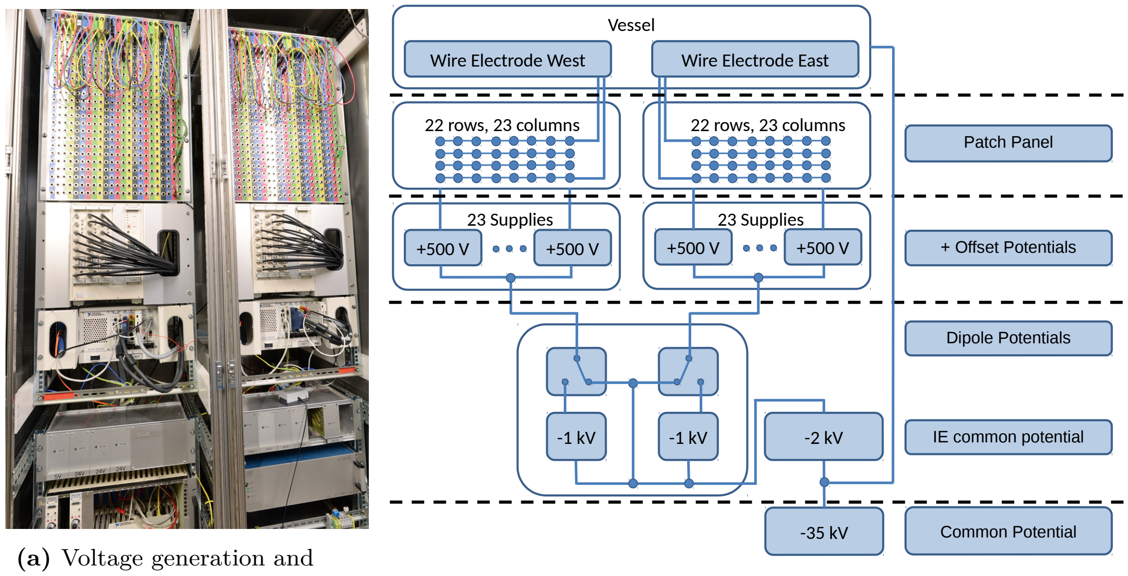

(a) Voltage generation and distribution at the main-spectrometer

(b) Schematic of the voltage generation and distribution at the main spectrometer

Figure 4.5: High voltage distribution and generation at the main-spectrometer. (a) Photography of the high voltage cabinet, being located in the basement of the KATRIN building. Kindly provided by Klaus Mehret. (b) Schematic overview of the complex HV system. A high voltage supply provides a global potential. Electrically based on this, negative offsets of up to $-2\,\mathrm{kV}$ can be generated for the whole inner electrode structure. Fine adjustments are performed through 46 offset power supplies that can provide $500\,\mathrm{V}$ each. The connection between these power supplies and the segments of the inner electrode is performed through the so-called patch panel. Consisting of a matrix with rows corresponding to different voltage supplies and columns to the rings of the electrode, arbitrary configurations are possible. This allows to apply exactly the same potential to a series of rings. Additionally the system is composed of two electrically isolated parts. As the inner electrode is made of half-rings, the west and east halves can be elevated onto different potentials, to allow a dipole mode for background investigations.

voltage. Corresponding investigations have shown that the offset power supplies are highly stable. Due to the functional principle of their controlling circuits this state os however only reached after more than $40\,\mathrm{s}$, [Ren14]. As standard scanning strategies foresee a change of the individual voltage points in the order of minutes. Such a long waiting time would significantly prolong the overall measuring time schedule. Therefore it is not feasible to perform neutrino mass measurements by means of shifting these potentials. However, the post-regulation proves to be most useful again as it provides the needed stabilities on very fast times scales of milliseconds only, see section 6.2. Further, a large total number of channels has to be monitored, but only a fraction of them is of direct interest to an operator during regular neutrino mass measurements. Of specific interest are the currents of all power supplies, as they give hint to leakage currents or discharges. The most important values of the spectrometer and detector system have been bundled into a status display that has proven to be most useful during the SDS-commissioning phases (fig. 4.7). The overview consists of the voltage values, as well as readings of temperature, magnetic fields, run status and other features. As can be seen in fig. 4.7, each segment of the inner electrode has an assigned voltage value.

In general, green numbers indicate sensor values that agree with preset reference values, while red numbers indicate that a sub-component differs from its measurement-conditions. The protocol to generate the figure can easily be adapted. A closer look at the voltage values only shows one number for each segment, despite the fact that the IE system is built with two layers. As the IE system is typically operated only with a single offset in both layers, the second value is only shown if the electrode is operated in two-layer mode. In close analogy to this, the dipole mode, the anti-Penning power supplies and inner electrode common potential only are drawn if active. Additionally, the system is capable of sending automated warning messages to operators in the case of a voltage not reacting according to the measurement schedule. All voltages generated have to be physically wired to the inner electrode segments. It can be necessary to apply exactly the same potential on two or more of the individual parts at the same time. Hence, instead of hard-wiring these connection a so-called patch panel is used. It consists of a matrix with rows corresponding to a single offset channel, while columns are associated with the layers of the half-rings. Jack plugs are then used to establish the actual connection. This allows to implement arbitrary configurations, as needed. The utilized plugs are of high quality to avoid contact voltages. After such a configuration has been chosen, the control and monitoring softwares is still unaware of the physical connection between inner electrode and power supply channels. Hence, fig. 4.6 shows a web page that gives the means to do so. Based on the patch panel physical layout, this figure rows are again the different voltage power supplies and columns the individual segments of the inner electrode. If a new patch panel configuration has been chosen, the software can easily be adapted to recent changes by entering them on a visual basis. The configurations is saved with a validity start timestamp and a name. Note that the lowermost column is not connected to an offset power supply but to the inner electrode common potential directly. The reason for this is that some measurements simply do not need positive offset voltages. In this case they are taken out of the chain, because the utilized devices are two quadrant power supplies that work reliably only above voltages of $U > 5\,\mathrm{V}$. Smaller set points would lead to floating and ill-defined outputs of the offset power supplies. Again, as this is on the expert level, a script has been implemented to automatically measure and save the current configuration ([Wac15]). The algorithm is easy to understand, all channels are set to different voltages. By measuring the potential of every inner electrode segment and comparing it to the applied voltages an unambiguous channel-map can be created. With this tool, the system is easy to understand and handle. In addition, the high-voltage libraries for operation include predefined standard potential settings. In other words, preparing the whole system for tritium, krypton, transmission or background measurements is simply a manner of adding one line of code to the controlling scripts.

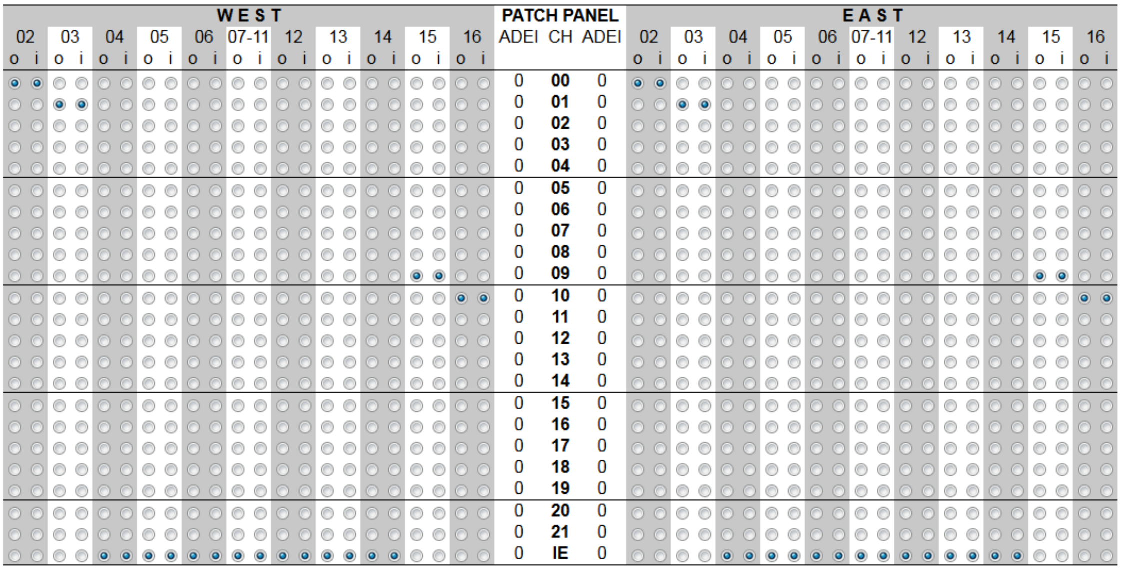

WEST																						PATCH PANEL			EAST																					
02		03		04		05		06		07-11		12		13		14		15		16		ADEI	CH	ADEI	02		03		04		05		06		07-11		12		13		14		15		16	
o	i	o	i	o	i	o	i	o	i	o	i	o	i	o	i	o	i	o	i	o	i				o	i	o	i	o	i	o	i	o	i	o	i	o	i	o	i	o	i	o	i	o	i
●	●	○	○	○	○	○	○	○	○	○	○	○	○	○	○	○	○	○	○	○	○	0	**00**	0	●	●	○	○	○	○	○	○	○	○	○	○	○	○	○	○	○	○	○	○	○	○
○	○	●	●	○	○	○	○	○	○	○	○	○	○	○	○	○	○	○	○	○	○	0	**01**	0	○	○	●	●	○	○	○	○	○	○	○	○	○	○	○	○	○	○	○	○	○	○
○	○	○	○	○	○	○	○	○	○	○	○	○	○	○	○	○	○	○	○	○	○	0	**02**	0	○	○	○	○	○	○	○	○	○	○	○	○	○	○	○	○	○	○	○	○	○	○
○	○	○	○	○	○	○	○	○	○	○	○	○	○	○	○	○	○	○	○	○	○	0	**03**	0	○	○	○	○	○	○	○	○	○	○	○	○	○	○	○	○	○	○	○	○	○	○
○	○	○	○	○	○	○	○	○	○	○	○	○	○	○	○	○	○	○	○	○	○	0	**04**	0	○	○	○	○	○	○	○	○	○	○	○	○	○	○	○	○	○	○	○	○	○	○
○	○	○	○	○	○	○	○	○	○	○	○	○	○	○	○	○	○	○	○	○	○	0	**05**	0	○	○	○	○	○	○	○	○	○	○	○	○	○	○	○	○	○	○	○	○	○	○
○	○	○	○	○	○	○	○	○	○	○	○	○	○	○	○	○	○	○	○	○	○	0	**06**	0	○	○	○	○	○	○	○	○	○	○	○	○	○	○	○	○	○	○	○	○	○	○
○	○	○	○	○	○	○	○	○	○	○	○	○	○	○	○	○	○	○	○	○	○	0	**07**	0	○	○	○	○	○	○	○	○	○	○	○	○	○	○	○	○	○	○	○	○	○	○
○	○	○	○	○	○	○	○	○	○	○	○	○	○	○	○	○	○	○	○	○	○	0	**08**	0	○	○	○	○	○	○	○	○	○	○	○	○	○	○	○	○	○	○	○	○	○	○
○	○	○	○	○	○	○	○	○	○	○	○	○	○	○	○	○	○	●	●	○	○	0	**09**	0	○	○	○	○	○	○	○	○	○	○	○	○	○	○	○	○	○	○	●	●	○	○
○	○	○	○	○	○	○	○	○	○	○	○	○	○	○	○	○	○	○	○	●	●	0	**10**	0	○	○	○	○	○	○	○	○	○	○	○	○	○	○	○	○	○	○	○	○	●	●
○	○	○	○	○	○	○	○	○	○	○	○	○	○	○	○	○	○	○	○	○	○	0	**11**	0	○	○	○	○	○	○	○	○	○	○	○	○	○	○	○	○	○	○	○	○	○	○
○	○	○	○	○	○	○	○	○	○	○	○	○	○	○	○	○	○	○	○	○	○	0	**12**	0	○	○	○	○	○	○	○	○	○	○	○	○	○	○	○	○	○	○	○	○	○	○
○	○	○	○	○	○	○	○	○	○	○	○	○	○	○	○	○	○	○	○	○	○	0	**13**	0	○	○	○	○	○	○	○	○	○	○	○	○	○	○	○	○	○	○	○	○	○	○
○	○	○	○	○	○	○	○	○	○	○	○	○	○	○	○	○	○	○	○	○	○	0	**14**	0	○	○	○	○	○	○	○	○	○	○	○	○	○	○	○	○	○	○	○	○	○	○
○	○	○	○	○	○	○	○	○	○	○	○	○	○	○	○	○	○	○	○	○	○	0	**15**	0	○	○	○	○	○	○	○	○	○	○	○	○	○	○	○	○	○	○	○	○	○	○
○	○	○	○	○	○	○	○	○	○	○	○	○	○	○	○	○	○	○	○	○	○	0	**16**	0	○	○	○	○	○	○	○	○	○	○	○	○	○	○	○	○	○	○	○	○	○	○
○	○	○	○	○	○	○	○	○	○	○	○	○	○	○	○	○	○	○	○	○	○	0	**17**	0	○	○	○	○	○	○	○	○	○	○	○	○	○	○	○	○	○	○	○	○	○	○
○	○	○	○	○	○	○	○	○	○	○	○	○	○	○	○	○	○	○	○	○	○	0	**18**	0	○	○	○	○	○	○	○	○	○	○	○	○	○	○	○	○	○	○	○	○	○	○
○	○	○	○	○	○	○	○	○	○	○	○	○	○	○	○	○	○	○	○	○	○	0	**19**	0	○	○	○	○	○	○	○	○	○	○	○	○	○	○	○	○	○	○	○	○	○	○
○	○	○	○	○	○	○	○	○	○	○	○	○	○	○	○	○	○	○	○	○	○	0	**20**	0	○	○	○	○	○	○	○	○	○	○	○	○	○	○	○	○	○	○	○	○	○	○
○	○	○	○	○	○	○	○	○	○	○	○	○	○	○	○	○	○	○	○	○	○	0	**21**	0	○	○	○	○	○	○	○	○	○	○	○	○	○	○	○	○	○	○	○	○	○	○
○	○	○	○	●	●	●	●	●	●	●	●	●	●	●	●	●	●	○	○	○	○	0	**IE**	0	○	○	○	○	●	●	●	●	●	●	●	●	●	●	●	●	●	●	○	○	○	○

Figure 4.6: Web page for updating the connection status. On the basis of the patch panel, rows represent channels of the voltage supplies and columns the segments of the inner electrode. Measurements have shown that it is necessary to bridge the offset potentials for some rings. Therefore the lowermost row is directly connected to the inner electrode common potential without further power supplies in between. Configurations are saved with their period of validity. Available online [KAT14a].

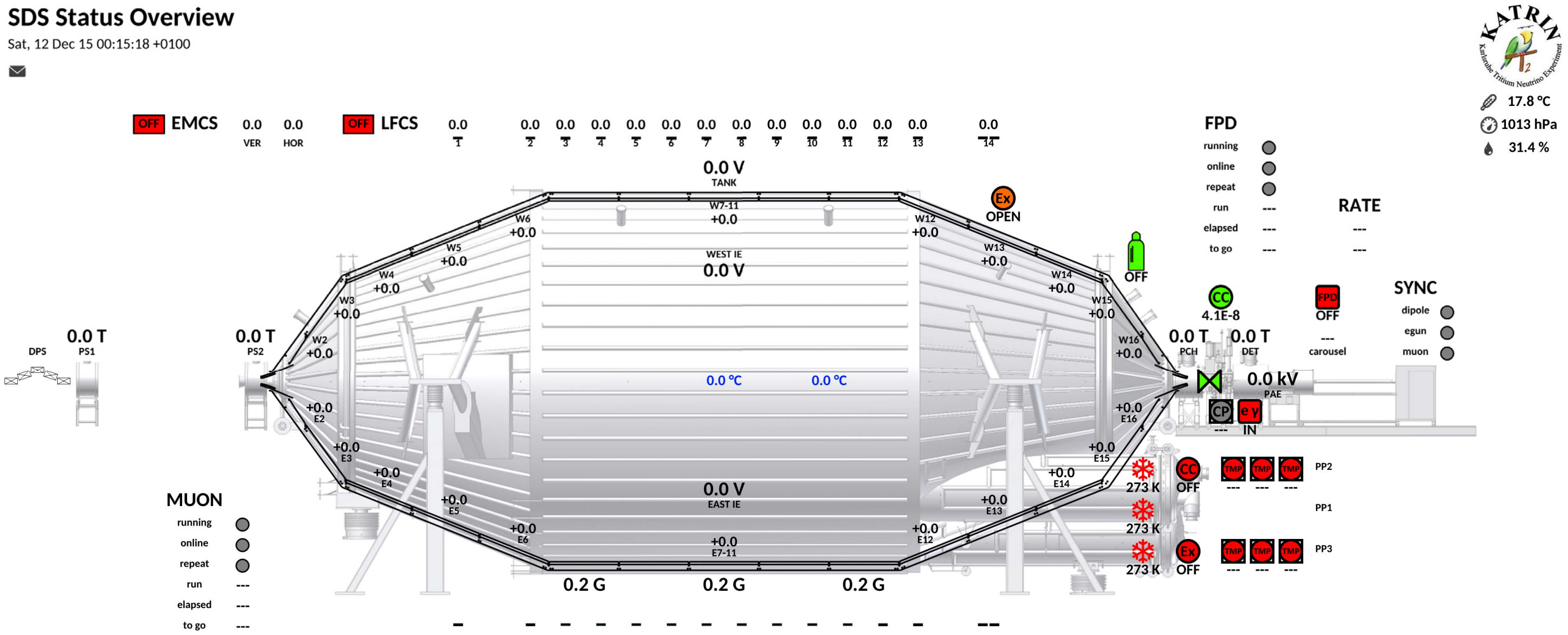

Figure 4.7: SDS-status display. The most important sensors of the main spectrometer are shown. The voltages are displayed at their corresponding electrode segments. In general, green values indicate the sensor value to be in the allowed range of parameters, whereas red values are associated with a warning. The program is adaptive and able to distinguish between several different modes of high voltage operation. Available online [KAT14b].

4.2.2 Voltage stabilization

With its large dimensions which consist mainly of conducting materials, the main spectrometer acts as antenna for propagating electromagnetic waves. These can couple into the high voltage and therefore also influence the retarding potential. Thereby such electromagnetic waves can lead to systematic effects. In addition, laboratory equipment can also cause ripples. Exemplary we mention the mains-voltage and turbo molecular pumps. The latter are necessary to achieve an UHV inside the large spectrometer volume. The electric distortions caused by them have been the subject of detailed investigations ([Chi13]). Together with all other devices that are connected to the main spectrometer these pumps lead to a ripple that gets actively countered by the so called post-regulation system, that is the central object of this section.

Before discussing this key system, two other cases which reduce voltage-fluctuations are mentioned. Because the KATRIN experiment is located close to other large users at the KIT Campus North site, the mains-voltage undergoes instabilities caused by these devices. Apart from this effect, the mains-voltage is only guaranteed to be stable up to $\pm 10\,\%$. As the KATRIN experiment is working with high voltages, that yet have to be stable in the order of $60\,\mathrm{mV}$, even the best voltage power supplies show the power frequency $f = 50\,\mathrm{Hz}$ at their output.

In a first step, the smoothing of fluctuations is performed by galvanically separating the entire high voltage system from the mains-voltage through a transformer. This component provides power for all units that are on the high potential side of the setup. This measure thereby reduces and, from a practical point completely avoids the coupling of fluctuations from the mains-voltage into the spectrometer retarding potential. This countermeasure for the most part suppresses low frequency AC-noise, while high frequencies above $f \approx 1\,\mathrm{MHz}$ are reduced by the means of smoothing capacitors. These still have to be installed.

At this stage, only fluctuations of the supply voltage and at high frequencies have been discussed. Lower frequencies have to be smoothened out by use of the post-regulation system. Figure 4.8 provides an schematic overview of the basic idea on which the sophisticated component is based on.

In principle, the working method is similar to techniques that were used to stabilize the cathode ray tube acceleration voltage in early tube televisions. In a first step the ripple has to be read out with adequate precision. As the applied voltage is $U_0 \approx 18.6\,\mathrm{kV}$ and the expected ripples are only of the order of $U_{\mathrm{ripple}} \approx 100\,\mathrm{mV}$, a two-path readout is employed. DC-voltages are measured by an auxiliary voltage divider, whereas the AC-component is decoupled through a capacitor with $C = 10\,\mathrm{nF}$. Hence, the AC-noise can be read out and measured without attenuation with good signal-to-noise ratio. Adjoint to the ripple probe is a an amplifier. During normal operation this device has a very high input impedance, resulting in an overall small cut-off frequency. Note that for electrical reasons the ripple probe has an internal resistance of $50\,\Omega$, resulting in a rather high cut-off $f_{\mathrm{cut}} \approx 32\,\mathrm{kHz}$. The amplified AC-signal is then used by the regulator to control the triode shunt in order to counter high voltage fluctuations. The connection between regulator and shunt is galvanically separated through optocouplers, so that the triode poses touchable voltages that are not allowed to propagate into the low-voltage electronics of the regulation. As a

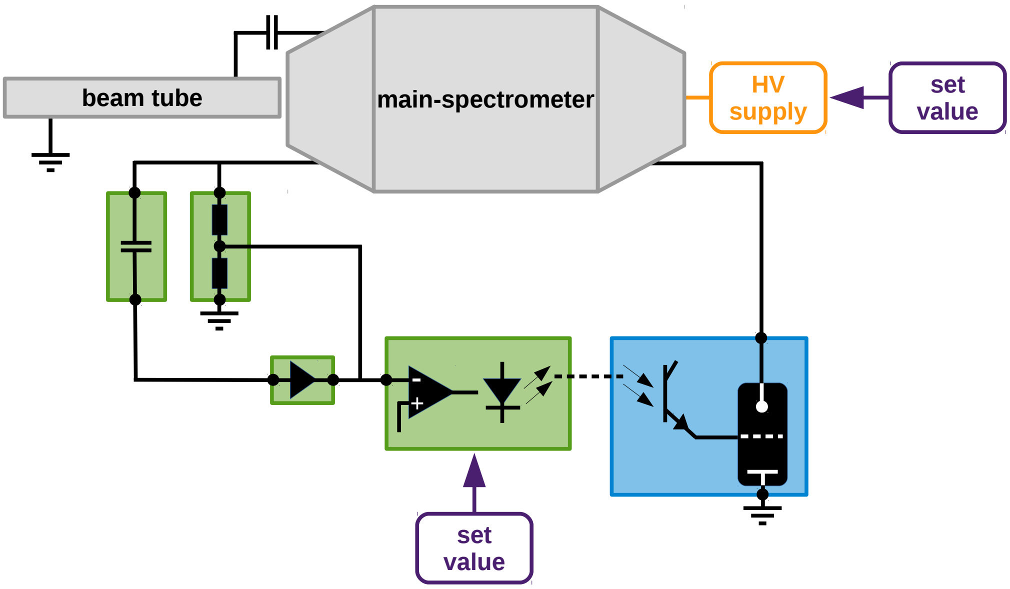

Figure 4.8: Schematic overview of the post-regulation setup. Components dedicated to read out and control are indicated in green, the triode-shunt is indicated in blue and the HV power supply in orange. A two-path voltage readout is used to gain a good signal to noise ratio for the AC-component. An auxiliary divider measures the DC-voltage, while the so called ripple probe decouples the AC-part, that is magnified afterwards with a high impedance amplifier. Fed with this information the regulator controls the triode shunt. Especially note that the series resistor of the shunt regulator leads to a voltage drop and the DC-component has to be re-stabilized. This requires the auxiliary divider, as well as the internal voltage reference to be of ultra-high precision. Furthermore this causes the initial stability of utilized high voltage supplies to be neglected. Therefore the originally applied potential only has to be medium accuracy. An additional advantage of this regulation tactic is given by its small response time. As electrical strokes $\Delta U = 20\,\mathrm{V}$ are possible, the post-regulation setup is able to accelerate the scanning during neutrino mass measurements greatly. At this point the only restricting factor is the auxiliary divider that has to be thermally stabilized to suppress drifts due to changing loads. Inspired by [Wüs16].

consequence, all electronics are placed outside the high voltage area, allowing easy access, while the auxiliary voltage divider and triode-shunt are placed inside the safety-envelope.

It is evident that the ripple has to be read out decoupled from the DC-component of the high voltage. On the other hand, the reason for the DC voltage being read out and fed into the regulation is not as obvious. The reason for doing so is given by a voltage drop across the series resistor of the shunt-regulator. In order to compensate for this effect, the post-regulation system in fact also provides DC-stability, in addition to suppressing noise. This in turn results in two extra conditions. The output of the auxiliary divider has to be compared to a reference to counteract drifts. If either of these units would be unstable, the resulting output would be as well. Consequently, the divider as well as the reference voltage have to be ultra-stable. However, the current configuration works with dividing ratios of 1 : 7000, yielding an output of roughly 3 V. Voltages of this size can easily be stabilized to fulfill the requirements. As shown in more detail insection 6.1, the measurements conducted in the scope of this thesis revealed that the auxiliary divider features systematics. The reason for this can be traced back to the fact that the setup is a temporary prototype, and that the divider is being neither housed nor-temperature stabilized. Changes of load or even regulating cycles of the air conditioning inside the experimental hall have proven to cause drifts until a new thermal equilibrium is reached.

Hence, a new auxiliary divider is currently being built in cooperation with the University of Münster following the well-proven principle of the KATRIN HV dividers. This method has been shown to be highly reliable and robust against external thermal influences as well as changing loads. Therefore, one can expect excellent results in the next SDS commissioning period which will improve the high voltage stability. It should be mentioned that the post-regulation in this way renders the stability of the high voltage source more or less obsolete. Only a medium accuracy of the order of 10^{-4} is therefore needed for those supplies. Aside from being an important experimental success, this method also this also has considerable impact on financial and availableness issues. Suitable triodes can be obtained very cost-efficiently as compared voltage power supplies with adequate characteristics. In addition, triode-shunts are available on short time scales, as they are off-the-shelf products. Equally stable supplies have long delivery times, which can easily reach several months or up to a year.

An additional advantageous feature of the post-regulation setup, is that it enables an extremely fast scanning. When changing the reference point of the regulator, the system will react and stabilize on time scales much faster than one second (section 6.2). The same technique allows to apply an arbitrary but a priori well-known distortion on the vessel. This possibility is exploited in section 6.2 to obtain detailed knowledge on the response of a MAC-E filters reaction to a rippled voltage. The present setup allows to distribute electrical strokes of up to 20 V. This value however is limited to a range of ≈ 1 V, because the triode-shunt is only able to remove negative electric charges (electrons) from the spectrometer, implying that it always has to be adjusted to a slightly more negative value than the output of the voltage power supply. This opens up a new scanning strategy: instead of shifting the potential by setting a new reference value at the supply, neighboring potentials can be accessed. To do so, setpoints can be grouped into intervals, where large steps between intervals still have to be achieved by defining a new set value of the supply voltage. Note also that the minimal step size of the post-regulation can be arbitrary small, which is a further advantage over conventional voltage supplies.

A photograph of the key components is shown in fig. 4.9. On the left side of the picture, the auxiliary divider is visible. It consists of only two isolated plates with the divider chain in between. Even in a configuration without any housing or temperature stabilization this divider was suitable for the 2014/2015 experimental investigations. However, as outlined above, the configuration will be refined for the later neutrino mass measurements. The right side of the picture shows the triode-shunt which is actively smoothening the high voltage. Both devices are located inside the high voltage envelope for two reasons. Firstly, both are not safe to touch, as they carry dangerous potentials. Secondly, when establishing a low impedance regulation between two voltage nodes, the connecting cables have to be

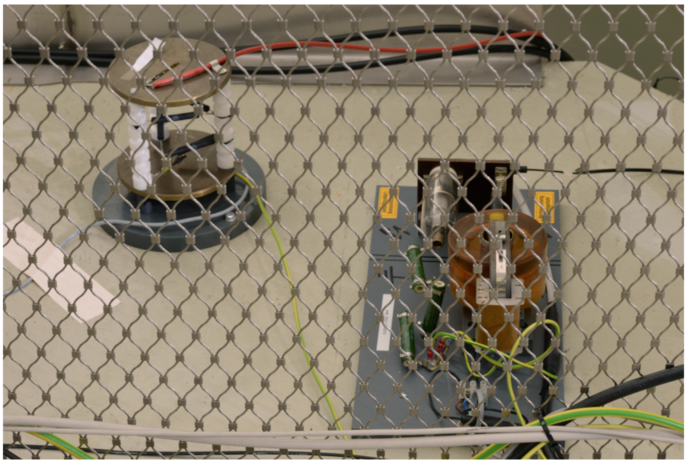

Figure 4.9: Picture of the post-regulation main parts, located at the source side of the spectrometer inside the high voltage area. On the left side of the picture the auxiliary voltage divider is seen, while the actual regulation happens with the triode-shunt on the right side. Both components are prototypes and will be upgraded for the next measurement phases, as their necessity has been proven during the second spectrometer and detector section measurement phase. Note that they are located inside the high voltage area for two reasons. For one, both are posing openly accessible high voltages and are not safe from touch. Secondly, fast regulating voltages between nodes implies their connection to be low-impedant, i.e. their connecting cables to be short.

as short as possible. Otherwise, distortions that are not present in the voltage but couple into the wiring on the way to the system could lead to a loss of efficiency. In the worst case, large impedances could even lead to a magnification of the distortion, once the phase shift between original ripple on the vessel and regulator is sufficiently large.

The analysis detailed in section 6.3 proves the system to be most useful to understand HV systematics as well as spectrometer characteristics. The component in particular allows to reduce systematics, as well as fast scanning methods (section 6.2). For further information, see [Wüs16].

4.3 Monitor-spectrometer

The high voltage system of the monitor-spectrometer is less extended than its large counterpart, but still requires a well-reasoned concept, which is described in the following. A key requirement here is that the setup has to be able to run in different scanning modes with easy ways of switching between them, while full safety for persons and equipment is guaranteed at all times.

Contrary to the main spectrometer, this MAC-E filter does not have any touchable surfaces, which would be dangerous. In this context, the only component mounted at the monitor spectrometer that would pose danger due to open voltage contacts is the auxiliary voltage divider, that is placed inside an enclosed cabinet. In this sense personal safety is already given. However, the safety system implemented has to cover the case of unforeseen accidents, like vacuum breakdowns or fire hazards. In such a case, the system can be decoupled from all voltages and immediately grounded with one central button, that triggers the whole system to automatically pass into a safe state. This button does however not affect the voltage at the main spectrometer, thus providing a safe working environment during local upgrade and rebuilding phases of the monitor spectrometer. During these phases the measurements at the main spectrometer can continue entirely unaffected. Additionally, microswitchs are mounted in all removable parts, again leading to an immediate shut-down and fall-back to a safe state in case of unauthorized disconnection. As in the case of the main spectrometer a programmable logic controller extended lock lists takes over handling of and protection from all other potential malfunctions.

An overview of the main spectrometer high voltage setup is given in fig. 4.10. A central difference between monitor and main spectrometer is the following: The integrated beta spectrum as measured by a MAC-E filter-type spectrometer depends on the surplus energy, i.e. the difference $E_\mathrm{kin} - E_\mathrm{ret} = E_\mathrm{kin} - qU_\mathrm{ret}$, implying that the retarding potential has to be shifted. Throughout this thesis the analyzing potential is directly regarded as the sole parameter defining the surplus energy. By defining $U_\mathrm{ret} = \Phi_\mathrm{filter} - \Phi_\mathrm{source}$, the difference between the potentials of the spectrometer Φ_filter and the potential of the source Φ_source, the retarding voltage can be varied by shifting either one of these potentials. As the windowless gaseous tritium source is formed by an extended plasma in the pressure range from $10^{-5} - 10^{-3}$ mbar, the application of strong voltage at this component could lead to a discharge or other systematic effects. It is therefore excluded from possible tritium-scanning methods. A further complication of varying the source potential arises from the fact that the plasma potential is defined by the rear wall [Sch16]. Subsequently the terms 'potential' and 'voltage' are used synonymously and set to $\Phi_\mathrm{source} = 0$. As the retarding potential of the monitor spectrometer is defined by the voltage applied to the main spectrometer, it is therefore necessary to shift the source voltage when a Kr-spectrum is scanned by the monitor spectrometer. Because of the relative positions of the tritium end point (18.6 keV) and the K-32 line of the krypton decay (17.8 keV), the utilized voltage supply only has to provide voltages in the order of 1 kV. Supplies providing potentials in this range with adequate precision and stability are commercially available.

In general, two distinct measurement modes are of interest. During regular tritium runs in the main beam line, the monitor spectrometer has to record the the analyzing potential of the main spectrometer. For the purpose of systematic investigations, the monitor spectrometer (MoS) system however is also able to run independently. Therefore the MoS is equipped with a full set of devices to generate and measure all needed potentials. Switching between parallel and stand-alone mode is provided by dedicated distribution units (section 4.6). For the discussion at this point these units simply can be thought of being relays. While in stand-alone mode, the filter is fed by its own high voltage supply and the potential is read out with an auxiliary voltage divider connected with a digital voltmeter. These two devices are not nearly as stable as KATRIN's high-precision dividers and voltmeters, so they are only used for redundancy. It is thus favorable to connect the MoS to the external high-precision measurement chain, even if in stand-alone mode. Furthermore, the source potential is measured by a high-precision voltmeter in all cases, which can be grounded if needed. This is especially useful when determining the additional broadening of the measured spectra caused by ripples of the additional power supply in

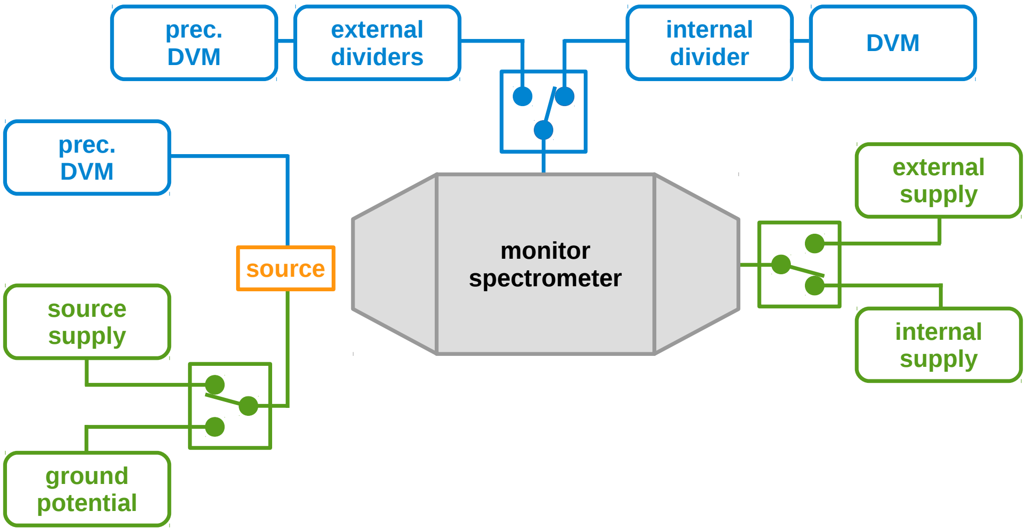

Figure 4.10: Overview of the high voltage system at the monitor-spectrometer. All devices marked in green represent voltage generating parts, the ones in blue components for measuring the potential. Central is of course the filter itself, keep in mind that the source, marked in orange, is a implanted solid source. Relays allow arbitrary combination of measuring modes. Generally all components are available externally, i.e. everything that originates at or leads to the main-spectrometer building, and internally, i.e. everything that is located inside the monitor spectrometer building. The most important modes are of course, the stand-alone operation and the parallel operation. Note that the source can be placed on voltage, to enable scanning with constant filter potential.

comparison to measurements where voltage only is applied to the filter itself.

In conclusion one can state that the MoS provides all necessary safety aspects and can alternately be operated for active monitoring of the analyzing potential at the main spectrometer (MS) and as stand-alone mode, for characterization of the Kr-sources. The latter modus is important, as the Rb/Kr-sources are depleted after a few months so that newly mounted ones have to be calibrated before continuing the long-term monitoring. By these measurements, uninterrupted tritium runs can be guaranteed.

4.4 Voltage dividers

As there is no direct way of measuring voltages in the regime of 18.6 kV with the required ultra-high accuracy and precision, two voltage dividers are used to solve this issue. The K35 divider features voltages of up to 35 kV, while the K65 divider features voltages of up to 65 kV, respectively. These units scale down the interesting potentials to about 10 V. Potentials of this magnitude can easily be measured by commercially available, state-of-the-art digital voltmeters. Because the voltage divider characteristics needed for reaching the aimed-for neutrino-mass sensitivity are beyond industrial standards, two such instruments have been specially developed for the KATRIN experiment. These combine ultra-high precision with likewise excellent stability, both units are leading in a worldwide comparison. The essential information in this section is taken from [Thü09], [Thü07], [Ros11] and [Bau13b].

The principal method of these voltage dividers does not differ from any other voltage divider. Instead it is their sophisticated construction, shown in fig. 4.11, which yields the ultra-high stabilities needed for the KATRIN experiment. The actual measurement chain is given by the gray-colored resistors that are mounted on a Polytetrafluoroethylene (PTFE) girder grid in a helix-like structure. The purpose of this arrangement is to keep the inductance at a minimum. Only preaged resistors are used to increase the stability of the divider.Each resistor has a resistance of about $1.84\,\mathrm{M}\Omega$. A total resistance of $184\,\mathrm{M}\Omega$ leads to a small measuring current of only $100\,\mu\mathrm{A}$. The low voltage chain is housed inside a Polymethylmethacrylate (PMMA) box and has a resistance of $93\,\mathrm{k}\Omega$. Both chains together yield a divider ratio of $1:1972$. Mainly serving for calibration purposes, a second scale factor of $1:95$ is additionally implemented, by using only the last resistor of the high voltage chain. In order to reduce the temperature dependency of the divider-chain, the installed resistors have been chosen in pairs with equally sized temperature dependencies but with opposite signs. Additionally the whole system is housed inside a vessel of stainless steel that is filled with temperature stabilized gaseous nitrogen. The stabilization is performed by tempered water circulation system. By using dry nitrogen with an over-pressure of about 70 mbar relative to atmospheric pressure, leakage currents due to humidity are suppressed. The surrounding vessel additionally acts as a Faraday cup and reduces radio frequency distortions that could otherwise couple into the system.

In parallel to the main measurement chain, a second, resistive-capacitive, divider chain is installed. The resistive part of this chain is used for control of the driven guard, it can be used additionally for low precision measurements. The latter is an important diagnostic tool and a fast way for consistency checks of data. As transients of the applied high voltage could harm the sensitive resistors, the capacitive part of the secondary chain is used as a protection against these.

Five copper electrode that are separated by insulators made of Polyoxymethylene (POM) form a driven guard. Corona discharges and leakages over surfaces decrease the precision of voltage dividers and therefore have to be avoided. All components are designed in a way to prevent the system from such defects. For instance, the insulators thus are designed with the maximum possible dimensions. Local field enhancements are avoided by only using parts that are geometrically shaped without edges and lead to a homogeneous field, whereas the field gradient over the spatial extension of a resistor is equal to the voltage drop over it.

Repeated calibrations of the dividers have been performed in cooperation with the University of Münster and the National Metrology Institute of Germany (PTB) ([Bau13b]). The principal idea is to use a third divider as defined reference and to calibrate the high-precision KATRIN dividers against this device. To gain a reliable calibration history and verify the stability this procedure was repeatedly conducted over years. For a detailed analysis of the results, see [Bau13a]. For the scope of this thesis the most important outcome is that the stability is as good as 0.04ppm/month, in the case of the K35 divider. The long-term stability of the K65 is currently under investigations, as a resistor recently has been replaced. Previous measurement of the long-term stability of this device however

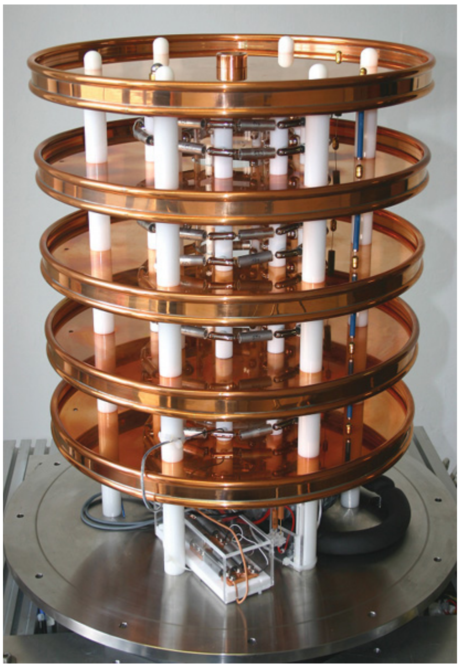

Figure 4.11: K35 high-precision KATRIN divider without vessel. The chain is separated in four different layers that are separated by POM insulators. At the end of each layer, a copper electrode is mounted, these electrodes form a driven guard. The gray resistors are arranged in a helix like structure and fixed on a PTFE girder grid. On the right side of the pictures, the resistors of the control divider are seen as connections between the copper electrodes in blue. At the bottom the low voltage resistors are housed inside a PMMA box. Adapted from [Bau13b].

are of the same order of magnitude as in case of the K35 divider. In comparison, the total budget for high voltage systematics only requires unknown instabilities to be smaller than 60 mV, showing the great success that has been achieved in constructing and characterizing these dividers. Nevertheless, calibrations at the PTB come at the price of having to transport the sensitive devices over long distances. A new method that has been developed at the University of Münster is very promising as an independent way of calibrating the dividers locally without the need of transporting them, and with even better absolute value calibrations ([Wei16]).

4.5 Low voltage calibration

The high-precision digital voltmeters for reading out the output of the dividers of course will undergo systematic uncertainties, like aging of integrated electronics. The prime reason for the divider ratio being around 1 : 2000 is that the voltages used at the KATRIN experiment then correspond to a divider output around 10 V. Voltages in this regime are measurable with ultra-high precision and, equally important, suitable calibration sources are available. Long-term investigations have shown that the calibration of the voltmeters is needed on a more frequent basis than is required in the case of the highly-stable dividers ([Kra12]).

Dedicated for this purpose is a system for automated calibrations of all voltmeters, which has been developed and installed into the framework [Wac15]. The entire calibration setup is shown in fig. 4.12 and explained in the following.

At the top of the photograph, one of the high-precision digital voltmeters is shown. It was produced by the company *Fluke*, here the model of the series 8508A is used. With a resolution of 8 1/2 digits and a measurement range up to 20 V these devices are able of reading DC voltages lower than 1 μV. Another characteristic of these instruments is their high input impedance, as reading voltages with this precision only allows small measuring currents. The four 10 V reference sources for calibrating the voltmeters are located at the second-lowest row. The manufacturer specifies the stability of these sources as being 0.3 ppm/month. By comparing different combinations of them, experience has shown this value to be much smaller in reality, so that these devices themselves only are calibrated in yearly cycles. Again conducted at the PTB, these calibrations of the references sources are exceedingly accurate, as the Josephson effect can be used for calibrating such small voltages. Calibrating the voltmeters is then performed in two steps ([Thü07]). First, the offset voltage U_0 of the voltmeter is measured by shorting its input. In the second step the gain k of the device is estimated by applying the $U_{10}^{\mathrm{ref}} = -10\,\mathrm{V}$ generated by the reference source to its input. It has been shown, that the gain factor remains the same for both signs of the potential ([Kra12]). Nevertheless, as the retarding voltage is negative, the same sign is used during calibrations. It is assumed that there is a linear relation between measured voltages and their corresponding real values

$$U_{10} = \frac{1}{k} U_{10}^{\mathrm{ref}} + U_0\,, \tag{4.1}$$

where U_{10} is the voltage as measured with the voltmeter. Note that the definition of the scaling factor entering this equation is $1/k$ rather than k. Solving for k, the gain is then given by

$$k = \frac{U_{10}^{\mathrm{ref}}}{U_{10} - U_0}. \tag{4.2}$$

Propagating the errors the variance of the gain σ_k^2 becomes

$$\sigma_k^2 = k \left[\cdot \left(\frac{\sigma_0}{U_{10} - U_0} \right)^2 + \left(\frac{\sigma_{10}}{U_{10} - U_0} \right)^2 + \left(\frac{\sigma_{10}^{\mathrm{ref}}}{U_{10}^{\mathrm{ref}}} \right)^2 \right]. \tag{4.3}$$

With the offset and the gain, the measured voltage can be corrected,

$$U = k \cdot (U_{\mathrm{meas}} - U_0), \tag{4.4}$$

yielding the true voltage U as a linear function of the measured voltage U_{meas}. Typically the offset is in the order of a few μV and the gain close to unity only deviates at the level of 10^{-6}, while the statistical uncertainty is well below 1 ppm ([Kra12]). An important

Figure 4.12: High precision measurement and calibration cabinet, described from top to bottom. High-precision digital voltmeter with 8 1/2 digits resolution. Matrix multiplexer connecting the high precision voltage dividers, voltmeters and reference sources to enable the automated calibration. Four reference sources that generate highly stable 10 V. Reference divider for calibrating the KATRIN dividers. The final arrangement contains two additional voltmeters, that can be integrated easily by plug and play.

practical point is that the calibration is only reliable during times of constant operation. If the voltmeters are turned off and on again, especially the offset factor will change so that a new calibration has to be conducted.

Strictly speaking, the obtained calibration values strongly depend on the temperature and have to be stated as a function of it. However, as the experimental hall of the KATRIN experiment is temperature and humidity stabilized, the dependency of surrounding thermal conditions are largely suppressed. To further reduce the environmental influence, the setup is installed inside a cabinet of stainless steel. A constant flow of air then guarantees a stable temperature. Even with a stabilized environment, the calibration will not be constant in time. This is due to the same processes that contribute to a change of the scaling factors of the dividers, i.e. the aging of resistors and alike. The corresponding drift has been found to be in the order of 0.3 ppm/week [Kra12]. This value may be beyond the design specifications and principally it is sufficient to calibrate the voltmeters only once before each tritium measurement cycle.

However, a calibration typically only takes 10 minutes and systematic uncertainties caused by drifting voltmeters can be suppressed to be negligible. Like the rest of the high voltage system, the routine calibrations are to be performed automatically in the background, without the need for operators with specific knowledge about the system.

For this reason, a fully automated way of calibrating the devices has been implemented. For detailed information about the system see [Wac15], the following provides a short summary of the results described there. The basic functional principle utilizes a matrix multiplexer that is able to connect the voltmeters to the references and also able to shortcut their inputs for measurements of the offset. Choosing the proper components is not an easy task, a setup that would use semiconductors for instance will increase the risk of systematics due to their dark current. Like for all other parts of the high voltage system safety standards have to be respected. Improper connections could destroy not only the stability and calibrations but also the sensitive equipment itself. To ensure the needed safety and accuracy, the implemented setup has been object of detailed investigations and the automation allows only strictly specified switching states on the hardware as well as the software side. In addition, the developed software calculates the calibration from the measured data automatically and outputs a warning if the data hint at a disorder, like drifts that are larger than to be expected.

Finally the last component that is installed inside the measurement and calibration cabinet is given by a reference voltage divider, seen at the bottom of the photograph. A self-calibration procedure allows the low-voltage calibration of the KATRIN voltage dividers to act as useful tool for checking their stability. For a detailed description of the process and its results, see [Res17].

By these means a fully automated system has been built, that provides high-precision calibrations in an easy to operate, yet reliable way. It implements the philosophy that operators only have to be aware of the existence of the calibrations, while only in the case of failure the system will return the corresponding warnings or errors.

4.6 Large scale distribution

For the final setup all the above described components have to be connected on a global scale in a way that fulfills highest safety standards, while still being easy to operate and allowing to switch between different measurement modes. A dedicated system has been developed and installed for this purpose in [Kra12]. A scheme of all parts is given in fig. 4.13. The two large boxes represent the experimental halls of both spectrometers, that are separated by about 20 meters. All main components that are discussed in the previous sections are located in the corresponding building. The components are connected to the two employed distribution units. These allow arbitrary configurations between the components, i.e. which divider is connected to the spectrometers and which voltage is used for the energy selection at the monitor-spectrometer. On the expert level, systematic investigations can be conducted by different configurations. Obviously, the most prominent mode will consist of one precision divider directly measuring the retarding voltage and the other one connected to the monitor-spectrometer. Especially during calibration cycles, both systems have to be able to run in standalone mode. Therefore, the second standard mode is defined with the K65 divider connected to the main-spectrometer and the K35 divider connected to the monitor-spectrometer, which is elevated by its own retarding potential.

The switching between different configurations could lead to transients that propagate to the sensitive dividers and break their calibrations or harm the systems themselves. To

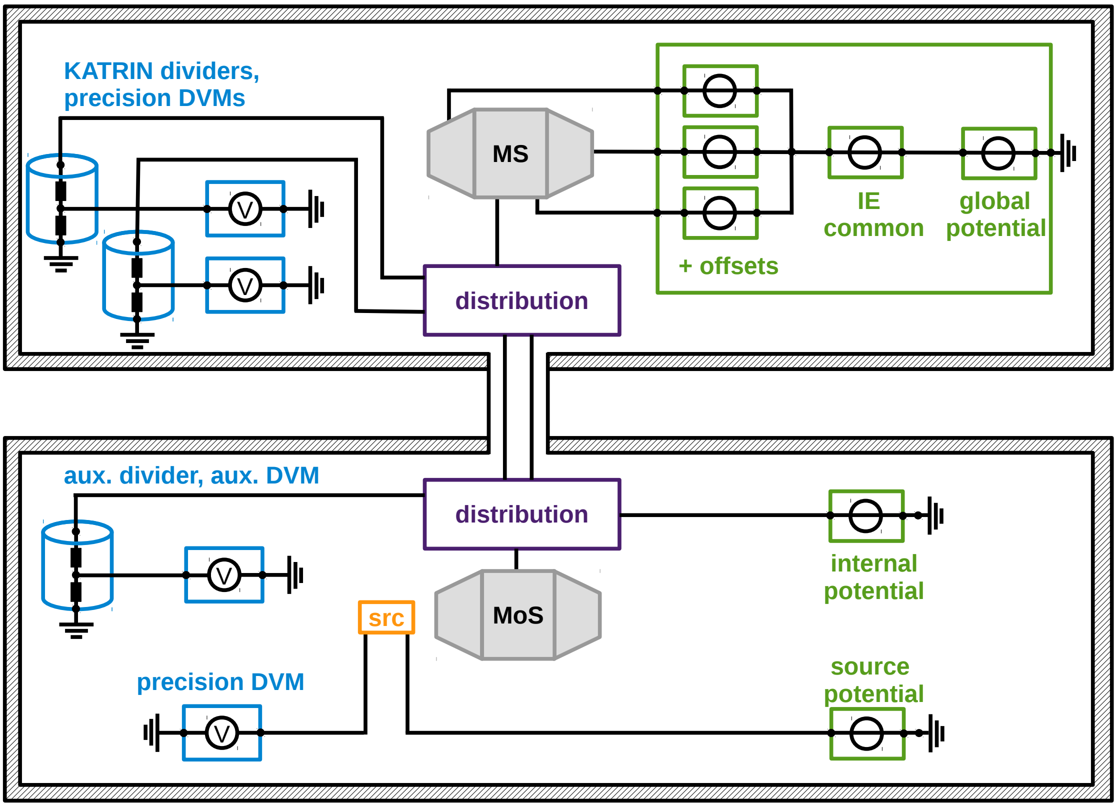

Figure 4.13: Schematic overview of the global high voltage distribution. The upper box represents the KATRIN experimental hall, the lower box the monitor-spectrometer hall respectively. Both high precision dividers (blue) are located inside the main-spectrometer building. The system to generate the needed voltages is indicated in green. The MoS is equipped with a voltage supply to generate its own retarding potential and an auxiliary divider for measuring it during stand-alone measurements. Two dedicated units allow to implement arbitrary configurations between all components. Of course, the control units limit the user to those setting, that are not harmful to the system. Such a configuration would be for instance, a connection of two different high voltage supplies to the same spectrometer.

prevent such events, the distribution units constantly monitor the voltage on all connections and allow changes only if all wires are free of potential. Additionally the status signals are indicated by green LEDs at the outside of the box. These are especially beneficial during maintenance or upgrade phases, when persons have to work on energized parts of the system and are able to instantly see if it is safe to continue. Furthermore, the connections to voltage sources are realized not via hardwired but as removable connectors. In the case of removal, the high voltage undergoes an immediate shut-down. A photograph together with a illustrative schematic drawing of the monitor-spectrometer distribution unit is given in fig. 4.14. Further information about the construction of these units can be found in [Kra12]. During the second spectrometer and detector measurement phase, the connections have ultimately proven their functionality, and freed of systematics (section 6.1.1).

The synopsis of this section is that the analyzing potential is being distributed by two dedicated units. Apart from allowing easy switching between measurement modes and enabling investigations of systematic effects, the setup supports the underlying safety concept developed for KATRIN.

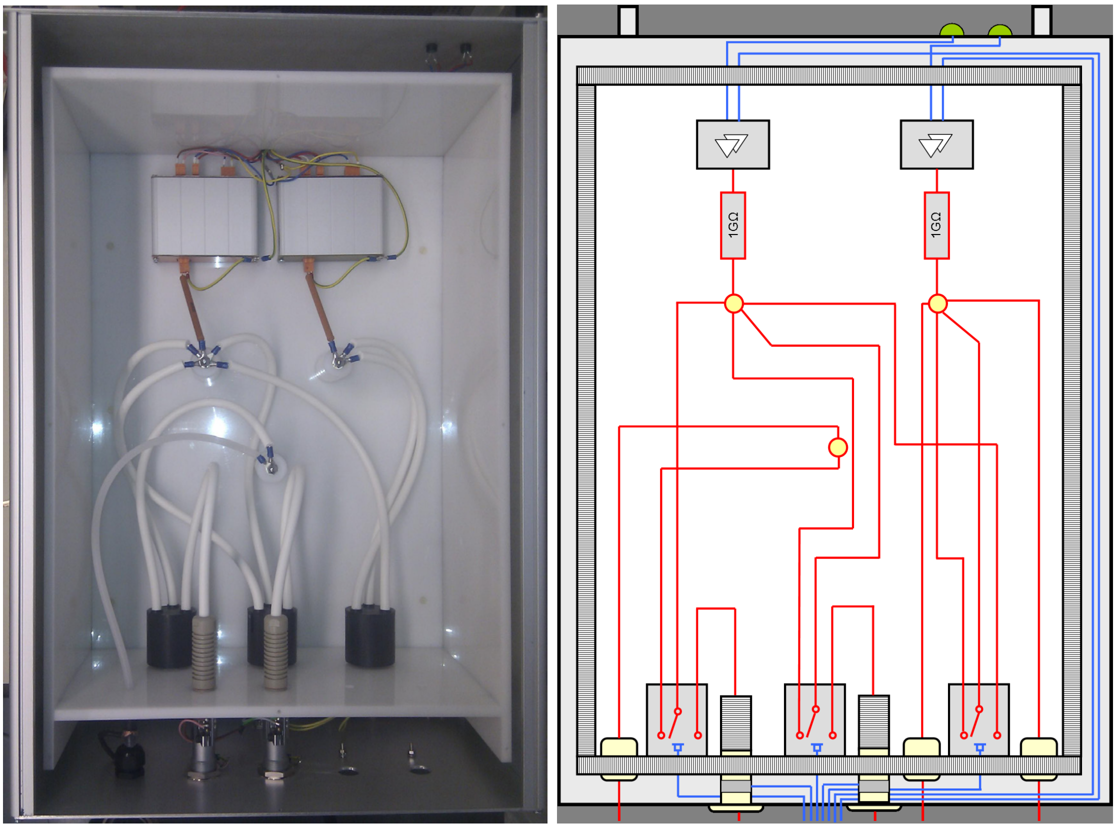

(a) Voltage generation and distribution at the main-spectrometer

(b) Schematic of the voltage generation and distribution at the main spectrometer

Figure 4.14: Photograph of the monitor-spectrometer distribution unit (a) and scheme (b) for illustrative purposes. The actual distribution is performed by three relays (black, at the bottom). Comparators (top) monitor the applied voltages, switching between configurations is only possible if all voltages are turned off. Due to safety reasons, the connections leading to the other distribution unit and the MoS voltage power supply are not hardwired, but realized with removable high voltage connectors. Both connectors are monitored by microswitches. If a connector is removed, an immediate shut-down of the voltage is initiated to that ensure no touchable voltages remain. Furthermore the voltage can only be switched on if all connectors are plugged in. Figures adapted from [Kra12].

CHAPTER 5

High voltage stability at the monitor spectrometer

Precise and accurate knowledge of the retarding potential is an essential prerequisite for all MAC-E filters, as has been shown in section 2.2.2. As detailed there, each ripple and for that manner each unknown shift, can potentially harm the neutrino mass measurement. For this reason, the KATRIN experiment utilizes not only ultra-stable high voltage dividers but also the separate monitor spectrometer. It allows the analyzing potential to be compared to a constant of nature, that is the line position of conversion electrons emitted by the decay of ^{83m}Kr. In doing so, a solid source of highly oriented pyrolytic graphite implanted with the is used, where the actual source nuclei are implanted. With a half-life of only 1.86 h, a source composed solely of krypton would decay on a much too small time scale compared to a standard measurement cycle in tritium mode (60 d). Therefore ^{83}Rb rather than krypton nuclei are implanted. As it decays with a half-life of $\tau = 86.2\,\mathrm{d}$ into krypton, so that a stable source over rather long time periods can be implemented. The sources are characterized with high precision by estimating the position of the K-32 conversion electron line, allowing to monitor the applied high voltage. It is this line that is most useful for KATRIN because of its energy of about 17.8 keV, being rather close to the tritium endpoint. The actual monitoring can be achieved by applying the voltage of interest to the filter, while scanning the spectral shape by changing the potential of the source. The equivalence of shifting source and filter potential has been shown in section 2.2.2. The long-term stability of the line position will then be the parameter to investigate the high voltage stability. Additionally, the monitor spectrometer is sensitive to fluctuations of the voltage as these will change its transmission probabilities and therefore the measured spectrum.

Working in the regime of stabilities at the parts-per-million (ppm) level, it is of utter importance to have suitable models to describe the K-32 line shape and its potential deviations with great accuracy, which could be caused by energy scale systematics. Therefore the first section of this chapter (section 5.1) will give an introduction to this within the framework of the common model used for estimation of the line position. Subsequently the model gets expanded by incorporating the influence of distortions. Once the necessary theoretical tools are at hand, the data analysis is first discussed with respect to the DC-stability (section 5.2), before focusing on the AC-component (section 5.3).

5.1 Physical Model

Ideally, an experimental electron spectrum measured with a MAC-E filter takes the universal form

$$\frac{\mathrm{d}N}{\mathrm{d}t} = \beta(E) \otimes \mathrm{T}(E - qU_{\mathrm{ret}}), \tag{5.1}$$

as described in section 2.2.2. However, as has already been outlined, the transmission function $\mathrm{T}(E - qU_{\mathrm{ret}})$ has to be modified according to the unique characteristics that the spectrometer may have. In particular, a specific source will introduce distinct features, that have to be taken into account by adapting a proper version of the electron spectrum $\beta(E)$. In recent years both the transmission function of the monitor spectrometer as well as the properties of implanted krypton sources have been investigated in great detail. In the following we adapt the discussion and strategy outlined in [Sle13], where a full deviation of the model is performed. Further information about the sources can be found in [Zbo11] and [Sle11], while a complete description of the system can be found in [Erh14] and [Sle16]. A variety of models and analyzing methods is investigated in these works. As this work concentrates on the total monitoring stability of the high voltage through the monitor spectrometer, only the relevant parts will be extracted. Previously,electron spectra were modeled without voltage imperfection, this will be extended to accommodate for the resulting systematics uncertainties in a last step.

5.1.1 Common line shape

In agreement with the nomenclature of [Sle13], the spectra of relevance here depend on a series of fitting parameters that can be summarized by a parameter vector $\mathbf{p}$. Before taking care of the actual parameters, the spectrum then takes the form

$$\frac{\mathrm{d}N}{\mathrm{d}t} = \beta\left(E;\mathbf{p}\right) \otimes \mathrm{T}(E - qU_{\mathrm{ret}}) + \mathrm{N}_0, \tag{5.2}$$

where N_0 is an additional parameter, representing the background rate. For the important K-32 line of ^{83m}Kr decays, this background parameter can be fitted to be simply a constant. The transmission function, as introduced in eq. (2.9) for an isotropically emitting source depends on the magnetic field at the point of emission and the corresponding field strength in the analyzing plane. Because of the finite size of the source and inhomogeneities of the electric and magnetic fields, this equation has to be corrected for electrons traveling along different field lines. To solve this is, one can construct a transmission function as weighted average

$$\mathrm{T}(E - qU_{\mathrm{ret}}) = \frac{\sum_i \mathrm{r}_i \mathrm{T}_i(E - qU_{\mathrm{ret}})}{\sum_i \mathrm{r}_i}. \tag{5.3}$$

Here the weights r_i, entering the discrete sum denote the radii at which the radial dependent transmission functions T_i and the corresponding electromagnetic fields have to be calculated. Naturally, the result will be more precise when the number of steps is increased. In order to keep computation times at a reasonable level, it is sufficient to carry out the sum with twenty or less summands. The net effect is a broadening and smearing out of the transmission function very similar to Gaussian distortions.

The previous modification was straightforward to obtain, whereas expanding the spectrum correctly needs more effort. It is possible to separate the extended version of the line shape into three parts,

$$\beta = \beta_{\text{elastic}} + \beta_{\text{loss}} + \beta_{\text{shake}}. \tag{5.4}$$

By doing so the complicated spectrum gets decomposed to more accessible individual parts, that are be described in the following.

Elastic part

The elastic part of the line shape has been derived to be of the form

$$D(E; a, E_0, \gamma, \alpha) = \frac{a}{\pi \left[\gamma^2/4 + (E - E_0)\right]^{\frac{1-\alpha}{2}}} \cos\left[(1-\alpha)\arctan(2\frac{E - E_0}{\gamma}) + \alpha\frac{\pi}{2}\right] \tag{5.5}$$

which is widely used in describing solid sources ([Don70]). Here the line position is denoted by the parameter E_0, the full width at half maximum of the spectrum by γ. Furthermore the function is not symmetrical which is represented by the shaping parameter α. In the case of $\alpha = 0$, the function degenerates to be Lorentzian, which is normalized to the amplitude a

$$\int_{-\infty}^{\infty} D(E; a, E_0, \gamma, \alpha) \mathrm{d}E = a. \tag{5.6}$$

For $\alpha \neq 0$, the above integral will diverge, which is a drawback introduced at the cost of the shaping parameter. As a consequence the integration boundaries have to be adjusted in agreement with the limits of the measured electron spectrum. Contrary to a naive expectation, the line position is not the mode of the distribution but rather the expectation value. Although the influence of voltage distortions is treated only in the next section, a Gaussian distributed statistical is implemented at this point with the PDF $f(\tilde{E}; \sigma)$. Such fluctuations can originate from the Doppler-effect or systematics of the implanted sources. Equivalent to the arguments in section 2.2.2, the elastic part of the line-shape then ultimately becomes

$$\beta_{elastic} = \int D(E + \tilde{E}; a, E_0, \gamma, \alpha) f(\tilde{E}; \sigma) \mathrm{d}\tilde{E}, \tag{5.7}$$

where the boundaries can be restricted if prior knowledge on the statistical variance is already preset. Otherwise it can be chosen to be arbitrarily large within the limits of available computation time.

Energy-loss part

Experience has shown that the probability for electrons to scatter within the source material is non-negligible resulting in corresponding non-zero energy-losses. In addition, the scattered electrons will obtain a different angular distribution than electrons that leave the source without scattering. This leads to an additional decrease in rate. Knowledge of the implantation energy allows to estimate the distribution in space throughout the source of the deposited rubidium atoms. Subsequently the differential cross section for emitted electrons to scatter off electrons in the substrate allows calculating the resulting energy loss of those electrons by means of Monte-Carlo simulations. As the K-32 line already has been modeled, the energy-loss part becomes

$$\beta_{loss} = \int \beta_{elastic}(E + \tilde{E}; a, E_0, \gamma, \alpha) M(\tilde{E}) \mathrm{d}\tilde{E}, \tag{5.8}$$

with the effective Gaussian energy distortion $M(\tilde{E})$, obtained by MC simulations. This effect becomes dominant only well below the line position. However, the effect will make precision fitting impossible if not taken into account.

Shake part

Electrons that are excited to a higher state or emitted entirely from the atom by the primary electron cause due to a scattering event lose energy. Consequently, the line position will be recorded below the purely elastic spectrum. It has empirically been found that this is best described by a Voigtian, being the convolution of a Gaussian and a Lorentzian distribution. Naturally, these electrons also can scatter inelastically. However, because of the smallness of the effect this gets neglected at this point. Taking into account all possible shake-off and shake-up processes, the last term of the spectrum then becomes

$$\beta_{\text{shake}} = \sum_i V(E; a_i, E_{0,i}, \sigma, \gamma_i). \tag{5.9}$$

Note that all profiles have been modeled to have distinct Lorentzian-widths γ_i, amplitudes a_i and line positions $E_{0,i}$ but share their common Gaussian-width σ with the elastic part of the spectrum.

Complete line-shape

Composing all above terms, the complete line-shape is

$$\beta = \mathrm{T} \otimes \left[\int D \cdot f \mathrm{d}\,\tilde{E} + \int \beta_{elastic} \cdot M \mathrm{d}\,\tilde{E} + \sum_i V_i \right], \tag{5.10}$$

where all parameters and variables have been suppressed. For purposes of reasonable computation times, it is advantageous to make use of the equivalence between distortions entering either the source or the transmission function

$$\mathrm{T} \otimes \int \beta_{\text{elastic}} \cdot M \mathrm{d}\,\tilde{E} = \int \mathrm{T} \cdot M \mathrm{d}\,\tilde{E} \otimes \beta_{\text{elastic}}. \tag{5.11}$$

In doing so the terms independent of fitting parameters get separated from the rest of the spectrum and have to be calculated only once. This procedure reduces the required computation time significantly. To highlight the quality of the model, fig. 5.1 presents a K-32 line measurement performed with the K35-divider and the corresponding fitted function. The results of the fit are the position $E_0 = 17828.15\,\mathrm{eV}$, the Gaussian standard deviation $\sigma = 0.26\,\mathrm{eV}$, the constant background rate $\mathrm{N}_0 = 73.02\,\mathrm{cps}$, the shaping parameter $\alpha = 117.02$ and the amplitude $a = 467.50\,\mathrm{cps}$, whereas the Lorentzian width $\gamma = 2.7\,\mathrm{eV}$ remains constant during the fit. Furthermore, the resulting chi-square value is $\chi^2/NDF = 41.4/37 = 1.1$ and shows good agreement between the actual physical line-shape and the constructed model. It has to be mentioned that the systematic uncertainties here are calculated by Poisson statistics. Because the setup of a MAC-E filter for a given source can be regarded as composition of Binomial and Poisson experiments, this approach in general will not hold. In the case of zero counts in one bin it yields the unphysical result of the uncertainty vanishing. A more realistic model is derived in section 6.3.1. This statistical model does not only provide a correct treatment of errors but also differs greatly from Poisson statistics for samples of small statistical population, resulting in a useful tool to describe a broad class of experiments. However, it also will be shown that the statistic model is close to the Poisson case for sufficiently large numbers. Due to the presence of conversion lines at higher energies, the background present in measurements of the K-32 line can be regarded to provide large enough numbers for the measured rates to follow a Poisson-statistic.

5.1.2 Influence of distortions

In order to understand the influence of ripples in the high voltage the transmission function has to be modified. As it has been mentioned above, ripples of the source side are also described by this feature. As arbitrary waveforms can be decomposed into sine and cosine functions by Fourier analysis, only those will be introduced here. As outlined in section 2.2.2, the analytical solution of this problem is only possible in case of an ideal transmission function. Taking the modified version from above, a solution can only be obtained numerically. Then, the formal definition of the distorted function $\mathrm{T}_{\mathrm{dist}}$ is

$$\begin{aligned}\mathrm{T}_{\mathrm{dist}} &= \frac{1}{2\pi}\int_{-\pi}^{\pi} \mathrm{T}(E - qU_{ret} + \sin(\varepsilon))\ \mathrm{d}\xi \\ &= \frac{\sum_i r_i \int_{-\pi}^{\pi} \mathrm{T}_i(E - qU_{ret} + \xi)\ \mathrm{d}\xi}{2\pi \sum_i r_i}.\end{aligned} \tag{5.12}$$

Summation and integration are interchangeable and the effective transmission function can be regarded as weighted average of distorted transmission functions. This also holds in a general case and therefore can be used for corresponding calculations at the main spectrometer.

The influence of such a distorted transmission function to the conversion line is illustrated in fig. 5.2. Beginning with the undistorted spectrum, the amplitude of the involved sine-wave is increased incrementally in one-volt steps from $0 - 10\,\mathrm{V}$. It is not to be expected that the ripples will be of this magnitude, however it is useful for illustrative purposes at

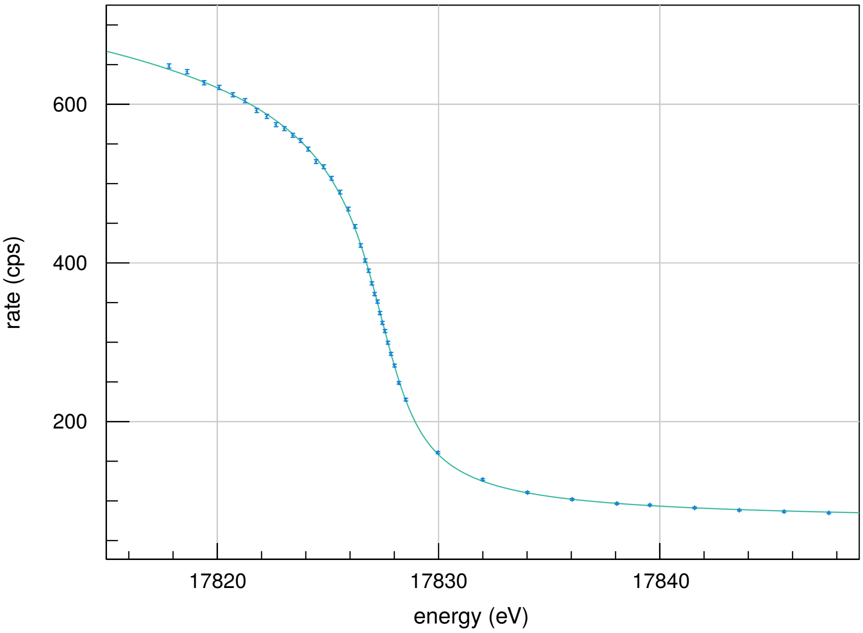

Figure 5.1: Measurement of the K-32 conversion line, recorded in the data-taking period in 2014. The data in blue are very well described by a fit with the above model, where $\chi^2/NDF = 41.4/37 = 1.1$, $E_0 = 17828.15\,\mathrm{eV}$, $\sigma = 0.26\,\mathrm{eV}$, $\mathrm{N}_0 = 73.02\,\mathrm{cps}$, $\alpha = 117.02$ and $a = 467.50\,\mathrm{cps}$. Underlined by the chi-square value the model is in very good agreement with the data. Simple Poisson-statistics have been used in order to calculate the error bars.

this point. As the transmission function gets broadened, consequently this also is true in case of the measured spectrum. Interestingly, a ripple present in the analyzing potential leads to a suppression of all other characteristic features of the line. Especially, the elastic region almost is degenerate with linear function, while distorted and undistorted spectra converge again in the background and energy-loss regions. Additionally, all lines meet at one point given by the line position. Therefore the DC-monitoring principle, apart from bad χ^2 values, is unaffected by ripples so that an interesting opportunity arises. By fitting the line-shape with implemented sinusoidal distortions, the monitor spectrometer is not only able to measure the DC-stability of the main retarding potential but also the AC-stability of the latter.

An additional source of imperfections of the voltage is Gaussian-noise, as this contribution is always present. With the established common model, as in use for analysis of monitor spectrometer data, the terms necessary to describe such a noise are already included. Gaussian-distributed imperfections are coupled in the source side of the above model, to take into account the Doppler-effects and similar influences. It is equivalent to implement fluctuations either on the side of the energy scale (i.e. the retarding potential) or the side of the energy distribution. This single term also allows to calculate the effect of Gaussian-distributed voltage fluctuations, see section 5.1.2. As above a total, of eleven spectra is shown, with the blue one again representing a line that has the Gaussian standard

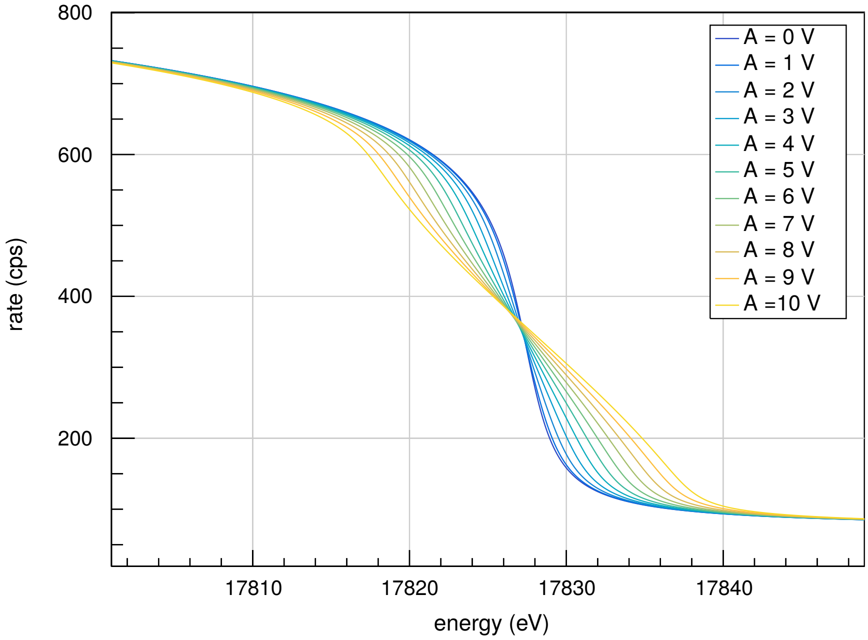

Figure 5.2: Influence of high voltage fluctuations on the K-32 conversion line. A total of eleven different functions are shown, with the undistorted spectrum displayed in blue. All other lines are obtained by incrementally increasing the sine-amplitude in one-volt steps. The resulting line-shapes are independent of the ripple frequency.

deviation $\sigma = 0.25\,\text{eV}$. Measurements have shown this value to be adequate during data taking with the monitor spectrometer and in case of negligible additional broadening due to voltage distortions. As the sum of two Gaussian-distributed variates again follows Gaussian statistics with $\sigma^2 = \sigma_1^2 + \sigma_2^2$, the effect of additional fluctuations can easily be described by a larger standard deviation. All other spectra are therefore gained by incrementally increasing the standard deviation in steps of one volt in size. Again the total variance increases according to the expectations from calculations concerning the transmission function. Also, the line-position remains trivial at the same point, while the other characteristics get smoothed out. This effect is even stronger than in the sine-wave case, where on the one hand the sharp edges of the arcsine distribution also cause the line shape to have sharper edges and on the other hand a more complex sub-structure remains visible. Comparison of both ripple-types suggest the normal-distribution to have a larger influence. Note that this in fact is not true, because of $\sigma = {}^{A}\!/\!\sqrt{2}$ for sinusoidal distortions. Like before, the most important outcome is that the line position is fixed and therefore the DC-monitoring remains unaffected, whereas the line shape gives the opportunity to estimate AC-imperfections.

The monitoring principle can thus be expanded to also measure ripples and not only the long-term stability of the main retarding voltage. As the hardware-based connection between the two spectrometers is done via the distributions units and rather long cables, this system possibly contributes ohmic resistance, capacitance and inductance. For this

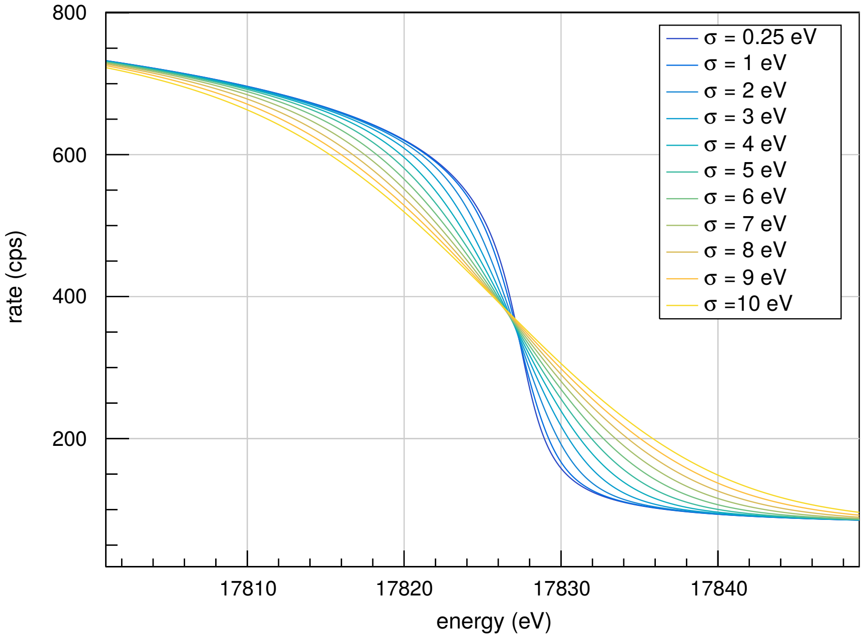

Figure 5.3: Impact of Gaussian-distortions on the K-32 conversion line. Like in the case of sinusoidal ripples, the blue spectrum indicates the distortion free line-shape. Note that distortion free at this points refers to $\sigma = 0.25\,\mathrm{eV}$, a value known to be intrinsic to monitor spectrometer measurements. All other lines are constructed by incrementally increasing the voltage from one to ten Volts.

reason the involved systematics have to be studied carefully. In terms of long-term stability, offsets, thermal voltages and alike can be an origin of failures. Therefore, these effects are investigated in section 6.1.1. Ad hoc AC-noise can not be expected to have exactly the same size at both spectrometers. The influence that a known ripple at the main spectrometer has on the line-shape measured by the monitor spectrometers is investigated in section 5.3. These investigations ensure a meaningful way to estimate the ripple of the main retarding voltage by means of the monitor spectrometer with the highest possible sensitivity.

5.2 DC Component

A leading purpose of the monitor spectrometer is to detect instabilities in the DC-component of the main-retarding voltage. To do so, the K-32 conversion line from the radioactive decay of ^{83m}Kr is measured. Here, the most interesting parameter is the position of the spectrum, i.e. its the expectation value. The retarding potential can thus be compared to a constant of nature, as the line position is fixed due to energy conservation during the decay. However, the utilized implanted sources yield systematics that result in an effective drift of the estimate. With more and more krypton and rubidium atoms decaying, the solid state potential changes as a function of time. Depending on the implantation energy used during the production of the sources, this also will turn into a function in space and cannot be regarded as being globally constant. To find an empirical model is a non-trivial task. The complicated interconnection of different processes that lead to a shift of the line position is a topic of on-going investigations, see [Sle16]. In a first step the time dependency of the sources gets investigated in section 5.2.1. After a functional description of this drift is found, the sensitivity for finding and evaluating drifts and offsets present in the retarding voltage is analyzed in section 5.2.2.

5.2.1 Longterm Stability

Beginning on September 10th, 2014, the line position stability of krypton sources with HOPG as a substrate has been investigated over a measurement period consisting of 50 days of data. To investigate systematic effects, both high-precision KATRIN-dividers have been used during these measurements. As this thesis aims at systematic uncertainties solely connected to the retarding voltage and the analyzing potential, only the K-32 line is considered during all following calculations. As will become evident during the analysis, this line suffices for monitoring purposes. All other lines can be used to characterize the sources in more detail. All measurements have been performed in standalone-mode, as described in section 4.6, with the source potential being set to zero, to neglect possible systematic uncertainties that are evaluated in section 6.1.2. Additionally, the distribution of measurement points has been chosen with respect to optimize the measurement time. This is advantageous, as the sources had already lost large parts of their activity, due to aging. Essentially, this implies that the density of points is proportional to the gradient of the spectrum. This will also be used for measurements with sources of high activity. When fitting all measured spectra with the above model, one obtains the stability of the line-position as shown in fig. 5.4. The left and right sides of this illustration correspond

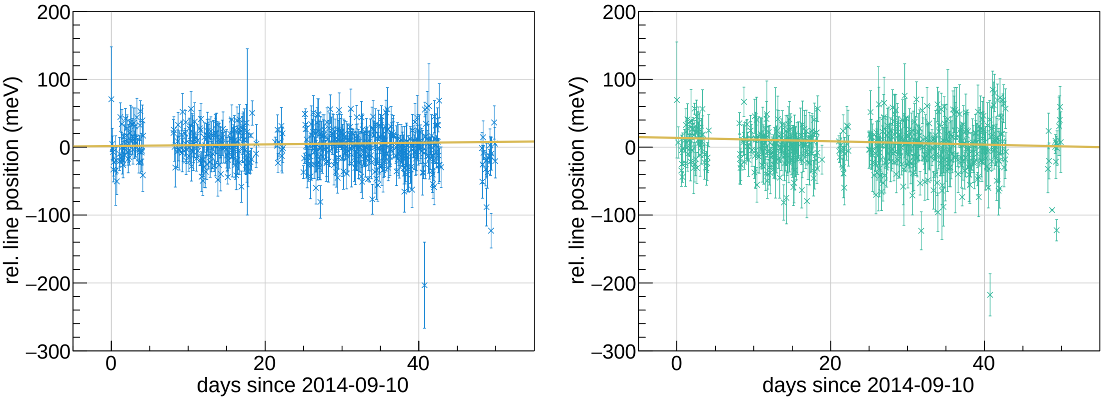

(a) K35 divider **(b)** K65 divider

Figure 5.4: Long-term stability measurements of the K-32 conversion line with both KATRIN high-precision voltage dividers. Beginning on the tenth of September 2015, a 50 day long measurement period was conducted. Each point corresponds to the line-position of one measured spectrum. In both figures, the yellow line represents a linear fit. (a) K35 divider with a drift of $(7.3 \pm 1.9)\,\mathrm{meV/cycle}$. (b) K65 divider with a drift of $(-14.9 \pm 2.3)\,\mathrm{meV/cycle}$. Note that these drifts are the net effect of divider systematics, source properties and external influences.

to measurements with the K35 and the K65 divider, respectively relative shifts in the line-position are of greater importance than the absolute value. Therefore not the actual line-positions but their difference to the global mean-value are shown. Visually, both figures seem to agree with no large-scale drifts. Empirically, the net effect has been proven to be well described by a linear function, as it is pictured in yellow. More quantitatively, the result is

$$\mathit{\Delta} E_0 = \begin{cases} (0.12 \pm 0.03)\,\mathrm{meV/day} & ,\text{for K35,} \\ (-0.25 \pm 0.04)\,\mathrm{meV/day} & ,\text{for K65,,} \end{cases} \tag{5.13}$$

or in a tritium measuring cycle of 60 days,

$$\mathit{\Delta} E_0 = \begin{cases} (7.3 \pm 1.9)\,\mathrm{meV/cycle} & ,\text{K35} \\ (-14.9 \pm 2.3)\,\mathrm{meV/cycle} & ,\text{K65.} \end{cases} \tag{5.14}$$

Compared to the maximum systematic HV error budget of 60 meV, that the high voltage system has to fulfill over one tritium measurement period, these numbers represent a significant breakthrough. Consequently, the monitor spectrometer, in principle, has already demonstrated its functionality. Even more, the setup exceeds the given design parameters by more than a factor of three. In an actual measurement cycle, the monitoring principle then will be used to estimate the line-position constantly. However, as this depends on the reproducibility in manufacturing the sources, the drift behavior can be expected to be small, but not identical for each source, so further analysis is necessary. A shift of the line-position can be thought of as being caused by a combination of a part that is due to source properties and one due to systematics of the utilized divider

$$\mathit{\Delta} E_0 = \mathit{\Delta} E_{\mathrm{source}} + \mathit{\Delta} E_{\mathrm{divider}}. \tag{5.15}$$

The shift caused by the source in both dividers remains the same, so that

$$\begin{aligned} \mathit{\Delta} E_{0,K35} &= \mathit{\Delta} E_{source} + \mathit{\Delta} E_{K35} \\ \mathit{\Delta} E_{0,K65} &= \mathit{\Delta} E_{source} + \mathit{\Delta} E_{K65}. \end{aligned} \tag{5.16}$$

Combining these equations by taking their difference,

$$\mathit{\Delta} E_{K35} - \mathit{\Delta} E_{K65} = \mathit{\Delta} E_{0,K35} - \mathit{\Delta} E_{0,K65}, \tag{5.17}$$

an important relation between shifts of the line-position and the shift caused by the dividers can be gained. Further, the shifts due to the dividers hold up to the equations,

$$\begin{aligned} \mathit{\Delta} E_{K35} &= \varepsilon \cdot \mathit{\Delta} M_{K35} \\ \mathit{\Delta} E_{K65} &= \varepsilon \cdot \mathit{\Delta} M_{K65}, \end{aligned} \tag{5.18}$$

where ε is an energy constant, representing the actual kinematic line position of the decay, and the scaling factors M_{K35}, M_{K65} of the two voltage-dividers. Ultimately this yields

$$\varDelta M_{K35} - \varDelta M_{K65} = \frac{\varDelta E_{0,K35} - \varDelta E_{0,K65}}{\varepsilon}. \tag{5.19}$$

By means of measuring the krypton spectrum this identity connects the drifts of the measured spectra with those of the scaling factors. Commonly the dividers are calibrated at the PTB, where a third device is used as a reference. The above relation allows the relative drift between the instruments to be calculated and thereby to validate the consistency of calibrations gained through electrical means. Even more important, this allows the calibration of both dividers against each other, if the drift of at least one is already known. Additionally, the drift of the source can be estimated with knowledge of the divider systematics, as shown in eq. (5.16). Together with a new calibration method [Wei16], that is being developed at the University of Münster, and the monitor spectrometer the calibration chain can be closed and regarded to be highly reliable, due to redundant techniques. Currently only the drift of the K65 divider is known precisely, as one of the resistors in the divider chain of the K35 had to be replaced, so that sufficient stability data of this divider is lacking at this point. The recent developments in calibrating the dividers will be described in [Res17]. However, as the drift of K65 is known, this can be used to estimate the behavior of K35

$$\begin{aligned} \varDelta M_{K35} &= \varDelta M_{K65} + \frac{\varDelta E_{0,K35} - \varDelta E_{0,K65}}{\varepsilon} \\ &= (-0.506 \pm 0.002)\,\mathrm{ppm/cycle}, \end{aligned} \tag{5.20}$$

where $\varepsilon = 17824.3\,\mathrm{eV}$ ([Zbo11]). Note that this value will differ in the range of a few electron-volts from the real value, due to source effects like the work-function, that lead to an offset. The relative uncertainties induced by this however will be small and therefore will play no role in this calculation. The interpretation of this result is in agreement with the expectations. Both dividers are built with carefully selected and pre-aged resistors. All calibration measurements that have been performed in the past show drifts well below 1 ppm/cycle. It has been observed for the drifts to slowly converge against a limit, because the mounted resistors remain in an aging state due to diffusion processes until equilibrium is reached.

To understand the coupling between source and divider systematics, the calibration of the high-voltage dividers has to be measured in the future with the recently developed technique. This allows to establish a reliable calibration history. Moreover, the ultra-stable HOPG-sources have to be further characterized. Nevertheless, the system already has shown to exceed the KATRIN design specifications in terms of monitoring the DC-stability on long time scales. In addition, these techniques allow the closure of calibration methods by not only calibrating the dividers by electrical means but also by the comparison against a constant of nature. As shown above, especially the source systematic uncertainties can be neglected entirely during this procedure, yielding a powerful tool for consistency checks.

5.2.2 Single measurement sensitivity

In terms of monitoring the main retarding voltage, the last section provides only the mean values necessary to decide whether the potential has been stable over a measurement cycle on average. As the common tritium data-taking invokes the retarding potential to be shifted on much smaller timescales of only minutes, the monitoring also has to happen on this timescale and single estimates of the line position have to provide criteria for accepting or rejecting a point of the tritium spectrum during run-time. Naturally, the determination of the line-position will undergo statistical fluctuations and therefore will yield a finite resolution. The time spectra given in the previous section are not suitable to calculate the size of this resolution, as they still incorporate the systematic drift in energy. In order to resolve this situation, fig. 5.5 shows two histograms that result from considering the difference of each energy-estimate from the value predicted by the linear fit. Agreeing with expectations, the resulting histograms are described by a Gaussian (yellow) distribution and the remaining variance of the line-position arises purely from statistics. The standard deviations are respectively

$$\sigma = \begin{cases} 27.7\,\text{meV} & ,\text{K35} \\ 32.7\,\text{meV} & ,\text{K65}. \end{cases} \tag{5.21}$$

A rule to reject a measurement remains to be defined, which is correlated with the sensitivity of the monitoring principle for single points. Here, the confidence level is chosen to be at 90 %, i.e. $\approx 1.65\sigma$. The sensitivity for monitoring deviations of single voltage points Σ then becomes

$$\Sigma = \begin{cases} 45.7\,\text{meV} & ,\text{K35} \\ 54.0\,\text{meV} & ,\text{K65}. \end{cases} \tag{5.22}$$

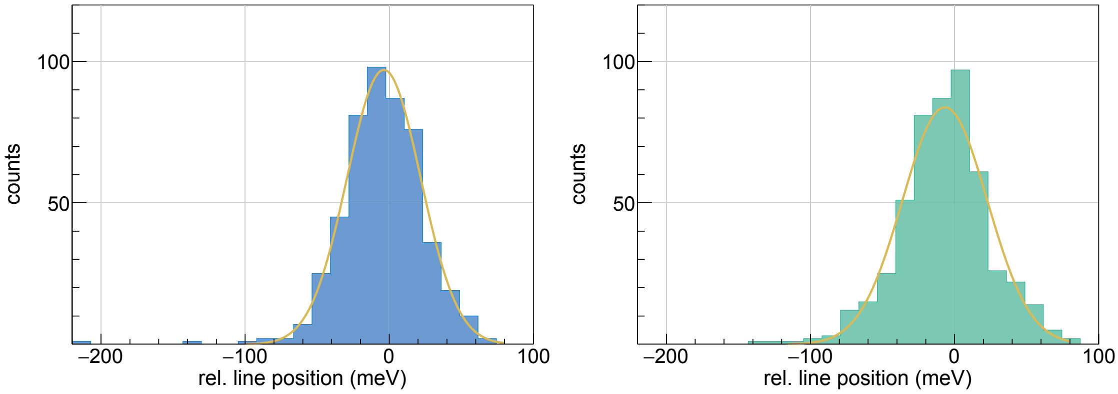

(a) K35 divider **(b)** K65 divider

Figure 5.5: Both figures show the difference between the estimated line positions and their corresponding value, as predicted by a linear fit-function. This is performed for both dividers separately, with the K35 divider (a) on the left side and the K65 divider (b) in green.

Again, both values meet the desired specifications. During spectroscopy in tritium mode, a measured point is proposed to be rejected if the line position, as estimated with the monitor spectrometer, will show a deviation, greater than the ones given above. As in case of monitoring of the long-term stability, this rejection can only happen at the end of an entire cycle, because the mentioned average value cannot be calculated beforehand.

One more addition to this result has to be made. All measurements that are reported here were performed in parallel to the commissioning of the spectrometer and detector section. Not surprisingly, the conditions at the monitor spectrometer were influenced by these investigations. To investigate the complicated background processes different magnetic field configurations were used, see [Har15]. The corresponding changes of the stray fields at the monitor spectrometer are sufficient to cause shifts in the line position. These influences are clarified in fig. 5.6. Again, the time dependency of the line-position is shown for both high-voltage dividers. By overlaying both data sets, systematic shifts of the line position are visible. The data-sets are uncorrelated on a global scale with $\mathrm{cov}(E_{0,\mathrm{K35}}, E_{0,\mathrm{K65}}) = 7 \cdot 10^{-5}$. However, data points that differ greatly from the average value show a correlation that is visible by eye, for example at day 40. There the estimated line-positions take on nearly the same values for measurements with both dividers. Statistically, the occurrence of coincidences of overlaying line-positions has to be expected. Previous measurements with the monitor spectrometer however, have proven such effects to be caused by varying stray fields at the main spectrometer. Establishing the a direct connection between variations of the stray fields an the line position will not be performed at this point, because retracing all field-adjustments of the magnets at the main-spectrometer takes tremendous affords. Furthermore this task would yield no deeper insight or additional information, as the system already is proven to exceed the design values. It is evident that these systematics will vanish during stable tritium mode measurements or would be rejected by the cut on σ.

In conclusion, the monitoring principle via the means of comparing fluctuations against a constant of nature, given by the line position of the K-32 conversion line from krypton-decay,

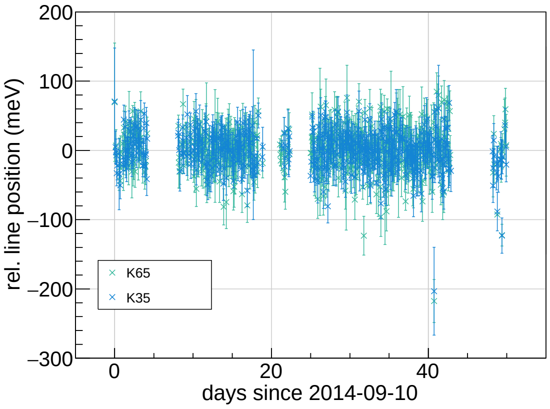

Figure 5.6: Time distribution of the estimated conversion line positions with data from both high-precision dividers. The global covariance is in the order of 10^{-5}, indicating no correlation. Changes of the stray-field at the MoS cause shifts of the line-position measured by both dividers.

provides a powerful tool to measure the long-term stability during a tritium run. Both the high voltage dividers and the implanted sources are ultra stable, resulting in a highly precise but also highly reliable monitoring of the retarding potentials' DC-component.

5.3 AC Component

As discussed in section 5.1.2, the measured krypton spectrum is influenced by fluctuations of the filter potential. As the exact line shape differs for Gaussian and sinusoidal distortions, the monitor spectrometer can not only be utilized to ensure the DC stability but in also allows to scan for AC instabilities. The following section explores this option. A priori, a fluctuation originating at the main spectrometer can not be expected to reach the monitor spectrometer unmodified with its initial amplitude. The equipment between the two spectrometers such as the distribution units with their rather long wiring has a small but non-vanishing ohmic resistance, capacitance and inductance. Therefore the first step to investigate a possible AC monitoring was performed by applying fluctuations with precisely known characteristics with measurements of the K-32 line. In this case, the line shape and total width are influenced by the distortions. The analysis of this data is carried out in section 5.3.1 and yields the influence of distortions originating from the retarding potential of the main spectrometer to their effective size at the monitor spectrometer. With this result at hand the section concludes with an exemplary estimation of the experimental sensitivity to detect fluctuations of the analyzing potential, see section 5.3.2.

5.3.1 Voltage Fluctuations

In order to investigate the influence of distortions which originate in the main spectrometer and to study propagation through the distribution system to the monitor spectrometer, sinusoidal distortions of known amplitude and frequency are applied. Specifically the post-regulation is fed with such a waveform. Due to the overall capacitance, resistance and inductance of the distribution system, the parameter of interest is the resulting amplitude that enters the monitor spectrometer potential. The measurement table is shown in table 5.1. Here, a run refers to the measurement of the K-32 spectrum. It consists of a total of 30 minutes measurement time and 42 non-equally spaced points to scan the spectrum. Note that the parameters are chosen such as to use the maximal amplitudes and frequencies that the post-regulation can reliably generate, having in mind the large capacitance of the main spectrometer. Rather large amplitudes are preferred due to the natural Kr-source line width of $\mathit{\Gamma} = 2.7\,\mathrm{eV}$, which could hide small-scale distortions and hinder fitting. In addition, two line scans with active post-regulation but no artificial ripple have been taken. Compared to the stand-alone mode, one expects that the Gaussian width is larger during measurements in parallel mode. Therefore the first two runs serve as reference for the following investigations.

The actual analysis is rather challenging. Referring to section 5.1.2, the line shape is expected to differ for Gaussian and sinusoidal distortions only at small scales and consequently these parameters are highly correlated. Their most prominent feature is to broaden the line. To clarify the situation, fig. 5.7 shows the data and the corresponding fit of data-taking run 173157. An amplitude of three volts has been used during the run.Due to the large correlation, the fitting algorithm finds a local minimum of the χ^2 distribution

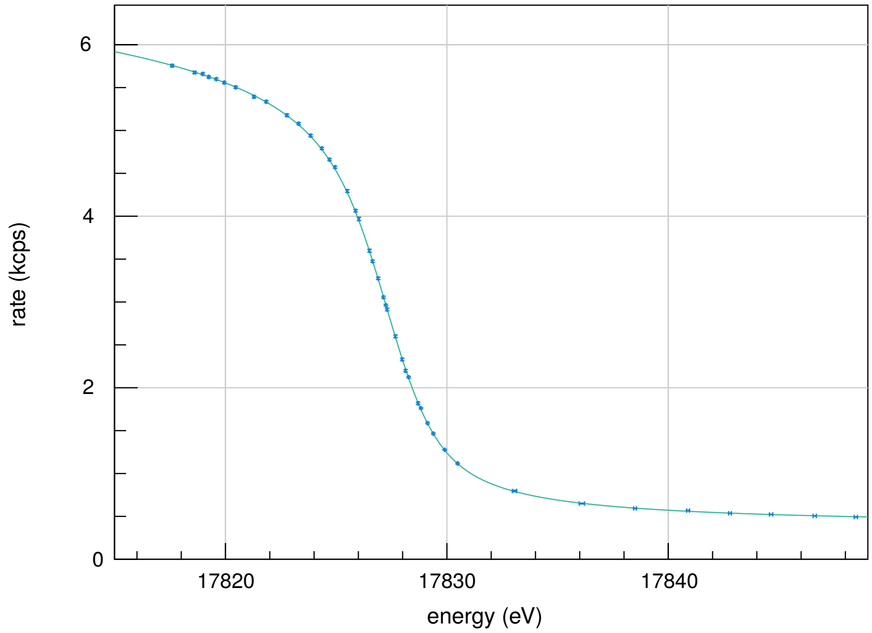

Figure 5.7: Measurement of the K-32 line with a sinusoidal distortion, A = 3 V, f = 50 Hz. The data (blue) has been fitted with the distorted spectrum (green). Although the ripple is known to be much larger, highly correlated parameters cause the fit to converge in an only local minimum. Within reasonable computation times the thereby gained results are not meaningful, as a large portion of the amplitude is swallowed by the Gaussian variance.

for the unreasonable parameter configuration shown in table 5.2. A large portion of the amplitude is 'swallowed' by the standard deviation, while the reduced $\chi^2/\mathrm{NDF} = 35.7/36$ value indicates no significant discrepancy between data and model. Accordingly, this could be real effect. However, the reference measurements and analysis of other data has shown it to be a problem of the fit algorithm. The same situation applies to the measurements at the main spectrometer section 6.3.3. There, using a Markov Chain Monte Carlo (MCMC) based fitting method with large sampling sizes solves the problem. Although the same fitting algorithm has been utilized during the analysis of monitor-spectrometer data, large chains are not possible due to the long computing times of the complex spectrum. An obvious way to bypass this circumstance is given by choosing a good set of initial parameters, i.e. by starting the fit with the applied amplitude as input. As the purpose of this section is to propose a way to identify unknown fluctuations, this approach is not performed. Instead, the sinusoidal amplitude is chosen to be initially equal to zero, which is the best a-priori assumption in this situation. A possible solution is given by using a model without distortions for the fit and to treat the ripple as variate adding quadratically to the Gaussian standard deviation

$$\sigma^2 = \sigma^2_{\mathrm{ref}} + \sigma^2_{\mathrm{sin}}, \tag{5.23}$$

where σ^2 is the effective variance, σ^2_{ref} the variance of the reference measurement without active distortion and σ^2_{sin} the variance causes by the ripple. The U-distribution then connects variance and amplitude A

$$\sigma^2_{sin} = \frac{A^2}{2}. \tag{5.24}$$

The effective amplitude that enters the filter potential is then given by

$$A = \sqrt{2(\sigma^2 - \sigma^2_{\mathrm{ref}})}. \tag{5.25}$$

This method strongly reduces the computation times, and the fit converges after a much smaller number of sampling steps. During the standard monitoring mode, the common line shape model can be utilized for fits, whereas the fitted Gaussian width has to be compared to a reference measurement, without the need for time-consuming fit algorithms.

One draw-back however has to be accepted. Strictly speaking, the model is known to be physically incorrect, as it incorporates the influence of the sine-wave into the size of the Gaussian standard deviation σ. Nevertheless, for the measurement with $A = 3\,\mathrm{V}$ the resulting is $\chi^2/\mathrm{NDF} = 49.8/37$. Together with the statistical significance of 0.05, and $P = 1 - F(49.8|37) \approx 0.078$ the fit is still acceptable.

All runs have been analyzed with this technique, and fig. 5.8 shows the corresponding results. To compare different amplitudes, the efficiency $\eta = \mathrm{A_{meas}}/\mathrm{A_{in}}$ is used with the estimated amplitude $\mathrm{A_{meas}}$ and the applied one $\mathrm{A_{in}}$, rather than using the amplitudes themselves. Due to the large frequency interval the abscissa is logarithmically scaled for better visibility. Four different amplitudes have been used as artificial ripple on the main spectrometer retarding potential. The modeling to estimate the efficiency is is difficult over the large range of amplitudes and frequencies. Especially the error bars are probably underestimated by the fit algorithm due to local minima of the parameter space. Further, several measurements yield efficiencies above unity. This unphysical behavior hints to

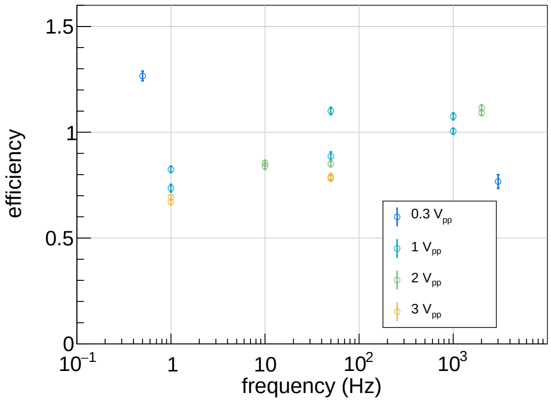

Figure 5.8: Analysis of rippled krypton spectra. For better comparison, the efficiency $A_{\mathrm{meas}}/A_{\mathrm{in}}$ rather than the amplitude is used as axis. Different colors represent the applied amplitudes.

systematic effects and underlines the need for further investigations. For instance, the post-regulation setup has shown to produce highly asymmetric signals in the low-frequency regime, an effect that has not been taken into account at this point. This newly developed feature, thus needs to be understood with higher precision. For the scope of this work the efficiency is equalled with unity, independent of amplitude and frequency.

5.3.2 Sensitivity

In order to estimate the sensitivity of this technique, the reduced χ^2/NDF value for the ideal model without distortions and the rippled functions is computed. In doing so, several assumptions are made. An optimized measurement distribution has been used, and the high voltage measurement is assumed to be accurate to 10 mV. Furthermore the statistical uncertainty is assumed to be at one percent of the count rate at each measurement point. For source activities of 5 kcps, such systematical uncertainties are achievable with short measurement times. The results for Gaussian and sinusoidal noise is shown in fig. 5.9. The yellow line indicates the 90 % confidence level. Consequently, distortions above this line will be detected and the measurement point of the tritium scan has to be rejected. In this manner, purely Gaussian distortions are detected if they are larger than 336 mV, sinusoidal ones if they are larger than 462 mV. This is equivalent for distortions above a 5 ppm and 8 ppm level, which is well above the specifications. This newly developed technique therefore cannot replace the direct monitoring of the ripple by measurements with an oscilloscope but only support them. However, the method signals potency for redundant noise monitoring. For this reason it will be subject to further investigations.

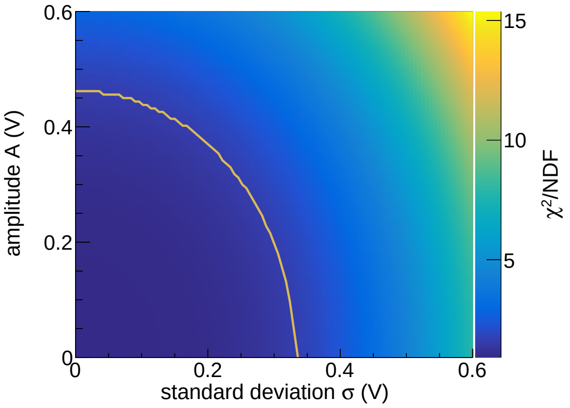

Figure 5.9: Sensitivity for detecting AC noise. The reduced χ^2/NDF value has been computed for different sizes of Gaussian and sinusoidal distortions. The yellow line indicates the sensitivity. Purely Gaussian distortions are measured above 336 mV, sinusoidal fluctuations above 462 mV. These values are well above the necessary precision of only one ppm. Without further investigations and improvement this method can only support direct measurements of the ripple but not replace them.

Table 5.1: Measurement table of the conducted investigations with the corresponding amplitudes and frequencies of the artificial ripple. Each data-taking run consists of a total of 30 mintes measurement time, whereas the measurement points are distributed non-equally spaced to scan the spectrum.

Run number	Amplitude ($\mathrm{V_{pp}}$)	Frequency (Hz)
173135	0	0
173136	0	0
173137	1	1
173138	1	1
173139	1	50
173140	1	50
173141	1	1000
173142	1	1000
173143	0.3	0.5
173144	0.3	0.5
173145	0.3	500
173146	0.3	500
173147	0.3	3000
173148	0.3	3000
173149	2	10
173150	2	10
173151	2	50
173152	2	50
173153	2	2000
173154	2	2000
173155	3	1
173156	3	1
173157	3	50
173158	3	50

Table 5.2: Best-fit output of run 173157

χ^2/NDF	Normalizatio (cps)	Position (eV)	σ (eV)	Amplitude ($\mathrm{V_{pp}}$)	Shape	Background (cps)
35.7/36	4674 ± 32	17828 ± 0.1	0.92 ± 0.017	0.21 ± 0.05	86.2 ± 3.7	383.4 ± 0.8

CHAPTER 6

High voltage stability at the main-spectrometer

The goal of this chapter is the in-depth characterization of the influence HV ripples have on the electric fields, i.e. the transmission properties. Moreover, the influence such ripples have on the background is investigated.

As the calculations performed in section 2.2.2 have shown, an approximative formula for the effect of disturbances in the electric fields is known. However, for this result to be applicable to the tritium analysis, the connection between ripples of the applied voltage and the potential in the analyzing plane has to be made. For this reason dedicated measurements have been performed during the second SDS commissioning phase. Data acquired in these measurements can be refined in a sophisticated analysis to gain full understanding of the radial, frequency and amplitude dependencies of potential distortions coupled into the inner fields. Fourier's theorem states that knowledge of sinusoidal-waves influence is sufficient for all signal-forms to be understood. It is self-evident that even equipped with these powerful analytical tools, preventing any imperfections of the voltage to happen in the first place is of major importance. Although the focus of this thesis is oriented towards transmission properties high voltage fluctuations are also of interest for background models, as such fluctuations might contribute to the generation of background or also might be able to lower the overall background level. The first section of this chapter illustrates the performance of the high voltage system that has been achieved during the measurement phase in respect to stability (section 6.1.1) and monitoring (section 6.1.2). Throughout all subsequent sections the AC component of the high voltage is investigated. First, the experimental ripple reduction that was achieved with active post regulation (PR) is investigated (section 6.2). As the post regulation allows to artificially apply arbitrary wave forms, the models can be experimentally verified. Before the construction of the actual physics model takes place (section 6.3.2), the proper statistical methods needed for the analysis of transmission data taken with the electron gun as source are derived section 6.3.1. After all needed methods are present, the data is analyzed and in conclusion the response of the electric fields inside the spectrometer to voltage fluctuations is established as central part of the chapter (section 6.3.3). At last, the measurements conducted for the investigation of AC voltage dependent background effects are presented.

6.1 DC component

As the developments in section 2.2.2 have shown the influence of any given distortion can be calculated to shift the estimated neutrino mass to smaller values with $\mathit{\Delta} m^2_{\bar{\nu}_e} = -2\sigma^2$. Given the total budget for systematic uncertainties for KATRIN to reach its aimed sensitivity, the maximal size of unknown distortions can then calculated to be of the order of

$$\mathit{\Delta} m^2_{\bar{\nu}_e} \leq 0.0075\,\mathrm{eV}^2 \tag{6.1}$$

and therefore

$$\sigma \leq 0.061\,\mathrm{V}, \tag{6.2}$$

see [Ang05] for further details. It is common to translate this into relative quantities, with a analyzing potential of 18.6 kV and the above value is then equivalent to 3 ppm. It is self-evident that this constrains the boundaries for ripples of the voltage. For this reason the two KATRIN voltage dividers measure the voltage in real-time, while the monitor-spectrometer allows comparison to a constant of nature. For practical reasons both spectrometers are located in different buildings and are separated by approximately 20 m, see section 4.6. After successfully proving the functionality and stability of the monitoring principle via a nuclear standard, these distribution units have to be investigated for possible systematic effects. With the KATRIN voltage dividers and the monitor-spectrometer exceeding the designed expectations, it is still reasonable to suppress slow drifts of the voltage, even if they are measurable with high precision. In this regard the limiting factor for measurements at the same vessel potential is given by the time scale for which the voltage is stable within the specifications. Measurements of both characteristics are described in this following.

6.1.1 Stability

Even if primary conceived to smoothen out ripples in the high voltage, the post-regulation setup is also able to compensate slow drifts of the voltage. Described in section 4.2.2 the post-regulation decouples AC and DC components of the high voltage. The latter is conducted over an additional voltage divider. During the second measurement phase, the built-in divider was just an auxiliary device. This unit does not provide high stabilities. Because the post-regulation was newly connected to the beam-line, joining higher valued dividers directly would possibly been harmful would not have posed significant additional value. For the main task of estimating the AC noise, the utilized voltage divider does not play any roll, whereas it has only be stable enough to prove the post-regulations capabilities to remain at the same DC voltage over a sufficient amount of time. A representative set of data is shown in fig. 6.1. Here the post-regulation was actively smoothening the vessel voltage, while the DC-component was measured with the K35 divider. Because the KATRIN divider has to be regarded as absolutely stable over even a day, every feature of the data has to be seen as purely systematic to the post-regulation, as the total measurement time is 300 s. The time-scale here has been chosen in order to accommodate for the most likely time-distributions in measurement time, where single retardation potentials are expected to be in the order of minutes or less. To illustrate possible systematic drifts more

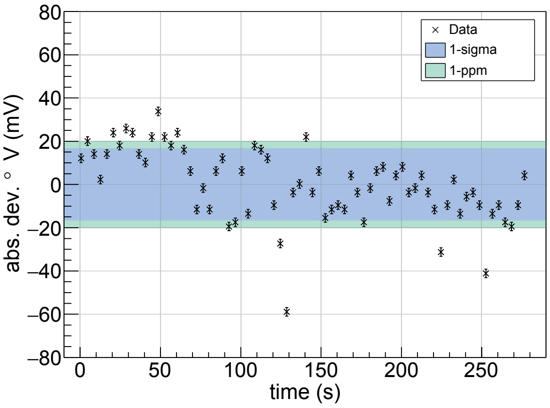

Figure 6.1: Stability measurement of the voltage with active post-regulation. The ordinate is given by the absolute deviation from the mean value of all data-points during the 300 s measurement period. Additionally the $1-\sigma$ and $1-\text{ppm}$ bands are drawn. The standard deviation of all points still lies within $1-\text{ppm}$ and is therefore agreeable with the hypothesis of no drift at all over the entire measurement time.

easily the ordinate is given as absolute deviation of the measured voltage from the mean value of all points. Additionally the bands corresponding to 1 ppm and $1\,\sigma$ have been drawn. First of all it should be noted that the scale is at the mV-level and the standard deviation of the data-points is only 16 mV. Comparing this to 1 ppm $\approx$ 20 mV, the already achieved stability is exceeding the desired value by a factor of three. By eye a drift to smaller values might not entirely be excluded. However, the null hypothesis of a stable voltage without drift is accepted for standard deviations smaller than 3 ppm, which is the case. Furthermore the result is only dependent on the voltage divider used for controlling the DC compensation of the post-regulation. As this divider is not temperature stabilized, it has to be expected to react extremely sensitive to temperature fluctuations or changing electrical loads. Even with the experimental-hall being air conditioned, convection air currents or direct ventilation are likely to cause temperature gradients of the order of one degree, as the divider does not posses any housing. As experience shows such temperature-differences are sufficient to cause drifts in the ppm-regime. Therefore, it is safe to assume that this stability is significantly increased by using one of the KATRIN dividers that have stabilities of 0.2 ppm/month. With this result, the needed DC stability for tritium measurements is already verified.

6.1.2 Parallel measurements with the monitor-spectrometer

Functionality and stability of the monitor spectrometer have already been verified in chapter 5 along with the influence of AC distortions originating in the main high voltage and propagating throughout the monitor spectrometer. Nevertheless the verification of the monitoring principle with both spectrometers coupled still has to be given, as it will in this section. The conducted measurements have been performed only over a time interval nine days instead of a full tritium cycle of two months. Systematic uncertainties like contact voltages or thermal effects inside the distribution units could lead to a relative

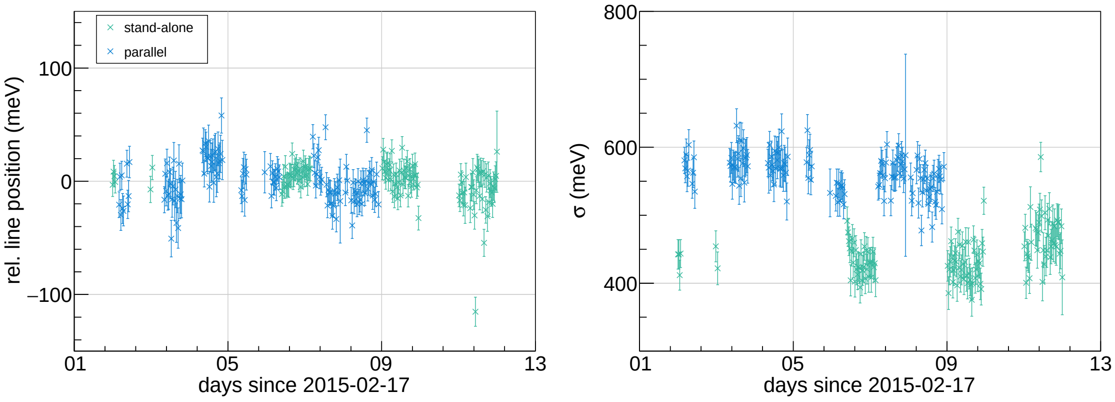

(a) Line positions **(b)** Gaussian σ

Figure 6.2: (a) Line positions of the K-32 line. Stand-alone (green) and parallel mode (blue) do not show signs of time dependence and seem to be in agreement. Here all positions are given relative to the stand-alone measurements mean value. (b) Gaussian sigmas gained from the same data. An offset between is present. This effect is expected and due to the ripple of the main retarding potential.

shift of the line position and it is therefore of interest to compare parameters gained from stand-alone measurements to those taken with active coupling. In order to enable this, the spectrometers have been electrically decoupled periodically and measurements in both modes have been performed. Furthermore the synchronization between main spectrometer measurements and krypton measurements is not trivial. Scanning through the krypton spectrum with the monitor spectrometer requires its source voltage to be adjusted accordingly to the main spectrometers retarding potential whereas the time distribution has to be optimized in terms of statistics and efficiency. Fast tritium scanning strategies therefore demand the monitor spectrometer parameters set to the corresponding values while the analyzing potential gets ramped. Hence, algorithms for remote controlling the monitor spectrometer by the main spectrometer have been developed and optimized.

A time series of line position and standard deviation for the K-32 krypton line is shown in fig. 6.2. Like it was previously mentioned, line scans alternate between the stand-alone mode and the parallel mode. All line positions are given relative to the global mean value estimated from the data in parallel mode to illuminate differences between the methods. Both methods provide line positions only fluctuating within a small band and seem to be yielding the same results. However, the situation is different for the estimated Gaussian σ that is entering the line-shape. With the results from chapter 5 and the ripple present in the retarding potential (see section 6.2) of the main spectrometer an increase in this parameter is to be expected. Nevertheless, neither of the time series points into the direction of any time dependent drift. To quantify these statements, histograms for both parameters are given in fig. 6.3.

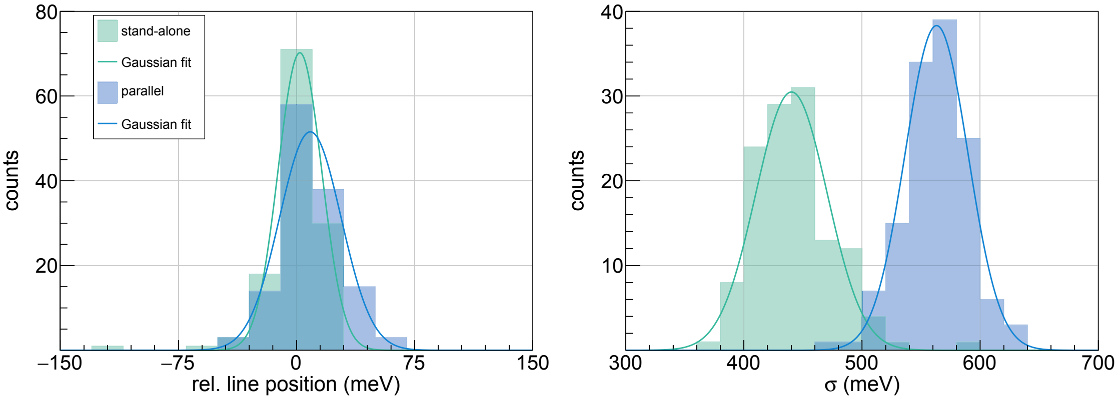

(a) Histogram of the relative line positions **(b)** Histogram of the Gaussian σ

Figure 6.3: (a) The relative line positions only differ statistically insignificant. Their numerical values have been obtained by means of a Gaussian fit to be (9 ± 2) meV and (7 ± 2) meV. In contrast to this the estimated sigmas, 440(30) meV for stand-alone and 536(27)meV for parallel mode differ by more than 3σ. As expected the sigma for measurements with connected main spectrometer is larger by nearly 100 meV.

6.2 Ripple suppression

It has been shown the DC-component of the high voltage is stabilized and measurable with ultra-high precision. Of course the initial main task of the post regulation is given by smoothing ripples. Explained in chapter 4 the high voltage system utilizes highly stabilized power supplies for the generation of the potential. Previous MAC-E filter experiments have shown that the vessels themselves are antennas and therefore the stability at the output of a power supply cannot be expected to be the same as at the vessels surface. Additionally it is common for the mains voltage to couple into the applied voltages among other components that might produce AC signals, like the turbo molecular pumps. The reason to stabilize the vessel rather than the inner electrode is easily understandable. If the post regulation was to stabilize the inner electrode its reference point would be the vessel voltage. For one, it would then be not possible to compensate drifts of the vessel voltage and one would have to rely solely on the stability of the connected supply. Secondly any distortion coupled into the vessel voltage would have the same impact on the electrodes voltage without the means to counter the effect. This explained by the strong capacitive coupling between vessel and electrode and of course the topology of the voltage system, where all voltage supplies of the inner electrode have their base point at the vessel potential. Hence, the remaining ripple on the spectrometer vessel without active smoothing has been measured, as shown in fig. 6.4. The left side of the figure shows a measurement taken over a time interval of two seconds. The present periodic waveform has a periodicity of $f = 1\,\mathrm{Hz}$ and is more complicated than the one of simply a sinusoidal. It is caused by control oscillations of the high voltage supply. This effect was anticipated, for the attached supply is not the highly stabilized that will be used during tritium mode, but rather one that is more suited for test measurements. The global variance of this waveform is $\sigma = 308\,\mathrm{mV}$ with a peak to peak value of $\mathrm{V_{pp}} = 1376\,\mathrm{mV}$. Even if the ripple caused by the control oscillation

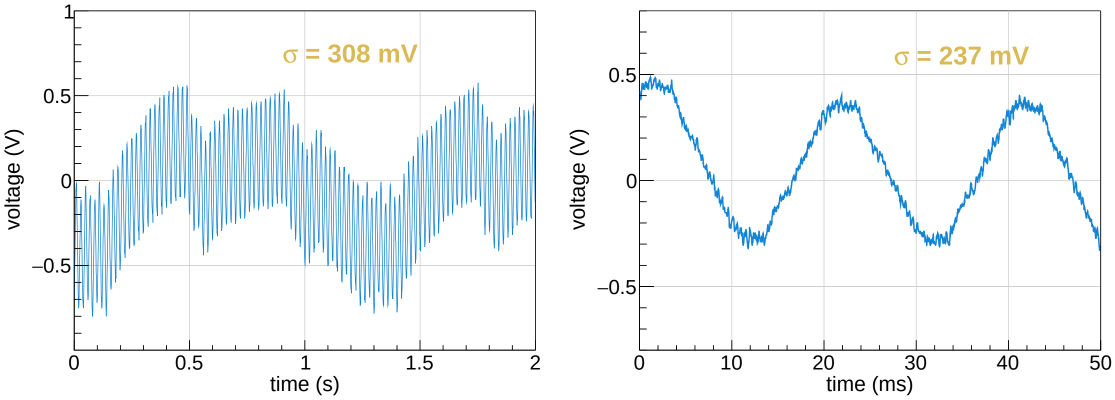

(a) Ripple at 1 Hz

(b) Ripple at 50 Hz

Figure 6.4: Measurements of the ripple without active smoothing. (a) Measurement at the time scale of seconds. A periodic signal with frequency $f \approx 1\,\mathrm{Hz}$ is present, originating from the voltage supply. Together with the higher-frequent part visible this leads to $\sigma = 308\,\mathrm{mV}$ and $\mathrm{V_{pp}} = 1376\,\mathrm{mV}$. (b) Measurement in the millisecond regime. The measured wave has a frequency of 50 Hz and is caused by the mains voltage. The standard deviation $\sigma = 237\,\mathrm{mV}$ and $\mathrm{V_{pp}} = 816\,\mathrm{mV}$ are smaller than the before but still exceed the specifications by one order of magnitude.

would be entirely absent with the high-quality supply, the higher frequent part can be expected to remain manifest. This component is shown on the right side of the figure with the more fitting time interval of 50 ms. Having a frequency of 50 Hz this is most likely caused by the mains voltage coupling into the system. Still the above argument holds and this is not caused by the supply but is rather coupled into the system capacitively at some unknown location, for the reason that the high voltage supply is not highly stable but poses good galvanic decoupling. With $\sigma = 237\,\mathrm{mV}$ and $\mathrm{V_{pp}} = 816\,\mathrm{mV}$ this remaining distortion contributes the largest part to the global variance.

Consequently active smoothing has been shown to be indispensable. With the post regulation as such a system actively smoothening the high voltage, the remaining ripple is shown in the left side of fig. 6.5. Only a total variance of $\sigma = 16\,\mathrm{mV}$ and a sinusoidal amplitude of $\mathrm{V_{pp}} = 816\,\mathrm{mV}$ are left. With this and the results of section 6.1.1 the post regulation setup already has shown to exceed the sought properties by more than a factor of three. Nevertheless it is possible to further reduce the noise that is left, because of frequencies the post regulation is not able to compensate for. These distortions are beginning at frequencies of approximately 100 kHz and only contribute in the millivolt range but can be counteracted with smoothing capacitors dimensioned accordingly. On the right hand side of fig. 6.5 direct comparison between active and non active post regulation is shown for further illustration. Apart from the significant reduction of noise this also validates the systems AC-stability on larger time scales.

In terms of measurement time it is interesting how quickly the data taking is allowed to start after a new voltage set value has been entered. Investigating this it is suitable to take advantage of a features that will also be exploited for the connection between vessel

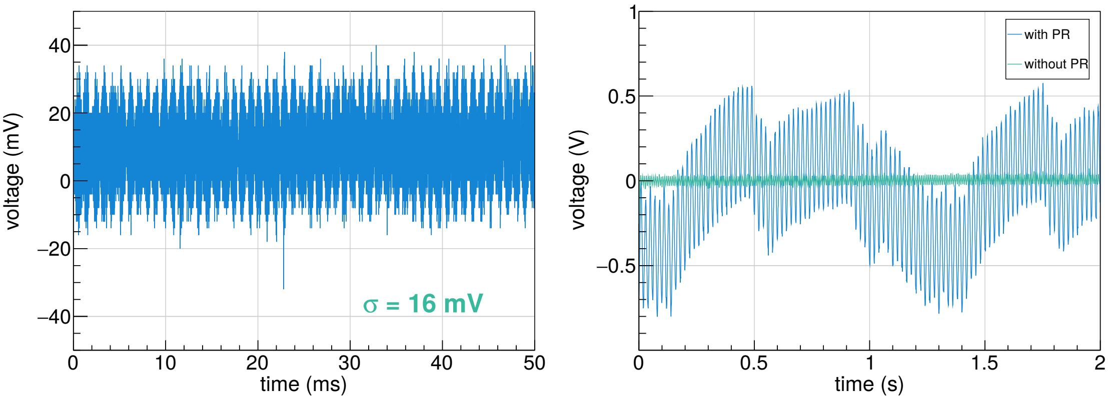

(a) Ripple with active post regulation **(b)** Comparison between measurements

Figure 6.5: Measurements with the post regulation actively smoothening the high voltage of the spectrometer vessel. (a) The active PR reduces the ripple to $\sigma = 16\,\mathrm{mV}$. Frequencies greater than 100 kHz remain as noise. What appears as slight drift is actually the impact of the lower frequent part. (b) Comparison between measurements with active and inactive PR. The timescale is of the order of seconds.

potential and fields inside the spectrometer, see section 6.3. As the reference point of the post regulation can be manipulated by application of an external voltage one can shift its output and therefore the vessel potential correspondingly. Square wave signals are most fitting for this, because they provide sharply defined flanks as reference in time. An illustration showing these measurements is shown in fig. 6.6. The utilized square wave, shown in green, incorporates a comparatively large electrical stroke of 2 V, in order to amplify the effect. After a negligible reaction time the vessel potential begins to increase with an equally steep slope. With the transition to zero gradient not manageable for the

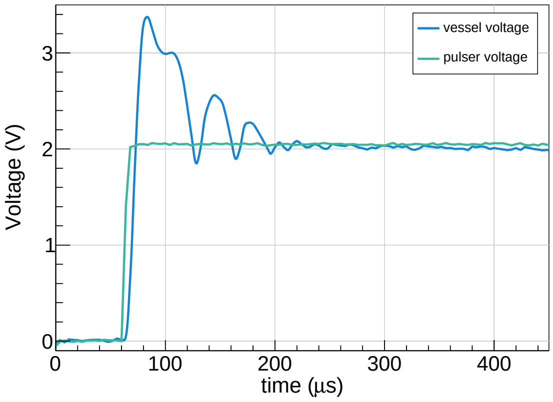

Figure 6.6: Measurement for investigating the time scale of the voltage to settle after a new voltage set value has been entered. Because of its sharply defined flanks a square wave is utilized as input for the post regulations base point. Even without exact numbers the process is evident to take place on small timescales.

setup to handle the output of the post regulation overshots and settles in a characteristic behavior. For reasons of better visibility the actual data have been re-binned to neglect noise but to keep the distinct wave-forms. Note that the whole process takes place on an interval of only 400 μs, even for such a high amplitude. In the next step, consider the residuals between the two signals, as shown on the left side of fig. 6.7. Directly after the input has started to increase, the residuals become negative because the electronics have a reaction time that can be estimated to be smaller than 20 ms. The subsequent steep increase in the output corresponds to the post regulation reacting to the the applied square wave, where the overshoot manifests in residuals larger than 1 V. A reliable way to quantify the time scale needed for the voltage to settle again is given by examining the time series for the residuals standard deviation, fig. 6.7(b). For this purpose the measurement points have been merged into bunches of ten points each, whereas every bunch was used to calculate one standard deviation. In this representation the settling can then be assumed to be finished as soon as the standard deviation drops below 20 mV. By means of this method, with an electric stroke larger than it is to expect for common scanning strategies, one gains a conservative estimate for the settling time. As presented in the figure, the estimated time scale is only 320 μs, a result showing another of the post regulations advantages. The time consumed solely by shifting the potential can by reduced to a negligible minimum by using the post regulation during scanning of the tritium spectrum. In comparison, other voltage supplies have shown to need times up to 40 seconds for this ([Ren14]). Assuming the fastest scanning strategy that was proposed for KATRIN, only 20 s will be spent at one voltage and therefore the time lost with waiting for the retarding potential to stabilize would even exceed the measurement time itself.

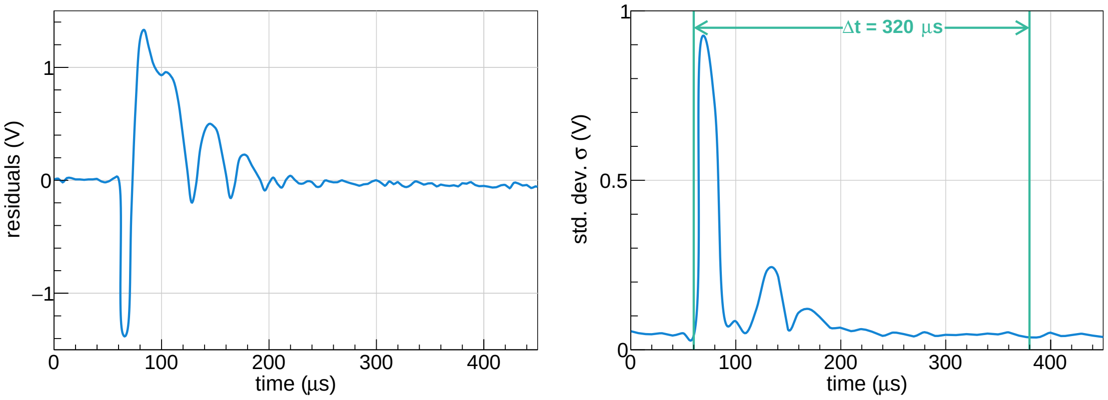

(a) Settling process with post regulation

(b) Variance time series during settling

Figure 6.7: (a) The residuals between the input square wave and the post regulation output. Directly after the beginning of the steep slope the output is smaller than the input because of the post regulation's small reaction time. After the initial square wave has already settled, the output overshoots because of the post regulations cut-off frequency being too small. (b) Quantification of the process via investigation of the time series for the standard deviation. It only takes 320 μs for the standard deviation to get below 20 mV again.

6.3 Connecting voltage and inner potential

Within this section the connection between any given voltage distortion and the affiliated response of the electric fields inside the vessel gets explored. Before this central relation can be obtained, some groundwork has to be made. First of all a proper statistical model has to be established. While this model is constructed against the background of measurements with the electron gun, all relations gained within this model hold for tritium measurements and therefore yield a valuable contribution to the KATRIN experiment. Afterwards the actual physics model is designed. Here the angular resolution of the given electron source gives strong arguments for simplification of the model, that in interaction with the distorted potential would otherwise provide complicated and hard-to-handle formulas. The proper cuts and correction factors among the utilized fitting algorithm are explained. In the last section the final result is presented.

6.3.1 Statistical model

As electrons are either transmitted or rejected by the filter, it is reasonable to acknowledge the spectrometer at a fixed potential as a binomial experiment with the probability mass function (PMF)

$$\mathrm{B}(X = k) = \binom{n}{k}\varepsilon^k(1-\varepsilon)^{n-k}, \tag{6.3}$$

where n is the total number of incoming electrons, k is the number of those that are transmitted and ε is the transmission probability for a given potential. In the case of transmission measurements with the electron gun, the statistical population n is not exactly known, but rather a variate for itself. It is reasonable assumption to describe the latter by the well-known Poisson statistics with the PMF

$$\mathrm{P}(N = n) = \frac{\nu^n}{n!}\mathrm{e}^{-\nu}. \tag{6.4}$$

To implement this into the binomial statistics that describe the spectrometer, one has to consult the law of total probability, which for a partition A_i of the event space Ω takes the form

$$\mathrm{P}(B) = \sum_{A_i \in \Omega} \mathrm{P}(B \mid A_i)P(A_i), \tag{6.5}$$

with the conditional probabilities $\mathrm{P}(B \mid A_i)$ and the total probability $\mathrm{P}(B)$ for B. If the binomial distribution is regarded as the conditional probability $P(X = k \mid N = n)$, the theorem is applicable and gives

$$\begin{aligned} \mathrm{P}_\nu(X=k) &= \sum_{\substack{n=0,\\ n\geq k}}^{\infty} \binom{n}{k} \varepsilon^k (1-\varepsilon)^{n-k} \frac{\nu^n}{n!} \mathrm{e}^{-\nu} \\ &= \frac{(\nu\varepsilon)^k}{k!} \mathrm{e}^{-\nu} \sum_{\substack{n=0,\\ n\geq k}}^{\infty} \frac{(\nu-\nu\varepsilon)^{n-k}}{(n-k)!} \\ &= \frac{(\nu\varepsilon)^k}{k!} \mathrm{e}^{-\nu} \mathrm{e}^{\nu-\nu\varepsilon} \\ &= \frac{(\nu\varepsilon)^k}{k!} \mathrm{e}^{-\nu\varepsilon}, \end{aligned} \tag{6.6}$$

where the summation can always be carried out for the reason that k can be assumed at a fixed value, so that $n-k \geq 0$. The outcome of this calculation might not entirely be unexpected as it is a Poisson-distribution around the new expectation value $\nu\varepsilon$. Still this allows to use the average count of incoming electrons as a parameter of the model instead of using the variate n and is therefore exactly the needed result.

However one problem still remains, as the interesting part is not given by the counted electrons but rather the transmission probability ε. Usually this is treated by the approach

$$\hat{\varepsilon} = \frac{k}{\nu} \qquad \text{and} \qquad V[\hat{\varepsilon}] = (\frac{1}{k} + \frac{1}{\nu})\hat{\varepsilon}^2. \tag{6.7}$$

In the limiting cases for $k=0$ and $k=n$ this yields the unphysical result $V[\hat{\varepsilon}] = 0$. A correct treatment of uncertainties can be achieved by using Bayes' theorem. The principle idea of this calculation goes back to [Ull12], where the method was originally applied to efficiency calculations but is transferable to the situation at hand with some changes. Bayes' theorem

$$\mathrm{P}(B \mid A) = \frac{\mathrm{P}(A \mid B)\mathrm{P}(B)}{\mathrm{P}(A)}, \tag{6.8}$$

can be used if one regards the transmission probability ε in the previously constructed PMF eq. (6.6) as a statistical variable instead a parameter,

$$\mathrm{P}_\nu(X=k \mid T=\varepsilon) = \frac{(\nu\varepsilon)^k}{k!} \mathrm{e}^{-\nu\varepsilon}. \tag{6.9}$$

Taking a normalization constant C into account this gives

$$\mathrm{P}_\nu(T=\varepsilon \mid X=k) = \frac{1}{C} \mathrm{P}_\nu(X=k \mid T=\varepsilon)\mathrm{P}(T=\varepsilon). \tag{6.10}$$

Here $\mathrm{P}(\varepsilon)$ is the a-priori probability connected to ε:

$$\mathrm{P}(T=\varepsilon)=\begin{cases}0 & ,0\leq\varepsilon\leq 1\\ 1 & ,\text{otherwise.}\end{cases} \tag{6.11}$$

Because of the normalization condition

$$\int\limits_{-\infty}^{\infty}\mathrm{P}_{\nu}(T=\varepsilon\mid X=k)\,\mathrm{d}\varepsilon=\frac{1}{C}\int\limits_{0}^{1}\frac{(\nu\varepsilon)^{k}}{k!}\mathrm{e}^{-\nu\varepsilon}\,\mathrm{d}\varepsilon=1, \tag{6.12}$$

one has to solve the integral on the right hand side of the equation. The result contains the incomplete gamma function

$$\gamma(m,x)=\int\limits_{0}^{x}t^{m-1}\mathrm{e}^{-t}\mathrm{d}t \tag{6.13}$$

and its useful representation as series

$$\gamma(m+1,x)=m!(1-\mathrm{e}^{-x}\mathrm{e}_{m}(x)), \tag{6.14}$$

where

$$\mathrm{e}_{m}(x)=\sum_{i=0}^{m}\frac{x^{i}}{i!}. \tag{6.15}$$

With this the following calculation is self explanatory and

$$\begin{aligned}\int\limits_{0}^{1}\frac{(\nu\varepsilon)^{k}}{k!}\mathrm{e}^{-\nu\varepsilon}\,\mathrm{d}\varepsilon&=\frac{1}{k!\nu}\int\limits_{0}^{\nu}t^{i-1}\mathrm{e}^{-t}\,\mathrm{d}t=\frac{1}{k!\nu}\gamma(i,1)\\&=\frac{1}{k!\nu}\gamma(k+1,1)=\frac{1}{k!\nu}k!(1-\mathrm{e}^{-\nu}\mathrm{e}_{k}(\nu))\\&=\frac{1}{\nu}(1-\mathrm{e}^{-\nu}\mathrm{e}_{k}(\nu)),\end{aligned} \tag{6.16}$$

so that the normalization is given by

$$C=\frac{\nu}{1-\mathrm{e}^{-\nu}\mathrm{e}_{k}(\nu)}. \tag{6.17}$$

Conclusively the final probability distribution is

$$\mathrm{P}_{\nu}(T=\varepsilon\mid X=k)=\frac{\nu}{1-\mathrm{e}^{-\nu}\mathrm{e}_{k}(\nu)}\frac{(\nu\varepsilon)^{k}}{k!}\mathrm{e}^{-\nu\varepsilon}. \tag{6.18}$$

As promised, even if originally developed for transmission function measurements this result holds for all experiments that count particles from a radioactive decay, including KATRIN. Figure 6.8 shows this probability density function (PDF) and the associated cumulative probability density function (CDF) for $n = 10$ and $k = 0,1,2,...,10$. The distribution is distinct from the one the usual Poisson statistics would return. First of all the distributions are only symmetric for $k \approx n/2$, while they develop to be highly asymmetrical at the boundaries. This reflects the information introduced by the a-priori probability for $\mathrm{P}_\nu(T = \varepsilon \mid X = k)$. An important feature is that the function has a non vanishing width and even with exact calculation still pending, the unphysical result from Poisson statistics is adjusted. Furthermore the CDF reassures the result, as the functions are clearly normalized. In the next step the statistical estimators are computed. With a completely analytical formula it is intriguing to implement asymmetrical errors by calculating suitable percentiles. Nevertheless, this consumes computation time and in the case of high statistics proves to be not possible, as examined below. Therefore the common estimators, average and variance, are used. Structurally all occurring integrals are of the same form as in the deviation of the statistical model itself, the only difference being the power of ε rising. In principle it is possible to give a closed formula for any given power of the transmission probability. However, as this is not instructive the results are directly given:

$$\hat{\varepsilon} := E[\varepsilon] = \frac{1 - \mathrm{e}^{-\nu}\mathrm{e}_{k+1}(\nu)}{1 - \mathrm{e}^{-\nu}\mathrm{e}_k(\nu)} \cdot \frac{k+1}{\nu} \tag{6.19}$$

and

$$V[\varepsilon] = \left(\frac{1 - \mathrm{e}^{-\nu}\mathrm{e}_{k+2}(\nu)}{1 - \mathrm{e}^{-\nu}\mathrm{e}_k(\nu)} \cdot \frac{(k+1)(k+2)}{\nu^2}\right) - \left(\frac{1 - \mathrm{e}^{-\nu}\mathrm{e}_{k+1}(\nu)}{1 - \mathrm{e}^{-\nu}\mathrm{e}_k(\nu)} \cdot \frac{k+1}{\nu}\right)^2 . \tag{6.20}$$

It is evident from eq. (6.18), eq. (6.19) and eq. (6.20) that several factors, which are hard to handle numerically, enter the formulas. Two factorials have to be computed, one in the incomplete exponential series and the other one in the denominator of the second factor. Furthermore the expression in the denominator of the first factor rapidly converges to zero, as n and k get bigger. In applications like transmission function measurements, the asymptotic behavior of the estimators is therefore of interest. They are actually quite easy to compute, because $\mathrm{e}_k(\nu)$ is a finite sum for powers of ν and the growth of the exponential function outweighs the one of any given power their composition will vanish in the limiting case. In further consequence this yields the manageable identities

$$\hat{\varepsilon}_{\nu\to\infty} = \frac{k+1}{\nu} \tag{6.21}$$

and

$$V[\varepsilon]_{\nu\to\infty} = \frac{k+1}{\nu^2}. \tag{6.22}$$

Taking the limit for large statistical populations the gained estimators have two interesting properties. For one, now the variance has non vanishing values in the limiting case and therefore more physical meaning. Secondly, for all numbers the estimated transmission probability is nonidentical to zero and also the naive estimator $\hat{\varepsilon} = k/\nu$. By computing the $mode(\varepsilon)$ through setting the first derivative equally to zero,

$$\frac{\mathrm{dP}}{\mathrm{d}\varepsilon} = \frac{\nu^2 \mathrm{e}^{-\nu}}{1 - \mathrm{e}^{\nu}\mathrm{e}_k(\nu)} \left(\frac{(\nu\varepsilon)^{k-1}}{(k-1)!} - \frac{(\nu\varepsilon)^k}{k!} \right) = 0 \tag{6.23}$$

from which follows,

$$mode(\varepsilon) = \frac{k}{n}. \tag{6.24}$$

Astonishingly in the constructed case of binomial experiment that is statistically populated by a variate with Poisson distribution it is the mode instead of the expectation value that yields the correct result. It is worth emphasizing the rapid convergence of those estimators for high statistics. Naturally this effect originates from the PDF that has been constructed above. Figure 6.9 highlights this characteristic, that is manifest even in the presented case of $n = 100$. In comparison to fig. 6.8 the distribution significantly sharpens out. Still the skewness of the function remains and only breaks into symmetric form for $k = n/2$. This feature evolves quickly as the statistical population increases and in the case of measurements with 50 kilo counts and more leads to very sharply defined estimators.

The model up to now has made one assumption that will not hold during measurements. Further investigated, the transmission function has a non-trivial energy dependence that has been suppressed during the above calculations. It is safe to assume the applied voltages to be Gaussian distributed. Equivalently to the calculation of the total probability above, the energy distribution then can be incorporated. However, the functional dependence of the transmission function together with the Gaussian probability density function of the voltage estimate are not manageable in any analytical enclosed form. A much more practical way is given by assuming the electron gun statistics to be statistically independent of voltage uncertainties of the main spectrometer and quadratically add the effects,

$$\sigma^2 = V[\varepsilon] + \left(\frac{\mathrm{d}\varepsilon(E)}{\mathrm{d}E} \right)^2 \sigma_E^2. \tag{6.25}$$

Now only the derivative of the transmission function remains to be calculated, methods for this will be given in one of the subsequent sections.

Even if this section and the involved math appear to be rather technical, the obtained results hold simple but strong relations. The power of the constructed statistic lies in its widely diversified applicability for all experiments using detectors with Poisson-like statistical populations, implying the tritium measurements of KATRIN. However, the developed insight that has been given on the technical level by the corresponding equations and is deepened by the shown graphics is necessary for the following sections, where the physical model gets build and the actual fitting of theory to data is conducted.

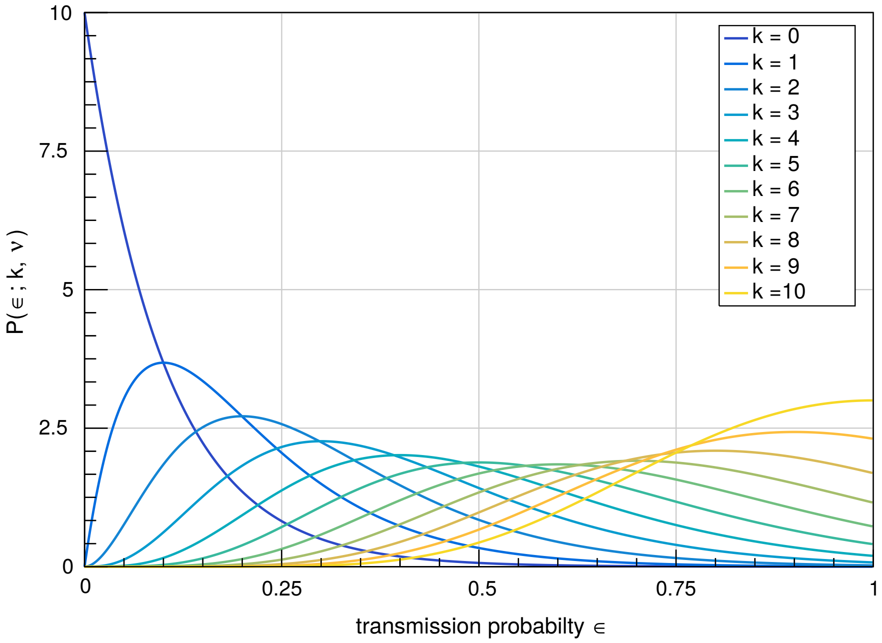

(a) PDF for $\nu = 10$

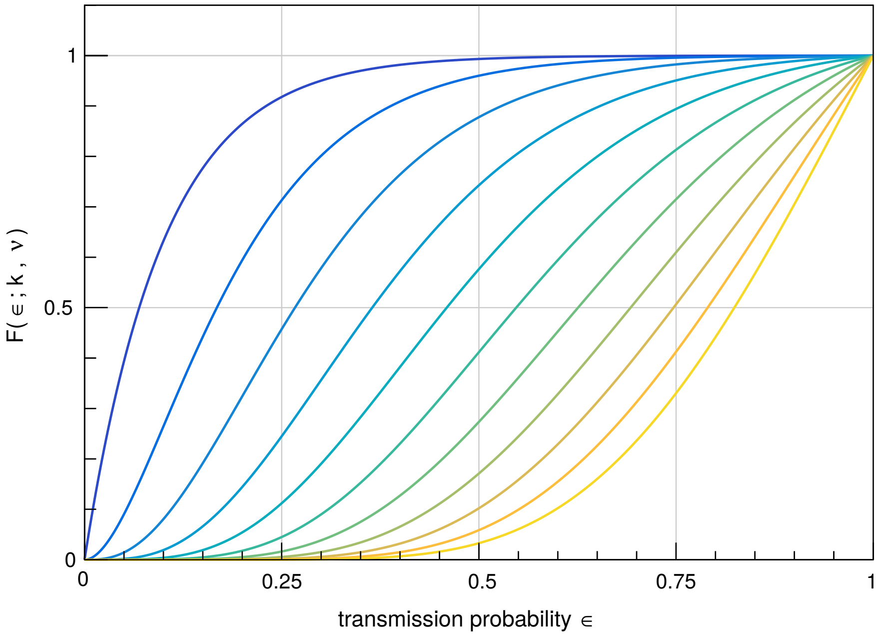

(b) CDF for $\nu = 10$

Figure 6.8: (a) The constructed PDF for $\nu = 10$ and different values for k. The behavior is evidently different to the one expected by simple Poisson statistics. Note the asymmetric behavior at the outer most edges. (b) Corresponding CDF. More easily to see by eye, the distribution is asymmetric and normalized.

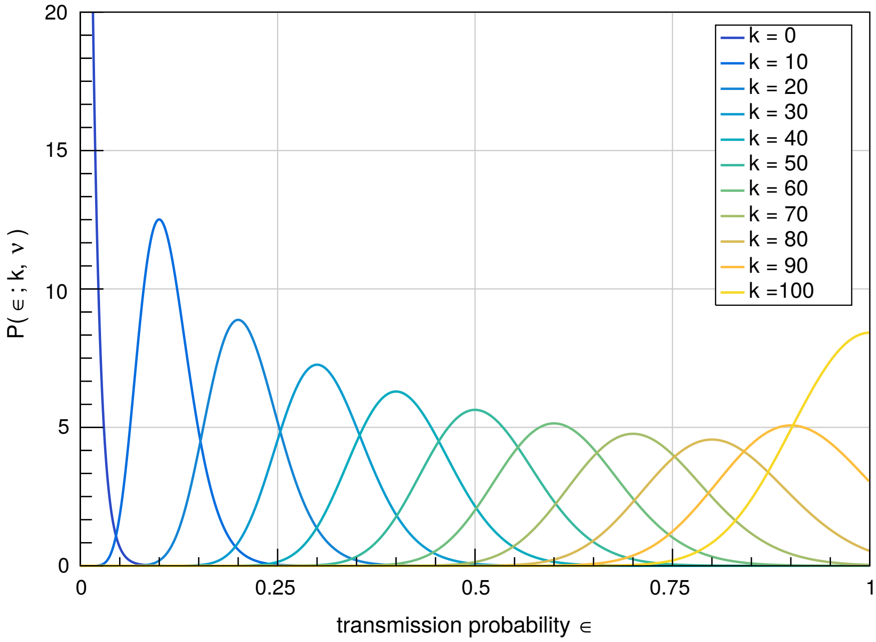

(a) PDF for $\nu = 100$

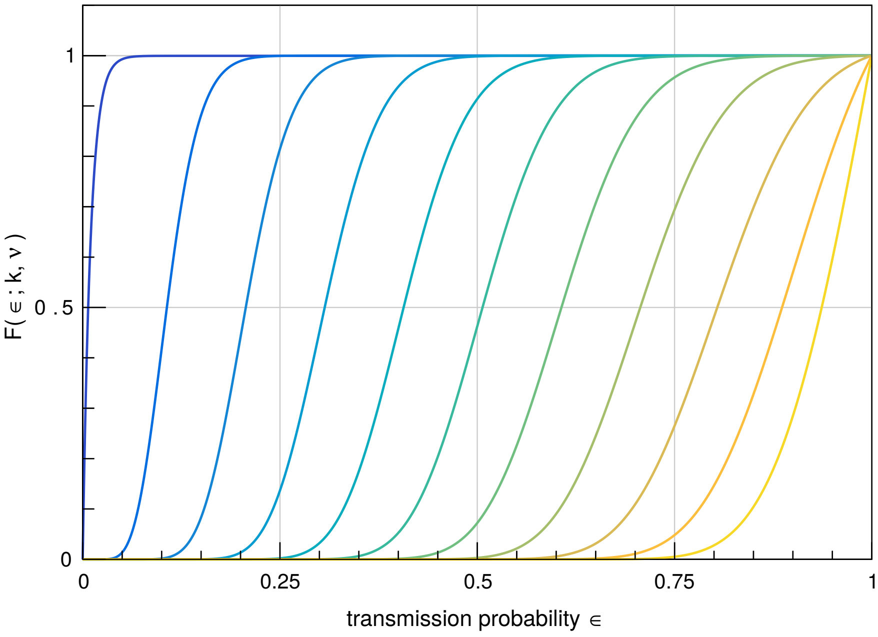

(b) CDF for $\nu = 100$

Figure 6.9: The probability density function and cumulative probability density function for a higher total statistical population $\nu = 100$. Here a distinct characteristic of the model manifests. For high statistics the functions become sharply defined. Note that the axis of ordinates has been truncated for better visibility, therefore the function with $\mathrm{k} = 0$ reaches out of scope.

6.3.2 Physical model

The actual physical model of the transmission function and its line-shape are the result of complex interplay by the precise properties of source and spectrometer. During the next section a general and well known approach will be given ([Gro15b]). As the transmission function measurements performed as part of this thesis are based on the electron gun as source the given universal identities can be reduced to a more comprehensible and numerically benign form. As a result the developed physical model will depend on electric fields and distortions within them only, which is exactly what is necessary to investigate the influence of fluctuations. In addition the statistical models constructed in the previous section are extended by the correlation between abscissa and ordinate.

Basic properties

As described in section 2.2 the transmission function of an ideal MAC-E filter can be characterized as the one of an ideal high pass filter, i.e. a Heaviside function

$$\varTheta(E, qU_{\mathrm{ret}}) = \begin{cases} 0 & , E - qU_{\mathrm{ret}} < 0 \\ 1 & , E - qU_{\mathrm{ret}} \geq 0, \end{cases} \tag{6.26}$$

where U_{ret} has to be regarded as the potential at the point of analysis and therefore already depends on the position inside of the spectrometer. This result only holds for electrons emitted with a starting polar angle $\varTheta = 0$. If this angle is non identical to zero the analyzing energy $E_{\mathrm{ana}} = qU_{\mathrm{ret}}$ has to be regarded as a function of the electric and magnetic fields as well as the starting polar angle,

$$E_{ana} = \frac{q(U_{\mathrm{ret}} - U_{\mathrm{src}})}{1 - \sin^2\varTheta_{src}\frac{\gamma_{src}+1}{\gamma_{\mathrm{ana}}+1}\frac{B_{ana}}{B_{src}}} \tag{6.27}$$

Here the indices correspond to the fields and relativistic gamma-factors in the source and the analyzing plane. By solving the above equation for the angle $\varTheta$, one is able to find the maximal angle for which electrons with a given energy and for a fixed retardation field pass the filter,

$$\varTheta_{max}(E) = \arcsin\left(\sqrt{\frac{\gamma_{ana}+1}{\gamma_{\mathrm{src}}+1}\frac{B_{src}}{B_{ana}}\frac{E - q(U_{ana} - U_{src})}{E}}\right). \tag{6.28}$$

A realistic model requires the starting angles and starting energies of the electrons to be distributed with non vanishing variances. Formally this can be expressed by the angular probability density $\varOmega(\varTheta)$ and the energy distribution $\varSigma(E_{src})$. With these definitions and in accordance with the above equations, the transmission function for a source with arbitrary angular distribution $\varOmega(\varTheta)$ and energy distribution $\varSigma(E_{src})$ can be calculated by solving

$$T(E - E_{ana}) = \int\limits_{E_{ana}}^{\infty} \int\limits_{0}^{\Theta_{max}(E)} \omega(\Theta)\, \Sigma(E_{src})\, \mathrm{d}\Theta \mathrm{d}E_{src}. \tag{6.29}$$

Generally this integral will not be solvable by analytical means, for its functional dependence of the angular and energy distributions, that can be arbitrarily complex. However, the given expression secures the formal existence of a transmission function that at least can be calculated by numerical means.

Adapted transmission function

Under certain conditions the universal formula for the transmission function can be simplified to have no angular dependence at all. As it was constructed to be a source of mono-energetic electrons with sharp angular resolution the e-gun can be adjusted to release electrons only in a narrow band around the direction of a magnetic field line. As shown in [Beh16], if set to such a setting, the angular distribution can be regarded independent of the energy, which is why the integrals decouple and the angular integral can be carried out to be unity always, yielding

$$T(E - E_{ana}) = \int\limits_{E_{ana}}^{\infty} \Sigma(E_{src})\, \mathrm{d}E_{src}, \tag{6.30}$$

which leaves only one integral to be performed. By means of the central limit theorem it is save to assume the emitted electrons energy distribution to be Gaussian, with some standard deviation σ, experimentally proven by [Beh16] and [Erh16b]. Thus the transmission function for measurements for which the electron gun is aligned to the magnetic field can be simply expressed as the CDF of a normal distribution,

$$T(E - E_{ana})_{\sigma;\mu} = \frac{1}{2}\left(1 + \mathrm{erf}\left(\frac{E - E_{ana} - \mu}{\sqrt{2}\sigma}\right)\right) \tag{6.31}$$

Here the indices denote a dependency on a parameter. Note that the somewhat arbitrary decision to take the expectation value of the distribution to be μ, rather than zero will be explained in section 6.3.3. The analysis of the data has shown to be better described by means of a generalized Gaussian with the PDF

$$\psi_{\zeta;\eta;\rho}(E - E_{ana}) = \frac{\mathcal{N}_{0;1}(\lambda)}{\zeta - \eta(E - E_{ana} - \rho)} \tag{6.32}$$

and the CDF

$$\Psi_{\zeta;\eta;\mu}(E - E_{ana}) = \mathrm{N}_{0;1}(\lambda), \tag{6.33}$$

where

$$\lambda = \begin{cases} -\frac{1}{\eta}\log\left(1 - \frac{\eta(E-E_{ana}-\rho)}{\zeta}\right) & ,\eta \neq 0 \\ \frac{E-E_{ana}-\rho}{\zeta} & ,\eta = 0, \end{cases} \tag{6.34}$$

with the standardized Normal distribution $\mathcal{N}_{0;1}(\lambda)$ and its cumulative distribution $\mathrm{N}_{0;1}(\lambda)$. The support of these function is

$$\lambda \in \begin{cases} (-\infty, \rho + \zeta/\eta) & ,\eta > 0 \\ (-\infty, \infty) & ,\eta = 0, \\ (\rho + \zeta/\eta, \infty) & ,\eta < 0. \end{cases} \tag{6.35}$$

A graphical representation of these functions is given in fig. 6.10. Most prominently this function is skewed and not symmetrical any longer. For positive values of the skewness parameter η the CDF develops a feature as it is seen in the data, the lower energetic part is smeared out with a comparatively slow rate of growth, while the higher energetic part becomes to be sharply defined with a steep slope. Apart from the measured data being better described with this model two heuristic arguments for using it shall be given. Determining the exact shape of the energy spectrum, the e-gun has been shown to provide electrons with an asymmetrical shaped energy distribution ([Erh16b]). Furthermore the ripples applied in the measurements with active post-regulation become asymmetric for low frequencies. A drawback of this model is its bad comparability with the non skewed version. In particular expectation value and variance now are given by

$$E[E - E_{ana}] = \rho - \frac{\zeta}{\eta}\left(\mathrm{e}^{\eta 2/2} - 1\right) \tag{6.36}$$

and

$$V[E - E_{ana}] = \frac{\zeta 2}{\eta^2}\mathrm{e}^{\eta 2}\left(\mathrm{e}^{\eta 2} - 1\right). \tag{6.37}$$

Therefore they are not identical to the common mean value and standard deviation of a Gaussian. The expectation value of the skewed version is named ρ, while the so called scaling parameter gets denoted as ζ and the shaping parameter is called η. The scaling factor is in a way connected to the usual standard deviation σ, but as one easily sees from eq. (6.37) this is also true for the shape η. Nevertheless for comprehensibility it is advisable to recall the scale as the parameter giving the function its width and the shape as the factor skewing the distribution.

With the generalized Gaussian distribution being the appropriate one for describing the data, the implementation of voltage fluctuations is conducted with the methods of

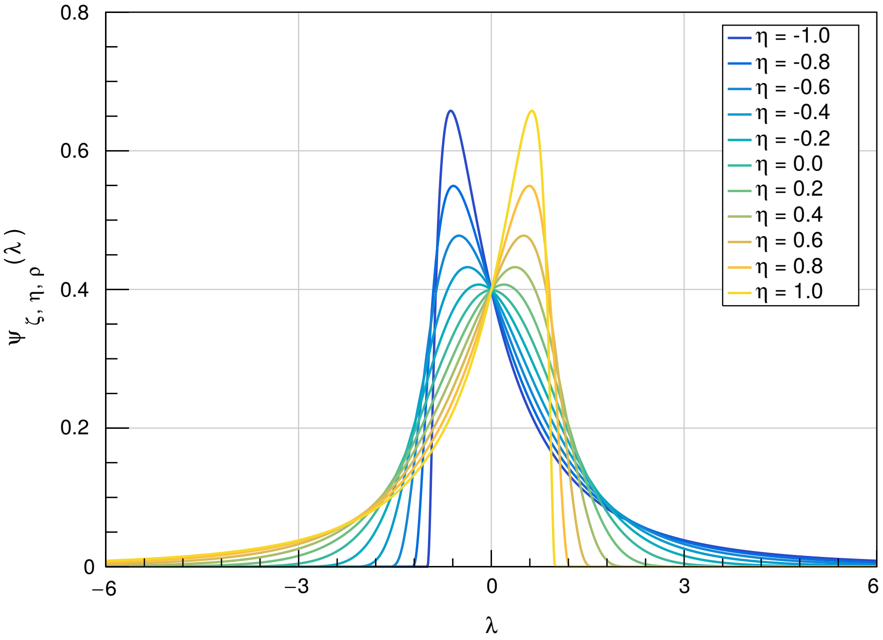

(a) PDF for $\zeta = 1$ and $\rho = 0$

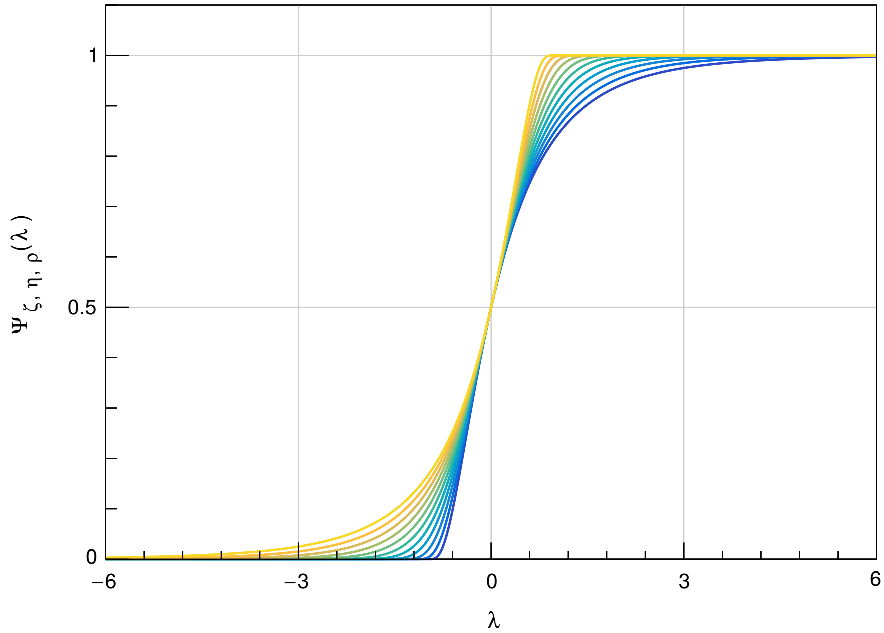

(b) CDF for $\zeta = 1$ and $\rho = 0$

Figure 6.10: Illustration of the generalized normal distribution with its PDF in (a) and its CDF in (b). Both were computed for constant $\rho = 0$ and $\zeta = 1$, while the shape parameter η takes on value from -1 to 1. Depending on the sign of η the distribution gets skewed to the left (negative values) or to the right (positive values), leading to one side with a steep slope, while the other slope flattens out and has a slowly decreasing tail. For $\eta = 0$ the function degenerates into the one of a normal distribution.

section 2.2.2,

$$T_{\zeta;\eta;A;\rho}(E - E_{ana}) = \int\limits_{-\infty}^{\infty} f(\xi) \Psi_{\zeta;\eta;A;\rho}(E - \tilde{E}_{ana}(\xi))\, \mathrm{d}\xi, \tag{6.38}$$

or in the case of sinusoidal fluctuations,

$$T_{\zeta;\eta;A;\rho}(E - E_{ana}) = \frac{1}{2\pi} \int\limits_{-\pi}^{\pi} \Psi_{\zeta;\eta;A;\rho}(E - E_{ana} + A\sin(\xi))\, \mathrm{d}\xi. \tag{6.39}$$

The generalized error function is known to be non-analytic and so will be integrals of it with complicated integration measures. Fortunately an algorithm for numerical evaluation of the integral can be adapted easily. In fig. 6.11 the final physical model is visualized, by its PDF and CDF. Both figures contain an array of curves, each one of them representing the function for different sinusoidal amplitudes but with the constants $\rho = 0$, $\zeta = 0.2$ and $\eta = 0.3$. The constants have been chosen to be close to the measured values. The distorted and skewed model is shown in fig. 6.11 with the PDF π and the CDF Π. Here, the PDF has two local maxima, which have their origin in the applied amplitude. It has to be pointed out, that in contrast to the sharply defined U-shaped distribution, these extrema are not located at $\pm A$, because of the asymmetric shape of the underlying Gaussian. Nevertheless, the global width of the function is increasing with the amplitude values. As a consequence the function does not only broaden with larger numerical values of A but also flattens out, for simple normalization reasons. The most important feature is a significant deformation of the line-shape.

To further clarify this picture, see fig. 6.12. Here, the parameter values are adapted to the output of the analysis that will be performed later in this chapter. The ordinate is given as relative deviation of the different parameters from their original value. Note that for each graphic only one of them gets varried and the others are fixed. The color gamut indicates the deviation from the function generated by the shifted parameter to the original function in percent of total transmission. This definition is not easy to comprehend but gives an elegant picture of the way the parameters influence the line-shape. In principle this even allows to estimate correlations between them in the beginning, but it shall be sufficient to give a qualitative explanation. Regions where two varying parameters produce the same absolute deviation will lead to correlations and a non reliable functional fit. Fortunately the amplitude, as the most important part of the constructed model, is mainly decoupled from the other variables and even in the worst case will yield trustworthy results. This condition is also for the location ρ, but not for shape and scale.The shape, previously introduced by empirical means based on the data, will actually cause the most correlations. Especially combinations of scaling parameter and shaping factor can mimic the effect of variations in the amplitude on the transmission function. Thereby they often yield unphysical results. It is quiet common for shaping parameters to be problematic, which is the reason why Markov chain Monte Carlo fitting methods will be applied in section 6.3.3, rather than classical ones that can not handle the complex parameter-space.

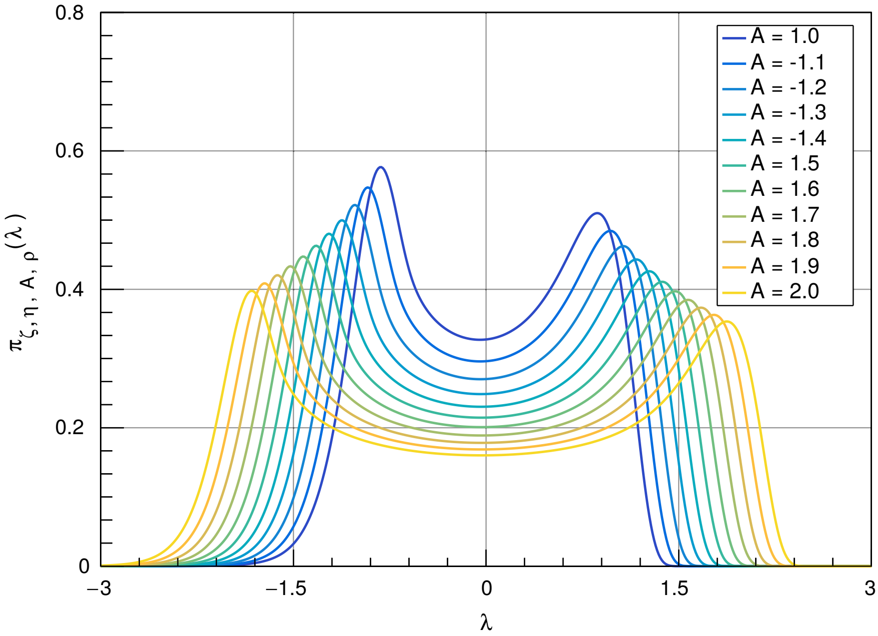

(a) PDF

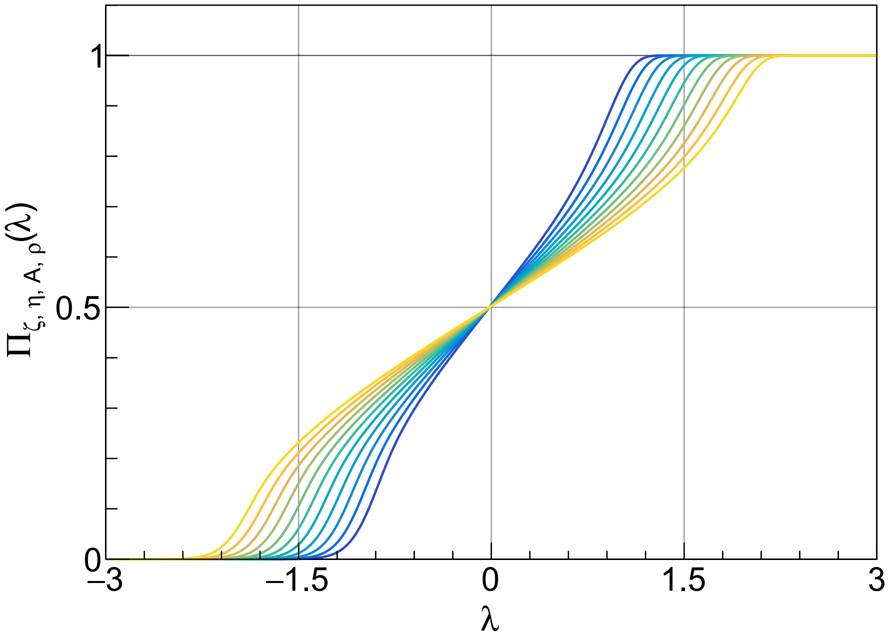

(b) CDF

Figure 6.11: (a) PDF of the distorted and skewed model. The distribution has two local maxima and is asymmetric. (b) CDF of the distorted and skewed model. The incrementally increasing amplitudes A cause the function to broaden.

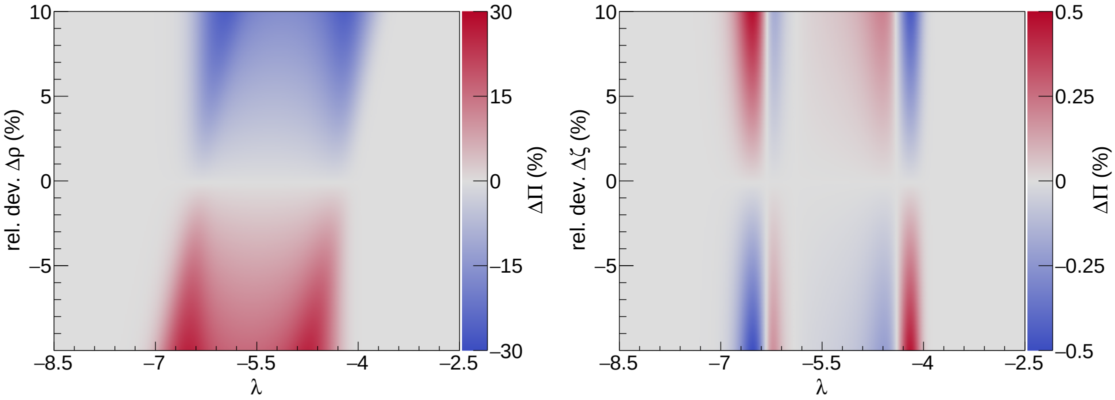

(a) Impact of mean value ρ **(b)** Impact of scale ζ

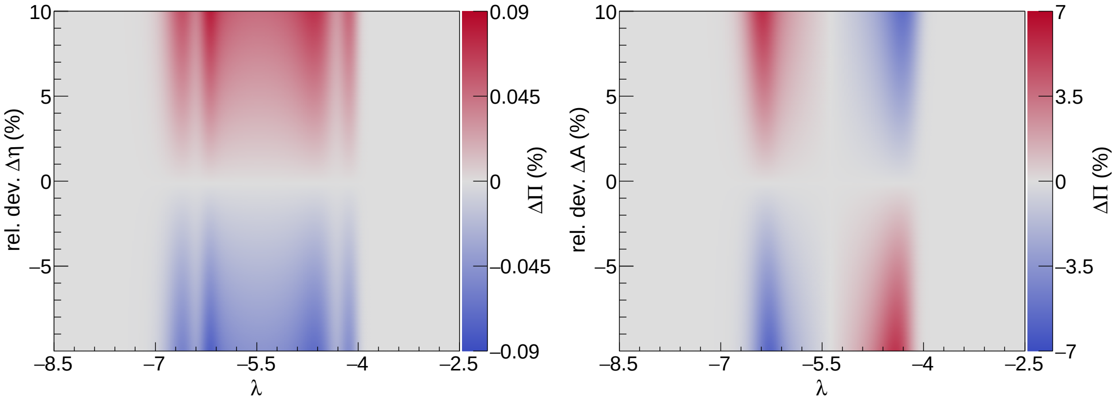

(c) Impact of shape ρ **(d)** Impact of amplitude A

Figure 6.12: The impact of the parameters onto the model. The relative deviation between the line shapes of different parameter values is obtained by varying a parameter on an interval of $[-10\%,10\%]$ of the original value. A color map reaching from blue ro red indicates the difference in percent of total transmission. Not too far from the actual deviation this representation allows the qualitative evaluation of parameter correlations. In terms of the amplitude being the most interesting parameter the mean value ρ is well behaved as its influence is entirely symmetric whereas the amplitude is asymmetrical. Shaping and scaling parameter provide a more complex structure. Combinations of these two parameters can mimic the the effect of variations in the amplitude and will lead to correlations during the function fit. Also note the different scales, the relative influence of the mean value is three orders of magnitude larger than that of the shaping factor.

This concludes the construction of the physics model for the transmission function. It has been modeled as functional of the analyzing energy and the maximal azimuthal angle. The magnetic angle has been shown to be neglectable, whereas the energy-distribution has been assumed to be Gaussian. In the next step the symmetrical line shape was replaced in favor of a skewed one, to accommodate a more realistic energy model and the known asymmetrical form of low frequency distortions. In the last step the conclusive model has been given and the influence of each parameter entering it has been illustrated in a qualitative way. Even if no quantitative knowledge has been gained this assures the occurring correlations to be manageable but most importantly gives the deep insight required to evaluate the actual data.

Correct data treatment

With the statistical and physical models being fully described a proper treatment of the measured data is the last open task before the analysis can be conducted. Several effects have to be taken into account, which would otherwise blur the results. First, all measurements have been conducted with the electron gun as source. Due to aging processes of the gold surface that is constantly being stressed by radiation by the UV light of the laser, the rate decreases slowly over time. Detailed investigations have shown that this effect is of the order of cps per hour ([Beh16]). As the total rate is approximately 10 kcps this can be neglected with measurements that only take a short period of time. The conducted measurements took only minutes, thus the loss of rate can be neglected. Furthermore, the flux of the laser is monitored by splitting the beam, with one bundle reaching to the fiber and the other on hitting a photo-diode. Voltage fluctuations of the diode then correspond to instable rates, that can be accounted for. The measurements have shown that these fluctuations are small after the LASER has gone through a reasonable heating time. All other systematic uncertainties are related to statistics and counting of the electrons. A look at the energy spectrum of a typical transmission function measurement (fig. 6.13) clarifies this picture. At least four distinctive peaks are visible. With the detection efficiency being a function of the rate, the ratio of counted to the total number reaching the detector will decrease and the transmission function artificially altered in its shape. Applying an exactly known periodic signal to the aimed detector pixel, this ratio can be measured and the effect compensated. Hence, the first peak is produced by the so called, lifetime pulser. By comparing the number of events inside this peak for measurements with electrons from the electron gun to measurements where only the pulser signal is present allows to calculate the correct rate by

$$k_{\mathrm{true}} = \frac{l_{\mathrm{w/\ e\text{-}gun}}}{l_{\mathrm{w/o\ e\text{-}gun}}} k_{\mathrm{meas}}, \tag{6.40}$$

where k_{true} is the corrected number of signal counts, k_{meas} is the measured number of electrons, $l_{\mathrm{w/\ e\text{-}gun}}$ is the number of events inside the pulser peak with additional events from the electron source and $l_{\mathrm{w/o\ e\text{-}gun}}$ are the counts with the pulser only.

All other peaks are due to actual signal electrons. Two or more of them might reach the

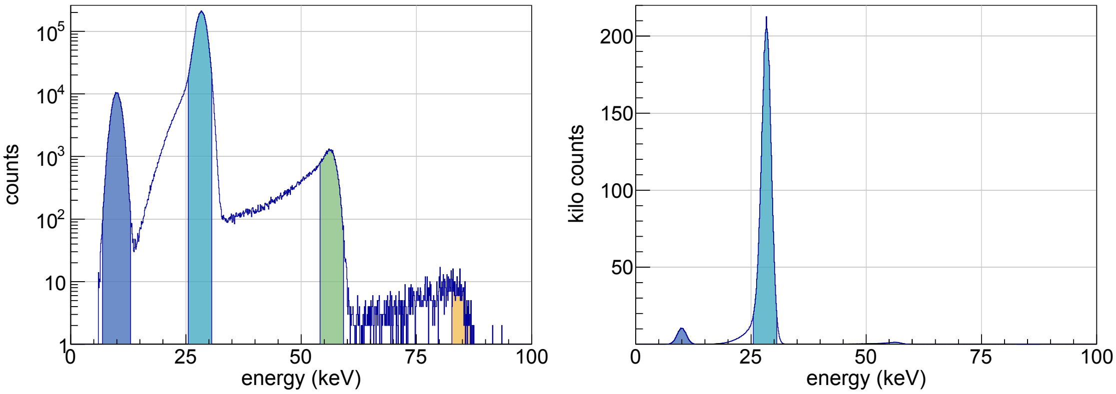

(a) Energy histogram for a typical measurement **(b)** Energy histogram on linear scale

Figure 6.13: (a) Four peaks are visible in the energy spectrum of a typical transmission function measurement. Starting from the left, the lifetime pulser accounts for the first peak. The second, third and fourth are the signal electron peaks. The colored areas highlight the regions of interest for each peak. For higher energy the distributions get broader, but for the logarithmic scale in a negligible way, as illustrated in (b). Here the scale is not logarithmic anymore and the sub-percent influence of these peaks is evident.

detector within its time resolution and therefore cause pile-up. Of course the probability for such effects decreases rapidly with the multiplicity of the peak. At total electron rates from the given source of $\approx 10\,\text{kcps}$, the two electron peak can be expected to contribute in the percent range, whereas the peak with multiplicity three can be neglected. As concrete example consider fig. 6.14. The first electron peak contains $5 \cdot 10^6$ counts, the second $4 \cdot 10^4$ and the third only $3 \cdot 10^3$. Weighting the events within the second peak with a factor of two, the final formula becomes

$$k_{\text{true}} = \frac{l_{\text{w/ e-gun}}}{l_{\text{w/o e-gun}}} \left(k_{\text{peak 1}} + k_{\text{peak 2}}\right). \tag{6.41}$$

The location of the peaks is above the energy corresponding to the retarding potential of 18.6 keV. This is due to the acceleration of electrons by the post acceleration electrode in the detector section. The electrode is elevanted onto 10 keV. Furthermore a cut off has been applied, removing the first 7 keV from the spectrum, where noise is prominent. Usually the region of interest is defined to be $[E - 3\,\text{keV}, E + 2\,\text{keV}]$ around a peak with the energy E. However, the bottleneck for counting signals at high rates is not the wafer but rather the electronics reading it out. Therefore, the pulser is coupled directly into the readout electronics and the usual region of interest does not apply. According to the specified output of the pulser and the shape of the first electron peak, located above it, the interval of the lifetime pulser has been chosen to be slightly larger with $[(10 - 3)\,\text{keV}, (10 + 3)\,\text{keV}]$. All events outside only pose a small proportion and can be disregarded. Constructing the proper windows for the electron peaks is more difficult. The one electron peak contains almost all signal electrons. For higher multiplicity peaks the asymmetry in shape increases drastically and it is not as easy to find arguments for the proper energy intervals. Because the probability for false counting increases with larger regions of interest, the peak with multiplicity two is assigned the same window. In total only a few hundred events lie within the three-electron peak and it is disregarded entirely. Well motivated by the high statistics of the main peak, the constructed method for data treating renders the estimated quantities with uncertainties well below the percent level, which is more than sufficient. For a more detailed description see [Beh16].

6.3.3 Data analysis

The main goal of this chapter is the connection between spectrometer properties and the potential, especially ripples coupled into the latter. After the characterization of the post regulation and its capabilities and all necessary theoretical preparations the connection between the inner potential and voltage fluctuations on the vessel will be established in this section. All measurements have been conducted with the post regulation, as described in section 4.2.2. By applying a known wave form to its base point this systems ripples the vessels potential in the desired way. Three different possible parameters come to mind, the amplitude, the radius inside the spectrometer and the frequency. Known from KATRIN's predecessor experiment and simulations, the inhomogeneity of the electric potential is small and therefore the radial dependency can be expected to be small. A hysteresis of the system would not be easy to explain but cannot be ruled out a priori. Most likely the coupling into the potential could depend on the frequency. Between vessel and inner electrode a total capacitance around 200 nF exists and the system could work as a high pass filter. With such a large capacitance the cut off frequency could be expected to be rather large. Nevertheless, the effective ohmic resistance of the apparatus is designed to be tremendously large in order to prevent leakage currents. In favor of the DC stability this large resistance can shift the cut-off frequency to values, where mid-frequency ripples can couple lossless into the fields. To cover all these possibilities the parameter-space has been chosen to be $[3\,\text{radii}] \otimes [3\,\text{amplitudes}] \otimes [4\,\text{frequencies}] = [36]$. Selecting the proper radii is straight-forward, measurements on-center, at the outer most pixel that could be reached with the electron gun and in the middle between them. The right choice of amplitude must be so that it is well above the variance in energy of the source. Therefore the amplitudes 1, 2 and 3 V_{pp} have been used. As the triode mounted in the post regulation setup can only provide limited currents this choice of amplitudes gives boundaries for the possible frequencies. Measurements have shown that stable conditions up to 3 kHz at 3 V_{pp} are provided. Consequently the utilized frequencies are 50, 100, 1000 and 1500 Hz.

Now to the actual analysis. Fig 6.14 presents a transmission function measurement with an active ripple of 3 V_{pp} and 1500 Hz. The best fit, drawn in yellow, describes the data very well with $\chi^2/NDF = 67/64$. This value strongly supports the sophisticated physical model that has been developed. To ensure the meaningfulness of the squared residuals, only data points where

$$T(\mathit{\Delta} E) > 3\sigma_T, \tag{6.42}$$

have been taken into account for the fit. By this the residuals are ensured to be Gaussian distributed and the squared residuals follow the χ^2 distribution. Additionally the one sigma

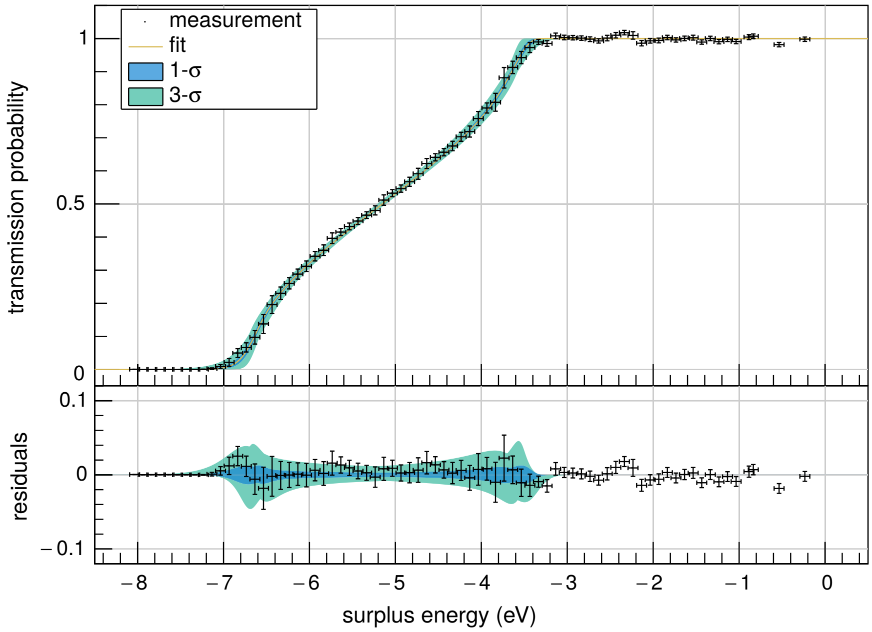

(a) Integral transmission function measurement

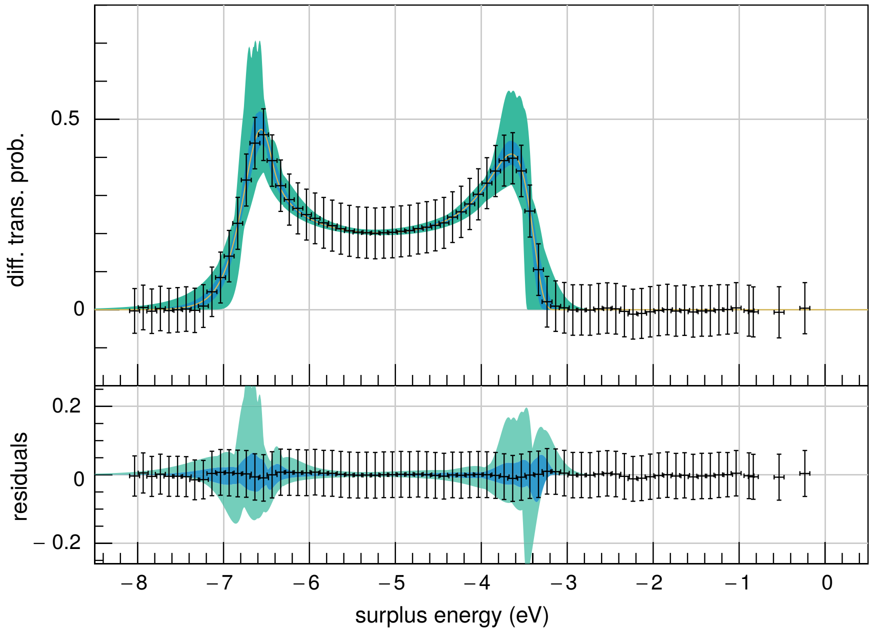

(b) Associated differential form

Figure 6.14: (a) Measurement with fit of a transmission function with ative distortion $A = 1.5\,\mathrm{V}$, $f = 1500\,\mathrm{Hz}$. The one and three sigma bands of the fit are drawn in blue and green, while the yellow line represents the best fit. Only points where it is safe to assume that they are Gaussian distributed around the function have been taken into account during the fit. Resulting in $\chi^2 = 67/64\,NDF$ the data are in good agreement with the model. (b) By means of functional differentiation the derivative of the data points has been calculated. In this picture, the yellow curve represents the analytic form of the function, only with the parameters gained from the previous fit of the integral spectrum. This representation strongly supports the model.

(blue) and three sigma (green) neighborhoods. The surplus energy takes on negative values. It has already been outlined that on the one hand, the correct title for this axis would be the difference between measured DC-voltages in electron source and spectrometer, which is suppressed for simplicity in fig. 6.15 and keeping in mind that the transmission function is defined to be over the space of surplus energy. On the other hand, the usual way of displaying transmission functions shall be kept, to show those systematic uncertainties from unknown fluctuations of the retarding potential. With the functional differentiating methods from above, the differential transmission function has been calculated, shown on the right side of the figure. Note that only the data points have been differentiated numerically, while the parameters gained from the fit of the integral form have been plugged into the analytic form of the differential spectrum. Following the same color scheme, this validates not only the differentiator but also strengthens the trust in the fitted function and the model. Here the error bars are given by the uncertainties of the fit. However, the data points are described with great accuracy by the function, any systematics would amplify greatly in the differential spectrum and together with the gained χ^2 value the model is ensured to describing the data properly.

With the physical, statistical and fitting methods shown to be working with a high level of precision and reliability, it is worth to take a closer look at the output of the utilized MCMC-chains, see fig. 6.15. By doing this, systematic effects of the methods can further be investigated, as the fitting method returns not only the parameters but also a posterior PDF for them. All four parameters have their best fit position at the mode of the distribution. As discussed in the theoretical section, mean value and sine-amplitude are well-behaved, while scaling and shaping parameter are not entirely symmetric. To further illustrate this, fig. 6.16 presents the correlation between the amplitude, being of most interest, and all other parameters. As the theory suggests, practically no correlation between mean value and amplitude exists. In the case of shape and scale this is not true. It is easy to understand that the amplitude and scale-parameter are anti-correlated. Both broaden the transmission function. However, especially for large amplitudes the effect is not significant. The shaping parameter introduces much stronger correlations. In fact, the distribution is not simply described by an ellipsoid but a complex functional dependency. Even for the largest amplitude utilized during the measurements, the contour suggests a very strong correlation for small values of the amplitude. Together with a systematic of the post regulation itself, that causes the applied ripples to be no longer symmetric, this leads to large error bars for measurement with small amplitudes and low frequencies. Nevertheless, the developed statistical and physical model among the fit and differentiation algorithms have been proven to be valid and trustworthy.

After the connection between the inner retarding potential and vessel voltage has been obtained with the above methods its dependency of radius, amplitude and frequency can be performed. In order to do so, the coupling-efficiency, i.e. the ratio $\eta = U_{\mathrm{out}}/U_{\mathrm{in}}$, will be considered. Because the data show no dependence regarding amplitude and radius further investigations about those parameters are skipped. Large capacitance and also large resistance between vessel and inner electrode allow it to treat the influence of a ripple on the retarding potential as AC-voltage propagating through a high-pass filter. The large radius of the main spectrometer make it reasonable to assume that has a small inductance

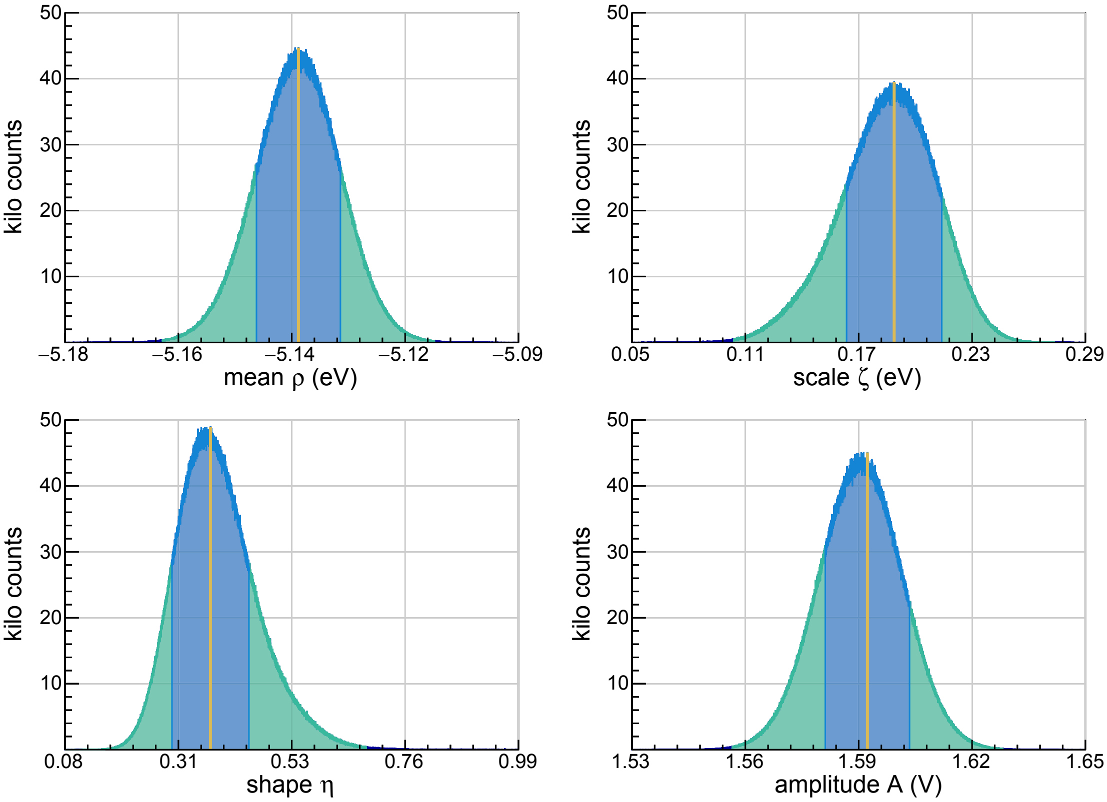

Figure 6.15: The parameter distributions resulting from the MCMC-fit. For purposes of illustration the chain size is relatively large with a burn-in of $1 \cdot 10^6$ and an actual sample-size of $100 \cdot 10^6$. Reasonable burn-in sizes are 10^5, where the sample size then only limits the resolution due to binning. The yellow line marks the position of the best-fit value where the blue and green areas correspond to the one and three sigma neighborhoods of this value. All distributions have their best-fit near the maximum, i.e. the mode, as one would expect. Amplitude and mean value behave Gaussian-like, while shape and scale are skewed because of correlations.

and therefore to regard the system as first order high-pass filter. The efficiency of such filter is described by

$$\eta = \frac{2\pi f RC}{\sqrt{1 + (2\pi f RC)^2}}, \tag{6.43}$$

with the resistance R and the capacitance C. An essential characteristic of a high-pass filter is its cutoff frequency

$$f_{\mathrm{cut}} = \frac{1}{2\pi RC}, \tag{6.44}$$

defined as the frequency for which the efficiency takes the value $\eta = 1/\sqrt{2}$. For simplicity

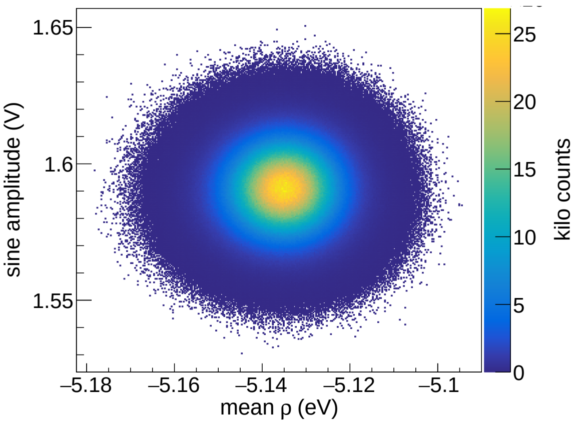

(a) Impact of ρ

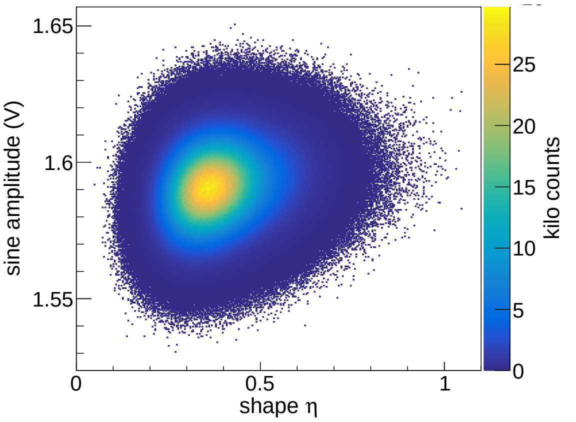

(b) Impact of ζ

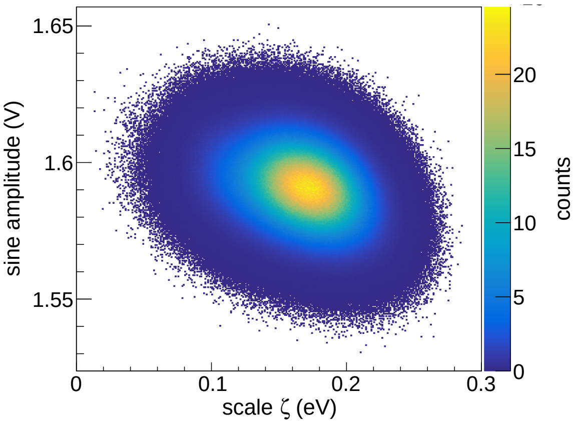

(c) Impact of η

Figure 6.16: Correlation between the amplitude and all other fit-parameters. Here, the mean value (a) shows not correlation with the amplitude, that is worth mentioning. Contrary to that, shape (b) and scale (c) are coupled significantly to the amplitude. As the shape of the distributions is not only an ellipsoid, but possesses a rather complex structure, it is evident that these parameters are subject of a non trivial parameter-space.

this can be regarded as the lower limit for ripples to propagate freely through the filter. Describing the influence that ripples pose for the electric fields then essentially means looking for the frequencies that have a significant impact on the transmission function and consequently the neutrino mass. A graphic illustration of this analysis is given by fig. 6.17.

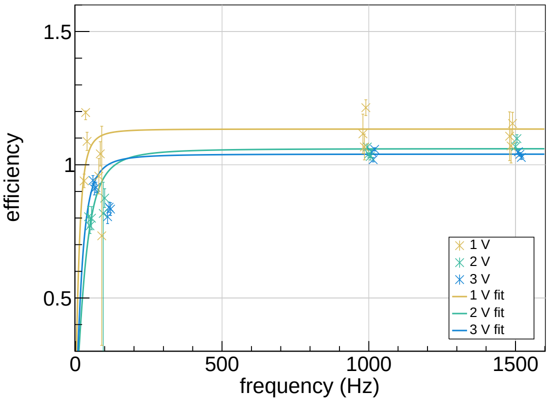

Figure 6.17: Frequency dependence of the coupling efficiency η. As there is no dependence of the radius this parameter is suppressed. Different colors correspond to the three applied amplitudes. Low amplitudes yield large error bars because of correlations with shaping and scaling parameters of the model. It is safe to assume the cutoff frequency below 50 Hz and therefore extremely low. Efficiency values larger than one can either be caused by the fitting algorithm, wrong estimation of the input voltage or complicated interactions between the control loop and the inner electrode potential that is capacitively coupled to the rippled vessel voltage.

The illustration gives the data corresponding to different amplitudes in different colors. Although there is no significant discrepancy between data with different amplitudes, measurements with only $A = 500\,\mathrm{V}$ lead to large error bars. This is explained by the fact that the amplitude is of the same order of magnitude as the energy resolution of the source and therefore causing large correlations between these two parameters. Furthermore measurements at large frequencies lead to values of η larger than one. In principle this can have several reasons. For one this could be an artifact from the fit. To exclude this, the starting values, stepping sizes and limits of all parameters have been varied all leading to the same optimum. Secondly the ripple probe that is used to measure the AC component of the high voltage consists of a 400 nF capacitance and a $50\,\Omega$ resistor. The probe gets read out with a high impedance amplifier so that it will have a small cutoff but neither its frequency response nor the amplifier's characteristics have been experimentally validated, so that they in fact can yield systematics. The third and most improbable option is given by the interaction between control loop of the inner electrode supplies and the post regulation setup. An applied ripple has two ways of propagating to the inner electrode. It can couple capacitively or can reach the inner electrode through the utilized voltage supplies that have their electrical reference point at the vessel potential (see section 4.2.1). If both options apply and a phase variance between the two waves exists the control loop of the supply will try to compensate. Depending on the exact phase variance this can actually amplify the distortion slightly. Nevertheless, the effect is small and for the moment not of major importance because it is the gradient in the efficiency rather than the absolute value, which by statistical means can be regarded to be at unity, that is of major interest. Additionally the post regulation setup itself introduces a systematic effect at low frequencies, see fig. 6.18. Being a prototype, the setup distorts the sinusoidal wave at low frequencies. The total amplitude is much smaller than the externally applied $V_{\mathrm{pp}} = 3\,\mathrm{V}$. More importantly, the wave is no longer sinusoidal, as an asymmetry between positive and negative flanks is introduced. The figure also shows the best fit of a sine-wave to the function. In the course of this an offset has been introduced. This offset reflects the asymmetric behavior of the function around zero, because all points have been weighted with the same factors in calculating the χ^2 value. Apart from this the peak-to-peak value of real wave and idealized sinusoidal are in agreement. Both functions differ greatly on the falling side, where the measured waveform is descending faster above zero and has a less steep gradient on the negative side. As already mentioned this is one of the reasons justifying the usage of a skewed Gaussian function to describe the distorted transmission function. With the wave being less symmetric in form for smaller frequencies the shaping parameter increases, leading to correlations and large errors during the fit. The important outcome is that all frequencies to couple unattenuated into the fields. To quantify this, eq. (6.43) together with an additional offset-parameter to compensate for the systematic shift to coupling efficiencies, has been fitted to the data. Respecting different systematic uncertainties that different amplitudes yield, this has been done for all three amplitudes separately. The final result then is

$$f_{\mathrm{cut}} = \begin{cases} 20.2\,\mathrm{Hz} & , V_{\mathrm{pp}=1\,\mathrm{V}} \\ 49.6\,\mathrm{Hz} & , V_{\mathrm{pp}=2\,\mathrm{V}} \\ 32.5\,\mathrm{Hz} & , V_{\mathrm{pp}=3\,\mathrm{V}}. \end{cases} \tag{6.45}$$

As described above the deviation at low frequencies only leads to an underestimation of

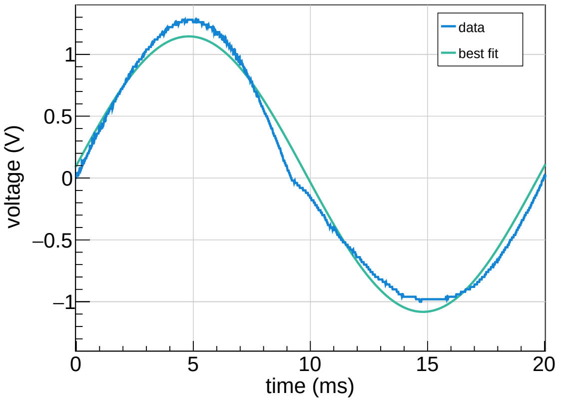

Figure 6.18: With an external wave of $V_{\mathrm{pp}} = 3\,\mathrm{V}$ the post regulation produces a much smaller output. The waveform differs greatly from a sinusoidal one and can no longer be regarded as such. Especially the shape is not symmetric anymore and prefers the positive flank. The fitted sine-wave (green) approximates the curve only but yields correct peak-to-peak values.

the amplitudes. Therefore these values are rather upper boundaries than exact parameters. Now that the connection between ripples of the vessel potential and their influence on the electric field is fully understood, one is able to compensate for any arbitrary noise of the potential during neutrino mass analysis. Thereby this result contributes greatly to the experiment's sensitivity. Furthermore the necessity of the post regulation setup has been proven. Without an active way of smoothening the vessel potential, the inner electric fields will unavoidably undergo disturbances by external electrical distortions that couple into the retarding potential, especially even the best high voltage supply can not avoid this effect.

To consolidate this result, consider the measured ripple without active post regulation, fig. 6.4. Stated already, with the full understanding of sinusoidal distortions, arbitrary waveforms can be implemented by switching to Fourier space. Transforming the measured ripple yields fig. 6.19. Above 100 Hz no major contributions are given, therefore the spectrum is truncated at this value. One peak is located at 50 Hz with an amplitude of $A_{50} = 0.61\mathrm{V}_{\mathrm{pp}}$. At the low frequency side at least two peaks are visible. For reasons of simplicity they get regarded as only one peak and the amplitudes belonging to them are summed. On the right hand side of the figure the measured transmission function that corresponds to this ripple is shown. The green line represents a model with two sinusoidal distortions, fixed at the previously mentioned values, whereas mean, scale and shaping parameters have been fitted. The corresponding chi square is $\chi^2/NDF = 29/23$, indicating a good agreement between model and data. Hereby the fitted function is visibly

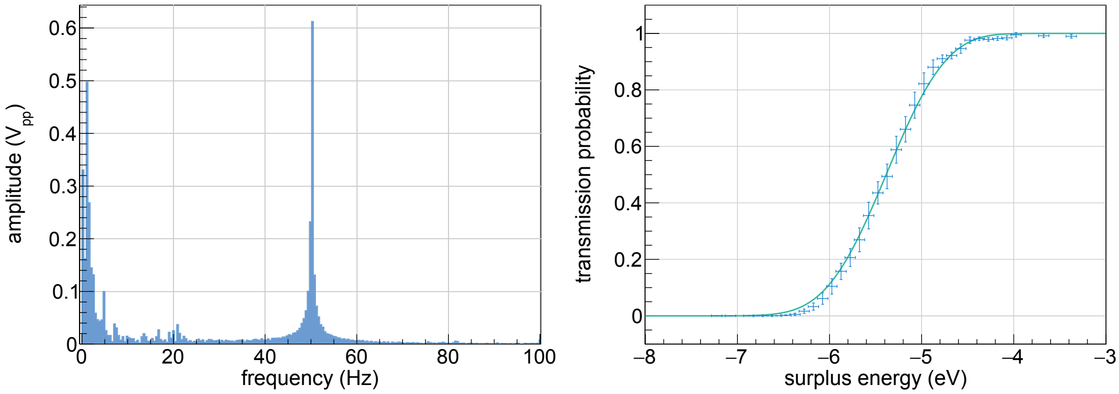

(a) Energy-time distribution **(b)** Rates

Figure 6.19: (a) Fourier transformation of the ripple without active post regulation. One peak is located at 50 Hz with the peak to peak amplitude $A_{50} = 0.61\,\mathrm{V}_{\mathrm{pp}}$. At least two more peaks are visible at low frequencies, for reasons of simplicity they get summed up and regarded as only one peak with $A_1 = 0.83\,\mathrm{V}_{\mathrm{pp}}$. Frequencies above 100 Hz have practically no impact and have been truncated. (b) Transmission function measurement with no active smoothening. The green line represents a model with two sinusoidal distortions, given by the previously gained amplitudes, whereas mean value, scale and shape have been fitted. With $\chi^2/NDF = 29/23$ the model is in good agreement with the data. The deviations at the boundaries are a result of overestimating the low frequency amplitudes by adding them.

broader than the measurement, a circumstance originating from the simple summation of amplitudes for low frequencies. This assumes the different waves to be in phase, which of course can not be fulfilled for sine-waves of different frequencies. Adding those then has to be regarded as upper limit for their influence. The whole reason to simplify the spectrum with summing different peaks is due to the computing time that is rapidly increasing with more sine-waves, as each of them adds one dimension to the integral to be solved. While this worsens the gained χ^2 value it underlines the power of the proposed way of treating high voltage systematics. Instead of having to know the exact shape of the transmission function, where for arbitrary waveforms high dimensional integrals have to be solved, the presented results allow to simply subtract an easy to calculate number during neutrino mass analysis. Combining the results from section 2.2.2 and the current section, the global shift of neutrino mass is easily computed with

$$\varDelta m_{\overline{\nu}_e}^2 = -\sum_{i=1}^{n} \frac{A_i^2}{2}. \tag{6.46}$$

Recall that the shift in neutrino mass for systematic effects associated with voltage fluctuations for any given distortion is $\varDelta m_{\overline{\nu}_e}^2 = -2\sigma^2$. Because for a single sine-wave the variance of the corresponding probability density function is given as $A^2/2$ and further sine-type distortions add quadratically to the variance the above result is straightforward. Here the number of summands n is given by the quantity of frequencies that contribute significantly in the Fourier spectrum. All presented equations have been independent of the frequency. Sufficient information about arbitrarily shaped distortions can be gained by utilization of the ripple probe. Nevertheless it is useful to have a way of verifying the measured ripples. The inter-arrival time spectrum offers a way in doing so, see fig. 6.20. The histogram is filled with data from a distorted transmission function, where $A = 1.5\,\mathrm{V}$

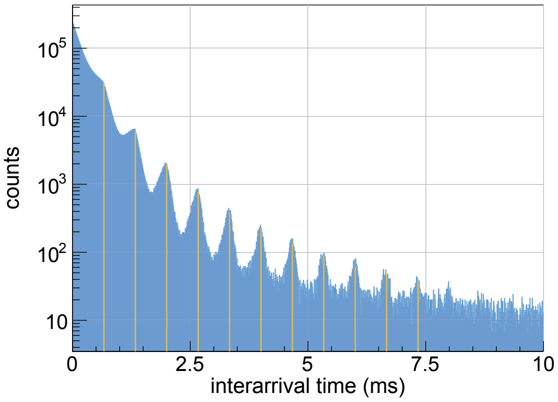

Figure 6.20: The inter-arrival times of electrons during a measurement with $A = 1.5\,\mathrm{V}$ and $f = 1500\,\mathrm{Hz}$. With local maxima located at multiples of the period length $\tau = 0.67\,\mathrm{ms}$ (yellow) the shape differs greatly from the one expected in the case of a rate that is solely Poisson distributed in time. The peaks arise from the filter oscillating between the two boundaries, letting larger or smaller numbers of electrons pass during the process.

and $f = 1500\,\mathrm{Hz}$. To understand the periodically distributed local maxima consider a Poisson distributed statistical population in energy space and the transmission function to be perfectly sharp with its step located at the expectation value of the energy. If the filter barrier then oscillates between two extremal values the proportion of electrons emitted will likewise fluctuate. Therefore the inter-arrival spectrum has peaks at the times that are associated with the period length of the wave. Without any fitting the yellow lines in the figure have been inserted as multiples of the period length $\tau = 0.67\,\mathrm{ms}$. They are in agreement and prove the above argumentation to be correct. Especially this is not limited by the Nyquist theorem as it is a statistical process, even if the ripple is periodic in time. Here an easy diagnostic tool is given. In estimating the background the time-interval spectrum will be investigated for all runs and hence, distortions can be searched for during standard analysis. This concludes the measurement and characterization of systematics induced by fluctuations of the voltage. Conclusively the post regulation has been shown to be necessary, and to smoothen distortions below the desired design value. Furthermore any remaining systematic effect caused by ripples can be corrected for, by the above means.

6.4 Ripple dependent background

As discussed during the chapter introducing the principles of MAC-E filter, several mechanisms that cause background are known from previous experiments. With this knowledge the KATRIN experiment has been designed to suppress these known sources. By means of a sophisticated electromagnetic design, Penning traps have been avoided entirely inside of the main-spectrometer. Especially the radioactive decay of certain radon isotopes has shown to be suppressed greatly with the installed baffles ([Goe14], [Har15]). Nevertheless, the KATRIN experiment cannot be regarded as a simple up-scaling of its predecessors. This has shown itself within the second measurement phase, where two new mechanisms in producing background have been discovered. One of these is due to the decay of ^{210}Pb. During the mounting period to install the inner electrode daughter nuclei of the ,naturally always present, ^{222}Rn have been adsorbed onto the inner surfaces of the spectrometer. Their decay chain ultimately leads to the implantation of the active lead isotope ([Har15]). The second background-source is due to neutral particles, entering the fiducial volume in excited states ([Dre15a]). Easily to apprehend, these particles will be most harmful, as there is no obvious measure to counter the induced background. Rydberg molecules have been proposed as such particles in [Dre15b]. These molecules provide a model that is in agreement with the remaining background, that is otherwise cannot be explained otherwise. Many production mechanisms for these molecules are possible, for further reading see [Har15]. For the scope of the investigations following only a few of the characteristics may be mentioned. Electrons with energies greater than 20 eV can interact with H_2 molecules, leading to the emission of a Rydberg state H^*,

$$H_2 + e^- \to H + H^* + e^-, \tag{6.47}$$

see [Jan03], [Sch75] and [Sch79]. As the number of electrons expected with these energies is very small this mechanism seems to be not very likely. According to the newest findings it is much more likely for the production mechanisms to be connected to the radioactive decay of lead. After the emission of an α-particle the daughter-nucleus will be in an excited state and can cause the emission of Rydberg states. However the Rydberg atom might be produced, an external field is needed in order to ionize it. With the electric fields that are present inside the spectrometer Rydberg atoms can be ionized. As a certain field strength is necessary for this process to take place, this can happen at both ends of the spectrometer and between vessel and inner electrode. The background has been known to depend on the potential difference between hull and electrode. In agreement with the Rydberg-model the background decreases with higher field strengths. Rydberg atoms emanated from surfaces are expected to get ionized by these higher fields between spectrometer and inner electrode, before they can enter the flux-tube. The Rydberg atoms that are already in the fiducial volume will then only decay due to interaction with black body radiation inside the vessel. As important parameters of the model, mean free path and velocity of the particles can be estimated by investigating the time dependent radial distribution of the background. Because the total rate of decays can only by as large as the measured background rate the process of hindering Rydberg particles to enter the flux tube has to be conducted many times in order to gain adequate statistics. This has been realized experimentally by an arbitrary waveform generator with an amplifier that were connected to the inner electrode. As the amplifier has a rather small cutoff frequency, the time period has been chosen to be 5 ms. Better comparability with non-pulsed measurements was achieved by setting the global inner electrode potential to $-75\,\mathrm{V}$ in relation to the vessel potential, while the time periodic electrical stroke has been chosen to be $-25\,\mathrm{V}$. Resulting in two plateaus with effectively $-50\,\mathrm{V}$ and -100 V inner electrode offset, values that are common during all background investigations. A first check of consistency of these measurements is given in fig. 6.21(a). Presented is a scatter plot of the energy incoming events have and their relative time in respect to the last trigger signal, that defined as rising edge of the pulse. During this and all following analyses the time window of one wave-period has been segmented into 0.1 ms bins. Right now this seems like a somewhat arbitrary definition but actually grounds on the statistics needed for reasonable radial-dependent analysis. The only visible energy contributing significantly is the band between 25.6 keV and 30.6 keV. With the post acceleration at a potential of 10 kV that is the expected region of interest. In consistency with the expectations for the energy, the data show a maximum between 3 and 4 ms. The right-hand side of the figure quantifies this feature. Here the rates are drawn in addition to the pulsed voltage signal for better comparability. Originally fed with a square wave signal the amplifier's output differs from this ideal form. It has linear flanks that overshoot at the maximal values to settle only slowly. This is caused by a small cuttoff frequency. Nevertheless, this only restricts the intervals whereas the signal can be regarded as stable. The boundaries of these plateaus are marked by black vertical lines. From previous measurements the rate is known to be smaller for higher offsets of the inner electrode potential. However, the blue lines indicate fits with $R_{-50} = 523\,(8)$ mcps and $R_{-100} = 519\,(9)$ mcps, that are statistically not distinguishable. In contrast to measurements with static potentials, this behavior is unsuspected. An interpretation shall be postponed until the end of the section, first consider the dynamic features of the data. Negative field gradients produce an increase in rate on all rings, while positive voltage-flanks do not provide this characteristic. Evidently the effect increases

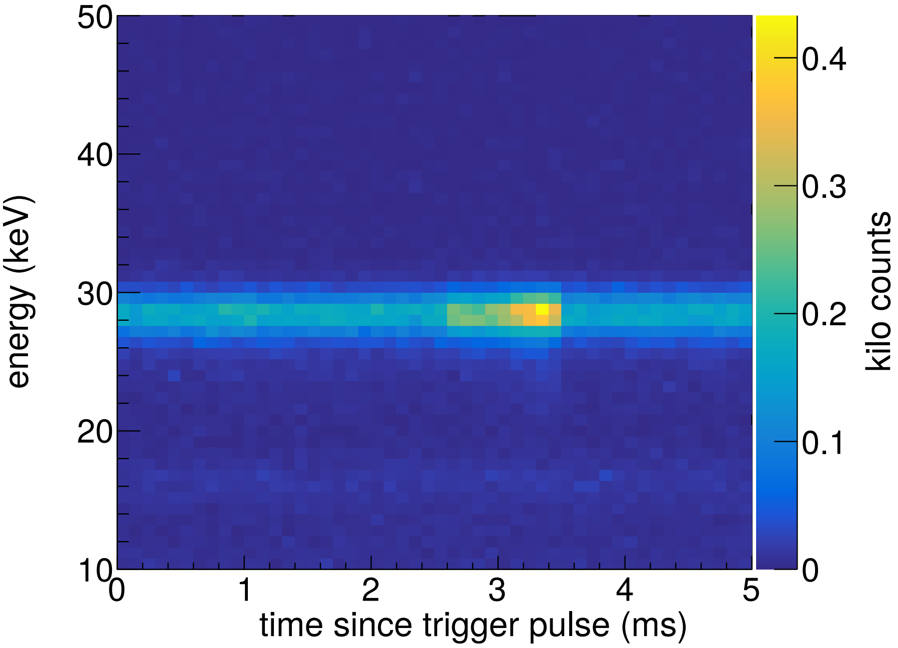

(a) Energy-time distribution

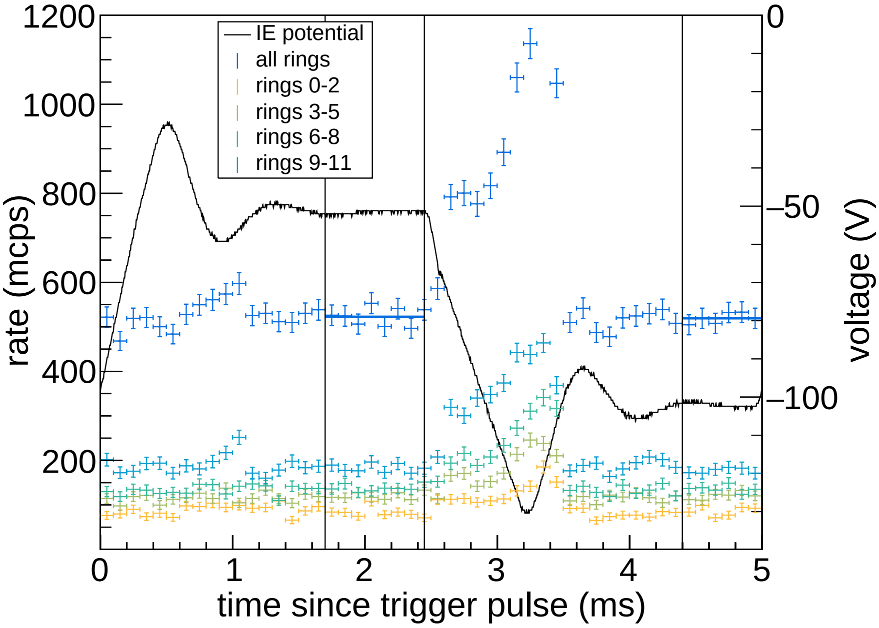

(b) Rates

Figure 6.21: (a) The energy-time distribution of the summed events. This figure mainly is a check of consistency and search for unexpected effects. With the spectrometer at 18.6 kV and with the post-acceleration at 10 kV, the region of interest is the interval [25.6,30.6] kV. For all times this is actually the only energy interval with a significant amount of events. A maximum is observable between 3 and 4 ms. To further illustrate the time dependency the rates of all rings and their summed rate between to pulses are drawn in (b). Because of the used amplifier has a rather low frequency, the voltage waveform differs from the ideal step-function. The two intervals, where the voltage has stable plateaus at −50 V and −100 V, the rates have been fitted to be $R_{-50} = 523\,(8)$ mcps and $R_{-100} = 519\,(9)$ mcps. Therefore no significant discrepancy between them can be found. The maximum from the energy spectrum is clearly visible, its size being different for the rings. Note that this is not normalized to volume.

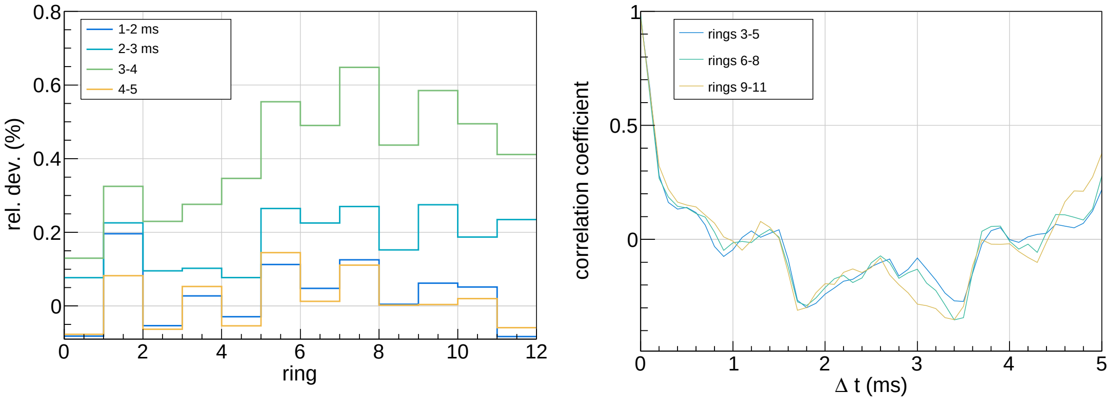

(a) Normalized rates **(b)** Covariances

Figure 6.22: (a) Further clarification of the radial dependency. As different radii correspond to different volumes the rates have to be normalized. In this picture the difference between the rate on each ring at the time of the trigger pulse and the rate at later times has been normalized to the original rate. The signals start at low values and increase with time until they reach their maximum between 3 and 4 ms after the trigger. After reaching the maximum the rates drop to the initial value. The effect caused by the negative field gradient increases with the ring number and therefore the radius. (b) Here the covariance between the most inner rings and the more outer ones has been calculated for different shifts in time. This enables the search for a Rydberg states average ionization time and velocity. However, the covariance is maximal for the time shift to be zero, so that within the time-resolution the effect has to be regarded as simultaneously on all rings.

with larger radii, however the presented rates are not yet normalized to the volume and therefore not representative. A scaled depiction is given in fig. 6.22. As the investigations for dependencies in time and radius are of interest, a different representation has been chosen here. The abscissa is given by the ring number, where the ordinate is not the rate normalized by the volume, but rather the difference between the rate of each ring for $t \in [0,1]\,ms$ and the rate at later times after the trigger pulse divided by its initial value again in the first time-bin. This representation has been chosen, because it elegantly avoids numerical and systematic failures due to the computation of the volume, while it still provides the necessary comparability between rings. In agreement with fig. 6.21, the incoming rate takes its minimal value directly after and directly before the trigger pulse. It is maximal in the time window between 3 and 4 ms. Furthermore there is a radial dependency, as the relative change increases with the ring number, i.e. the radius. In the next step the originally goal of searching for a time shift between the rates on individual rings, which would correspond to the statistical decay of Rydberg state particles that move from the surface to the inner part of the spectrometer. A suitable way in doing so, is to calculate the covariances of the inner ring as reference and the rings with larger radii, see fig. 6.22(b). Here the rings have been bunched for better statistics and the covariances for time shifts up to the period of the pulser signal have been calculated. Reaching the values closest to unity, all rings have to be regarded as reacting simultaneously. That is of course within the timing resolution of 1 ms.

Summarized one new feature has been found and one expected behavior is not prominent. Actually this is not in contrast to the Rydberg model, but underlines the theory and the need for more investigations concerning this sophisticated background source. Firstly, the dynamic response of the background to negative field gradients can have its origin in complicated electric charging processes. Different segments of the inner electrode have non identical capacitances and therefore also individual time constants. Shown in [Hil16] this can cause electrons to reach from the vessel surface into the flux-tube. Further, Rydberg particles in alternating electromagnetic fields near metallic surfaces are known to change their number of enclosed orbits with active oscillating field in dependence of their distance to the surface ([Wan08b], [Wan08a]). This hints into the right direction but the exact situation at the KATRIN experiment is slightly different. As this an own research field, a detailed elaboration is well beyond the scope of this thesis, but elucidates the need of further data taking and modeling. Secondly, the fact that the rates are the same for both potentials, whereas they actually differ for static measurements, can be explained by several mechanisms. Of course the above argument also applies to this situation. For certain field and geometrical configurations many orbits of the Rydberg particles will be caused to be not closed anymore and consequently to decay before they reach the fiducial volume. However this argument needs many preconditions. With the results of the previous section a much easier and direct answer is given. Every distortion in the vessels potential couples electrical undamped into the inner electrode potential. Even if the present case reverses this process it is still likely to hold. The coupling will only be damped because in the case of the previous section it does not only happen capacitively but also through shifting the base potential of the inner electrode supplies. The latter effect will be reduced for the reversed direction but will still be manifest. From this it directly follows that AC-fluctuations, i.e. electrical pulses, can maximally lead to a phase shift between the voltages of vessel and electrode and therefore no large potential differences can be realized between them with AC-applications. In conclusion the measurements at hand do not reject the Rydberg hypothesis but rather strengthen the picture of a background source that is new to MAC-E filters and needs careful modeling and detailed investigations.

CHAPTER 7

Response function

To achieve a ν-mass sensitivity of $200\,\mathrm{meV}$ at $90\,\%$ C.L. the KATRIN experiment requires systematic uncertainties to be known to an extraordinary high degree. Until now, the effects studied include the variation of the energy of electrons emitted by the source or fluctuations of the analyzing potential of the filter. The former gives a quantitative insight to the systematic shift that estimates of the neutrino mass will undergo due to distortions. Detailed investigations of a theoretical model to describe the influence of fluctuations and their experimental verification have been conducted throughout this thesis. To ultimately complete the course of energy scale systematics, i.e. of voltage fluctuations and their measurement, the impact of the developed models on the neutrino mass analysis is discussed in this chapter. The transmission function is an idealized representation of more complex experimental conditions. For example, the transmission function neglects source effects and a series of other systematics, for neutrino mass analysis it has to be expanded. The resulting function is called response function and has been described in great detail in [Gro15b]. For the scope of this work it is sufficient to only heuristically motivate its shape shortly. For further reading the reader may be referred to the cited thesis from which the basic information is summarized.

7.1 The response function

Formally, the response function $\mathrm{R}(E - qU_{\mathrm{ret}})$ is introduced in exactly the same way as the transmission function

$$\left(\frac{\mathrm{d}^2N}{\mathrm{d}t\,\mathrm{d}E}\right)_{\mathrm{conv}} = \frac{\mathrm{d}^2N}{\mathrm{d}t\,\mathrm{d}E} \otimes \mathrm{R}(E - qU_{\mathrm{ret}}), \tag{7.1}$$

to implement all characteristics of the experimental apparatus. As in the case of the monitor spectrometer, the response function has to be extended to incorporate the finite size of the source and spectrometer. Put in a simpler way, the transmission function is only valid for electrons starting at one specific field line in the source and propagating on the same path through the filter. Due to inhomogeneities of electric and magnetic fields, the response function has to be calculated as the weighted average of transmission functions at different radeii. Additionally, the main spectrometer is not exactly symmetric in azimuthal direction. Therefore the summation is has to be performed not only for different radii, but also for different angles. In case of the monitor spectrometer, the finite summation is chosen with a somewhat arbitrary number of terms, in the case of the main spectrometer the segmentation of the detector gives a more natural discretization. Electrons that are emitted inside the tritium source can scatter off tritium molecules, thereby losing a certain amount of energy ε in the process. According to

$$\mathrm{R}(E - qU_{\mathrm{ret}}) = \int\limits_{0}^{E-qU_{\mathrm{ret}}} \sum_{i=0}^{N} \mathrm{T}(E - \varepsilon - qU_{\mathrm{ret}})\, P_i\, f_i(\varepsilon)\, \mathrm{d}\varepsilon, \tag{7.2}$$

each scattering process will change the shape of the response function. Here the parameters P_i are the scattering probabilities and $f_i(\varepsilon)$ the corresponding energy loss functions. The summation is taken up to N subsequent scatterings. Both, source density and cross sections are needed to determine the response function and also a meaningful number of implemented scatterings. These can be calculated by analytical or Monte Carlo (MC) methods, see [Gro15b]. As the response function is already implemented into the global analysis and simulation framework KASPER of the KATRIN experiment, these calculations are not discussed here. It is well known that charged particles lose energy due to synchrotron radiation due to their propagation on cyclotron paths along magnetic field lines.

All effects result in a response function that is shown in fig. 7.1, where nominal field settings with $\mathrm{B}_{\mathrm{source}} = 3.6\,\mathrm{T}$ and $\mathrm{B}_{\mathrm{ana}} = 3\,\mathrm{G}$ have been used. The first part of the function on the interval $[0, 0.93]$ eV is dominated by the radially and angular weighted transmission function. A characteristic plateau for surplus energies of a few eV is a consequence of electrons that leave the source without any scattering, because the process takes at least 10 eV. The following increase of transmission probability is caused by single, twofold and eventually n-fold scattering. The probability for these processes significantly decreases with increasing number of interactions. Therefore, the effect on the response function also decreases with this number. From a mathematical point of view this function is no longer

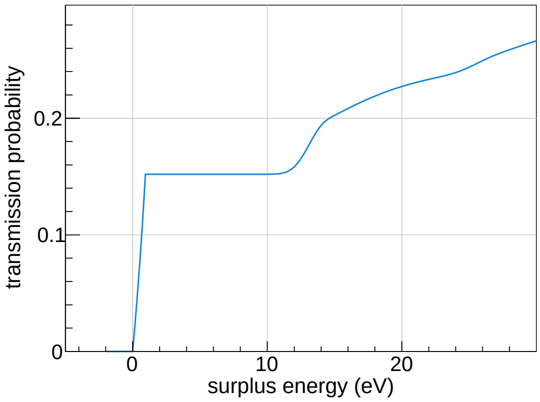

Figure 7.1: Response function as outputted by the KASPER framework for nominal magnetic fields, $\mathrm{B}_{\mathrm{source}} = 3.6\,\mathrm{T}$, $\mathrm{B}_{\mathrm{ana}} = 3\,\mathrm{G}$. The transmission function

a CDF, as it is not normalized to unity. This scaling constant has no deeper physical meaning.

7.2 Energy scale distortions of the response function

The influence of high voltage distortions on the response function is investigated by the same method that is used to implement the feature into the transmission function. Therefore it is sufficient to calculate

$$\mathfrak{R}(E - qU_{ret}) = \int\limits_{-\infty}^{\infty} \mathrm{R}(E - q\tilde{U}_{\mathrm{ret}}(\xi))f(\xi)d\xi, \tag{7.3}$$

or for numerical reasons in the case of sinusoidal ripples

$$\mathfrak{R}(E - qU_{ret}) = \frac{1}{2\pi}\int\limits_{-\pi}^{\pi} \mathrm{R}(E - qU_{\mathrm{ret}} + A\sin(\xi))d\xi. \tag{7.4}$$

Combining the response function and ripples then yields fig. 7.2. For better visibility, the amplitudes of ten rippled functions are incrementally increased starting from 0.1 V to 1.0 V. As expected, the largest effect is caused in the region of small surplus energies, where the transmission function dominates the response function. Here the effect is practically the same as in the ideal transmission function. For the region of single and twofold scattering the influence is suppressed. However, the effect is the same as in the case of the distorted transmission function. Interestingly, electrons with negative surplus energies now have non-vanishing transmission probabilities. Equivalently, the end point of the measured tritium spectrum is shifted to larger energies, causing the estimated neutrino mass to systematically shift to smaller values. Detailed investigations with MCMC methods have shown that the effect scales in fact with $\Delta m_{\bar{\nu}_e} = -2\sigma^2$ in case that the fitting algorithm does not detect active ripples, i.e. the χ^2 value remains unchanged [Kle14].

In conclusion, one can state that the hardware reduces the size of ripples to a very small minimum enabling a high-precision ν-mass measurement. It can thus be expected that the HV-ripple-induced systematic uncertainties will be of no concern for the final ν-mass analysis.

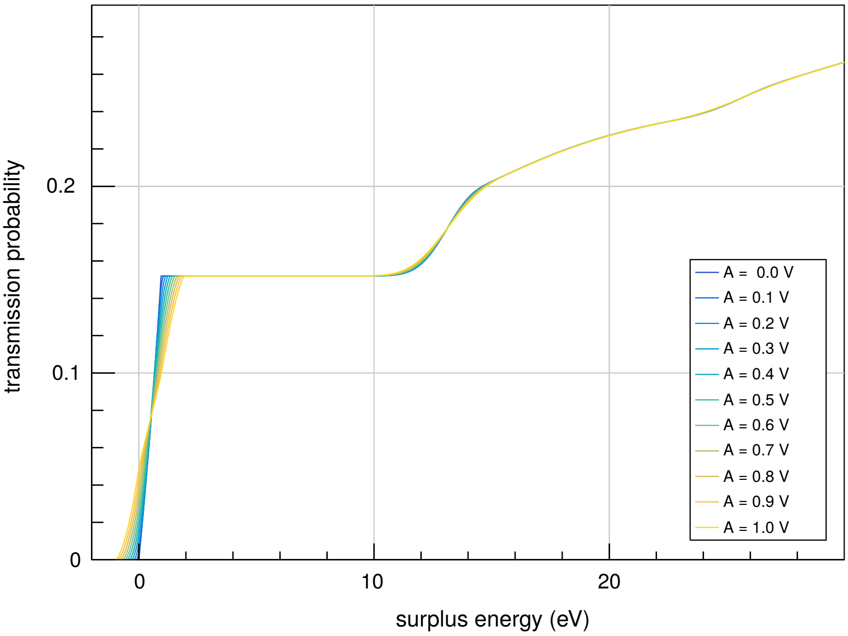

(a) Distorted response functions

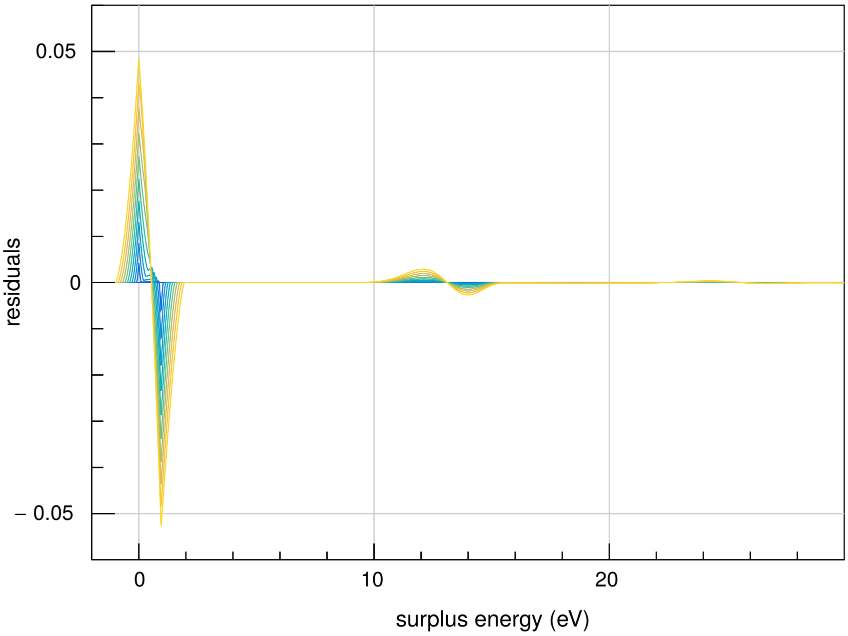

(b) Residuals of the distorted response function

Figure 7.2: (a) Distorted response functions. Sinusoidal fluctuations with different amplitudes A have been implemented. A total of eleven functions are drawn, out of them ten are distorted with amplitudes incrementally reaching from 0.1 V to 1.0 V. (b) Residuals between the undistorted and rippled functions, to amplify the effect. The functions behave as expected, the ripple yields the greatest influence for low surplus energies, where the transmission function plays the most important role.

CHAPTER 8

Conclusion and outlook

The thesis in hand describes work carried out to generate, stabilize and monitor retarding potentials for the KATRIN main and monitor spectrometers at ultra-high precision. In particular, the influence of remaining ripples at the analyzing potential was characterized in detail. The results obtained play a crucial role in determining the absolute mass scale of electron antineutrinos with the targeted ν-mass sensitivity of 200 meV   90% (C.L.).

The observation of neutrino oscillations has yielded irrefutable evidence for non-vanishing neutrino masses, however the absolute mass scale of neutrinos cannot be accessed by these studies. Hence, a variety of experimental techniques is being developed and refined to determine the absolute mass of neutrinos. The leading experimental approach and most mature technology is based on high-resolution spectroscopy of tritium β-decay spectrum close to the β-decay endpoint of molecular tritium (18.6 keV). The next-generation experiment KATRIN combines a large electrostatic retarding spectrometer with an ultra-luminous windowless gaseous tritium source. In doing so, the KATRIN experiment will improve the current neutrino mass sensitivity by one order of magnitude to 200 meV (90%C.L.) after five years of measurement time. To reach this goal, the retarding potential has to be maintained and monitored at an ultra-stable level over this extended period of time.

During 2013, a 4-months-long data taking period was successfully concluded during which the KATRIN main spectrometer was elevated for the first time onto high voltage. The measurements revealed the basic functionality of the complex high voltage system. This includes the implementation of a robust safety and control system. The results obtained were then used to further improve the high voltage setup. The upgraded system features automated calibrations of the voltmeters and, most importantly, a post-regulation setup for active smoothening of the high voltage at 18.6 kV.

In the second commissioning phase in 2014/2015, the refined HV system was subject to detailed investigations. Of particular interest was the elevation of the short and long term stability of the retarding potential with active smoothening by the post-regulation setup. This included DC as well as AC stability and an in-depth study of the influence of remaining ripples on the analyzing potential. The observed fluctuations on the 10 mV level highlight that the high voltage system operates at stability levels which are better than the design values. In addition, the commissioning measurements of the second data-taking phase SDS-II allowed to fine tune the high voltage system to requirements, in particular with respect to transmission properties and background characteristics.

Generation and stabilization of the retarding potential

As the main spectrometer vessel acts as antenna for electromagnetic distortions, it is not sufficient to utilize voltage power supplies with a stable output. Therefore, the employed post-regulation setup allows to actively smoothen the high voltage. Measurements with inactive post-regulation have revealed a ripple with a standard deviation of $\sigma = 308\,\mathrm{mV}$. The active post-regulation setup suppresses this ripple to the size of $\sigma = 16\,\mathrm{mV}$ only. Compared to the design value of $\sigma = 60\,\mathrm{meV}$, the systematic uncertainties of HV fluctuations are reduced by more than a factor of three. The DC stability that is reached with the post-regulation system corresponds to an uncertainty of 16 mV. This yields a total uncertainty budget of $\sigma_{\mathrm{total}} = 23\,\mathrm{mV}$, so that the global uncertainty caused by the high voltage system is better than the design value by a factor of ≈ 3. In addition, the settling time of the post-regulation setup after a new set value was entered has been reduced to only $320\,\mu\mathrm{s}$. As voltage power supplies usually have settling times of $\approx 10 - 40\,\mathrm{s}$, the tritium scanning possibilities with the large main spectrometer are significantly improved by utilizing the post-regulation.

Monitoring of the retarding potential

The monitoring chain of the HV system consists of the two high-precision custom-made voltage dividers (K35, K65) and the separate monitor spectrometer (MoS) beam line. The KATRIN voltage dividers allow precise measurement of the retarding potential (18.6 kV) with state-of-the-art digital voltmeters that are calibrated in fully automated mode. By measuring conversion electron lines of the ^{83m}Kr decay, the MoS allows long-term monitoring and calibration of the analyzing potential, in particular via the K-32 line position of the krypton decay which acts as a 'constant of nature'. The combined devices have a stability of $(7.3 \pm 1.9)\,\mathrm{mV/60days}$ in the case of the K35 voltage divider, and of $-(14.9 \pm 2.3)\,\mathrm{mV/60days}$ in the case of the K65 voltage divider. Here, 60 days of data taking correspond to a standard KATRIN measuring cycle. The monitoring system of the KATRIN experiment allows voltage measurement with highest (world-leading) precision.

Influence of distortions on the transmission properties

During the SDS-II measurement phase, an angular selective electron gun allowed the detailed study of transmission characteristics of the main spectrometer. A new technique was developed by applying distortions of known amplitude and frequency to study their influence on transmission properties. Due to rather strong capacitive coupling of the inner electrode and the main spectrometer vessel, each external distortion will couple into the analyzing potential with efficiency $\eta = 1$. To counteract the resulting systematic uncertainties, the of influence distortions on the neutrino mass analysis was modeled and implemented into the KATRIN analysis framework. As the effect of remaining ripples now can reliably be predicted and precisely be modeled, their associated systematic uncertainties can be accounted for during the top level ν-mass analysis.

Summary and outlook

In the scope of this thesis, major contributions were made to the commissioning and refinement of the high voltage system of KATRIN to characterize its systematic uncertainties. The high voltage system performs at stabilities that result in overall systematic uncertainties of only $\sigma = 23\,\mathrm{mV}$. This small value improves the design requirements by a factor of three. The monitoring of the retarding potential by combining high-precision voltage dividers with an ^{83m}Kr-source as nuclear standard yields long-term stabilities that are better than 1 ppm/60days. Remaining fluctuations of the high voltage can be measured and counteracted, as their influence has been fully characterized. In conclusion, it can be stated that the current HV setup exceeds the already very stringent KATRIN design specifications. The remaining systematic uncertainties can be evaluated and taken into account of by the implemented HV systematics as part of the final ν-mass analysis.

Future steps will focus on integrating the source section into the existing HV system, an upgrade of the post-regulation setup based on a new auxiliary voltage divider and finally the installation of smoothing capacitors. Once these refinements are implemented, long-term data taking with the unique KATRIN setup can proceed with minimized systematics from high-precision tritium scanning at the β-decay endpoint to unravel the remaining mysteries of neutrinos and their rest mass.

APPENDIX A

Differential transmission function and numerical differentiation

Given that energy resolution is proportional to retarding potential, the differential transmission function can almost directly be translated into an energy distribution for a given source, like the electron gun. Apart from this, the differential transmission function lacks physical meaning. However, the adapted model shown above has features that become more evident in the differential form and it is worth investigating them solely for reasons of data analysis. Sharp edges and peaks usually provide faster convergence during fitting as their line shape reacts sensitively on parameter variations. The same method used to highlight the behavior of the integral spectrum in respect to variable parameter settings can be applied to the differential case (fig. A.1).

In direct comparison much sharper features are provided. Characteristics that are prominent globally in the integral form become clearly distinct in the differential transmission function. Not only manifested as sharpness, but also by a much richer structure and especially asymmetrical overlaps, the expected correlation between the four different parameters is much smaller. Most importantly the functions scaling is improved by a factor of three for the ripple amplitude. As suggested by the spectrum itself, all changes concentrate around the two local maxima but are easily separable for their clearly distinguishable influence on the line shape. For these reasons the differential form is of interest and numerical differentiation methods become necessary.

One such method is given by the common three-point differentiation rule. For a data set $\{\mathrm{T}(\mathit{\Delta} E)\}_i$ distributed on a non uniform grid $\{\mathit{\Delta} E\}_i$ together with the associated Lagrangian polynomial becomes

$$\mathrm{T}'(\mathit{\Delta} E_i) = \gamma_{i-1}\mathrm{T}(\mathit{\Delta} E_{i-1}) + \gamma_i \mathrm{T}(\mathit{\Delta} E_i) + \gamma_{i+1}\mathrm{T}(\mathit{\Delta} E_{i+1}), \tag{A.1}$$

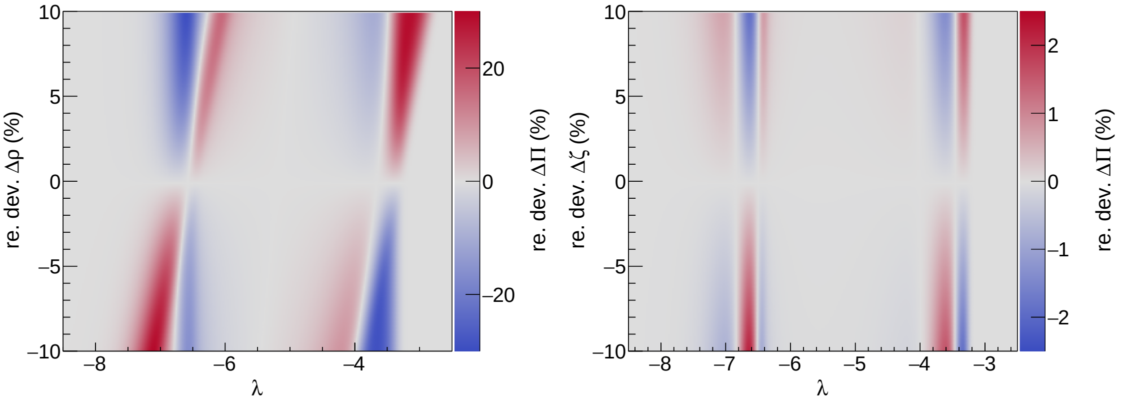

(a) Impact of ρ **(b)** Impact of ζ

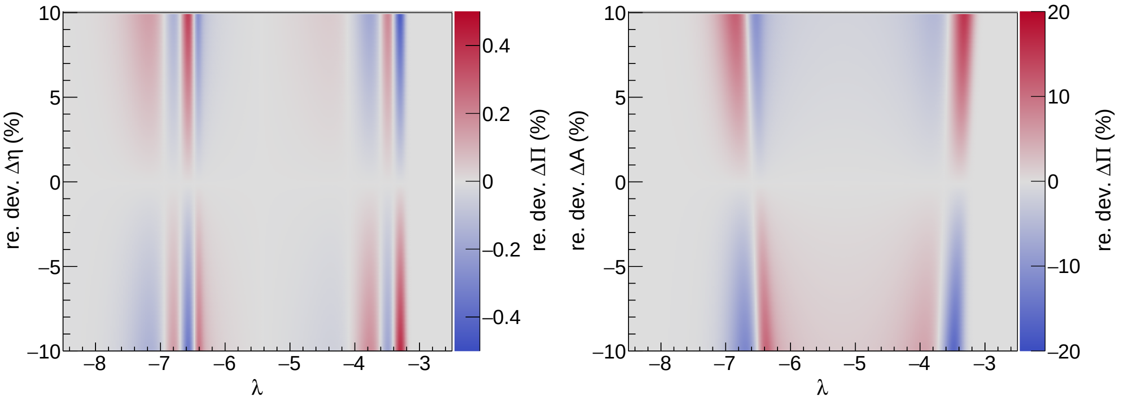

(c) Impact of η **(d)** Impaft of A

Figure A.1: With the same method like in the integral case the figure illustrates the impact of the parameters on the differential transmission function. All parameters now lead to much sharper defined deviations. Previously symmetric, the mean value now causes asymmetric changes. Shape and scale are richer in structure and decouple because of small intervals of λ where their deviations are now associated with opposite signs. Especially the amplitudes influence ist amplified by a factor of three, whereas the mimicking effect by interactions of shape and scale is now less pronounced. Fitting functions to the differential model has to be favored in this manner.

where the coefficients γ_i are given by

$$\begin{aligned}
\gamma_{i-1} &= \frac{\mathit{\Delta} E_i - \mathit{\Delta} E_{i+1}}{(\mathit{\Delta} E_{i-1} - \mathit{\Delta} Ei)(\mathit{\Delta} E_{i-1} - \mathit{\Delta} E_{i+1})} \\
\gamma_i &= \frac{2\mathit{\Delta} E_i - \mathit{\Delta} E_{i-1} + \mathit{\Delta} E_{i+1}}{(\mathit{\Delta} E_i - \mathit{\Delta} Ei - 1)(\mathit{\Delta} E_i - \mathit{\Delta} E_{i+1})} \\
\gamma_{i+1} &= \frac{\mathit{\Delta} E_i - \mathit{\Delta} E_{i-1}}{(\mathit{\Delta} E_{i+1} - \mathit{\Delta} Ei - 1)(\mathit{\Delta} E_{i+1} - \mathit{\Delta} E_i)}.
\end{aligned} \tag{A.2}$$

An advantage of this technique is its simplicity, calculating the derivative of a dataset consumes practically no computing time. Being an approximate to the second order the formula will yield well defined results in many cases. Analytically the absolute value function is continuous and therefore differentiable in every point. Datasets consisting only of a finite size limit the accuracy, regions where the function has a large gradient will worsen the results. In the case of the absolute value function this is given at the coordinate systems origin, here the deviation even is discontinuous. If large gradients are expected within a measurement, this can be counteracted by decreasing the interval size between points. Naturally this has its limits, as every measurement device has a certain resolution. Noisy data can wash out important features of a function entirely. Considering the absolute value again, added with a Gaussian variate with $\sigma = 0.1$, the above three-point rule is not sensitive to the sign change in the gradient at all, see fig. A.2. Shown are the noisy function on the left and the estimated derivative on the right (yellow). Well known from numerics the differential ratio is not good conditioned and greatly amplifies noise in the data. Even the small standard derivative applied to the considered points leads to a derivative that neglects every feature of the original function. Not drawn in this figure are the error bars one would usually assign trough propagating errors. Likewise, these would be amplified, leaving a derivative whose points are compatible with values that are more than one order of magnitude away from the real value. Without previous knowledge this differentiation procedure hides literally every feature of the true function, because neither the sign nor the absolute value of the derivative is correct and the entire function even agreeable with constantly being equal to zero. In this picture statistical uncertainties of the

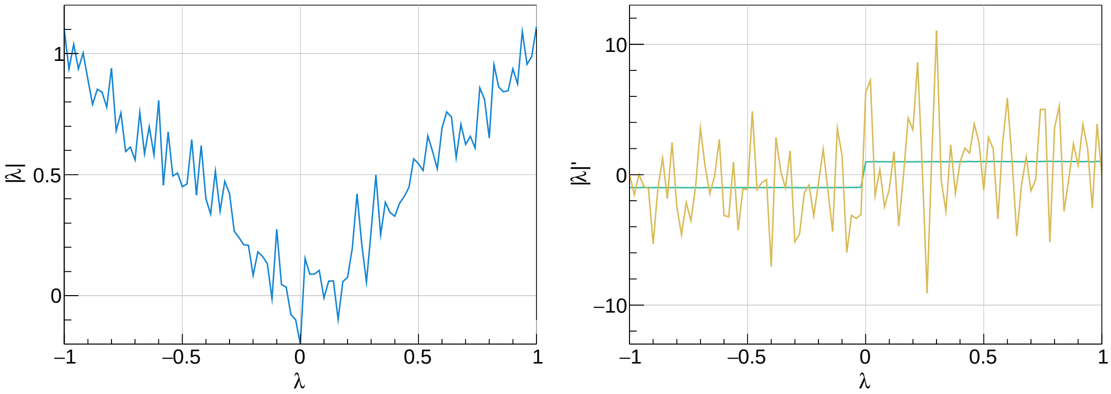

(a) Noisy absolute value function **(b)** Calculated derivatives

Figure A.2: Illustrated in this figure is the effect of noisy data numerically differentiated with the central three point formula. (a) shows the original function, that is the absolute value function with an additional Gaussian distributed noise, where $\sigma = 0.1$. Still, even the noisy data is perceived as the absolute value, even by eye. Numerically differentiating with classical methods yields an unsatisfactorily result (yellow). All important features, i.e. sign, numerical value and the discontinuity at $\lambda = 0$, are washed out entirely and the function is compatible with constantly being equal to zero. This absurd result is in contrast to the one gained from functional methods (green). The fluctuation of this curve is almost zero, whereas the correct numerical values and a sharply defined edge at the right position are provided.

abscissa have not been accounted for, naturally they would also contribute in a negative way. With the transmission function being normalized to take values between zero and one and uncertainties in the energy, for instance caused by the finite energy resolution of the electron gun, in the order of $\sigma = 100\,\mathrm{meV}$ and the intentionally introduced distortions of the filter potential it is not an option to use these conventional methods. However, the figure also provides the derivative that has been gained through a different method, that solves this problem.

The subsequent developments have originally been developed for signal processing, where functions with sharp edges play a crucial role. Adapting them to the task at hand is however possible, the mathematical foundation is published in [Cha11] while the necessary optimization algorithms have been implemented differently into the KATRIN analysis framework. As numerical differentiation is a badly conditioned problem, it is common to solve the inverse problem instead. A way of doing this, established for many years, is minimizing the functional

$$S\left[u\right] = \gamma P\left[u\right] + \delta F\left[Ku - f\right], \tag{A.3}$$

known as the Tikhonov regularization. Here u denotes the derivative, P is a penalty term that disfavors irregularities, K the operator of anti-differentiation and F a data fidelity term. Balancing these terms is achieved with the two parameters γ and δ. For the most common Gaussian noise, the fidelity term can be assumed to be just the L^2 norm and it is reasonable to take the same norm for regularization. By this, the total curvature of the derivative will be minimized, so it is clear how this term suppresses noise. Furthermore the data fidelity term is easily understood to minimize the area between the original curve and the inverse problem. On an interval $[x_0, x]$, this leads to

$$S\left[u(x)\right] = \gamma \int\limits_{x_0}^{x} \left|u'(x)\right| \mathrm{d}x + \delta \int\limits_{x_0}^{x} \left|Ku(x) - f(x)\right|^2 \mathrm{d}(x). \tag{A.4}$$

Deciding how α and γ should be treated is somewhat arbitrary and naturally the point where a weakness of the method becomes obvious. If the regularization term is overweighted actual gradients could be suppressed, if chosen to be too small noise could still be present. A reasonable assumption is to let the regularization parameter itself become a function and taking it to be the reduced χ^2 of the data and the inverse problem. Ideally this parameter then takes a value near unity and it has been empirically found to be a good choice for the other weight to be $\delta = 1/2$.

As this functional needs to be optimized with respect to data and the corresponding derivative every data point will add one degree of freedom. Usual transmission function measurements consist of eighty points, for which the necessary computing time becomes problematic. Even worse, the parameters will be strongly correlated resulting in an arbitrary number of local minima in the parameter-space. A mighty tool for applications is given by Markov chain Monte Carlo algorithms. In the framework of the KATRIN experiments global analysis and simulation package Kasper such a fitting class using MCMC is provided

([Kle14]). Even with this the needed sample sizes are large and consume time. One solution for this is the knowledge of the derivative in the beginning, as good initial start values will significantly decrease the needed efforts. In the most cases this of course will not be possible, with the easy to calculate three-point differentiation shown to be not reliable. However, the transmission function itself provides a strong argument to accelerate the process. It is known to be necessarily zero at small energies and a monotonic function of the energy. Therefore the utilized algorithm begins at the low energy side neglecting all but two points to estimate the derivative of the third. After this the process loops, successively adding one point at a time while fixing all points that have already been treated in previous steps until the last point is reached. Every cycle can be done with a small chain size and only consumes a minimum of computing time. This results in an good approximation of all parameter's initial values. The actual fit can then be performed in reasonable amounts of time. In advance to the conducted transmission function measurements one data set is shown in fig. A.3. On the left-hand side the actual measurement is shown, for reasons of simplicity this is drawn without proper errorbars for the time being. Again, the right-hand side directly compares both differentiation methods, with the result of the three-point formula in yellow and the output of the functional method in green. As expected, the classical approach yields a highly fluctuating outcome and takes on values that have to be regarded as unphysical with significantly negative values on the high energy side. Additionally this algorithm is not able to keep the skewness as a characteristic of the function, or even causes the function to be skewed into the wrong direction. Contrary to this, the functional method shows its immense capabilities. The function is much smoother and keeps important features manifest. Even without artificially introduced boundaries at the low and high energy sides the result provides physically sound values.

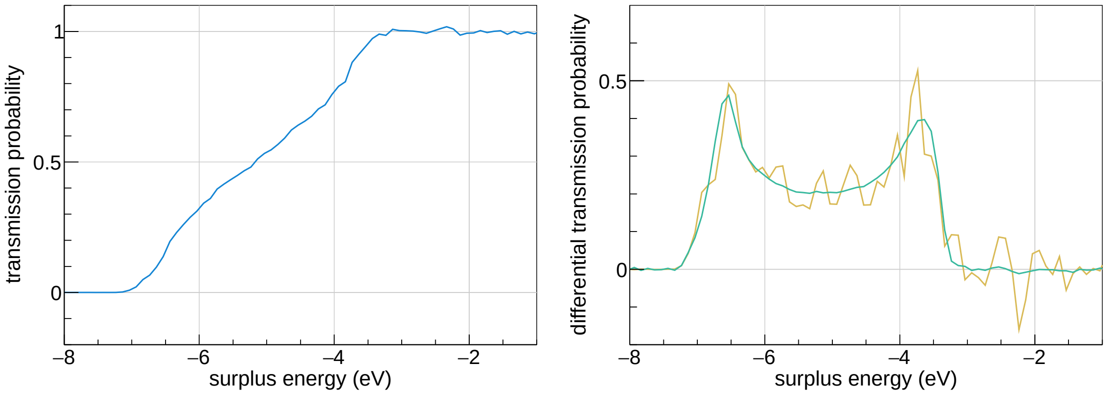

(a) Noisy transmission function **(b)** Classical and functional differentiation

Figure A.3: (a) The transmission function data from an actual measurement. The noisy function gets differentiated (b) by use of the three-point rule (yellow) and the functional method (green). As before, the conventional method amplifies noise greatly and yields bad if not even unphysical results. Especially the skewness parameter will be changed, as the right peaks high increases. Applying the functional method, the gained result is much smoother and describes the data well, as will be shown in the analysis section.

Bibliography

[Ade15] Ade, P. A. R. et al. (Planck Collaboration): 'Planck 2015 results. XIII. Cosmological parameters'. *Astr. and Astrophys.* (2015), vol. arXiv:1502.01589 (cit. on p. 5).

[Ago13] Agostini, M. et al.: 'Results on Neutrinoless Double-β Decay of ^{776}Ge from Phase I of the GERDA Experiment'. *Physical Review Letters* (2013), vol. 111. DOI: 10.1103/PhysRevLett.111.122503: p. 122503 (cit. on p. 6).

[Ams15] Amsbaugh, J. F. et al.: 'Focal-plane detector system for the KATRIN experiment'. *Nucl. Inst. and Meth. in Phys. Res. A* (2015), vol. 778: pp. 40–60 (cit. on pp. 30, 31).

[Ang05] Angrik et al., J.: 'KATRIN Design Report 2004'. *FZKA Scientific Report 7090* (2005), vol. (cit. on pp. 36, 92).

[ATL12] ATLAS Collaboration: 'Observation of a new particle in the search for the Standard Model Higgs boson with the ATLAS detector at the LHC'. *Physics Letters B* (2012), vol. 716(1). DOI: 10.1016/j.physletb.2012.08.020: pp. 1–29 (cit. on p. 1).

[Bab14] Babutzka, Martin: 'Design and development for the Rearsection of the KATRIN experiment'. doctoral thesis. 2014 (cit. on p. 26).

[Bab11] Babutzka, Martin: 'Untersuchung eines verfahrbaren Monitordetektors zur Überwachung der Aktivität des β-Zerfalls in der kryogenen Pumpstrecke bei KATRIN'. diploma thesis. 2011 (cit. on pp. 26, 27).

[Bau13a] Bauer, S et al.: 'Next generation KATRIN high precision voltage divider for voltages up to 65kV'. *Journal of Instrumentation* (2013), vol. 8. DOI: 10.1088/1748-0221/8/10/P10026: P10026 (cit. on p. 64).

[Bau13b] Bauer, Stephan: 'Energy calibration and stability monitoring of the KATRIN experiment'. doctoral thesis. 2013 (cit. on pp. 27, 48, 64, 65).

[Bea80] Beamson, G., H. Q. Porter, and D. W. Turner: 'The collimating and magnifying properties of a superconducting field photoelectron spectrometer'. *Journal of Physics E* (1980), vol. 13(1). DOI: 10.1088/0022-3735/13/1/018: p. 64 (cit. on p. 10).

[Bec10] Beck, M. and K. et al. Valerius: 'Effect of a sweeping conductive wire on electrons stored in a Penning-like trap between the KATRIN spectrometers'. *The European Physical Journal A* (2010), vol. 44(3). DOI: 10.1140/epja/i2010-10959-1: pp. 499–511 (cit. on p. 15).

[Beh16] Behrens, Jan. doctoral thesis in preparation. 2016 (cit. on pp. 24, 29, 41, 43, 107, 113, 115).

[Bel95] Belesev, A. I. et al.: 'Results of the Troitsk experiment on the search for the electron antineutrino rest mass in tritium beta-decay'. *Physics Letters B* (1995), vol. 350(2). DOI: 10.1016/0370-2693(95)00335-I: pp. 263–272 (cit. on p. 15).

[Bes10] Beskers, Bastian: 'Messung und Optimierung der Eigenschaften des Monitordetektors für keV-Elektronen in der kryogenen Pumpstrecke des KATRIN Experiments'. diploma thesis. 2010 (cit. on p. 27).

[Bod11] Bode, Tobias: 'Optimierung des 2-Phasen-Kühlkonzepts für den WGTS-Demonstrator von KATRIN'. diploma thesis. Karlsruhe Institute of Technology, 2011 (cit. on p. 26).

[Bot12] Bottesch, Richard: 'Set-up of the motion control and characterization of the ablation laser for the condensed $^{83\mathrm{m}}$Kr conversion electron source of the KATRIN experiment'. diploma thesis. 2012 (cit. on p. 27).

[Byr05] Byrne, J.: 'Experience with high electric and magnetic Penning traps'. *FZK Karlsruhe* (2005), vol. released talk (cit. on p. 15).

[Cha11] Chartrand, Rick: 'Numerical Differentiation of Noisy, Nonsmooth Data'. *ISRN Applied Mathematics* (2011), vol. vol. 2011. DOI: 10.5402/2011/164564 (cit. on p. 140).

[Chi10] Chilingaryan, S., A. Beglarian, A. Kopmann, and S. Vöcking: 'Advanced data extraction infrastructure: Web based system for management of time series data'. *Journal of Physics: Conference Series* (2010), vol. 219(4). DOI: 10.1088/1742-6596/219/4/042034: p. 042034 (cit. on p. 44).

[Chi13] Chirkov, Stanislav: 'Verifikation der Energiekalibration und Untersuchung von Störeinflüssen am KATRIN Hochspannungssystem'. diploma thesis. 2013 (cit. on p. 58).

[CMS12] CMS Collaboration: 'Observation of a new boson at a mass of 125 GeV with the CMS experiment at the LHC'. *Physics Letters B* (2012), vol. 716(1). DOI: 10.1016/j.physletb.2012.08.021: pp. 30–61 (cit. on p. 1).

[Cor14] Corona, Thomas: 'Methodology and Application of High Performance Electrostatic Field Simulation in the KATRIN Experiment'. doctoral thesis. 2014 (cit. on p. 39).

[Don70] Doniach, S. and M. Sunjic: 'Many-electron singularity in X-ray photoemission and X-ray line spectra from metals'. *Journal of Physics C: Solid State Physics* (1970), vol. 3(2). DOI: 10.1088/0022-3719/3/2/010: p. 285 (cit. on p. 75).

[Dre13] Drexlin, G., V. Hannen, S. Mertens, and C. Weinheimer: 'Current Direct Neutrino Mass Experiments'. *Advances in High Energy Physics* (2013), vol. DOI: 10.1155/2013/293986: p. 293986 (cit. on p. 6).

[Dre15a] Drexlin, Guido: *Excited Molecules and Atoms as background source.* internal KATRIN talk, 28th collaboration meeting. 2015 (cit. on p. 124).

[Dre15b] Drexlin, Guido: *Rydberg states of hydrogen atoms - a novel source of background.* internal KATRIN talk, SDS2b Workshop, KIT. 2015 (cit. on p. 124).

[Dyb16] Dyber, Stephan. doctoral thesis in preparation. 2016 (cit. on p. 27).

[Eic08] Eichelhardt et al., F.: 'First Tritium Results of the KATRIN Test Experiment Trap'. *Fusion Science and Technology* (2008), vol. 54(2): pp. 615–618 (cit. on p. 27).

[Erh14] Erhard et al., M.: 'High-voltage monitoring with a solenoid retarding spectrometer at the KATRIN experiment'. *Journal of Instrumentation* (2014), vol. 9. DOI: 10.1088/1748-0221/9/06/P06022: P06022 (cit. on pp. 29, 74).

[Erh16a] Erhard et al., M.: *The air coil system of the KATRIN experiment.* publication in preparation. 2016 (cit. on p. 39).

[Erh12] Erhard, M.: 'Untersuchung der Langzeitstabilität des nuklearen Standards für die Energieskala des KATRIN-Experiments'. diploma thesis. Karlsruhe Institute of Technology, 2012 (cit. on p. 29).

[Erh16b] Erhard, Moritz. doctoral thesis in preparation. 2016 (cit. on pp. 17, 24, 39, 41, 43, 107, 108).

[Fis15] Fischer, Sebastian: 'Commissioning of the KATRIN Raman system and durability studies of optical coatings in glove box and tritium atmospheres'. doctoral thesis. 2015 (cit. on p. 25).

[Fra10] Fraenkle, F.: 'Background Investigations of the KATRIN Pre-Spectrometer'. doctoral thesis. 2010 (cit. on p. 28).

[Fra14] Fraenkle, F., F. Glück, and K. Valerius et al.: 'Penning discharge in the KATRIN pre-spectrometer'. *Journal of Instrumentation* (2014), vol. 9(1). DOI:10.1088/1748-0221/9/07/P07028: P07028 (cit. on p. 15).

[Fra06] Fraenkle, Florian: 'Erste Messungen der elektromagnetischen Eigenschaften des KATRIN Vorspektrometers'. diploma thesis. Karlsruhe Institute of Technology, 2006 (cit. on p. 28).

[Glu13] Glueck, F. et al.: 'Electromagnetic design of the large-volume air coil system of the KATRIN experiment'. *New Journal of Physics* (2013), vol. 15. DOI: 10.1088/1367-2630/15/8/083025: p. 083025 (cit. on p. 38).

[Goe14] Goerhardt, Stefan: 'Background Reduction Methods and Vacuum Technology at the KATRIN Spectrometers'. doctoral thesis. 2014 (cit. on pp. 14, 28, 29, 35, 124).

[Gou10] Goullon, Johannes: 'Installation and commissioning of the monitor spectrometer'. diploma thesis. Karlsruhe Institute of Technology, 2010 (cit. on p. 29).

[Gro15a] Groh, S. et al.: 'First measurement and simulation of the electromagnetic properties of the KATRIN main spectrometer'. *New Journal of Physics* (2015), vol. paper in preparation (cit. on p. 43).

[Gro15b] Groh, Stefan: 'Modeling of the Response Function and Measurement of Transmission Properties of the KATRIN Experiment'. doctoral thesis. 2015 (cit. on pp. 12, 14, 17, 24, 26, 43, 106, 129, 130).

[Gro13] Grohmann and T. Bode and M. Hötzel and H. Schön and M. Süsser and T. Wahl, S.: 'The thermal behaviour of the tritium source in KATRIN'. *Cryogenics* (2013), vol. 55 - 56. DOI: 10.1016/j.cryogenics.2013.01.001: pp. 5–11 (cit. on p. 26).

[Gro11] Grohmann, S., T. Bode, H. Schön, and M. Süsser: 'Precise temperature measurement at 30 K in the KATRIN source cryostat'. *Cryogenics* (2011), vol. 51(8). DOI: 10.1016/j.cryogenics.2011.05.001: pp. 438–445 (cit. on p. 26).

[Grö10] Grössle, Robin: 'Konzeptionierung und Systematik der Hochspannungsversorgung für das KATRIN Experiment'. diploma thesis. 2010 (cit. on p. 18).

[Hab09] Habermehl, Florian: 'Electromagnetic measurements with the KATRIN pre-spectrometer'. doctoral thesis. Universität Karlsruhe, 2009 (cit. on p. 28).

[Hac15] Hackenjos, Moritz: 'Die Differentielle Pumpstrecke des KATRIN-Experiments - Inbetriebnahme und Charakterisierung des Supraleitenden Magnetsystems'. master thesis. 2015 (cit. on p. 27).

[Hae53a] Haefer, R.: 'Die Zündspannung von Gasentladungen unter dem Einfluss eines transversalen Magnetfeld in Druckbereich von 10 bis 10^{-8} Torr'. *Acta Physica Austriaca* (1953), vol. 7: pp. 52–90 (cit. on p. 14).

[Hae53b] Haefer, R.: 'Über den Mechanismus der Zündung einer elektrischen Gasentladung unter der Einwirkung eines transversalen Magnetfeldes in Druckbereich 10 bis 10^{-8} Torr'. *Acta Physica Austriaca* (1953), vol. 7: pp. 251–278 (cit. on p. 14).

[Han13] Hannen, V., S. Bauer, L. Josten, H.-W. Ortjohann, C. Weinheimer, D. Winzen, M. Zacher, and M. Zboril: *Main Spectrometer Electron-Gun Specification.* internal KATRIN document. 2013 (cit. on pp. 42, 43).

[Har89] Haraa, M., H. Shigematsua, S. Yanoa, K. Yamafuji, M. Takeo, and K. Funaki: ‘Influence of transverse magnetic field on breakdown characteristics of vacuum, gaseous helium at low temperature and liquid helium’. *Cryogenics* (1989), vol. 29(4). DOI: 10.1016/0011-2275(89)90278-6: pp. 448–456 (cit. on p. 14).

[Har12] Harms, Fabian: ‘Assembly and First Results of the KATRIN Focal-Plane Detector System at KIT’. diploma thesis. 2012 (cit. on p. 30).

[Har15] Harms, Fabian Thomas: ‘Characterization and Minimization of Background Processes in the KATRIN Main Spectrometer’. doctoral thesis. 2015 (cit. on pp. 5, 14, 26, 29, 34–36, 40, 45, 85, 124).

[Hel02] Helmer, R. L. et al.: ‘First Results from the Sudbury Neutrino Observatory’. *Nucl. Phys. B (Proc. Suppl.)* (2002), vol. 111(1 - 3). DOI: 10.1016/S0920-5632(02)01693-6: pp. 122–127 (cit. on p. 2).

[Hig08] Higaki, H., K. Ito, K. Kira, and H. Okamoto: ‘Electrons Confined with an Axially Symmetric Magnetic Mirror Field’. *AIP Conference Proceedings* (2008), vol. 1037. DOI: 10.1063/1.2977830: pp. 106–114 (cit. on p. 14).

[Hig07] Higaki, H., K. Ito, W. Saiki, Y. Omori, and H. Okamoto: ‘Properties of non-neutral electron plasmas confined with a magnetic mirror field’. *Phys. Rev. E* (2007), vol. 75(6). DOI: 10.1103/PhysRevE.75.066401: p. 066401 (cit. on p. 14).

[Hil16] Hilk, Daniel. doctoral thesis in preparation. 2016 (cit. on pp. 29, 128).

[Hil11] Hillen, Bjoern: ‘Untersuchung von Methoden zur Unterdrückung des Spektrometeruntergrunds beim KATRIN Experiment’. doctoral thesis. 2011 (cit. on p. 15).

[Hug10] Hugenberg, K.: ‘An angular resolved pulsed UV LED photoelectron source for KATRIN’. *Progress in Particle and Nuclear Physics* (2010), vol. 64(2). DOI: 10.1016/j.ppnp.2009.12.031: pp. 288–290 (cit. on p. 26).

[Jan03] Janev, R. K., D. Reiter, and U. Samm: ‘Collision Processes in Low-Temperature Hydrogen Plasmas’. *Berichte des Forschungszentrums Jülich* (2003), vol. 4105 (cit. on p. 124).

[Jan15] Jansen, Alexander: ‘The Cryogenic Pumping Section of the KATRIN Experiment - Design Studies and Experiments for the Commissioning’. doctoral thesis. 2015 (cit. on pp. 27, 28).

[Kaj98] Kajita, T. for the Super-Kamiokande and Kamiokande collaborators: ‘Atmospheric neutrino results from Super-Kamiokande and Kamiokande’. *Nucl. Phys. B (Proc. Suppl.)* (1998), vol. 77. DOI: 10.1016/S0920-5632(99)00407-7: pp. 123–132 (cit. on p. 2).

[KAT14a] KATRIN Collaboration: *Patch Panel Configuration.* internal KATRIN document. 2014 (cit. on p. 56).

[KAT14b] KATRIN Collaboration: *SDS status dislpay.* internal KATRIN document. 2014 (cit. on p. 57).

[Kle14] Kleesiek, Marco: 'A Data Analysis and Sensitivity-Optimization Framework for the KATRIN Experiment'. doctoral thesis. 2014 (cit. on pp. 3, 24, 25, 30, 43, 48, 131, 141).

[Kos12] Kosmider, Andreas: 'Tritium Retention Techniques in the KATRIN Transport Section and Commissioning of its DPS2-F Cryostat'. doctoral thesis. Karlsruhe Institute of Technology, 2012 (cit. on p. 27).

[Kra12] Kraus, Marcel: 'Kalibration und Entwicklung von Komponenten für das KATRIN Präzisions-Hochspannungssystem'. diploma thesis. 2012 (cit. on pp. 18, 23, 65–69, 71).

[Kru83] Kruit, P. and F. H. Read: 'Magnetic field paralleliser for 2π electron-spectrometer and electron-image magnifier'. *Journal of Physics E* (1983), vol. 16(4). DOI: 10.1088/0022-3735/16/4/016: p. 313 (cit. on p. 10).

[Lei14] Leiber, Benjamin: 'Investigations of background due to secondary electron emission in the KATRIN-experiment'. doctoral thesis. Karlsruhe Institute of Technology, 2014 (cit. on p. 14).

[Lob85] Lobashev, V. M.: 'A method for measuring the electron antineutrino rest mass'. *Nucl. Inst. and Meth. in Phys. Res. A* (1985), vol. 240(2). DOI: 10.1016/0168-9002(85)90640-0: pp. 305–310 (cit. on p. 7).

[Luk12] Lukic et al., S.: 'Measurement of the gas-flow reduction factor of the KATRIN DPS2-F differential pumping section'. *Vacuum* (2012), vol. 86(8). DOI: 10.1016/j.vacuum.2011.10.017: pp. 1126–1133 (cit. on p. 27).

[Luo06] Luo and Chr. Day and V. Hauer and O.B. Malyshev and R.J. Reid and F. Sharipov, X.: 'Monte Carlo simulation of gas flow through the KATRIN DPS2-F differential pumping system'. *Vacuum* (2006), vol. 80(8). DOI: 10.1016/j.vacuum.2005.11.044: pp. 864–869 (cit. on p. 27).

[Mer12] Mertens, Susanne: 'Study of Background Processes in the Electrostatic Spectrometers of the KATRIN experiment'. doctoral thesis. 2012 (cit. on pp. 15, 27, 28).

[Oli14] Olive, K. A. et al. (Particle Data Group): '090001 (2014) Review of Particle Physics'. *Chin. Phys. C* (2014), vol. 38. DOI: 10.1088/1674-1137/38/9/090001 (cit. on pp. 2, 3, 7).

[Ott94] Otten, E.: 'The Mainz neutrino mass experiment'. *Prog. Part. Nucl. Phys.* (1994), vol. 32. DOI: 10.1016/0146-6410(94)90016-7: pp. 153–171 (cit. on p. 7).

[Pen36] Penning, F. M.: 'Die Glimmentladung bei niedrigem Druck zwischen koaxialen Zylindern in einem axialen Magnetfeld'. *Physica* (1936), vol. 3(9). DOI: 10.1016/S0031-8914(36)80313-9: pp. 873–894 (cit. on p. 14).

[Pic92] Picard, A. et al.: ‘A solenoid retarding spectrometer with high resolution and transmission for keV electrons’. *Nucl. Inst. and Meth. in Phys. Res. B* (1992), vol. 63(3). DOI: 10.1016/0168-583X(92)95119-C: pp. 345–358 (cit. on p. 15).

[Pra12] Prall, M., P. Renschler, and F. Glück et al.: ‘The KATRIN pre-spectrometer at reduced filter energy’. *New Journal of Physics* (2012), vol. 14. DOI: 10.1088/1367-2630/14/7/073054: p. 073054 (cit. on p. 28).

[Pra11] Prall, Mathias: ‘Background Reduction of the KATRIN Spectrometers: Transmission Function of the Pre-Spectrometer and Systematic Test of the Main-Spectrometer Wire Electrode’. doctoral thesis. 2011 (cit. on p. 15).

[Rei09] Reimer, Stefan: ‘Ein elektrostatisches Dipolsystem zur Eliminierung von Ionen in der DPS2-F des KATRIN Experimentes’. diploma thesis. Karlsruhe Institute of Technology, 2009 (cit. on p. 27).

[Ren14] Renner, Christoph: ‘Charakterisierung und Kalibration der Spannungsquellen zur Versorgung der Drahtelektrode des KATRIN-Experiments’. bachelor thesis. 2014 (cit. on pp. 53, 54, 98).

[Res17] Rest, Oliver. doctoral thesis in preparation. 2017 (cit. on pp. 27, 49, 68, 83).

[Rob88] Robertson, R. G. H. and D. A. Knapp: ‘Direct measurement of neutrino mass’. *Annual Review of Nuclear and Particle Science* (1988), vol. 38: pp. 185–215 (cit. on p. 24).

[Röl13] Röllig, M and F. et al. Priester: ‘Activity monitoring of a gaseous tritium source by beta induced X-ray spectrometry’. *Fusion Engineering and Design* (2013), vol. 88(6 - 8). DOI: 10.1016/j.fusengdes.2012.11.001: pp. 1263–1266 (cit. on p. 26).

[Röl11] Röllig, Marco: ‘Studien zu einem Röntgendetektorsystem zur Überwachung der KATRIN Tritiumquelle’. diploma thesis. Karlsruhe Institute of Technology, 2011 (cit. on p. 26).

[Röl15] Röllig, Marco: ‘Tritium analytics by beta induced x-ray spectrometry’. doctoral thesis. 2015 (cit. on p. 26).

[Ros11] Rosendahl, Stephan: ‘Präzisionsüuberwachung und Kalibration der Hochspannung für das KATRIN-Experiment ’. doctoral thesis. Westfälische Wilhelms-Universität Münster, 2011 (cit. on p. 64).

[Sch75] Schiavone, J. A., K. C. Smyth, and R. S. Freund: ‘Dissociative excitation of H_2 by electron impact: Translational spectroscopy of long-lived high Rydberg fragment atoms’. *J. Chem. Phys.* (1975), vol. 63. DOI: 10.1963/1.431445: pp. 1043–1051 (cit. on p. 124).

[Sch79] Schiavone, J. A., S. M. Tarr, and R. S. Freund: ‘High-Rydberg atomic fragments from electron-impact dissociation of molecules’. *J. Chem. Phys.* (1979), vol. 70. DOI: 10.1063/1.437283: pp. 4468–4473 (cit. on p. 124).

[Sch13a] Schlösser, M. et al.: 'Accurate calibration of the laser Raman system for the Karlsruhe Tritium Neutrino Experiment'. *Journal of Mol. Struct.* (2013), vol. 1044. DOI: 10.1016/j.molstruc.2012.11.022: pp. 61–66 (cit. on p. 25).

[Sch13b] Schlösser, Magnus: 'Accurate calibration of the Raman system for the Karlsruhe Tritium Neutrino Experiment'. doctoral thesis. 2013 (cit. on p. 25).

[Sch16] Schönung, Kerstin: 'Unknown'. doctoral thesis. Karlsruhe Institute of Technology, 2016 (cit. on p. 62).

[Sch11] Schupp, Michael: 'Inbetriebnahme des Monitorspektrometers und erste Messungen'. diploma thesis. Karlsruhe Institute of Technology, 2011 (cit. on p. 29).

[Sch14] Schwarz, Johannes: 'The Detector System of the KATRIN Experiment - Implementation and First Measurements with the Spectrometer'. doctoral thesis. 2014 (cit. on pp. 14, 29, 30).

[Sie14] Siemens AG: *Prozessleitsystem SIMATIC PCS 7*. Catalog. 2014 (cit. on p. 43).

[Sle13] Slezak, M. et al.: 'Electron line shape of the KATRIN monitor spectrometer'. *Journal of Instrumentation* (2013), vol. 8. DOI: 10.1088/1748-0221/8/12/T12002: T12002 (cit. on p. 74).

[Sle16] Slezak, Martin. doctoral thesis in preparation. Charles University in Prague, NPI Rez, 2016 (cit. on pp. 74, 81).

[Sle11] Slezak, Martin: 'The source of monoenergetic electrons for the monitoring of spectrometer in the KATRIN neutrino experiment'. diploma thesis. Charles University in Prague, NPI Rez, 2011 (cit. on pp. 29, 74).

[Stu10] Sturm, Michael: 'Aufbau und Test des Inner-Loop-Systems der Tritiumquelle von KATRIN'. doctoral thesis. Karlsruhe Institute of Technology, 2010 (cit. on p. 25).

[Thü09] Thüemmler, T., R. Marx, and C. Weinheimer: 'Precision high voltage divider for the KATRIN experiment'. *New Journal of Physics* (2009), vol. 11. DOI: 10.1088/11367-2630/11/10/103007: p. 103007 (cit. on p. 64).

[Thü07] Thümmler, Thomas: 'Präzisionsüberwachung und Kalibration der Hochspannung für das KATRIN-Experiment '. doctoral thesis. Westfälische Wilhelms-Universität Münster, 2007 (cit. on pp. 64, 66).

[Tro16] Trost, Nikolaus. doctoral thesis in preparation. 2016 (cit. on p. 29).

[Ubi09] Ubieto-Diaz and D. Rodriguez and S. Lukic and Sz. Nagy and S. Stahl and K. Blaum, M.: 'A broad-band FT-ICR Penning trap system for KATRIN'. *International Journal of Mass Spectrometry* (2009), vol. 288(1 - 3). DOI: 10.1016/j.ijms.2009.07.003: pp. 1–5 (cit. on p. 27).

[Ubi11] Ubieto-Diaz, M.: 'Off-line commissioning of a non-destructive FT-ICR detection system for monitoring the ion concentration in the KATRIN beamline'. doctoral thesis. Ruprecht-Karls-Universität, Heidelberg, Germany, 2011 (cit. on p. 27).

[Ull12] Ullrich, T. and Z. Xu: *Treatment of Errors in Efficiency Calculations.* arXiv:physics/0701199v2. 2012 (cit. on p. 100).

[Val11] Valerius, K., H. Hein, H. Baumeister, M. Beck, K. Bokeloh, J. Bonn, F. Glück, H.W. Ortjohann, B. Ostrick, M. Zboril, and Ch. Weinheimer: 'Prototype of an angular-selective photoelectron calibration source for the KATRIN experiment'. *Journal of Instrumentation* (2011), vol. 6. DOI: 10.1088/1748-0221/6/01/P01002 (cit. on p. 26).

[Wac15] Wack, Oliver: 'Automation of high-precision calibrations for the KATRIN high-voltage system'. master thesis. 2015 (cit. on pp. 55, 66, 68).

[Wal13] Wall, Brandon Lee: 'Karlsruhe Tritium Experiment: Detector System Commissioning and In-Situ PIN-Diode Array Dead-Layer Measurement'. doctoral thesis. 2013 (cit. on p. 30).

[Wan13] Wandkowsky, Nancy: 'Study of background and transmission properties of the KATRIN spectrometers'. doctoral thesis. 2013 (cit. on pp. 28, 29, 42).

[Wan08a] Wang, D., S. Ding, and S. Lin: 'The influence of the oscillating electric field on the recurrence spectra of a Li Rydberg atom in a strong magnetic field'. *Journal of Physics B: Atomic, Molecular and Optical Physics* (2008), vol. 36(21). DOI: http://dx.doi.org/10.1088/0953-4075/36/21/003: p. 4225 (cit. on p. 128).

[Wan08b] Wang, D and A. Wub: 'The recurrence spectra of the Rydberg hydrogen atom interacting with a metallic surface and an electric field'. *Journal of Electron Spectroscopy and Related Phenomena* (2008), vol. 165. DOI: 10.1016/j.elspec.2008.07.001: pp. 36–41 (cit. on p. 128).

[Wei16] Weinheimer et al., C.: *New independent absolute calibration of precision high voltage dividers.* publication in preparation. 2016 (cit. on pp. 65, 83).

[Wie12] Wiedmann, Vanessa: 'Systematische Untersuchungen zur Hochspannungsstabilisierung am KATRIN Monitorspektrometer'. diploma thesis. 2012 (cit. on p. 18).

[Win11] Windberger, Alexander: 'Berechnungen und Simulationen zum Verhalten von Ionen in der differenziellen Pumpstrecke des KATRIN-Experiments'. diploma thesis. Karlsruhe Institute of Technology, 2011 (cit. on p. 27).

[Wol16] Wolf, J. et al.: *Commissioning of the vacuum system of the KATRIN Main Spectrometer.* paper in preparation. 2016 (cit. on pp. 34, 35).

[Wol15] Wolf, Joachim: *Radon Processes in the KATRIN Experiment.* Spring Meeting of the German Physical Society, Berlin. 2015 (cit. on p. 34).

[Wüs16] Wüstling et al., S.: *High precision high voltage post regulation system for the KATRIN experiment.* paper in preparation. 2016 (cit. on pp. 59, 61).

[Wüs13] Wüstling, S.: *Personal communication.* 2013 (cit. on p. 52).

[Zac09] Zacher, Michael: ‘Electromagnetic design and field emission studies for the inner electrode system of the KATRIN main spectrometer’. diploma thesis. Westfälische Wilhelms-Universität Münster, 2009 (cit. on p. 11).

[Zac15] Zacher, Michael: ‘Electromagnetic design and field emission studies for the inner electrode system of the KATRIN main spectrometer’. doctoral thesis. Westfälische Wilhelms-Universität Münster, 2015 (cit. on p. 43).

[Zbo11] Zboril, Miroslav: ‘Solid electron sources for the energy scale monitoring in the KATRIN experiment’. doctoral thesis. Westfälische Wilhelms-Universität Münster, 2011 (cit. on pp. 29, 74, 83).

[Zub11] Zuber, Kai: ‘Neutrino Physics’. *CRC Press* (2011), vol. 2. ISBN: 978-1-4200-6471-1 (cit. on pp. 2, 4).

List of Figures

List of Tables

Acronyms

Notation	**Description**
ADEI	advanced data-extraction infrastructure
$C\nu B$	cosmic neutrino background
CDF	cumulative probability density function
cFP	compact field point
CKM	Cabibbo-Kobayashi-Maskawa
CPS	cryogenic pumping section
DAQ	data acquisition
DET	detector
e-gun	electron gun
EMCS	earth magnetic field compensation system
FPD	focal plane detector
FT-ICR	Fourier transform-ion cyclotron resonance
GUT	Grand Unified Theory
HOPG	highly ordered pyrolytic graphic
HV	high voltage
IE	inner electrode
KaLi	KATRIN library
KATRIN	Karlsruhe Tritium Neutrino
KIT	Karlsruhe Institute of Technology
LFCS	low-field correction system
LHC	Large Hadron Collider
LN2	liquid nitrogen
MAC-E	Magnetic-adiabetic collimation combined with an electrostatic filter
MC	Monte Carlo
MCMC	Markov Chain Monte Carlo

Notation	Description
MoS	monitor spectrometer
MS	main spectrometer
NEG	non-evaporable getter
ORCA	object-oriented real-time control and acquisition
PCH	pinch
PDF	probability density function
PLC	programmable logic controller
PMF	probability mass function
PMMA	Polymethylmethacrylate
POM	Polyoxymethylene
PR	post regulation
PS1	pre-spectrometer magnet 1
PS2	pre-spectrometer magnet 2
PTB	National Metrology Institute of Germany
PTFE	Polytetrafluoroethylene
SDS	spectrometer and detector section
SDS-I	first commissioning phase of the spectrometer and detector section
SDS-II	second commissioning phase of the spectrometer and detector section
SDS-IIA	SDS-II part A
SDS-IIB	SDS-II part B
SM	Standard model of elementary particles
SNO	Sudbury Neutrino Observatory
TMP	turbo molecular pump
UHV	ultra high vacuum
WGTS	windowless gaseous tritium source

Acknowledgments

Hiermit möchte ich mich bei allen Menschen, die zum gelingen dieser Doktorarbeit beigetragen haben, bedanken.

- Prof. Dr. Guido Drexlin für die außgesprochen gute und sehr motivierende Betreuung während der letzten drei Jahre und dafür, dass er mir die Möglichkeit gegeben hat meine Promotion in einem so spannenden und abwechslungsreichen Umfeld wie dem KATRIN Experiment durchzuführen.
- Prof. Dr. Ulrich Husemann der sich freundlicherweise zur Übernahme der Korreferenz dieser Arbeit bereiterklärt und mir mit tollen Korrekturen geholfen hat.
- Thomas Thümmler dafür mich durch alle akademischen Höhen und Tiefen zu begleiten.
- Klaus Schlösser, der mich insbesondere am Anfang meiner Arbeit am Monitorspektrometer unerstützt hat.
- Sascha Wüstling, Oliver Wack, Oliver Rest und Christian Weinheimer für die tolle Zusammenarbeit im HV-Task.
- Moritz Erhard, Fabian Harms den konstanten Beschuss durch Nerf-Guns.
- Dr. Stefan Groh, Dr. Marco Kleesiek und Dr. Johannes Schwarz für die unendlich viele Hilfe in den letzten Jahren .
- Allen Ingenieuren und Technikern ohne deren unerbittlichen Einsatz keine der in dieser Arbeit beschriebenen Messungen hätte stattfinden können. Ein besonderer Dank geht hierbei an Armen Beglarian, Bernard Bender, Holger Frenzel, Martin Jäger, Alan Kumb und Klaus Mehret!
- Allen KATRIN Young Scientists für die sehr gute Atmosphäre innerhalb der Arbeitsgruppe.
- Franz Sefrin, Marc Staiger und Dalma Staiger für ihre Freundschaft

Besonders möchte ich mich bei meinen Eltern bedanken, die mir immer den Rücken stärkten und die Promotion erst möglich gemacht haben.